

High-Order Harmonic Spectroscopy with Water Droplets

Von der Fakultät für Mathematik und Physik
der Gottfried Wilhelm Leibniz Universität Hannover
zur Erlangung des Grades

Doktor der Naturwissenschaften

- Dr. rer. nat. -

genehmigte Dissertation

von

Dipl.-Phys. Heiko Gustav Kurz

geboren am 25.04.1982 in Gifhorn

2013

Referent: Prof. Dr. U. Morgner
Korreferent: Prof. Dr. M. Lein
Korreferent: Dr. H. Merdji
Tag der Promotion: 14.02.2014

Kurzfassung

Heiko G. Kurz

Spektroskopie von Wassertröpfchen unter Verwendung hoher harmonischer Strahlung

Hohe harmonische Strahlung (engl.: *high-order harmonic generation*, HHG) kann zur Messung ultraschneller Prozesse, wie der Dynamik von Elektronenbewegungen auf atomarer Größenordnung genutzt werden. Durch den HHG-Prozess beinhaltet die emittierte Strahlung intrinsisch Informationen über die Struktur des verwendeten Mediums (engl.: *Target*), welche mit Hilfe spektroskopischer Methoden analysiert werden kann. Für gewöhnlich werden gasartige Targets für die nichtlineare Frequenzkonversion vom infraroten- in den extrem-ultravioletten Spektralbereich verwendet. Diese sind jedoch in ihrer maximalen Dichte limitiert, was eine Beschränkung der Anzahl der zur Konversion beitragenden Emitter zur Folge hat und daher die Effizienz des Prozesses begrenzt.

In dieser Arbeit wird die Erzeugung hoher harmonischer Strahlung mit Wassertröpfchen auf der Mikrometerebene in einem *in-situ* Anregungs-Abfrage-Experiment (engl.: *pump-probe experiment*) untersucht. Das Tröpfchen vollzieht dabei nach der Bestrahlung mit dem Anregungspuls einen thermodynamischen Phasenübergang von der flüssigen in die gasartige Phase. Durch die Zeitverzögerung zwischen den beiden Pulsen kann das Tröpfchen in einem weiten Dichtebereich präpariert werden, welcher von Flüssigkeiten bis hin zu stark verdünnten Gasen reicht. Zur Erzeugung der harmonischen Strahlung innerhalb des präparierten Targets wird der Abfragepuls verwendet. Da die emittierte Strahlung strukturelle Informationen über den Zustand des Tröpfchens enthält, ermöglicht diese das Target mit Hilfe spektroskopischer Methoden zu charakterisieren. Eine Analyse der Phasenangepassungseigenschaften des Tröpfchens lässt dabei die Identifikation des zeitabhängigen thermodynamischen Phasenverlaufs zu, wodurch die optimalen Bedingungen für die Erzeugung hoher harmonischer Strahlung ermittelt, sowie deren Konversionseffizienz bestimmt werden kann.

Von besonderem Interesse sind die Dichten des Targets, welche zu einem kleineren mittleren Teilchenabstand als die Exkursionslänge des Elektrons während des HHG-Prozesses führen. In diesem Fall werden die Elektronentrajektorien von benachbarten Partikeln gestört, was in einer Unterdrückung des Emissionsprozesses resultiert. Zum tieferen Verständnis der Messwerte werden Simulationen der Elektronentrajektorien verwendet.

Nach der Ermittlung der optimalen Bedingungen für HHG wird die emittierte Strahlung verwendet, um den Expansionsprozess des Tröpfchens detailliert zu untersuchen. Während der Expansionsmechanismus für hohe Intensitäten des Anregungspulses plasmabasiert ist, kann die Expansion des Tröpfchens für niedrigere Intensitäten durch nichtlineare Absorption beschrieben werden. Die emittierte Strahlung erlaubt zwischen beiden Expansionarten zu unterscheiden und ermöglicht Rückschlüsse auf die Zusammensetzung des Targets auf atomarer Ebene. Die Messungen zeigen, dass das Tröpfchen bei hohen Pulsintensitäten von Ionen dominiert wird. Mit Hilfe von Simulationen wird ein Maß für die Ionisation innerhalb des Targets ermittelt, was die Beobachtung ionisationsinduzierter Störungen der Elektronentrajektorien ermöglicht. Darüber hinaus kann das Tröpfchen in einem Zustand präpariert werden, welcher von neutralen Partikeln dominiert ist und durch die emittierte harmonische Strahlung beobachtet werden kann.

Schlagnworte: ultrakurze Pulse, Erzeugung hoher harmonischer Strahlung, Wassertröpfchen, laserinduzierter optischer Durchbruch

Abstract

Heiko G. Kurz

High-Order Harmonic Spectroscopy with Water Droplets

High-order harmonic generation (HHG) is a well-established tool which can be applied for the measurement of ultra-fast dynamics, such as the dynamics of electrons on the atomic length scale. Through the process of HHG, the emitted radiation intrinsically contains structural information on the target, which can be retrieved by applying spectroscopic methods. Common approaches apply gaseous targets for the non-linear frequency conversion from the infrared into the extreme-ultraviolet spectral domain. These targets are however limited in the applicable density which confines the number of emitters and therefore limits the efficiency of the process.

In this thesis, high-order harmonic generation from dense micrometer-sized water droplets is investigated in an *in-situ* pump-probe experiment. The droplet therein performs a thermodynamic transition from the liquid into the gas phase upon irradiation by the pump pulse. By adjusting the time delay between the two pulses, the target can be prepared in an extraordinary wide density range, reaching from liquid density to diluted gases. The harmonic radiation is thereafter generated by the probe pulse in the prepared droplet. Since information on the state of the target is imprinted onto the harmonic radiation, the droplet is characterized by applying high-order harmonic spectroscopic methods. Studying the phase-matching properties of the target allows to identify the expansion of the droplet and its thermodynamic phase as a function of time. Optimized conditions of the target for HHG are determined and the harmonic yield is measured.

In particular, the droplet is prepared at high densities, resulting in a mean inter-particle distance smaller than the electronic excursion during HHG. In this case, the electronic trajectories are perturbed by surrounding particles which leads to a suppression of the emission process. Simulations of the electronic excursion are used to interpret the experimental results for high densities.

After determining the optimized conditions for HHG, the emitted radiation is used to characterize the expansion process of the droplet in detail. The expansion mechanism is plasma triggered for pulse intensities above the threshold intensity for *laser-induced breakdown*, while it is described by nonlinear absorption for lower intensities. The emitted harmonic radiation is used to distinguish between these two expansion schemes and allows to determine the composition of the droplet on the atomic level as a function of its density evolution. The measurements indicate that the droplet is dominated by ions for high intensities of the pump pulse. Simulations allow to determine a measure for the amount of ionization within the target and ionization-induced trajectory distortions are observed. Furthermore, the droplet is prepared in a composition dominated by neutral particles for low intensities of the pump pulse, which is observed by the emitted harmonic radiation.

Key words: ultra-short pulses, high-order harmonic generation, droplets, water, laser-induced optical breakdown

Contents

1	Introduction	1
1.1	Motivation	2
1.2	Organization of the Thesis	3
2	Theory	5
2.1	Light-Matter Interaction	5
2.2	Ionization by Intense Laser Fields	5
2.2.1	Free Electrons in the Laser Field	6
2.3	Laser-Induced Plasmas	7
2.3.1	Description of Plasmas	7
2.4	Calculations on Droplet Expansion	8
2.4.1	Expansion Velocity	9
2.4.2	Number-Density Evolution of the Droplet	10
2.4.3	Calculation of Number Densities	10
2.4.4	Limitations of the Calculations	12
2.5	High-Order Harmonic Generation	14
2.5.1	Three-Step Model of High-Order Harmonic Generation	14
2.5.2	Lewenstein Model	17
2.5.3	High-Order Harmonic Generation in Molecules	18
2.6	Phase Matching of High-Order Harmonic Radiation	20
2.6.1	Consequences from Phase Matching	24
2.6.2	HHG in Dense Targets	25
2.7	Generation of Attosecond Pulses	27
2.8	The Target for High-Order Harmonic Generation	28
2.8.1	From Liquid Jets to Droplets	29
3	High-Order Harmonic Generation from Water Micro Droplets	31
3.1	Experimental Setup	31
3.1.1	Optical Setup	31
3.1.2	Vacuum Setup	32
3.2	Identifying Parameters for High-Order Harmonic Generation from Liquid Droplets	35
3.2.1	Influence of the Pump-Probe Time Delay	36
3.2.2	Influence of the Intensity of the Pump Pulse	38
3.2.3	Influence of the Pulse Duration	39
3.2.4	Interaction between the Delay and the Intensity of the Pump Pulse	40
3.3	Conclusions	41
4	Phase-Matching Experiments	43
4.1	Propagation Effects	43
4.1.1	Phase Matching in a Xenon Gas Jet	43
4.1.2	Phase Matching in Water Droplets	44

4.1.3	Focus and Delay	46
4.2	Ionization-Induced Effects	48
4.2.1	Transient Phase Matching	48
4.2.2	Influence of the Pulse Duration	51
4.3	Influence of the Intensity of the Probe Pulse	55
4.3.1	Transition of Harmonic Orders from the Cutoff into the Plateau	56
4.3.2	The Highest Observed Harmonic Order	60
4.4	Mapping Time to Density	62
4.5	Selecting Electronic Trajectories via the Density of the Droplet	63
4.5.1	Calculation of Electronic Trajectories	63
4.5.2	Selecting Single Trajectories	66
4.5.3	Correlation between Intensity and Density-Dependence of the Harmonic Signal	69
4.6	The Conversion Efficiency	73
4.7	Conclusions	75
5	Revealing the Dynamics of the Droplet	77
5.1	The Expansion of the Droplet	77
5.1.1	Laser-Induced Breakdown	78
5.1.2	The Influence of the Intensity of Pump Pulse	79
5.1.3	The Threshold Intensity for Laser-Induced Breakdown	83
5.1.4	The Time and Intensity-Dependent Expansion Process	86
5.2	An Ionized Target	89
5.2.1	Distinguishing between Neutral and Ionic Targets	90
5.2.2	Ionization-Induced Trajectory Splitting	92
5.3	High-Order Harmonic Generation below the Threshold for Laser-Induced Breakdown	95
5.4	Conclusions	98
6	Conclusion and Outlook	99
	Bibliography	103
	List of Figures	115
	List of Tables	123

Abbreviations and Mathematical Symbols

ADK	Ammosov-Delone-Krainov
ATI	above threshold ionization
CCD	charge-coupled device
CE	conversion efficiency
CPA	chirped pulse amplification
FWHM	full width at half maximum
HHG	high-order harmonic generation
HOH	high-order harmonic
HOHO	highest-observed harmonic order
HOMO	highest-occupied molecular orbital
IAP	isolated attosecond pulse
IR	infrared
LIB	laser-induced breakdown
MPI	multiphoton ionization
MCP	multi-channel plate
OTBI	over-the-barrier ionization
PM	phase matching
SAEA	single active electron approximation
SFA	strong-field approximation
SHG	second harmonic generation
SIGC	semi-infinite gas cell
Ti:Sa	Titanium-Sapphire
TPM	transient phase matching
FROG	frequency-resolved optical gating
SPM	self-phase modulation
TDSE	time-dependent Schrödinger equation
TI	tunnel-ionization
THG	third harmonic generation
UHV	ultra-high vacuum
XUV	extreme ultra violet

Table 1: Abbreviations.

A	vector potential
$\alpha_{s,l}$	slope of atomic phase Φ_{at}
b	confocal parameter
β	group delay dispersion
c	speed of light in vacuum
$c.c.$	complex conjugate
d	nozzle diameter
d_x	dipole matrix element
ϵ_0	permittivity of vacuum
e	electron charge
f	frequency
E	electric field
E_L	amplitude of the fundamental field
f	focal length
ϕ_{CEO}	carrier-envelope offset phase
$\Phi_{at,q}$	atomic phase
$\Phi_{geo,q}$	geometric phase
$\Phi_{neu,q}$	phase from dispersion of neutral atoms
$\Phi_{el,q}$	phase from dispersion of free electrons
$\Phi_{tot,q}$	total phase
$\Delta\Phi$	complex phase mismatch
γ	Keldysh parameter
Im	imaginary part
I	intensity
I_{LIB}	threshold intensity for laser-induced breakdown
I_p	ionization potential (cf. Tab. 1)
I_{probe}	intensity of the probe pulse
I_{pump}	intensity of the pump pulse
I_{sat}	saturation intensity
k	wave vector
\mathbf{k}_{at}	atomic phase mismatch wave vector
Δk_{el}	phase mismatch wave vector induced by electrons
Δk_{neu}	phase mismatch wave vector induced by neutral particles
$\Delta \mathbf{k}_{tot,q}$	phase-mismatch wave vector
κ	absorption coefficient
k_B	Boltzmann constant
\mathbf{k}_{geo}	geometric wave vector mismatch
L	decay length
L_{abs}	absorption length
L_{coh}	coherence (build-up) length
L_{med}	length of the medium
λ_D	Debye length
λ_L	wavelength of the fundamental field
λ_{pert}	wavelength of perturbation

m_e	electron mass
M	ion mass
n	refractive index
$n_{\text{crit.}}$	critical density of free electrons
n_2	nonlinear refractive index
N_D	Debye sphere
n_e	density of free electrons
n_i	density of ions
η	viscosity
\mathbf{p}	canonical momentum
\mathbf{P}	polarization
P	pressure
q	harmonic order
r_0	droplet radius
r_{el}	classical electron radius
\bar{r}	mean inter-particle distance
Re	real part
ρ	number density
ρ_{cutoff}	maximum tolerable density attributed to the cutoff trajectory
ρ_{mass}	mass density
ρ_{short}	maximum tolerable density attributed to the short trajectory
S	quasi classical action
σ	surface tension
t	delay
t_i	ionization time
t_r	recombination time
T	time in optical cycles
T_e	electron temperature
T_i	ion temperature
$\tau_{\text{exc.}}$	excursion time
τ	pulse duration
U_p	ponderomotive potential
v	jet velocity
v_{ion}	ion velocity
V	droplet volume
ω_L	angular frequency of the fundamental field
ω_p	plasma frequency
x_{max}	maximum excursion distance
χ	susceptibility
z	coordinate in propagation direction
z_R	Rayleigh length
Z	degree of ionization

Table 2: Mathematical symbols.

Chapter 1

Introduction

The invention of photography in the 19th century allowed for the first time to analyse movements with a higher time resolution than the human eye. The first study of this kind was a series of photographs of a galloping horse, which allowed to identify that there was a moment in time where all four hooves of the horse were not touching the ground [Muy78]. Revealing the dynamics of this macroscopical movement required a time resolution in the millisecond range and was enabled by pure mechanical shutters of the camera. With the beginning of the exploration of the microcosm during the last century, dynamics on much shorter time scales became observable. The movement of water molecules in a liquid is for example within the picosecond range, while chemical reactions are even faster and take place within femtoseconds. An even higher time-resolution is needed when the movement of an electron on the atomic length scale is considered, which occurs on the attosecond time scale. Since mechanical solutions are limited to the millisecond range, novel techniques had to be developed in order to study these highly dynamical events.

The laser [Mai60] and the chirped-pulse amplification (CPA) technique [Str85] for the first time allowed to generate intense infrared (IR) light pulses with durations on the femtosecond time scale, which was sufficiently short to study dynamics on the molecular but not on an atomic or electronic level. The field strength of these pulses however reaches a magnitude in the order of the atomic Coulomb field, and enables light matter-interaction in a highly non-linear regime. These non-linear processes can be applied for the generation of new frequencies of the fundamental radiation in the extreme-ultraviolet spectral domain (XUV) by the process of high-order harmonic generation (HHG) which supports coherent light pulses on the attosecond time scale. High-order harmonic radiation was first observed by MCPHERSON *et al.* and FERRAY *et al.* [McP87, Fer88] in rare gas targets. A semi-classical theoretical model describing the process of HHG was developed by CORKUM [Cor93], followed by a quantum-mechanical approach by LEWENSTEIN *et al.* [Lew94]. Meanwhile, HHG is a well-established tool for the analysis of light-matter interaction [L'H91, L'H93b, L'H93a, Wah93, Sal95, Alt96, deL97, Tak07, Pap01]. The unique characteristics of the radiation allow to perform experiments which require a high temporal and a high spatial resolution, revealing phenomena on the attosecond timescale [Hen01, Kie04, Sch10] with high spatial [Dit96, LD00] and temporal coherence properties [Bel98, Lyn99]. Today, the shortest measured attosecond pulse has a duration of 67 as [Zha12], which is already less than three times the atomic unit of time (24 as).

A wide range of targets has been used for HHG, such as atoms [Fer88], molecules [Sak95] and clusters [Don96, Ruf13] in several thermodynamical phases, like gaseous [McP87], liquid [Fle03, DiC09, Kur13], solid state [Aki92, Qué06, Ghi11] or plasmas [Gan05, Whe12, Hae13]. Information on the target itself can be retrieved by applying high-order harmonic spectroscopy, which allows to study molecular dynamics during chemical reactions [Wör10b], rotational or vibrational dynamics of molecules and their influence onto the

emission of XUV-radiation [Kan05, Tor07, Vel01, Smi09, Voz11, Li08] with sub-nanometer spatial and attosecond time resolution. Even structural characteristics can be extracted on the molecular level from the harmonic signal [Tor07] by disposing tomographic imaging techniques and retrieving the structure of molecular orbitals [Ita04, Hae10, Voz11]. Also complex molecules can be analysed [Gan13], and only recently HHG from water molecules gained attention [Fle03, DiC09, Won10, Fal10, Zha11], where also the contributions of different molecular orbitals to the harmonic signal could be identified [Far11].

1.1 Motivation

The thesis examines three major topics of HHG from dense water droplets which will be motivated in the following. First, the unique properties of the liquid droplet as a target for HHG are presented and its dynamics are introduced. Second, the influence of the target on the HHG process is investigated at different densities. In particular, the influence of a high-density target onto electronic dynamics is studied theoretically and through in-situ experiments. Moreover, optimum parameters for the frequency conversion are determined. Finally, the optimized conditions for HHG are used to determine the thermodynamical phase of the droplet, as well as changes from a molecular towards an ionic target by applying high-order harmonic spectroscopy.

Different setups have been applied for the experimental realization of HHG, such as the *finite gas cell* [Tak07, Bou11] and the *semi-infinite gas cell* [Pap01, Ste09], but the most frequently used setup is the *gas jet* [Sal95, Sal97]. However, the common approaches for HHG are limited in the density of the target and in the applicable target material. Hence, an innovative approach is used to support high densities of the target: The liquid droplet. The interaction of intense laser pulses with water droplets has been studied under atmospheric conditions but on time scales from microseconds to milliseconds where complex macroscopical expansion dynamics were observed [Lin04]. The time scales of the dynamics covered by this thesis are within the nanosecond range and below, where changes of the target are even more complex. There are no measurements concerning the expansion of the droplet on these short time scales at the time of this work and in fact, not even a theoretical approach has described the dynamics so far, since the changes on the microscopical level within the droplet are too drastic to accurately model them [Lin04].

Liquid droplets also experience more attention in recent experiments concerning light-matter interaction [Fle03, Cha11, Bar11, Kur13] and can be used under vacuum conditions to overcome some of the above mentioned limitations to HHG. Supporting a high repetition rate in the MHz range, a new sample is provided for each laser pulse. Moreover, the interaction between the laser and the droplet is *debris-free*, which means no other particles are accelerated away from the interaction region and destroy the vacuum conditions, which is an advantage to solid state targets. The droplet itself benefits from its spatial confinement and mass-limitation, while similarly providing number densities up to the liquid-density regime, which is $3.35 \times 10^{22} \text{ cm}^{-3}$ in the case of water. This is a 10^5 times higher density compared to common gas jet setups. A high target density is of particular interest, as it results in a larger number of possible emitters. This might deliver a higher pulse energy in the XUV spectral domain, which is due to a maximum conversion efficiency of 10^{-5} low and large effort has to be made for the generation of pulses in the μJ -energy range [Her02, Tak02, Tos03, Bou11].

The droplet however is not a static target, and as soon as it is hit by an intense laser pulse, the ensemble of water molecules undergoes a complex transition on different levels. This

can be divided in: A time and intensity-dependent macroscopic evolution of the density reaching from liquid to gaseous densities, and a microscopic transition on the atomic level via dissociative processes of the droplet into water clusters, free water molecules, atoms and ions. The droplet therefore enables an extra-ordinary wide range of macroscopic and microscopic states, which can be studied via high-order harmonic spectroscopy. However, the droplet's dynamics are barely explored. Therefore, the laser parameters defining the different transitions of the droplet is identified first by studying the signal of the harmonic radiation.

At high densities of the target, there is a large number of potential emitters which can lead to an increase of the XUV-signal. But besides the number of emitters, the conversion efficiency from the IR to the XUV spectral domain is also determined by the single atom response [Lew94], phase matching [Sal95] and re-absorption effects [Alt96]. Since a wide range of target densities is accessible, a large variety of conditions for HHG can be prepared, such as low-density gases, gases and liquids. This makes the liquid droplet an ideal tool for studying the conversion efficiency as a function of the target density. Optimizing the conditions of the target and of the phase-matching properties for HHG is a main task of this thesis in order to achieve a high yield of the XUV-radiation. Distinguishing between the different density states however is non-trivial. A comparison of the signal of the harmonic radiation with experiments from gas targets assists in the identification of the different density regimes. Once this is done, high-density targets can be studied, where the *mean inter-particle distance* becomes smaller than the *electronic displacement* during HHG and the electron may be perturbed during its excursion in the continuum. This perturbation can lead to a loss of coherence and an enhanced suppression of the harmonic yield. In the present work, methods are therefore developed to determine the different density regimes of the droplet, enabling conclusions on the distortion of electronic trajectories during the process of HHG.

Finally, the optimized parameters for HHG and the knowledge of the density evolution of the target are used to identify the microscopic transitions of the droplet. This is done by using high-order harmonic spectroscopy, since the information on the state of the target is imprinted onto the emitted harmonic radiation. Applying a pump-probe setup, the composition of the droplet can be manipulated on the atomic level. The preparation of the target in a state dominated by clusters, molecules, atoms or ions therefore seems possible. Moreover, a theoretical study predicts the deflection of electronic trajectories in a highly ionized medium [Str05], while no distortion should be observed in neutral targets. This study can be used to measure the amount of ionization within the target and to identify the necessary parameters for the preparation of the target in different microscopical states.

1.2 Organization of the Thesis

This thesis is organized in five parts. Chapter 2 provides the theoretical concepts and models of laser-matter interaction, basic plasma physics and high-order harmonic generation. In chapter 3, the experimental setup and first HHG experiments with the liquid droplet source are presented, which lead to the identification of the parameter space defining the characteristics of the droplet. In chapter 4 high-order harmonic spectroscopy is used in in-situ experiments to identify the optimum conditions for HHG and the influence of high densities of the target onto the generation process. Chapter 5 aims to reveal the dynamics of the droplet and its composition on the macroscopic, as well as on the atomic level, upon irradiation by intense laser pulses. A conclusion and an outlook to this thesis are presented in chapter 6.

Chapter 2

Theory

This chapter describes theoretical aspects of light-matter interaction and of the generation of micrometer-sized liquid water droplets. First, light-matter interaction (sec. 2.1) and laser-induced plasma dynamics (sec. 2.3) are introduced, followed by a model for the droplet expansion (sec. 2.4). High-order harmonic generation (sec. 2.5) and phase-matching effects are described (sec. 2.6). Finally, the droplet generation is described (sec. 2.8).

2.1 Light-Matter Interaction

The classical interaction between light and matter is described by the Maxwell equations. Whenever an electro-magnetic field \mathbf{E} interacts with an atom, its electron shell is deformed and a microscopic dipole moment is induced. Summing over all microscopic dipole momenta delivers the macroscopic polarization $\mathbf{P} = \chi \mathbf{E}$, where χ denotes the susceptibility of the medium. Laser pulses can easily deliver intensities sufficiently high enough, that the nonlinear terms of χ have to be taken into account. The polarization is therefore treated in terms of perturbation theory and developed into a Taylor series

$$P = \varepsilon_0 \chi^{(1)} E + \varepsilon_0 \chi^{(2)} E^2 + \varepsilon_0 \chi^{(3)} E^3 + \dots, \quad (2.1)$$

where ε_0 describes the vacuum permittivity and $\chi^{(n)}$ the nonlinear susceptibility ($n > 1$). Using this concept, many effects like second-harmonic generation (SHG), third-harmonic generation (THG) and self-phase modulation (SPM) can be described [Mor07]. But laser pulses can be sufficiently intense to release an electron by optical field ionization which cannot be described with this concept. The quantum mechanical models of optical field ionization are therefore introduced in the next section.

2.2 Ionization by Intense Laser Fields

Optical field ionization occurs when the intensity of the incident laser field reaches a strength that is comparable to the magnitude of the atomic potential. In this case, perturbation theory fails and equation (2.1) cannot be used, so the problem has to be treated quantum-mechanically. The optical field ionization of atoms by short laser pulses was first described by Keldysh [Kel65]. Several models exist to calculate the ionization rates, like KELDYSH theory [Kel65], AMMOSOV-DELONE-KRAINOV theory (ADK) [Amm86] or PERELOMOV-POPOV-TERENT'EV theory (PPT) [Per66]. A detailed description has been done by STEINGRUBE [Ste11] and VOCKERODT [Voc12]. Depending on the intensity of the laser pulse, different ionization mechanisms dominate the process. These are in order of increasing intensity:

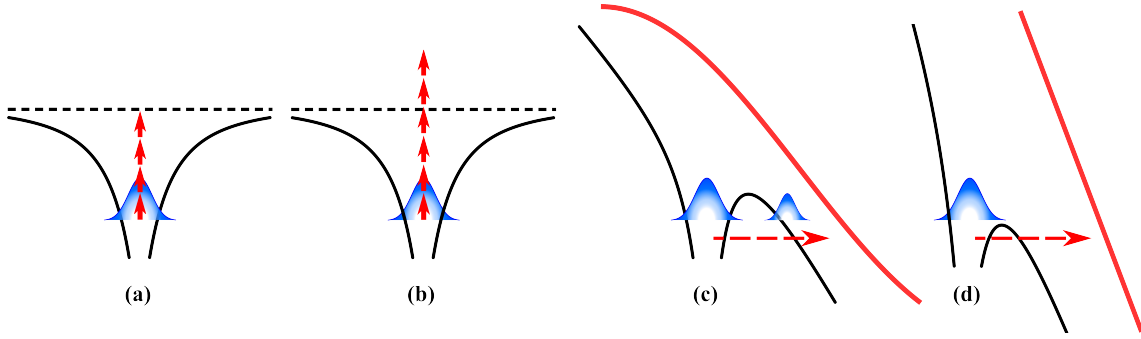


Figure 2.1: Ionization mechanisms for different intensities. All figures show the atomic potential (black), the electron wave function (blue), the external electric field (solid red) and the ionization threshold (dashed black). The different ionization mechanisms are (a) MPI, (b) ATI, (c) TI and (d) OTBI. See text for details.

Multi-Photon Ionization During multi-photon ionization (MPI), the electron simultaneously absorbs multiple photons and is lifted via virtual energy levels towards the ionization threshold (see Fig. 2.1 (a)). For example, intensities of $1.0 \times 10^{13} \text{ W/cm}^2$ are sufficient to observe MPI in Xe atoms at a wavelength of 800 nm.

Above Threshold Ionization Figure 2.1 (b) shows the above-threshold ionization mechanism (ATI). Due to the higher intensity of the laser field compared to the case of MPI, the electron absorbs more photons than necessary to reach the ionization threshold. The energy of these additional photons is transformed into kinetic energy of the electron.

Tunnel Ionization Further increase of the laser intensity to $1.0 \times 10^{14} \text{ W/cm}^2$ leads to a perturbation of the atomic potential (see Fig. 2.1 (c)). It is deformed in a way that the electron is bound only by a finite barrier through which it may tunnel with a certain probability (tunnel ionization (TI)). TI is the necessary ionization mechanism for high-order harmonic generation, which is subject of this thesis. Though the mechanism is often used in both theoretical models and experiments, there are still open questions regarding the TI process e.g. it still is unclear whether the tunnelling time is to be treated as imaginary [Sha12b] or as a real parameter [Gal12]

Over the Barrier Ionization If the intensity of the laser pulse is increased beyond values needed for TI, the atomic potential can be distorted in a way that the electron is no longer bound. The potential is tilted in a way that the electron overcomes the ionization threshold and is accelerated by the field (see Fig. 2.1 (d), over the barrier ionization (OTBI)).

2.2.1 Free Electrons in the Laser Field

Once the electron is ionized, it is accelerated by the laser field. Since the laser field is oscillating, the net acceleration only depends on the ionization time. The time averaged kinetic quiver energy the electron accumulates during the acceleration is the ponderomotive potential energy

$$U_p = \frac{e^2 E_L^2}{4 m_e \omega_L^2} = 9.34 \times 10^{-20} I \lambda_L^2 \quad \text{with } [U_p] = \text{eV}, [I] = \text{W/cm}^2, [\lambda_L] = \text{nm}, \quad (2.2)$$

where m_e and e denote the electronic mass and charge, E_L the amplitude of the electric field and ω_L the frequency and λ_L the wavelength of the laser [Win08, Lei07].

Regarding the generation of harmonic radiation, the electron is ionized via TI (cf. sec. 2.5). However, there is no strict separation between the different mechanisms of ionization. Which of the mechanisms dominates, depends on intensity and frequency of the laser, as well as the ionization threshold of the atom or molecule. A good estimate to distinguish between MPI and TI is given by the Keldysh parameter

$$\gamma = \sqrt{\frac{I_p}{2 \cdot U_p}}, \quad (2.3)$$

where I_p denotes the ionization potential [Kel65]. In the weak-field case ($\gamma > 1$), the ionization potential is large compared to the ponderomotive potential. Thus, the predominant ionization path is via MPI (see Fig. 2.1(a)). In the strong-field case, the intensity is high and $\gamma < 1$. The atomic potential is significantly perturbed and the dominant ionization path is TI (see Fig. 2.1(c)).

2.3 Laser-Induced Plasmas

In the experiments performed and described in this thesis, the intensities of the laser pulses are sufficiently high enough to ignite a plasma. This thermodynamic state can be generated by highly ionizing the target, creating a gaseous, electro-conductive ensemble of ionized and unionized particles. Since the plasma is generated from neutral matter, the sum over all charged particles stays neutral. This means the number of electrons equals the degree of ionization multiplied with the number of ions. The plasma itself is ignited most efficiently by ionizing the target via multi-photon ionization (see 2.2). The generated free electrons are accelerated in the laser field and transfer their energy in collisional processes to the surrounding particles. In these collisional processes, additional free electrons and ions are generated. A plasma is ignited.

2.3.1 Description of Plasmas

A plasma consists of many charged particles that are coupled to each other through their electric and magnetic fields. Since this is a macroscopic phenomenon, it is best described by macroscopic parameters. The temperature and density of the electrons T_e and n_e , as well as the ionic temperature and density T_i and n_i are used to characterize the plasma. In the case of a thermodynamic equilibrium, the temperature is defined by a MAXWELL-BOLTZMANN energy distribution. For an ensemble of moving electrons with velocity v_e , the temperature is defined by the mean kinetic energy:

$$E_{kin} = \frac{1}{2} m_e \bar{v}_e^2 = \frac{1}{2} k_B T_e \quad \Rightarrow \quad \bar{v}_e = \sqrt{\frac{k_B T_e}{m_e}}, \quad (2.4)$$

where k_B denotes the Boltzmann constant and m_e the mass of the electron [Düs02].

Two parameters mainly influence the characteristics of the generated plasma: The external driving field and the collision between the particles. The plasma is ignited by the external laser field. Collisional processes contribute to the energy transfer between the particles and lead to further ionization. The resulting charge distribution leads to an electric field within the plasma that influences the electrons and ions within. It is common to divide the internal electric field into two sub-fields \mathbf{E}_1 and \mathbf{E}_2 [Kru88]. The microscopic field \mathbf{E}_1 describes the vast fluctuations due to chaotic, collisional processes between the

particles. It is defined within the Debye length λ_D , within which the charge of a single particle is shielded by surrounding charges [Düs02]:

$$\lambda_D = \frac{\varepsilon_0 k_B T_e}{e^2 n_e}, \quad (2.5)$$

The Debye length allows the construction of the Debye sphere with radius λ_D

$$N_D = \frac{4}{3}\pi \cdot \lambda_D^3 \cdot n_e, \quad (2.6)$$

which allows an estimate of the number of particles within the plasma. Dense plasmas with a high density of free electrons result in a low value for N_D . In this case, a macroscopic description is justified and the second sub-field \mathbf{E}_2 is used to characterize the plasma. It describes the collective motion of electrons, forming collective oscillations named plasma waves [Teu09].

The frequency of this oscillation is the plasma frequency

$$\omega_p = \sqrt{\frac{e^2 n_e}{\varepsilon_0 m_e}}. \quad (2.7)$$

After being hit by the external field that disturbs the charge distribution, the electrons tend to oscillate with the frequency ω_p . In equation (2.7), the only variable is the density of electrons. The plasma frequency allows to distinguish between two plasma states, under-dense and over-dense. In an under-dense plasma, the frequency of the incident light is large compared to the plasma frequency. Due to the high frequency, there is no time for the electrons to respond and the plasma is transparent for the light. Its refractive index depends on the electron density and is described by:

$$n_q^e = \sqrt{1 - \left(\frac{\omega_p}{q \omega_L}\right)^2} \quad q = 1, 2, \dots, \quad (2.8)$$

where q denotes higher orders of the fundamental laser frequency ω_L [L'H91]. In an over-dense plasma, the frequency of the laser is low, compared to the plasma frequency. The electronic response is fast enough, so that a plasma mirror is formed by the electrons, reflecting the incident laser pulse. The determination between under-dense and over-dense is done by the critical electron density:

$$n_{crit} = \frac{\varepsilon_0 m_e \omega_L^2}{e^2}. \quad (2.9)$$

For $n_e < n_{crit}$ the plasma is under-dense, and vice versa. Using a Ti:Sa laser with central wavelength of 780 nm, the critical density is reached at $n_{crit} = 1.8 \times 10^{21} \text{ cm}^{-3}$.

During the laser induced ignition of a plasma, energy of the laser pulse is transferred into kinetic energy of the particles of the plasma. The irradiated target therefore starts expanding and changes its density. A model can be used to calculate the expansion process and the density evolution of the target, which is described in the following section.

2.4 Calculations on Droplet Expansion

In this thesis, micrometer-sized liquid water droplets have been used to generate high-order harmonic (HOH) radiation of the incident fundamental radiation (cf. sec. 2.5). Therefore,

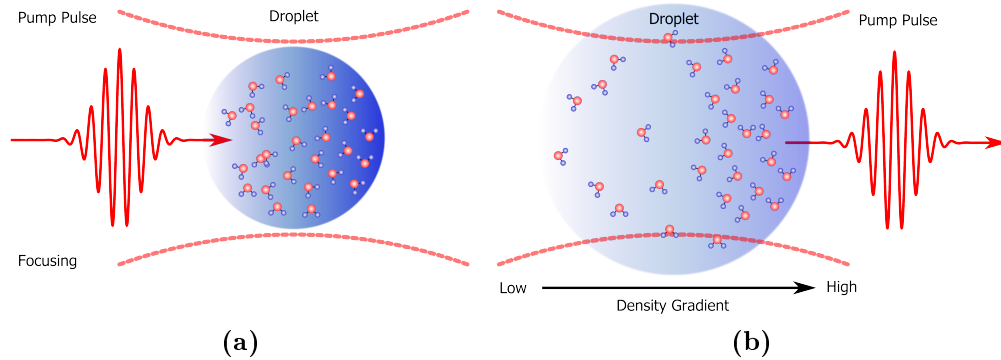


Figure 2.2: Schematic of the laser-droplet interaction. (a) depicts the incident pump pulse (solid red line) and its focusing geometry (dashed red line). The droplet is shown (blue), as well as contained water molecules. (b) shows the expanding droplet after being hit by the pump pulse. Since more energy of the laser pulse is absorbed at the side facing the incident pump pulse, the formation of a density gradient along the propagation direction of the laser is likely (black).

two time delayed intense laser pulses interact with a single droplet in a pump-probe setup under vacuum conditions. As the droplet is hit by the pump pulse (see Fig. 2.2 (a)), energy is deposited within the droplet, and it performs a transition from the liquid state to a gaseous one (cf. Fig. 2.2 (b)). The second pulse is used for high-order harmonic generation (HHG) to probe the thermodynamic state (liquid, gaseous, plasma), the microscopical state (clusters, molecules, atoms, ions), and the density of the target, depending on the energy and the time delay of the pulses. At the intensities used, a plasma can be ignited from the droplet. In order to estimate the spatio-temporal dynamics of the droplet after being hit by the pump pulse, a model will be introduced within this section to calculate the density of the target.

2.4.1 Expansion Velocity

The spatio-temporal dynamics of the droplet are critically influenced by two parameters: the intensity of the pump pulse and the time delay between pump and probe pulse. Their influence on the density of the target can be calculated by a model developed by PÜLL [Pue70]. This one-dimensional model considers the interaction of an intense laser pulse with a solid-state target. Therein, a plasma is ignited and the energy of the laser pulse is transferred into kinetic energy of the generated electrons and ions. Therefore, the target is heated and starts expanding. The expansion velocities of electrons and ions can be calculated, but since the ions are much heavier, the ion velocity is well suited for describing the expansion process. The model itself has been experimentally validated using a liquid-droplet setup by DÜSTERER [Düs02]. Therein, a comparable setup to this work has been used and the ion velocities were measured.

In the model, the averaged velocity of an ionic ensemble is given by:

$$\bar{v}_{ion} = \sqrt{5 \cdot Z k_B T_i / 3 \cdot M} \quad (2.10)$$

where $k_B T$ is the ion temperature and M the ionic mass. Z denotes the degree of ionization, which is equal to 1 for single ionization.

The expansion energy is equal to the incident flux of light divided by the ion flux and

can be expressed as:

$$E_{\text{expn.}}(I) = 5 \cdot \alpha Z k_B T = 5 \cdot \alpha^{\frac{1}{3}} \left(\frac{3}{50} \cdot M C r_0 \right)^{\frac{2}{9}} \cdot I^{\frac{4}{9}} \quad (2.11)$$

with r_0 as radius of the target, $\alpha = (Z + 1)/Z$ and I the intensity of the laser pulse. The constant C is calculated according to the manuscript by PÜLL [Pue70] using the central frequency of the Ti:Sa-laser system of 793 nm.

Inserting equation (2.11) into (2.10) leads to the following expression of the ion velocity:

$$\bar{v}_{\text{ion}}(I) = \frac{1}{\sqrt{3 \cdot M}} \cdot \sqrt{5 \cdot Z \alpha^{-\frac{2}{3}} \left(\frac{3}{50} M C r_0 \right)^{\frac{2}{9}} \cdot I^{\frac{2}{9}}}. \quad (2.12)$$

Thus, the expansion velocity of the target is a function of the intensity of the incident laser pulse and scales $v_{\text{ion}} \propto I^{\frac{2}{9}}$.

2.4.2 Number-Density Evolution of the Droplet

Using the model for the ion velocities, equation (2.12) allows the calculation of the number-density evolution of the target. First, the volume of the droplet as a function of time and intensity is calculated by

$$V(t, I) = \frac{4}{3} \pi (r_0 + v_{\text{ion}}(I) \cdot t)^3 \quad (2.13)$$

where the radius is $r_0 = 10 \mu\text{m}$ and t is the time. During the expansion of the target, a uniform velocity is assumed. From equation (2.13), the change of volume can be calculated by

$$\Delta V(t, I) = \frac{V(t, I)}{V_0} \quad (2.14)$$

with the volume at time zero $V_0 = V(0, I)$. Using the number density of liquid water $\rho_0 = 3.35 \times 10^{22} \text{ cm}^{-3}$, the density evolution can be calculated as function of time and intensity using equation (2.14):

$$\rho(t, I) = \frac{\rho_0}{\Delta V(t, I)} = \rho_0 V_0 / \left\{ \frac{4}{3} \pi \left(r_0 + \frac{1}{\sqrt{3 \cdot M}} \cdot \sqrt{5 \cdot Z \alpha^{-\frac{2}{3}} \left(\frac{3}{50} M C r_0 \right)^{\frac{2}{9}} \cdot t \cdot I^{\frac{2}{9}}} \right)^3 \right\}. \quad (2.15)$$

Therefore, the density scales with intensity as $\rho(t, I) \propto I^{-2/3}$.

2.4.3 Calculation of Number Densities

Figure 2.3 (a) shows the temporal evolution of the number density of the droplet after being hit by an intense laser pulse for a fixed degree of ionization of $Z = 1$ and different intensities. The coloured areas estimate the density regimes of different thermodynamic states, liquid density (blue), clustered media and high-density gas (green) and gaseous density (yellow). With growing time, a decrease in the density is observed. The decline becomes steeper with increasing intensity, according to equation (2.15). For an intensity of

$5.0 \times 10^{14} \text{ W/cm}^2$ (black line), the droplet performs the transition from liquid density to the density of clustered media and high-density gases after 0.3 ns. This means, a liquid-density target is present at times $t < 0.3 \text{ ns}$ with densities $\rho \geq 5.0 \times 10^{21} \text{ cm}^{-3}$. After 3.0 ns, the density has lowered to a gaseous level with $\rho \leq 1.0 \times 10^{19} \text{ cm}^{-3}$ and is further reduced to the level of diluted, dry gases with increasing time. By choosing the right intensity of the pump pulse and the right time delay, a wide range of densities becomes accessible as a target for HHG [Kur13].

The influence of different degrees of ionization is shown in Fig. 2.3 (b). A maximum degree of ionization of $Z = 8$ is chosen due to the fact that the oxygen atom has eight electrons and since water is regarded, this is the highest degree of ionization possible. The graphs in Fig. 2.3 (b) were calculated for a fixed intensity of the pump pulse of $5.0 \times 10^{14} \text{ W/cm}^2$, since it is a rather typical value for the experiments. A similar behaviour as in Fig. 2.3 (a) can be seen. With an increasing degree of ionization, the density decrease becomes more rapid. This behaviour becomes obvious, when equation (2.12) is regarded. The expansion velocity scales with Z as

$$v_{ion} \propto \sqrt{a \cdot Z [(Z+1)/Z]^{-2/3}} = \sqrt{a \cdot [Z^2 (Z+1)]^{-2/3}}, \quad (2.16)$$

where a is a constant. Therefore, the v_{ion} increases with Z and the number density decreases more rapidly with increasing degree of ionization.

Comparing the two degrees of ionization $Z = 1$ and $Z = 8$ at time $t = 0.3 \text{ ns}$, the ratio of the densities is approximately a factor of ≈ 9 , from $\rho = 2.5 \times 10^{21} \text{ cm}^{-3}$ at $Z = 1$ to $\rho = 3.6 \times 10^{20} \text{ cm}^{-3}$ at $Z = 8$. As time increases to $t = 3.0 \text{ ns}$, the difference in density grows larger to $\rho = 1.0 \times 10^{19} \text{ cm}^{-3}$ at $Z = 1$ and $\rho = 7.0 \times 10^{17} \text{ cm}^{-3}$ at $Z = 8$. With growing time, the difference in density between the various degrees of ionization grows more prominent, since the curves diverge.

However, for the calculations concerning the experiments, a fixed degree of ionization of $Z = 1$ is used, since during HHG ionization is weak and only the single electron of the highest occupied orbital is considered. Using $Z = 1$, the model by PÜLL accurately reproduces the expansion velocities measured in droplets [Düs02] and in a water jet during interaction with a laser pulse [ST06].

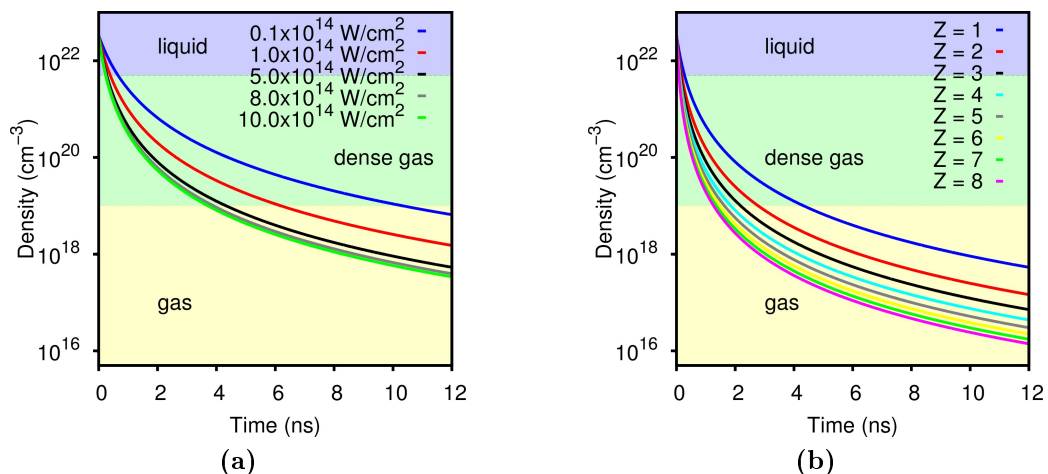


Figure 2.3: Temporal evolution of the density of the droplet after being hit by a laser pulse with (a) a fixed degree of ionization $Z = 1$ but different intensities and (b) for different degrees of ionization Z but fixed intensity of $5.0 \times 10^{14} \text{ W/cm}^2$.

2.4.4 Limitations of the Calculations

The time and intensity dependent density evolution of a liquid water droplet upon irradiation by an intense laser pulse can be calculated with the model described above. However, several limitations of the model arise, which will be discussed below.

In the calculations, the thermal energy is neglected and it is assumed that all thermal energy has been transferred into kinetic energy [Pue70]. This assumption may lead to an error in the model for very small time delays between pump and probe pulse.

The model only delivers a one-dimensional estimate, but the expansion of the target is in three dimensions. Moreover, the front of the droplet facing the laser pulse will be hit first and will start expanding, while the light has not propagated to the back of the droplet. At high intensities, the plasma formation will be very localized and limited to a penetration depth of $\approx \lambda_L$ [Fei04]. This means a density gradient along the propagation axis of the laser z is formed, leading to lower density of the droplet at its front and higher density of the droplet at its back (cf. Fig. 2.2 (b)). Additionally, the spherical shape of the droplet leads to an additional focusing of the pump-pulse and thus to intensities up to 100 times higher [Cou03] and can result in the formation of a liquid jet emerging from the droplet if the focus is smaller than the target [Ahn12a, Ahn12b]. However, during the experiments described in this thesis, the focus has been larger than the droplet. As a result, the droplet is irradiated completely and all parts start expanding.

In section 2.4.3 it is stated that only the first degree of ionization is regarded. Although higher degrees of ionization are present, they only have a minor part at the intensities used and can therefore be ignored. More important is the neglect of non-adiabatic effects during ionization as reported by CHRISTOV *et al.* [Chr96, Chr97] and by PRIORI *et al.* [Pri00]. Therein, the use of laser pulses with a duration of 25 fs leads to a suppressed ionization, when compared with 100 fs and therefore will directly affect the expansion velocity.

In spite of these limitations of the model, it still supplies sufficient accuracy to estimate the time and intensity-dependent density evolution of the droplet [Düs02, ST06, Kur13].

Nevertheless, the liquid droplet is a very complex, macroscopic target which develops highly dynamical spatio-temporal processes on the microscopical level after being hit by an intense laser pulse. It is unclear, how the target develops through all thermodynamic states on the path from a liquid towards a plasma and several possibilities arise, depending on the time delay and intensity of the laser pulses. Figure 2.4 depicts four possible transitions, that may also mix or follow one another. In the case of Fig. 2.4 (a), the intensity of the laser pulse is moderate, dissolving the hydrogen bonds between the water molecules. Therefore, a molecular gas is created. Increasing the intensity may lead to dissociation of the molecules and the droplet can decay into an atomic gas (cf. Fig. 2.4 (b)). However, due to its permanent dipole moment the water molecule tends to cluster and the fragmentation of the droplet into clusters of different sizes is likely (see 2.4 (c)). As stated above, at high intensities a plasma may be ignited (cf. Fig. 2.4 (d)).

Distinguishing between the different states of the target is a non-trivial task. Hence, high-order harmonic generation is a well suited tool for probing microscopic answers from macroscopic targets with sub-femtosecond time resolution. HHG as will be shown, therefore is the ideal instrument to study the spatio-temporal dynamics of the droplet.

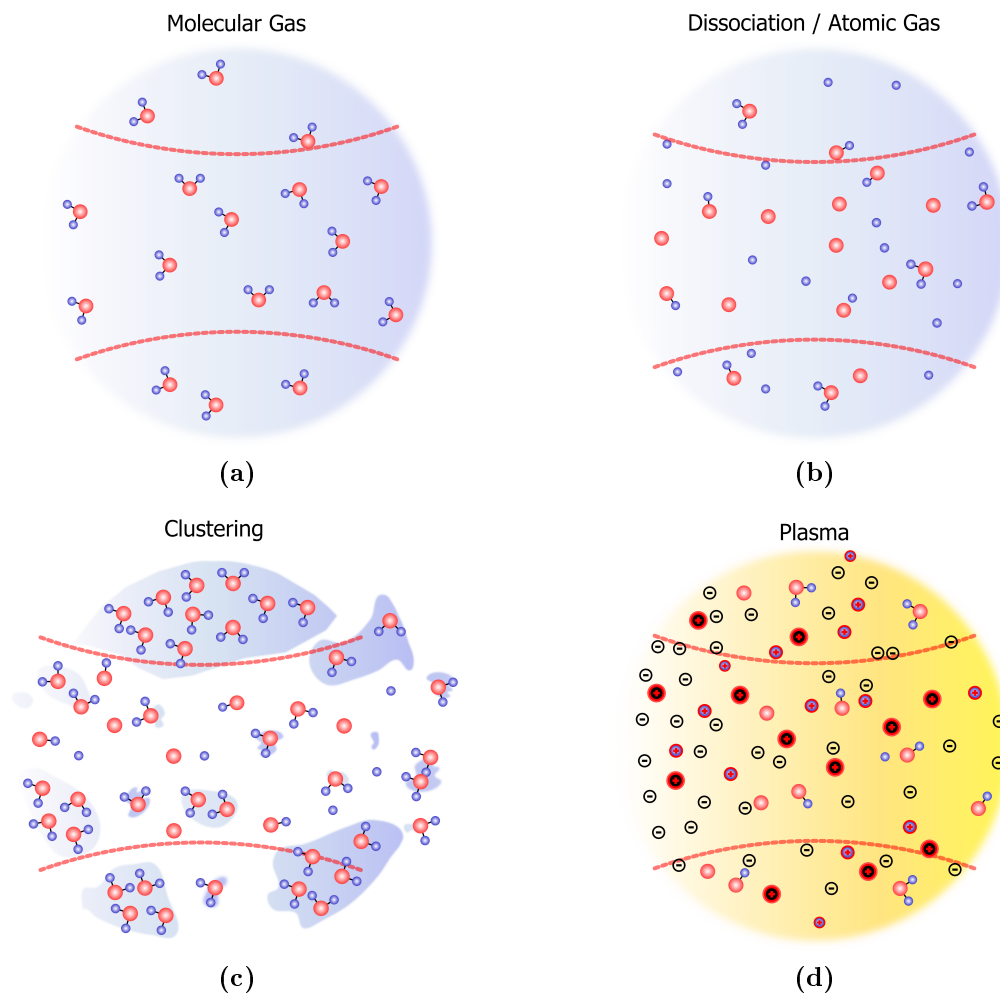


Figure 2.4: Schematics of possible spatio-temporal dynamics of the droplet after being hit by the pump pulse. (a) depicts the expanding volume of the droplet (blue) as a molecular gas. The focusing geometry (dashed red line) and water molecules (oxygen as red circles and hydrogen as small blue circles) are shown. (b) Dissociation into fragments of water molecules. The target decays into an atomic gas. (c) Cluster development and fragmentation of the target into water clusters of different sizes. (d) Plasma ignition with ions (red pluses), electrons (black minuses) and neutral particles.

2.5 High-Order Harmonic Generation

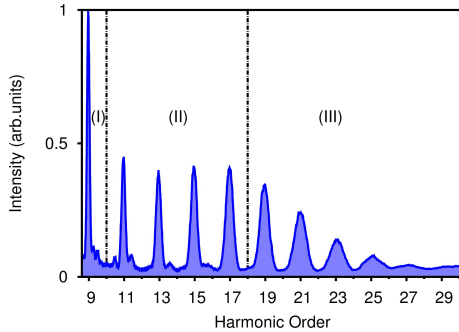


Figure 2.5: Measured spectrum of high-order harmonic radiation from water droplets generated with intense laser pulses. The three regimes are indicated by the numbers and divided by the dashed lines. (I) describes the decrease in intensity according to perturbation theory, (II) the plateau region and (III) the cutoff.

to 17). This *plateau* region contradicts with perturbation theory and can only be explained quantum-mechanically. The plateau is followed by the *cutoff*-region, where the intensity of the harmonic orders decreases again (see Fig. 2.5 region (III), 19 and higher). The generation of high-order harmonic radiation allows the conversion of infrared radiation (IR) into the extreme ultraviolet spectral region (XUV) and therefore enables the generation of coherent radiation with wavelengths below 10 nm. The first observation of HHG was by FERRAY and MCPHERSON [McP87, Fer88], and by now it has been well established as a source of coherent XUV radiation. The unique characteristics of the radiation are ideally suited to perform experiments requiring high temporal and a high spatial resolution and allow to study phenomena on the attosecond timescale [Hen01, Kie04, Sch10].

The characteristic behaviour of the spectrum of HHG will be described in the following two sections. First, the semi-classical three-step model will be explained [Cor93]. In the second part, the quantum-mechanical LEWENSTEIN model will be introduced [Lew94].

2.5.1 Three-Step Model of High-Order Harmonic Generation

The semi-classical model developed by CORKUM [Cor93] divides the harmonic generation process into three parts. First, an intense laser field perturbs the atomic or molecular potential and the electron is ionized from the ground state via tunnel ionization with zero kinetic energy, which is considered as step one (cf. section 2.2 and Fig. 2.6 (a)). In step two, the electron gains kinetic energy, as it is accelerated by the electric field and propagates into the continuum (see Fig. 2.6 (b)). It is thereby treated as a classical particle in the model. As the external field changes sign, the electron may be driven back towards its parent ion. With certain probability, it recombines in step three with the ion and releases the kinetic energy accumulated during the excursion in the continuum, plus the energy given by the ionization potential by emitting a single XUV photon (cf. Fig. 2.6 (c)).

Nonlinear crystals are used for SHG, THG or sum-frequency generation. As stated in section 2.1, the nonlinearity is described by perturbation theory and the order of nonlinearity heavily influences the conversion efficiency (CE), which decreases with increasing harmonic order. The frequency conversion of laser radiation by nonlinear light matter interaction is a common tool for the generation of harmonics of the fundamental frequency. In these processes, multiple photons are absorbed by an electron that is excited into a virtual energy level and emits the sum of the energy of all photons within a single photon.

High-order harmonic generation (HHG) however is a different mechanism, which cannot be described with the perturbation theory in sec. 2.1. A typical spectrum of HHG is shown in Fig. 2.5. The decrease of the intensity of the harmonic orders in region (I) according to perturbation theory (orders nine and eleven) is followed by an area of constant intensity of adjacent orders (see Fig. 2.5 region (II), orders 11

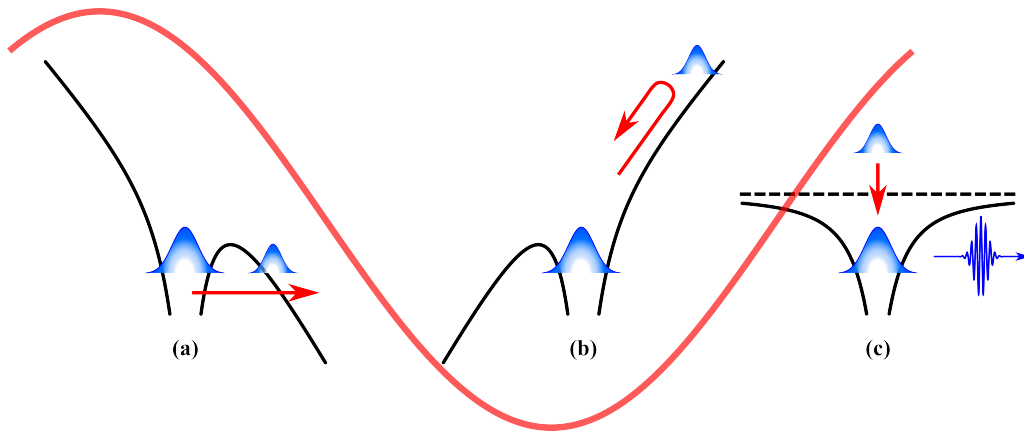


Figure 2.6: Three-step model according to CORKUM. The figures (a) - (c) depict the atomic potential (black), the electronic wave function (blue) and the incident laser field (red). The ionization threshold is indicated by the dashed line. (a) shows the tunnel ionization process. (b) acceleration of the electron in the laser field. (c) Recombination of electron and parent ion with emission of one XUV photon.

As the electron is treated like a classical particle once it has tunnelled, its possible trajectories can be calculated. Figure 2.7 depicts calculations of the movement of electrons, accelerated by the external field $E = E_0 \cdot \sin \omega t$ for different ionization times t_i as function of the optical cycles T . Electrons ionized for times $t_i < T/4$ will not contribute to HHG since they are released before the field maximum and do not experience sufficiently high acceleration towards the parent ion. Therefore, they do not recombine and are lost for the process (dashed-blue line in Fig. 2.7). However, electrons released between $T/4 < t_i < T/2$ will be driven back towards the parent ion and recombine by emission of an XUV photon (solid-blue line in Fig. 2.7), as long as the amplitude of the field is sufficiently high enough for ionization.

The process repeats itself every half cycle and harmonic radiation with frequency $\omega_q = q \cdot \omega_L$ is emitted, where q is the harmonic order. Considering two adjacent events, the resulting electric field is given by

$$E(t) = \hat{E}(t) \cdot e^{-i\omega_q t} + \hat{E}(t + T/2) \cdot e^{-i\omega_q t - i\omega_q T/2}. \quad (2.17)$$

Since $\hat{E}(t + T/2) = -\hat{E}(t)$, the two fields interfere destructively for $\omega_q \cdot T/2 = q \cdot \pi$ whenever q is even. Hence, only *odd* harmonics of the fundamental radiation are emitted [Klü12].

Figure 2.7 shows that the electron can take different trajectories from ionization to recombination. But how do the different trajectories influence the kinetic energy release, i.e the energy of the XUV photon?

Figure 2.8 (a) depicts the return energy as function of the ionization time (blue), which is calculated from the classical model. Except from the maximum, two ionization times lead to the same energy release. They differ in the time spent in the continuum (cf. Fig. 2.8 (a) red line) and are therefore referred as short and long trajectory. The maximum return

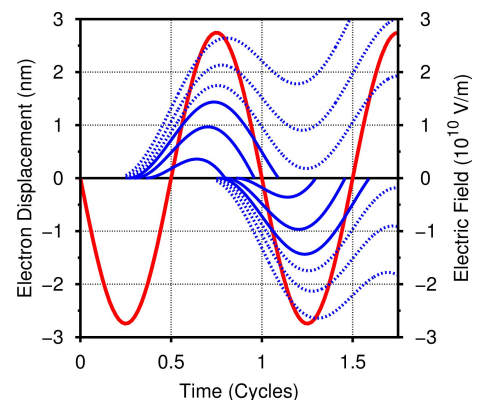


Figure 2.7: Electron trajectories (blue) for different ionization times as a function of time and the electric field (red) with $I = 1 \times 10^{14} \text{ W/cm}^2$ at a central wavelength of 780 nm.

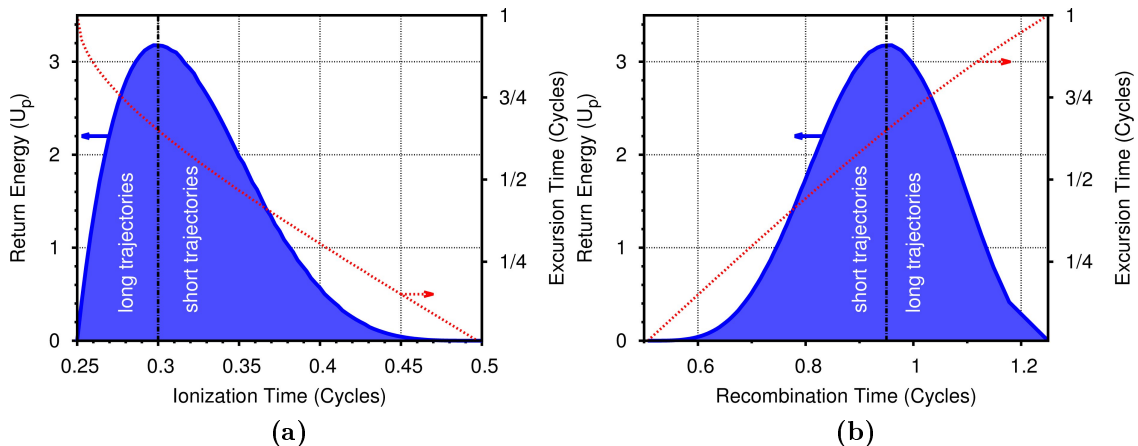


Figure 2.8: (a) Kinetic energy of electrons (blue) and excursion time (red) as function of the ionization time. (b) Kinetic energy of electrons (blue) and excursion time (red) as function of the recombination time.

energy is $3.17 \times U_p$ (cf. Fig. 2.2) and the maximum photon energy is

$$E_{cutoff} = I_p + 3.17 \times U_p, \quad (2.18)$$

defining the cutoff (cf. Fig.2.5 region (III)). A similar calculation for the return energy as function of the return time is shown in Fig. 2.8 (b), leading to the same definition of the cutoff and distinction between short and long trajectory [L'H93b].

The outstanding feature of the plateau region is the constant intensity with increasing order (cf. Fig. 2.5), which can be explained by the ionization process. Return energies in the plateau region are below the maximum and two trajectories contribute (see Fig. 2.8 (a)). As the electrons contributing are released shortly after the maximum of the electric field, the difference in the ionization probability is small and so is the conversion efficiency [Ste11].

The calculation of the emission of harmonic radiation within the three-step model is performed by the calculation of the time-dependent dipole moment of the electron-ion couple. Therefore, the electron wave function is treated as a superposition of the ground state Ψ_g and continuum states Ψ_c :

$$\Psi = \Psi_g + \Psi_c. \quad (2.19)$$

The expected value of the dipole operator $\hat{d} = e \cdot \hat{r}$ is then given by:

$$\langle \Psi | e \hat{r} | \Psi \rangle = \langle \Psi_c | e \hat{r} | \Psi_g \rangle + c.c. \quad (2.20)$$

and is sufficiently accurate for qualitative interpretations of the harmonic spectrum. For quantitative simulations the fully quantum-mechanical LEWENSTEIN model is used [Lew94], which is described in the following.

2.5.2 Lewenstein Model

Since the semi-classical three-step model treats the electron as a classical particle during excursion in the continuum, quantum-mechanical effects are neglected during this step. However, solving the time-dependent Schrödinger equation (TDSE) is time consuming and needs a lot of calculating capacity [Lei07]. The model developed by LEWENSTEIN *et al.* [Lew94] includes effects like quantum diffusion and quantum interference effects during excursion of the electron and delivers a closed form equation for the calculation of the time dependent dipole response $x(t)$ of a single atom without solving the TDSE. The Schrödinger equation in length gauge for the electron in the laser field is given by (in atomic units):

$$i \frac{\partial}{\partial t} |\Psi(\mathbf{x}, t)\rangle = \left[-\frac{1}{2} \nabla^2 + V(\mathbf{x}) - E(t) \right] |\Psi(\mathbf{x}, t)\rangle, \quad (2.21)$$

with the atomic potential $V(\mathbf{x})$. Thereby, only electrons in the ground state $|0\rangle$ are considered and the depletion of $|0\rangle$ is neglected. The strong-field approximation (SFA) is applied, i.e. the influence of the ionic potential onto the free electron is disregarded. With these assumptions, the wave function of the electron can be written as

$$|\Psi(t)\rangle = \left[a(t) |0\rangle + \int d^3\nu b(\nu, t) |\nu\rangle \right] \cdot e^{i I_p t}, \quad (2.22)$$

where I_p describes the ionization potential, $a(t)$ the amplitude of the ground state. The continuum states and amplitudes are denoted as $|\nu\rangle$ and $b(\nu, t)$. Solving the Schrödinger equation delivers the time-dependent dipole moment

$$\mathbf{x}(t) = i \int_0^{t_r} dt_i \int d^3p E(t_i) d_x(\mathbf{p} - \mathbf{A}(t_i)) \cdot \exp[-i S(\mathbf{p}, t_i, t_r)] \cdot d_x^*(\mathbf{p} - \mathbf{A}(t_r)) + c.c. \quad (2.23)$$

where d_x expresses the dipole-matrix element for the transition from the ground state into the continuum, S the quasi-classical action, $\mathbf{p} = \mathbf{v} + \mathbf{A}$ the canonical momentum and \mathbf{A} the vector potential of the external field. Equation (2.23) can be interpreted in terms of the three-step model. The first integrand describes ionization of the electron, while its propagation is described by the second term. Recombination at time t_r is expressed by the third integrand.

Equation (2.23) can be further simplified using the fact that major contributions to the harmonic spectrum are only provided by stationary points of the quasi-classical action, where $\nabla_{\mathbf{p}} S(\mathbf{p}, t_i, t_r) = \mathbf{0}$. This means ionization and recombination have to happen at the same position, since $\nabla_{\mathbf{p}} S(\mathbf{p}, t_i, t_r) = x(t_r) - x(t_i)$. A more detailed discussion can be found in reference [Ste11], the derivative of equation (2.23) is given in reference [Voc12].

In order to simulate the high-order harmonic spectrum of a single atom, the Fourier transform of the second time derivative of the dipole momentum in equation (2.23) has to be calculated numerically. Figure 2.9 depicts a simulation of the 45th harmonic order from a neon atom as a function of the driving intensity by LEWENSTEIN *et al.* [Lew94]. For low intensities of the driving pulse, the signal increases steeply and the harmonic order is situated within the cutoff region (cf. section III in Fig. 2.5) where a single electronic trajectory contributes to the emission of the harmonic order. As the intensity is increased, the cutoff region is shifted towards higher orders and the 45th order enters the plateau region (green line, see also section II in Fig. 2.5) where two electronic trajectories participate in

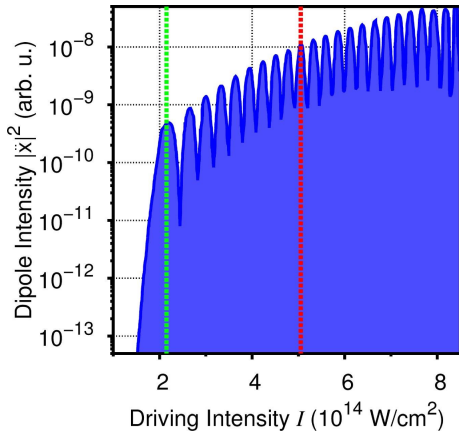


Figure 2.9: Calculated intensity of the 45th harmonic order in a single neon atom as a function of the driving intensity by LEWENSTEIN *et al.* [Lew94]. The green line indicates the intensity needed for the harmonic to transit from the cutoff into the plateau region. The red line indicates the saturation intensity.

The structure of molecules is more complex and several interesting features arise during HHG.

2.5.3 High-Order Harmonic Generation in Molecules

Within a molecule, the electronic states are classified by energy and assigned to a molecular orbital. The calculation of the molecular orbital is performed by the *linear combination of atomic orbitals*. For the HHG process in molecules, usually the molecular ground state is regarded, and its *highest-occupied molecular orbital* (HOMO) contributes to the signal [Lei07]. Lower lying orbitals with higher ionization threshold are denoted as HOMO-1, HOMO-2, etc. High-order harmonic generation in molecules can be described by solving the TDSE, using the Three-Step-Model or the LEWENSTEIN model [Le08].

According to the LEWENSTEIN model, molecular effects are easiest accessible regarding the most simple molecule, the H_2^+ molecular ion. In this case, the Hamiltonian within the Schrödinger equation (2.21) is replaced by:

$$H = -\frac{1}{2}\nabla^2 + V(\mathbf{r}, \mathbf{R}) - E(t) \mathbf{x}, \quad (2.24)$$

where the molecule lies within the $x - y$ -plane and \mathbf{R} denotes the intermolecular distance. Applying this ansatz, the dipole-matrix elements for ionization and recombination can be expressed as [Cia07]:

$$d_{ion,x}(\mathbf{k}, \mathbf{R}, t) = \langle \Psi_c(\mathbf{k}) | E(t) \cdot \mathbf{x} | \Psi_g(\mathbf{R}) \rangle, \quad (2.25)$$

and

$$d_{rec,x}(\mathbf{k}, \mathbf{R}) = \langle \Psi_c(\mathbf{k}) | (-\mathbf{r}) | \Psi_g(\mathbf{R}) \rangle, \quad (2.26)$$

where \mathbf{k} denotes the wave vector of the fundamental radiation. The dipole matrix elements in equations (2.25) and (2.26) are function of \mathbf{k} and \mathbf{R} , which indicates that there might be

the emission process. The two contributions interfere and perturb the dipole which leads to a less steep slope and oscillations of the signal as a function of the intensity [Sal97]. A third change in the intensity-dependence of the harmonic signal can be observed in experiments when the ground state of the medium is depleted. Since the Lewenstein model neglects the depletion, it is not observable in Fig. 2.9. However, for the 45th order in neon, the change is situated around an intensity indicated by the red line and becomes observable by a saturation of the harmonic signal. The driving intensity where saturation sets in defines the *saturation intensity* I_{sat} . Since the emission of higher orders than the 45th order starts at increased values of I , more intensity is needed for their transition into the plateau region [Wah93], which also leads to a higher value of I_{sat} .

High-order harmonic generation is not limited to atoms as a target but also molecules [Sak95], clusters [Don96], liquids [DiC09]. In principle, the mechanism of HHG from atoms and molecules is identical.

a dependence on the relative orientation between the molecular axis and the polarization direction of the fundamental radiation. Using the molecular ground state of the hydrogen molecule, the dipole matrix element for recombination allows more insight into the orientation dependence when it is expanded to:

$$d_{rec,x}(\mathbf{k}, \mathbf{R}) = -i \sqrt{\frac{2}{1+s(R)}} \left[-\frac{\mathbf{R}}{2} \sin\left(\frac{\mathbf{k} \cdot \mathbf{R}}{2}\right) \tilde{\Psi}_h(\mathbf{k}) + \cos\left(\frac{\mathbf{k} \cdot \mathbf{R}}{2}\right) \frac{\partial \tilde{\Psi}_h(\mathbf{k})}{\partial \mathbf{k}} \right], \quad (2.27)$$

where $\tilde{\Psi}_h(\mathbf{k})$ denotes the Fourier transformed wave function of the ground state of the hydrogen atom (see CIAPPINA *et al.* [Cia07] for details). The matrix element includes terms with scalar products of \mathbf{k} and \mathbf{R} , which means it is a function of the angle between \mathbf{k} and \mathbf{R} . Therefore recombination depends on the relative orientation of the molecule with respect to the laser polarization. A comparable behaviour is valid for ionization. Thus, the harmonic yield depends on the relative orientation of the molecule with respect to the polarization of the laser.

The first experimental observation of HHG in molecules has been done by SAKAI *et al.* [Sak95] using nitrogen molecules. The research field has vastly developed and the ionization and recombination characteristics of molecules are studied by using techniques like the field free alignment of macroscopic molecular ensembles [Sta03]. Therein, a dynamical rotational wave packet is induced in the ensemble with a short laser pulse. The wave packet evolves in time and features revival structures. High-order harmonic radiation is generated at the rotational revivals, and the orientation dependence is probed by changing the laser polarization [Vel01, Hay01, Lei03, Mai08, Kan05]. Since HHG also depends on the internuclear distance \mathbf{R} (cf. equation (2.27)), not only rotational but also vibrational dynamics [Li08, Chi06, Far11] can be probed. Moreover, chemical dynamics [Wör10a, Wör11] or structural information of the molecule [Won11] can be extracted from the harmonic signal. In oxygen molecules, an elongation of the cutoff compared to xenon has been observed and is explained with a suppressed ionization due to the molecular orbital structure [Sha02].

Besides induced dynamics, structural information of the participating orbitals is imprinted onto the harmonic radiation [Lei07, Tor07, McF08, Wör10b]. Minima in the harmonic spectrum are observed and can be attributed to the electronic structure of the HOMO, as in the case of N_2 [Wör10b]. The HOMO however is not always the solitary orbital contributing to HHG, but HOMO-1 and lower orbitals may contribute to HHG and lead to dynamical minima in the harmonic spectrum due to interference between the orbitals, as in the case of CO_2 [Smi09, Wör10b]. The encrypted structural information can be used to reconstruct the HOMO by tomographic imaging techniques [Ita04, Hae10, Voz11, Ber12].

Recently, high-order harmonic generation from water molecules has gained interest. Water is used for HHG in the liquid state [DiC09, Fle03] or as a gaseous target [Zha11, Won10, Far11]. Theoretical calculations [Fal10] and experiments study the influence of nuclear motion onto HHG and reveal contributions from HOMO and HOMO-1 to the harmonic yield [Far11].

Up to now the single particle response has been taken into account. However, HHG is performed in a macroscopic target of many particles. That is why macroscopic effects have to be considered and will be discussed in the next part.

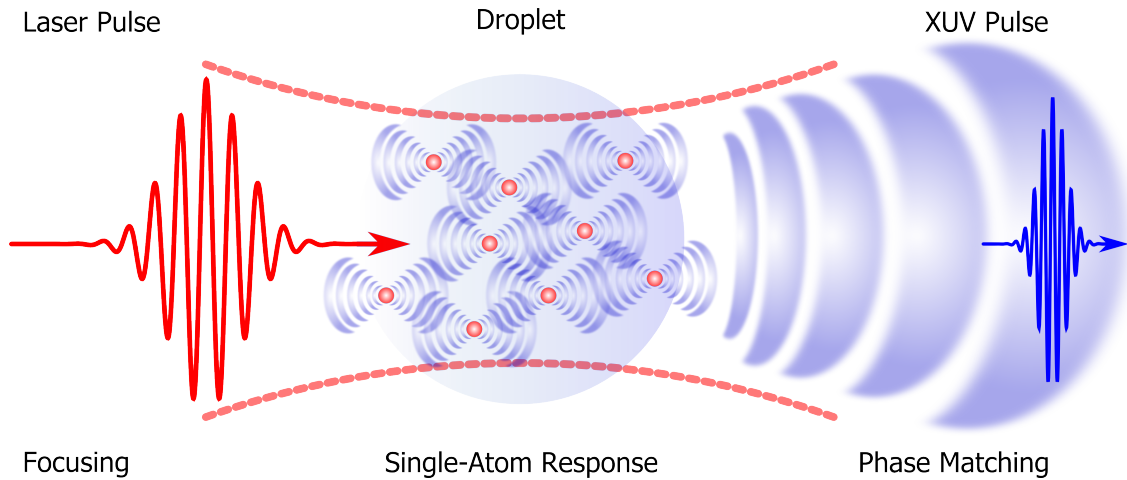


Figure 2.10: From microscopic to macroscopic response. The incident laser pulse (red) is focused (dashed red) onto the droplet (light blue). The single particles emit harmonic radiation of the fundamental frequency. The coherent sum of all emitted XUV photons forms the XUV pulse (dark blue).

2.6 Phase Matching of High-Order Harmonic Radiation

Since harmonic radiation is generated in a macroscopic ensemble of emitters, the above described single-emitter response (cf. section 2.5.1 and Fig. 2.10) lacks any information on the phase relationship between the emitting atoms or molecules. As the net harmonic signal is formed by the coherent sum of the emitted XUV photons within the target, the phases of all emitters have to be matched for constructive interference in the far field, in order to maximize the yield of the harmonic radiation (cf. Fig. 2.10). Thus, not only microscopic but also macroscopic effects are crucial for efficient HHG. Four different contributions can lead to a phase mismatch between the emitters: atomic $\Phi_{\text{at},q}$ and geometric phase $\Phi_{\text{geo},q}$, as well as dispersion from neutral atoms $\Phi_{\text{neu},q}$ and electrons $\Phi_{\text{el},q}$. Summing over these four contribution leads to the total phase:

$$\Phi_{\text{tot},q} = \Phi_{\text{at},q} + \Phi_{\text{geo},q} + \Phi_{\text{neu},q} + \Phi_{\text{el},q}. \quad (2.28)$$

In the following, a gas jet is considered as target for HHG. Figure 2.11 shows the total phase as function of the propagation direction z for a radial component $r = 0$ (on-axis) in (a) and for a radial component $r > 0$ (off-axis) at a fixed intensity. Moreover, the individual phase contributions are depicted. The origin of each summand will be discussed within this section. However, for constructive interference of harmonic radiation generated in several spatially distributed atoms, the emitted radiation of the atoms has to be in phase. This can be expressed by the wave vector mismatch $\Delta\mathbf{k}_{\text{tot},q}$, since minimizing the mismatch maximizes the phase matching:

$$\Delta\mathbf{k}_{\text{tot},q} = \mathbf{k}_q - \nabla\Phi_{\text{tot},q}, \quad (2.29)$$

where \mathbf{k}_q denotes the wave vector of the q^{th} harmonic order.

Atomic Phase As explained in section 2.5.1, two different quantum paths of the electron (short and long trajectory) may lead to the same energy release in the plateau region and thus contribute to the dipole moment. In section 2.5.2, the excursion of the electron is

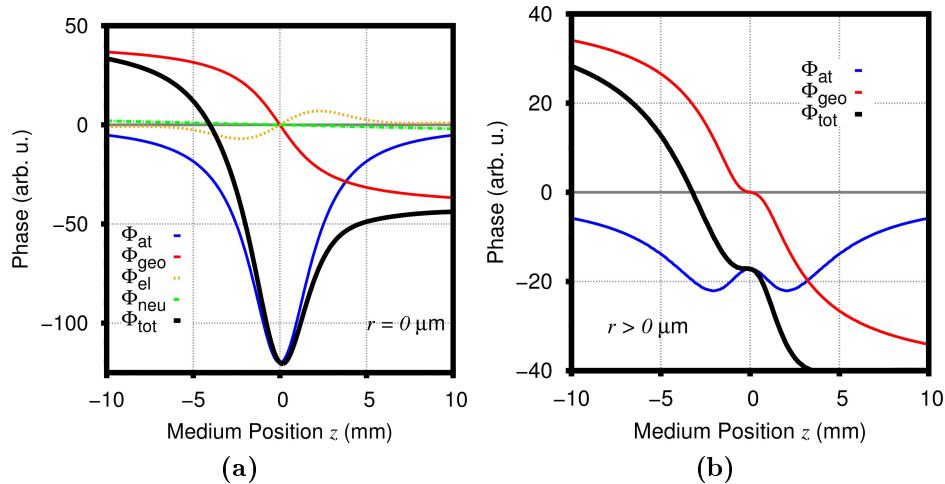


Figure 2.11: Calculated phase contributions for the 27th harmonic order at an intensity of $5 \times 10^{15} \text{ W/cm}^2$. A phase slope factor of $\alpha = 24 \times 10^{15} \text{ cm}^2/\text{W}$ is estimated, so that the harmonic is situated within the plateau [Gaa02]. (a) On-axis phase contributions as function of the propagation direction z for a fixed value of the radial coordinate r . (b) Off-axis phase contributions as function of z .

described in equation (2.23) by the term $\exp[-i S(\mathbf{p}, t_i, t_r)]$ and $S(\mathbf{p}, t_i, t_r)$ is the accumulated phase of the electron. This phase is accumulated by a spread of the electron wave function during excursion and the time delay between recombination and the reference time of the laser field. It is called *dipole* or *atomic phase* and depends on the intensity of the laser field and the excursion time of the electron [Lew94, Bal97]:

$$\begin{aligned} \Phi_{\text{at}} &= q \cdot \omega t_r - S(\mathbf{p}, t_i, t_r) \approx -\tau_{\text{exc}} \cdot U_p \\ &= \alpha_{s,l} \cdot I(r, z, t), \end{aligned} \quad (2.30)$$

where $S(\mathbf{p}, t_i, t_r)$ denotes the quasi-classical action and $\tau_{\text{exc}} = t_r - t_i$ the excursion time of the electron (cf. Fig. 2.8). The constant $\alpha_{s,l}$ is the slope of the atomic phase and has different values for short (s) and long trajectory (l) [Bal97, Gaa02, Cor06, Kre13], which can be calculated using the LEWENSTEIN model. Applying focused laser pulses, the influence of the intensity on Φ_{at} is most crucial, as it is a function of time and space (cf. Fig. 2.11).

The corresponding wave vector can be calculated for a given time by

$$\mathbf{k}_{\text{at}}(r, z) = \nabla \Phi_{\text{at}}(r, z). \quad (2.31)$$

A scheme of k_{at} as function of the propagation direction z and the radial coordinate r is depicted in Fig. 2.12 with the focus located at $z = 0 \text{ mm}$. Remarkably, k_{at} points into directions away from the focal region [Bal97].

As the intensity is a function of time, this is also true for the atomic phase. This immediately leads to a chirp of the harmonic radiation in analogy to the time dependent phase in the case of self-phase modulation (SPM) [Mor07] and becomes obvious in Fig. 2.8 as different energies are generated at different times [Mai03].

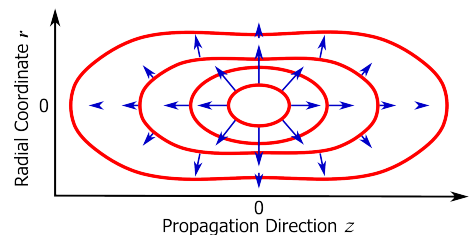


Figure 2.12: Scheme of the atomic wave vector in the focal region (blue). Lines of equal intensity are shown in red.

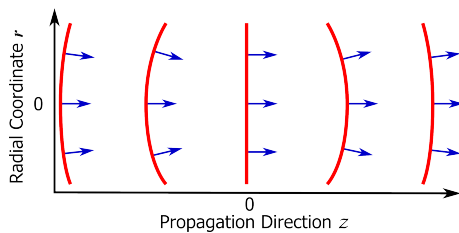


Figure 2.13: Scheme of the geometric wave vector in the focal region (blue). Wave fronts of the fundamental radiation are shown in red.

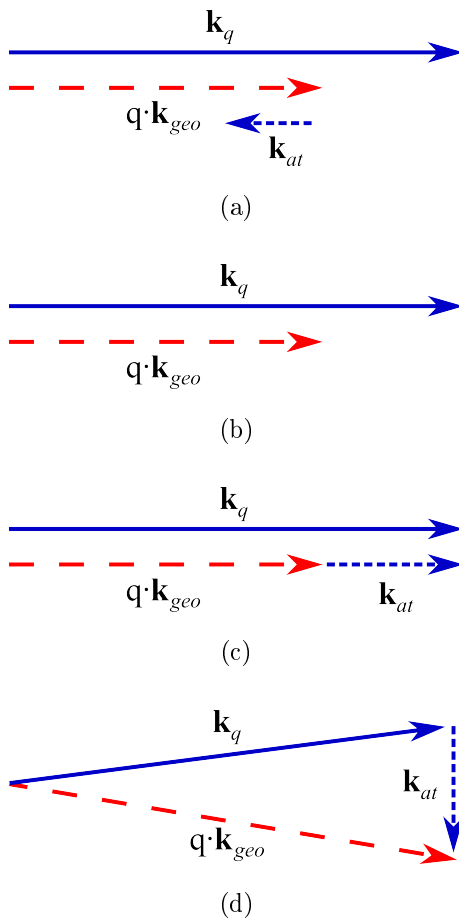


Figure 2.14: Sum of figs. 2.12 and 2.13 at different propagation positions. Depicted are the wave vector of the q^{th} HOH \mathbf{k}_q (solid blue), q times the geometric wave vector \mathbf{k}_{geo} (red) and the atomic wave vector \mathbf{k}_{at} (dashed blue). (a) on axis before the focus, (b) at the focus, (c) on axis after the focus and (d) off-axis before the focus.

Geometric Phase Focusing a laser pulse with Gaussian intensity distribution leads to a curvature of the wave fronts of the laser. Therefore, a space-dependent *geometric phase* is induced

$$\Phi_{geo} = -q \cdot \left(\arctan\left(\frac{2z}{b}\right) - \frac{2k_1 r^2 z}{b^2 + 4z} \right), \quad (2.32)$$

where b is the confocal parameter. The first term is the GOUY phase, whereas the second describes the radial component [Bal97, Sal97]. For an on-axis position, Φ_{geo} is the GOUY phase (cf. Fig. 2.11 (a)). The radial component gains influence for an off-axis position (cf. Fig. 2.11 (b)). As the laser pulse propagates through the medium while generating HOH radiation, this phase shift is imprinted onto the non-linear polarization and thus onto the emission process. A sketch is shown in Fig. 2.13. The wave vector points towards the focus for $z < 0$ and diverges afterwards.

Figure 2.11 indicates that the total phase is dominated by the atomic and geometric phases. Considering a single harmonic of the fundamental radiation with wave vector \mathbf{k}_q , the combination of figs. 2.12 and 2.13 allows the illustration of the phase mismatch as phase-matching diagrams using the atomic and the geometric wavevector. In Fig. 2.14 (a) a situation before the focus is depicted at an on axis position. In this special case for a given harmonic, the sum of $q \cdot \mathbf{k}_{geo} + \mathbf{k}_{at}$ does not match with the HOH wave vector \mathbf{k}_q , since \mathbf{k}_{at} points into the opposite direction. At the focus, there is no contribution from \mathbf{k}_{at} ($\nabla I = 0$), which results again in non-optimized phase-matching conditions (cf. Fig. 2.14 (b)). This behaviour is in good agreement with Fig. 2.11 (a). Phase matching is satisfied for an on-axis position for the medium after the focus (see 2.14 (c)) and an off-axis position for the medium before the focus (cf. Fig. 2.14 (d)) [Bal97].

Though absorption and dispersion from neutral particles as well as the phase contribution from free electrons seem negligible, some interesting effects arise from Φ_{neu} and Φ_{el} and the two phase contributions will be introduced.

Absorption and Dispersion by Neutral Particles

As the fundamental radiation propagates through the target, a phase shift between the laser field and the q^{th} HOH is induced due to dispersion. The refractive index of the gaseous target is nearly equal

to one for the fundamental field. However, for the HOH radiation it is determined by the density of the target ρ , the atomic scattering factor $f(q\omega)$ [Hen93] and the harmonic order:

$$n_{\text{neu}}(q\omega) = 1 - 2\pi \left(\frac{c}{q\omega} \right)^2 \cdot r_{\text{el}} \cdot \rho \cdot \text{Re} \{ f(q\omega) \}, \quad (2.33)$$

where r_{el} denotes the classical electron radius. Absorption is considered by the imaginary part of the refractive index [Ste11]

$$\kappa_{\text{neu}}(q\omega) = -\frac{4\pi c}{q\omega} \cdot r_{\text{el}} \cdot \rho \cdot \text{Im} \{ f(q\omega) \}. \quad (2.34)$$

From the refractive index, the mismatch of the wave vectors between fundamental and q^{th} can be derived

$$\Delta k_{\text{neu}} \approx \frac{q\omega}{c} \cdot (n_{\text{neu}}(q\omega) - 1). \quad (2.35)$$

Integration over the propagation coordinate of Δk_{neu} yields Φ_{neu} .

Dispersion by Free Electrons Since the intensity is high enough to ionize, free electrons are generated during HHG. As explained in section 2.3, free electrons induce a refractive index which depends on the electron density (cf. equation (2.8)). According to the phase contribution by neutral particles, the free electrons induce a phase shift Φ_{el} . The wave vector mismatch is given by

$$\Delta k_{\text{el}} = \frac{\omega_p^2}{2cq\omega} \cdot (q^2 - 1). \quad (2.36)$$

Since high intensities are used in the experiments and the water molecule has an ionization potential of 12.6 eV, the contribution from free electrons is larger than depicted in Fig. 2.11 and cannot be neglected. Their influence will be further discussed in chapter 4.

Coherence Length The build-up of the harmonic field along the propagation direction is limited by the phase mismatch. The induced phase mismatch $\Delta \mathbf{k}_{\text{tot},q}$ results in a periodic generation of harmonic radiation in the medium. The total distance in which energy is transferred from the fundamental field to the field of the q^{th} HOH is the *coherence length*

$$L_{\text{coh},q} = \frac{\pi}{|\Delta \mathbf{k}_{\text{tot},q}|}. \quad (2.37)$$

Therefore, minimizing the phase mismatch is crucial for efficient HHG and can be achieved by matching the medium length L_{med} to the coherence length. Longer medium lengths also result in re-absorption effects, that increase with the density of the medium. The absorption length is given by [Con99, Dac09]:

$$L_{\text{abs},q} = \frac{1}{2 \cdot \kappa_{\text{neu}}(q\omega)}. \quad (2.38)$$

Optimum conditions are achieved for $L_{\text{med}} > 3L_{\text{abs},q}$ and $L_{\text{coh},q} > 5L_{\text{abs},q}$ [Con99].

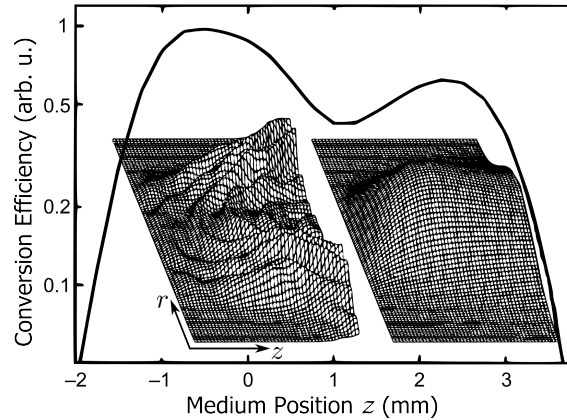


Figure 2.15: Conversion efficiency of the 45th harmonic order in a neon gas jet as function of the position of the medium z from SALIÈRES *et al.* [Sal95]. The inset shows the radial dependence of the CE as function of z . For positions $z < 0$, the focus is positioned after the medium with respect to the propagation direction, and vice versa.

2.6.1 Consequences from Phase Matching

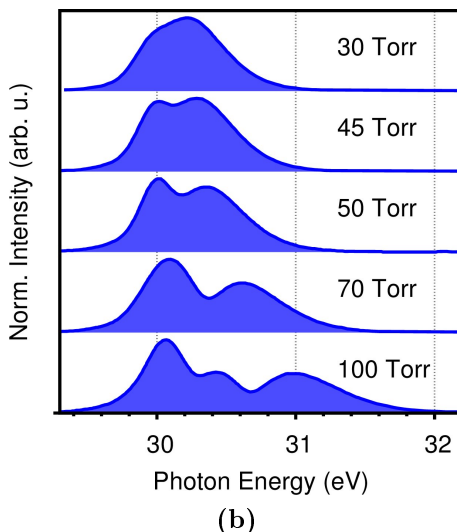
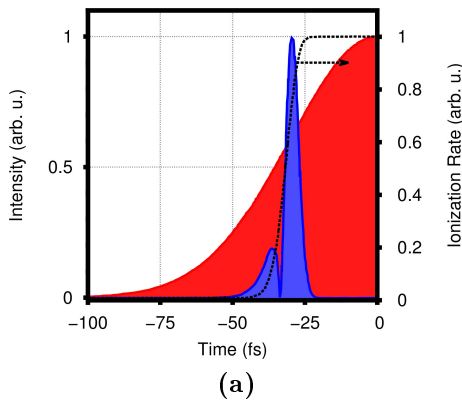


Figure 2.16: Simulation of the HHG process by ZHONG *et al.* [Zho00]. (a) Intensity of the fundamental pulse (red), the intensity of the 19th harmonic order (blue) and the ionization rate (black) as function of time. (b) Intensity of the harmonic radiation versus photon energy for different gas pressures.

The different contributions to the phase matching result in spectral, transient and intensity-dependent effects during HHG. Since these effects supply information on the spatio-temporal dynamics of the target, they are introduced within this section. Well-studied geometries for HHG like the gas jet [Sal95, Sal97], the finite gas cell [Tak07, Bou11], and the semi-infinite gas cell [Pap01, Ste09] supply simulations and observations of phase-matching effects. The gas jet is the best studied geometry and is therefore well-suited for the comparison with the liquid droplet.

Influence of the Medium Position As explained in section 2.6, for a given intensity the total phase critically depends on the propagation direction and the radial coordinate (cf. Fig. 2.11 (a) and (b)). Only in regions where the variation of the total phase is low, phase matching can be achieved in a volume of significant elongation and HOH radiation can be generated efficiently. This is the case for $z < -5$ mm and $z > 5$ mm in Fig. 2.11. A simulation of the conversion efficiency (CE) by SALIÈRES *et al.* is depicted in Fig. 2.15 [Sal95]. Note that in this case the CE is a function of the medium position. Throughout the medium position, the intensity of the laser is sufficiently high enough for HHG. Two maxima are observed, one for $z < 0$ mm and a second for $z > 0$ mm. A minimum appears, when the medium is placed at the focus.

The maximum for $z > 0$ mm is caused by phase matching at an on-axis position due to low variation of the total phase. Since there is a phase mismatch

at an on-axis position for $z < 0$ mm, the second maximum at $z < 0$ mm originates from phase matching at an off-axis position. The minimum is explained by the high variation of the total phase at the focus which leads to a phase mismatch. This behaviour is shown in more detail in the inset of Fig. 2.15. The two maxima can also be attributed to the short trajectory for on-axis PM ($z > 0$ mm) and the long trajectory for off-axis PM ($z < 0$ mm).

Transient Phase Matching As depicted in Fig. 2.6, HHG also is a time-dependent process. Phase-matching conditions not only depend on spatial coordinates but also may change in time. The density of free electrons for instance is a time-dependent parameter, as the ionization increases on the rising edge of the fundamental pulse (cf. Fig. 2.16 (a)). Since the free electrons induce a phase mismatch (cf. equation (2.36)) and their density varies in time, phase-matching conditions change along the fundamental pulse. This effect is called *transient phase-matching* (TPM) [Alt96, Alt99, Wan00, Zho00, Ste09, Kur13]. Figure 2.16 (a) shows a calculation of the temporal evolution of the fundamental field and the field of the 19th harmonic order by ZHONG *et al.* [Zho00]. Since ionization increases with time (cf. Fig. 2.16 (a) black curve), a temporal varying refractive index is induced by the free electrons. This leads to a time-dependent induced phase and the generation of new higher frequencies, due to the monotonical rise of the density of free electrons. The harmonic lines therefore become blue-shifted. A strong time-dependent phase variation leads to a spectral splitting,

comparable to SPM. Two time-delayed maxima in the field of the harmonic radiation appear. The higher the target density is, the more free electrons are generated and the effect becomes more pronounced (cf. Fig. 2.16 (b)).

Since it is an effect caused by Φ_{el} , the pulse is long enough for a reaction of the medium. It is therefore called *adiabatic spectral splitting*.

On the contrary, there is a *non-adiabatic spectral splitting* effect, strictly caused by the single atom response. It becomes observable for intense few-cycle pulses, where the time derivative of Φ_{at} leads to the generation of new frequencies similar to SPM and also results in a spectral splitting [Kan95, Bru08].

2.6.2 HHG in Dense Targets

As seen in Fig. 2.11, the influence of the neutral particles is estimated to play a minor role. In a naive approach, the increase of emitting particles would lead to a higher yield of the harmonic radiation. However, this is only true for low densities $\rho < 10^{19} \text{ cm}^{-3}$. As the density of the medium increases, absorption of the generated harmonic radiation will increase as well. Moreover, the electron can be scattered during excursion in the continuum by surrounding particles and coherence will be lost (cf. Fig. 2.17 (a)). The distortion of the quantum paths will become more prominent with ions present, neighboring the emis-

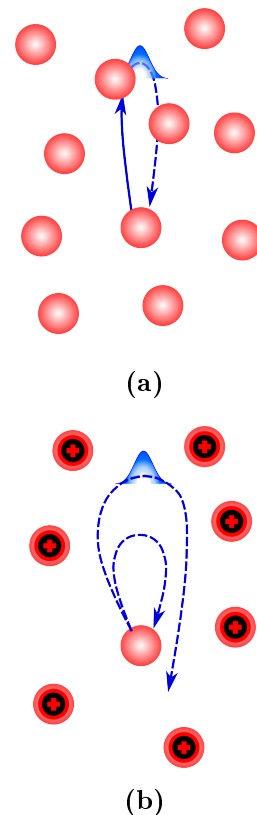


Figure 2.17: Excursion of the electron in the presence of a surrounding medium. (a) atomic medium and (b) ionic medium.

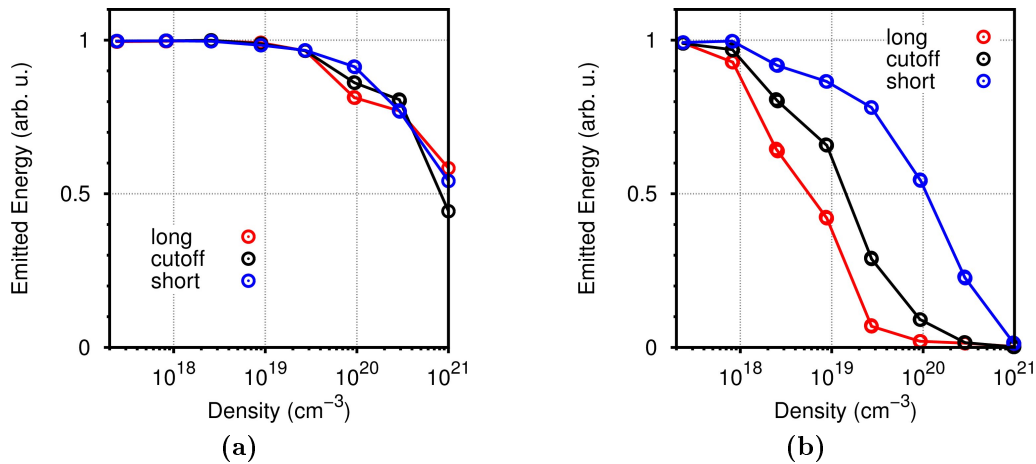


Figure 2.18: Emitted energy of harmonic radiation as function of the medium density simulated by STRELKOV *et al.* [Str05]. Short (blue) and long trajectory (red) as well as the quantum path leading to the cutoff (black) for (a) an atomic medium and (b) an ionic medium

sion process. The ionic field can deflect the electron in a way that recombination becomes impossible (cf. Fig. 2.17 (b)).

However, dense targets for HHG are desirable, since the harmonic yield depends on the number of emitting particles. First experiments on HHG in dense media have been performed by FLETTNER *et al.* [Fle03], where a transition from incoherent to coherent emission of radiation with decreasing density of the medium was observed. A theoretical approach in argon has been performed by STRELKOV *et al.* [Str05]. Therein, the influence of a surrounding medium onto the single emitter response is studied by introducing the potential of the medium $V_{med}(\mathbf{r})$ into the SCHRÖDINGER equation:

$$i \frac{\partial}{\partial t} |\Psi(\mathbf{r}, t)\rangle = \left[-\frac{1}{2} \nabla^2 + V(\mathbf{r}) + V_{med}(\mathbf{r}) - E(t) \mathbf{x} \right] |\Psi(\mathbf{r}, t)\rangle, \quad (2.39)$$

where $V_{med}(\mathbf{r})$ is the sum over all potentials of the particles contained in the considered volume. The results from the simulation by STRELKOV *et al.* of the emitted HOH energy for an atomic medium is depicted in Fig. 2.18 (a) [Str05]. The quantum paths for a HOH from the plateau region and the path leading to the cutoff are shown. The energy is normalized to the single atom case. The emission does not significantly differ for the three quantum paths and a drop in the signal is observed for densities higher than $3 \times 10^{19} \text{ cm}^{-3}$. This behaviour changes when an ionic medium is considered (cf. Fig. 2.18 (b)). The long trajectory contribution decreases more rapidly than the path belonging to the cutoff. Least affected is the short trajectory.

Comparing the discrepancy between an atomic and an ionic medium, the difference can be attributed to the short range of the atomic potential in comparison to the long-ranging ionic potential. The difference between the three quantum paths in the case of an ionic medium is the excursion time τ_{ex} . The long trajectory has the largest value of τ_{ex} and therefore the spread of the electron wave packet is larger compared to the short quantum path. Thus, the electron accumulates a larger phase contribution for the long trajectory and emission is suppressed. Increasing the ionic density leads to larger distortion and the effect becomes more expressed.

As the excursion time is the defining parameter for the decrease of the harmonic signal, a transition density ρ_{trans} as function of τ_{ex} can be defined, where the emitted energy drops by a factor of two. Figure 2.19 shows ρ_{trans} as function of the fundamental intensity for short and long trajectory of a harmonic line belonging to the plateau [Str05]. The difference of the transition density for a given trajectory with increasing intensity is low, since the excursion time is independent of the laser intensity [Str05]. Comparing short and long trajectory, ρ_{trans} differs about a factor of ten. In conclusion, a trajectory selection seems possible by increasing the density of the target for HHG. Since the liquid droplet delivers densities reaching from $\rho = 3.35 \times 10^{22} \text{ cm}^{-3}$ to $\rho < 10^{17} \text{ cm}^{-3}$, the influence of high-density targets onto HHG will be systematically studied in sec. 5.2.

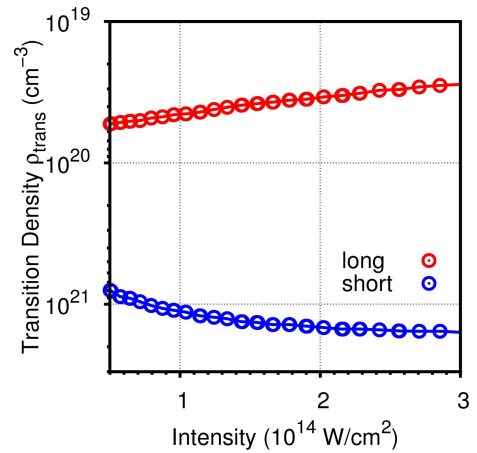


Figure 2.19: Transition density for short (blue) and long (red) trajectory as function of the intensity of the laser pulse simulated by STRELKOV et al. [Str05].

2.7 Generation of Attosecond Pulses

High-end laser systems support bandwidths larger than one octave [Wir11, Har12], corresponding to *Fourier-limited* pulse durations below 5 fs. The duration of laser pulses is linked to their spectral bandwidth by the time-bandwidth product. Shortening the pulses is limited, as the optical cycle determines the minimum pulse duration. One optical cycle at a wavelength of 780 nm for example is 2.6 fs. Though the generation of half-cycle pulses through pulse synthesis is possible [Wir11], HHG is commonly used and converts the fundamental radiation towards shorter wavelengths in a coherent process. A shortening of the pulse can be achieved and the generation of attosecond pulses becomes accessible [Pau01, Hen01, Kie04, Sch10].

As explained in section 2.5.1 the process of HHG can occur every half cycle of the driving field. For intense multi-cycle driver pulses, the field rises many times over the ionization

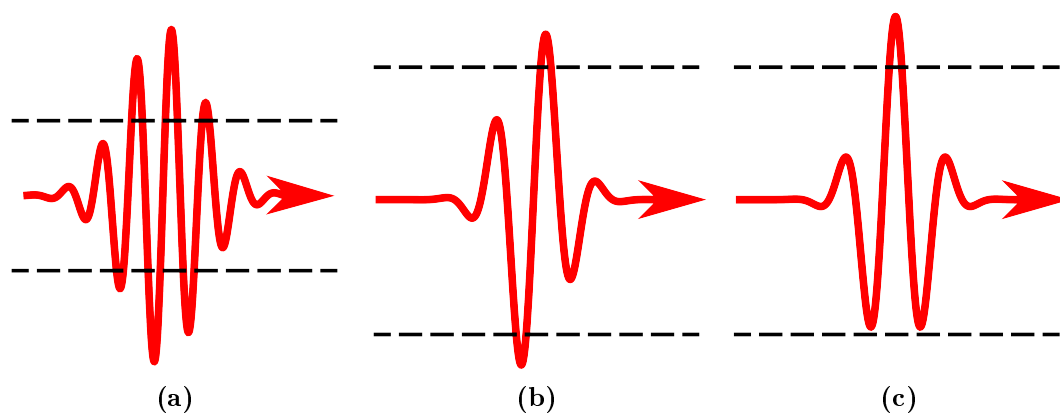


Figure 2.20: Schematic of attosecond pulse generation with few-cycle pulses (red). (a) Multi-cycle pulse. (b) and (c) few-cycle pulses. Different values of ϕ_{CEO} lead to varying number of ionization events (ionization potential in dashed black). (a) $\phi_{CEO} = \frac{\pi}{2}$ results in a sine wave form with two ionization events. (b) $\phi_{CEO} = 0$ leads to a cosine wave form with a single ionization event.

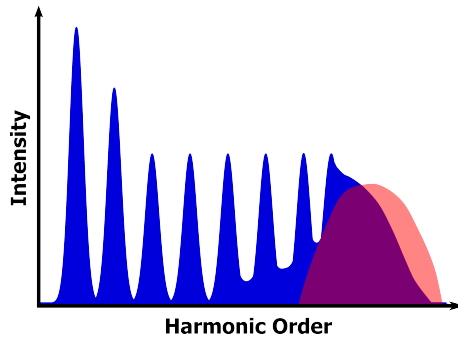


Figure 2.21: Schematic of isolated attosecond pulse generation with few-cycle laser pulses. The HOH spectrum develops a continuum in the cutoff region (blue). The continuous part of the spectrum is then filtered (red) and results in an isolated attosecond pulse.

potential (cf. Fig. 2.20 (a)), resulting in many events contributing to HHG and a discrete spectrum of odd harmonics (cf. Fig. 2.5). An *attosecond pulse train* is emitted. Regarding Fig. 2.20 (b), a few-cycle pulse with *sine*-shaped wave form is depicted (red). The field rises two times over the ionization potential of the atom (dashed black), leading to two consecutive ionization events. Therefore, HHG takes place at two events and the emission of two attosecond pulses. The emission process changes, regarding a *cosine*-shaped wave form (cf. Fig. 2.20 (c)). In this case, HHG takes place at a single event, and an isolated attosecond pulse (IAP) is emitted. In the spectral domain, the single event leads to the development of a continuous spectrum in the cutoff region (cf. Fig. 2.21). The only difference between the two driver pulses lies within the phase between the carrier

and the envelope, the *carrier-envelope offset phase* ϕ_{CEO} . In Fig. 2.20 (b) the phase is $\phi_{\text{CEO}} = \frac{\pi}{2}$, whereas it is $\phi_{\text{CEO}} = 0$ in (c). Thus, few-cycle pulses with defined waveform are necessary for the generation of IAPs. Using a few-cycle driver pulse with cosine-shaped waveform leads to the generation of an IAP, but the generated IAP still co-propagates with the discrete part of the spectrum. Metallic filters (like Zr or Al) therefore can be applied to separate the IAP and compensate the intrinsic chirp of HHG (cf. section 2.5.1).

2.8 The Target for High-Order Harmonic Generation

The interaction of gases with intense laser pulses under vacuum conditions is a common approach to study the structure of atoms and molecules and for HHG [Kra09]. Different setups are applied for the experimental realization of HHG, such as the *finite gas cell* [Tak07, Bou11] and the *semi-infinite gas cell* (SIGC) [Pap01, Ste09], which is depicted in Fig. 2.22 (a). In the SIGC, the laser pulse enters a gas-filled cell through an entrance window and exits the cell through a self-drilled pinhole into a second chamber with ultra-high vacuum conditions. The interaction between laser and gas takes place in a region close to the pinhole. However, the most used setup is the gas jet [Sal95, Sal97] (cf. Fig. 2.22

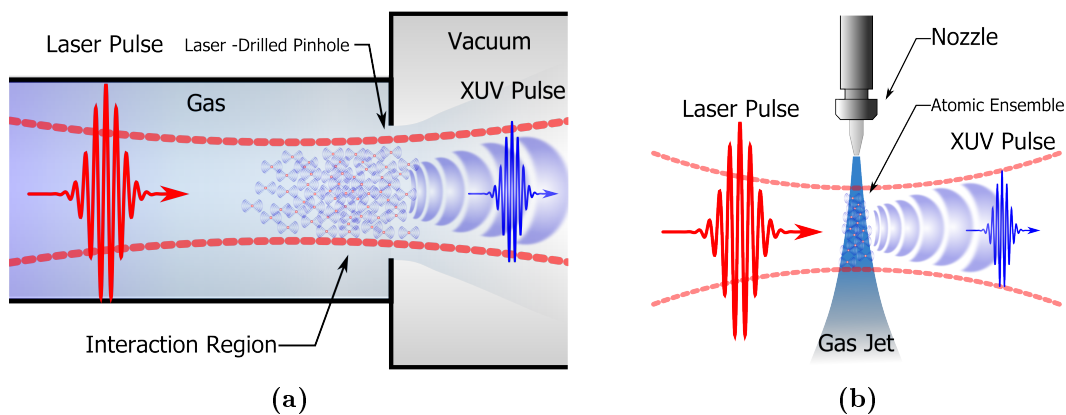


Figure 2.22: Schemes of the semi-infinite gas cell (a) and the gas jet setup (b). The incident laser pulse (red) is focused (dashed-red) into the interaction region and XUV-radiation is emitted (blue).

(b)). It consists of a thin capillary nozzle in a vacuum chamber that is fed with a backing pressure of several atmospheres. It provides a spatially confined target for the interaction with a LORENTZIAN density profile [Alt96] and is comfortable to use.

These described setups are however limited to gaseous targets and this not only confines the accessible thermodynamic state, but also target material and densities. To overcome some of these limitations, instead of gas jets, liquid jets can be used under vacuum conditions. This setup is comparable to the gas jet and also consists of a capillary nozzle. However, during the interaction with intense laser pulses, target material of the liquid jet is accelerated away from the interaction region and destroys the vacuum conditions. In order to prevent this effect, a liquid droplet setup has been used in the experiments described in this thesis, since it delivers a confined target with no material surrounding the interaction region between laser and droplet.

2.8.1 From Liquid Jets to Droplets

Whenever a liquid is forced to exit through a small opening, a cylindrical, laminar flow is generated close to the opening (cf. Fig. 2.23). In this case the opening is given by the end of a capillary nozzle. The length of this so-called *jet* depends on the viscosity of the liquid η , the mass density ρ_{mass} , the velocity of the liquid v and the diameter of the opening d . The REYNOLD number is a measure for the length of the jet and is given as:

$$Re = \frac{\rho \cdot v \cdot d}{\eta}. \quad (2.40)$$

For $Re < 1000$, a jet is observed [Ber98]. However, the jet is only a part of the liquid flow, since it decays after a certain length into a chaotic series of droplets [Ray79]. Small irregularities in the opening of the capillary imprint perturbations onto the jet that result in a contraction close to the opening and surface oscillations with the wavelength λ_{pert} . The oscillations are amplified by the surface tension σ along the propagation on the jet and the jet decays after a decay length L . Irregular, chaotic droplet formation sets in [Web31, Ber98]. A scheme of the decay is depicted in Fig. 2.23. The decay length is given by [Ber98]

$$L = 12 \cdot v \left(\sqrt{\frac{\rho \cdot d^3}{\sigma}} + \frac{3 \cdot \eta \cdot d}{\sigma} \right), \quad (2.41)$$

while the velocity of the jet can be calculated using the backing pressure inside the nozzle P_{nozzle} :

$$v = \sqrt{\frac{2 \cdot P_{\text{nozzle}}}{\rho}}. \quad (2.42)$$

Using this hydrodynamical instability, the chaotic formation of droplets can be transferred into a non-chaotic regime by artificially imprinting a perturbation with wavelength λ_{pert} onto the jet. This also results in a reduction of L . In order to achieve non-chaotic droplet formation, the λ_{pert} cannot be chosen arbitrarily, but depends on the liquid, the pressure and the diameter of the opening. The parameter ζ

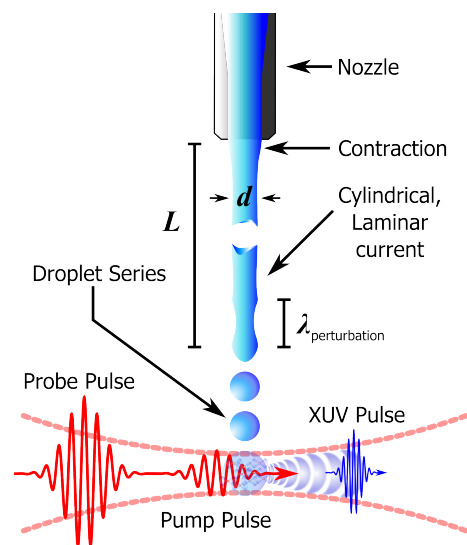


Figure 2.23: Schematic of the generation of a determined series of liquid droplets.

allows to estimate whether chaotic or non-chaotic formation exists and is given by [Egg97]:

$$\zeta = \frac{\pi \cdot d}{\lambda_{\text{perturbation}}} = \frac{\pi \cdot d}{v} \cdot f, \quad (2.43)$$

where f denotes the frequency of the perturbation. For values of $\zeta > 1$ a chaotic decay is observed, whereas $1 > \zeta > 0.35$ guarantees non-chaotic droplet formation. The second harmonic of the perturbation frequency becomes dominant for values of $\zeta < 0.35$ and chaotic droplet formation occurs again [Egg97].

During the experiments, the perturbation is imprinted onto the liquid jet with a piezoelectric aperture, that is implemented within the nozzle and non-chaotic droplet formation is satisfied. The droplets are then irradiated with intense laser pulses, which is described in the next chapter.

Chapter 3

High-Order Harmonic Generation from Water Micro Droplets

The liquid droplet allows the study of HHG in a wide density range reaching from liquid to gaseous densities and enables the investigation of the influence of many particles onto the scaling of the harmonic yield. During the interaction with the laser pulses, the droplet performs a transition reaching from liquid, over clusters to free molecules and atoms. The target however features complex spatio-temporal dynamics on the macroscopical and on the microscopic level that are not well studied. Using HHG, these transitions within the droplet can be probed directly, since structural information on the target is imprinted onto the harmonic radiation. The parameters defining the path of the transition and the final state of the droplet however are unknown.

In this chapter the experimental setup is described (sec. 3.1). Different parameters are identified that influence HHG from liquid water droplets and the harmonic yield is studied as function of the pump-probe time delay (sec. 3.2.1), the intensity of the pump pulse and of the pulse duration (sec. 3.2.2).

3.1 Experimental Setup

3.1.1 Optical Setup

Two different chirped-pulse-amplification (CPA) laser systems are used for HHG that deliver different pulse durations, energies and repetition rates. The first one is a modified Alpha 10C/CS by Thales (referred as laser system *A*). The second one is a KMLabs Dragon (laser system *B*). Both systems are used in combination with a MACH-ZEHNDER-type interferometer for the generation of two time-delayed laser pulses as a pump-probe setup (cf. Fig. 3.1 (a) and (b)).

System *A* delivers laser pulses with a duration of 100 fs centered at 792 nm. A pulse energy of up to 5 mJ at a repetition rate of 20 Hz has been used for performing the experiments. The pulse duration has been measured with a self-constructed 2nd-order single-shot autocorrelator. As a pump-probe setup, a MACH-ZEHNDER interferometer with two polarization-dependent beam splitters with an angle of incidence of 45° has been used. A time delay between the two pulses reaching from 0 ns to 21 ns can be set, using a manual positioning stage. The delay is measured with a photo diode (Melles Griot 13DAH001) and attached oscilloscope (Tektronix TDS3052). Additionally, there is one attenuator in each arm adjusting the pump-probe energy ratio. The attenuators consist of two thin film polarizers (TFPs) reflecting the beam and a half-wave plate (WP 01 and WP 02) at the front (cf. Fig. 3.1 (a)). The pulses are focused by a CaF₂-lens (L01, $f = 500$ mm) through a CaF₂-entrance window of 1 mm thickness into the vacuum chamber. Unless it is not ex-

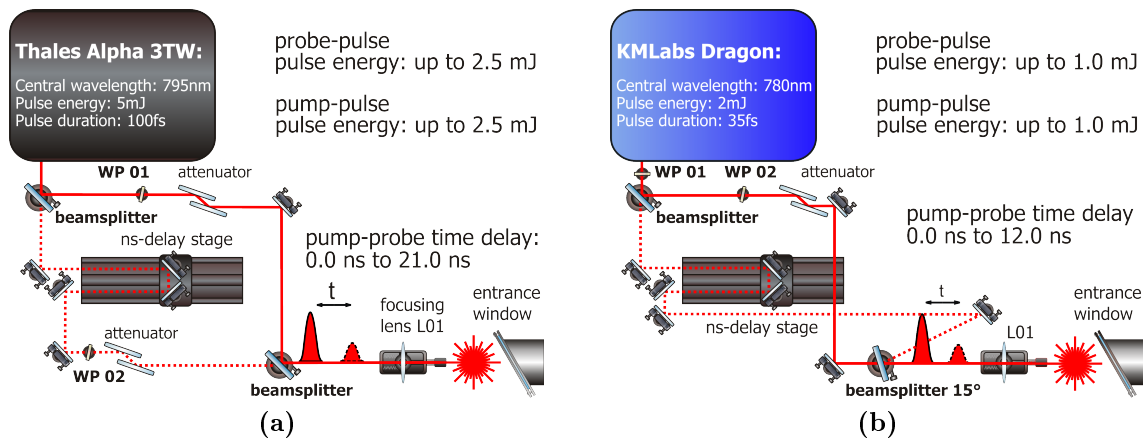


Figure 3.1: Optical setup for the generation of the pump and the probe pulse using a Mach-Zehnder interferometer. Two CPA laser systems were used: (a) modified Alpha 10C/CS by Thales and (b) KMLabs Dragon (see text for details).

licitly stated otherwise, the focal position always is 2 mm before the droplet with respect to the propagation direction, optimizing the harmonic yield (cf. sec. 4.1).

System B delivers pulses with a duration of 35 fs centered at 780 nm and up to 3 mJ pulse energy. The repetition rate is 1 kHz. Since the repetition rate is higher compared to system A, data acquisition is much faster. The pump-probe setup differs from the one used in combination with system A. The pulses are split by a polarization-dependent beam splitter with an angle of incidence of 45° . Their intensity ratio is set by a half-wave plate (WP 1) and there is only one attenuator within the arm serving the probe pulse. The attenuator is identical in construction with the one used with system A. Within the interferometer arm serving the pump pulse, there is a manual positioning stage, supporting a time delay from 0 ns to 12.0 ns. The two pulses are combined using a polarization-independent beam splitter with an angle of incidence of 15° . The pulse duration has been measured using the 2nd-order *Frequency-Resolved Optical Gating* technique (SHG-FROG) [Tre97]. The pulses are focused into the vacuum chamber according to system A.

3.1.2 Vacuum Setup

Since the generated radiation during HHG lies within the XUV and soft X-ray spectral range, the interaction has to be studied under vacuum condition. Otherwise, the generated radiation will be re-absorbed over very short length scales by ambient air. In Fig. 3.2, an overview of the vacuum setup is depicted. The pulses enter the vacuum chamber, where the interaction between the laser pulses and the droplet takes place (HHG chamber). Directly after the entrance window, there is a stainless-steel vacuum shutter (Vakom) in order to prevent condensation on the inside of the window during starting and shutdown procedure. The shutter is followed by the HHG chamber, which will be described in the next paragraph. A second vacuum shutter separates the adjacent differential pumping stage that further reduces the background pressure along the propagation direction. A third shutter isolates a grazing incidence XUV-spectrometer (LHT 30, Horiba-Jobin-Yvon, 500 lines/mm) from the liquid droplet source. The data is recorded with an attached micro-channel plate (MCP) and a computer. The distance between the droplet and the detector is 1.4 m.

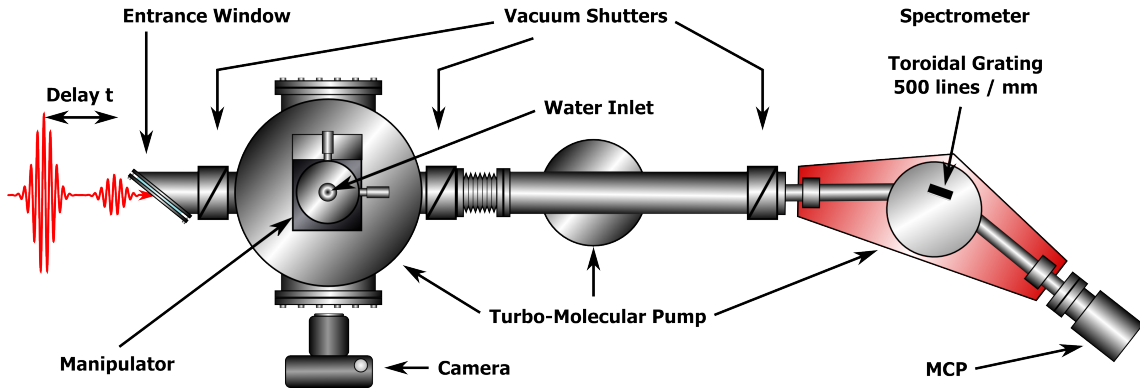


Figure 3.2: Experimental overview for HHG from liquid droplets. The capillary nozzle for droplet generation can be replaced by a larger nozzle to perform HHG in gas jets (see text for details).

Liquid Droplet Source The HHG chamber consists of a stainless-steel ISO-K 160 chamber (cf. Fig. 3.3). The capillary nozzle (Micro Jet Components, inner diameter $10\ \mu\text{m}$) generating the droplet series according to section 2.8, is mounted at the top on a three-axis ultra-high vacuum (UHV) manipulator (VAb KPM 12-50). The nozzle is fed by a capillary and an HPLC-pump (Knauer, WellChrom K-120), supplying a background pressure of up to 60 atm of de-ionized water. Inside the nozzle, there is a piezo-electric aperture which imprints the perturbation λ_{pert} onto the liquid jet (cf. sec. 2.8). The piezo-element is driven by a waveform generator (Tektronix AFG3011), delivering a voltage of 20 V at a frequency of 1.0 MHz. The diameter of the droplets during experiments was measured to $15\ \mu\text{m}$ [Kur09] at a repetition rate of 1.0 MHz. The distance the droplets propagate within the vacuum is 4 cm at a calculated velocity of $v \approx 110\ \text{m/s}$.

Liquid water however is one of the least desirable elements inside a vacuum chamber. Inserting a liquid droplet into a chamber with ultra-high vacuum condition, leads to immediate evaporation from the surface of the droplet due to the higher, temperature-dependent vapor pressure of the liquid (22 mbar for water at $20\ ^\circ\text{C}$ [Wea80]). The fastest fraction of the molecules from the droplet will be able to cross the liquid-vacuum interface and form a vapor atmosphere. Since the vacuum conditions are preserved by the turbo-molecular pumps, no saturation of the vapor pressure is reached and the droplet permanently loses matter and energy. As a result it cools down and its vapor pressure is reduced. The decrease of the vapor pressure is accompanied by a reduction of the number of evaporating molecules, leading after a short distance to a propagation of the droplet with nearly no additional loss of matter [Kur09]. As the time-of-flight of the droplet within the vacuum is about $360\ \mu\text{s}$, the temperature loss is insufficient to freeze the droplet and it remains in the liquid state.

However, a water vapor atmosphere is developed by the molecules evaporating from the droplet and a part will condensate at the interior of the vacuum chamber, forming an ice layer. Sublimation increases the water vapor atmosphere. Therefore, precautions have to be taken in order to minimize the amount of water vapor inside the vacuum chamber in a way that re-absorption effects or even damage to the data recording instrumentation are

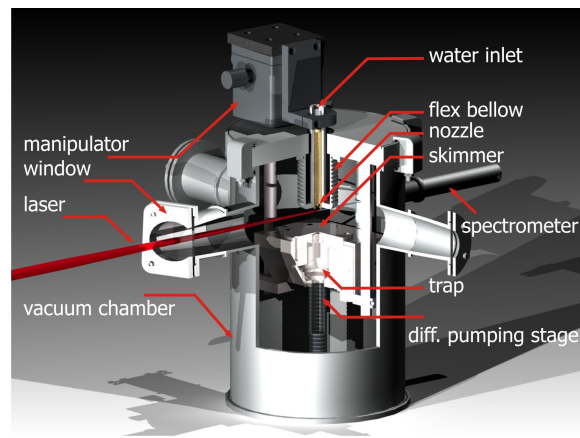


Figure 3.3: Setup of the liquid droplet source.

prevented. Hence, a trap catches the droplets after 4 cm of propagation in the vacuum.

The trap consists of a stainless-steel block and a skimmer with a hole of 500 μm . Inside the stainless-steel block, there is a drilled hole which is attached to a differential pumping stage. The whole trap is heated to 140 $^{\circ}\text{C}$ to prevent the growths of ice stalagmites that will lead to the destruction of the capillary nozzle. The droplets are shot through the skimmer into the trap and removed from the HHG chamber by the differential pumping stage. In order to catch the evaporated molecules, a liquid N_2 trap that is formed in a helix around the nozzle catches the water particles. During interaction between the laser and the target, the whole droplet is evaporated. Since there is no interaction with neighboring droplets, no shock wave is induced into any surrounding media. Thus, the process does not accelerate any other particles away from the interaction region. The vacuum conditions are preserved and the process is *debris free*. A pressure within the HHG chamber of $2.0 \cdot 10^{-5}$ mbar has been achieved under experimental condition. Measurements confirm that less than 1.7% of the matter evaporating from the droplet is not bound by the trap and contributes to a gas atmosphere inside the vacuum chamber [Kur09]. Thus, re-absorption effects are well suppressed.

The setup is comparable to the ones used by DÜSTERER *et al.* [Düs01] and FLETTNER *et al.* [Fle03]. A detailed description (in German language) of the characterization of the capillary nozzles, the evaporation characteristics of the water molecules, the setup of the trap and the efficiency of the trap can be found in ref. [Kur09].

Droplet Surveillance and Synchronization Two large view-ports are installed perpendicular to the propagation direction of the laser for the observation of the liquid droplet series. A camera (Canon EOS 500D) with commercial objective (Canon EF-S 60 mm f 2.8 macro USM, cf. Fig. 3.2) which is attached to the HHG chamber is used to supervise the correct injection of the droplet series into the skimmer. The correct spatial overlap between the focus and the droplet can be observed with the camera and is adjusted in the direction perpendicular to the propagation direction by an industrial linear stage, onto which the whole HHG chamber is mounted. Since the droplets form a determined series, their vertical position can be adjusted by the height of the nozzle or by the phase of the voltage applied to the piezo-electric element inside the nozzle. A self-constructed controlling system is used for the generation of a phase lock between the laser system and the droplets. The controlling system takes the RF-signal of the oscillator of the laser systems (80 MHz) with a photo diode and divides them to 1.0 MHz. The 1.0 MHz signal is afterwards used to trigger the signal generator which supplies the piezo-electric aperture inside the nozzle. Therefore, synchronization between droplet and laser pulses is accessible by shifting the phase of the perturbation signal.

However, the nozzle is cooled constantly by the water flux, leading to a deformation of its opening (cf. sec. 2.8). As a result, the vertical position of the droplets is changed, with respect to the laser pulse and synchronization is lost. By manually adjusting the vertical position of the droplets, synchronization can be restored. A thermodynamic equilibrium between nozzle and water flux only arises after hours of operation.

Gas Jet Setup Since the droplet is a very complex target for HHG, reference measurements in a well determined target are inevitable for reasons of comparison. Xenon (Xe) is used for HHG in a gas jet (cf. chapter 4). Since the I_p is comparable to water ($I_p = 12.13$ eV in Xe and $I_p = 12.61$ eV for the H_2O molecule), Xe is a comparable, well-defined gaseous target. As Xe is an atomic, rotationally symmetric target, only the probe pulse is used. The capillary nozzle for droplet generation can be replaced by a larger capillary for

HHG in a continuous gas jet [L'H93a, Sal95] (cf. Fig. 2.22 (b)). The nozzle is also mounted in the three-axis UHV-manipulator. The inner diameter of the capillary is $300\ \mu\text{m}$.

3.2 Identifying Parameters for High-Order Harmonic Generation from Liquid Droplets

The liquid water droplet is a rather unexplored target for HHG, although it contains rich dynamical properties and thus shows the potential of a variable target with adjustable density. As soon as the droplet is hit by the pump pulse, the ensemble of water molecules will undergo a quite complex transition on different levels, which can be described as: a time and intensity-dependent macroscopic evolution of the density reaching from liquid to gaseous densities and a microscopic transition on the atomic level via dissociative processes of the droplet into water clusters, free water molecules, atoms and ions. The different states of the droplet can be analysed with the probe pulse by HHG. However, it is a highly complex target with non-trivial spatio-temporal dynamics that depend on many parameters. Since the droplet is not well studied [Fle03, Kur13], identifying the parameters that determine the state of the target is crucial for the understanding of HHG and maximizing the harmonic yield.

This section therefore describes the identification of the different parameter settings, influencing the harmonic yield and determining the state of the target. It provides comparisons and first tests of the validity of the time and intensity-dependent density model developed in sec 2.4 and poses questions on how to identify the macroscopic and the microscopic dynamics. The section therefore is intended to establish a basis for more detailed analysis, which are described in the chapters 4 and 5.

Previous Measurements A proof-of-principle experiment of HHG from liquid water droplets has been performed by FLETTNER *et al.* [Fle03]. The measurements consist of a pump-probe experiment, where the harmonic yield is measured as a function of the harmonic order and the delay (cf. Fig. 3.4). Spectra of the emitted radiation are measured for delays from $t = 0.2\ \text{ns}$ to $t = 1.0\ \text{ns}$. At delays $t < 0.6\ \text{ns}$, incoherent radiation is emitted and attributed to ionized states of oxygen atoms. However, for delays $t > 0.6\ \text{ns}$, there is a change in the emission scheme from incoherent emission to coherent emission of high-order harmonic radiation. An increase in the intensity of the harmonic radiation, as well as in the highest observed harmonic order (HOHO) is observed (cf. Fig. 3.4). The HOHO during the measurements was the 27th order.

The authors explain the transformation in the emission patterns from plasma radiation towards HHG by the expansion of the droplet. The first laser pulse hits the droplet and generates a hot and dense plasma. The plasma starts expanding (cf. section

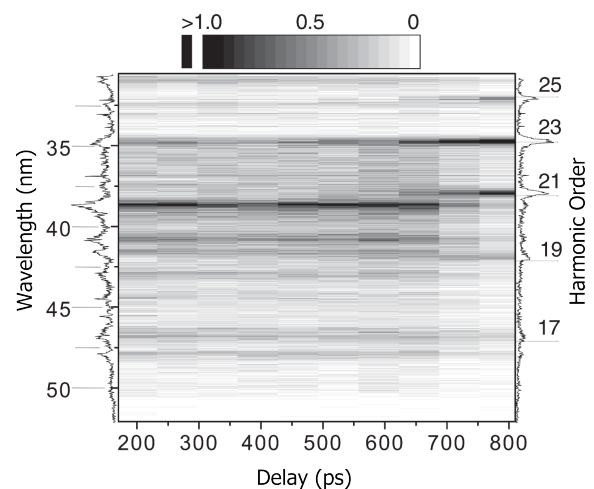


Figure 3.4: Measurement by FLETTNER *et al.* [Fle03]. Harmonic yield from water droplets as function of the harmonic order and the pump-probe time delay.

2.4.1) and is hit after the delay t by the probe pulse. As the second pulse interacts with the target, ionization takes place and the electrons are accelerated by the laser field (cf. sec. 2.2). At short time delays ($t < 0.6$ ns), the density of the target is too high and the average distance between two particles in the droplet is smaller than the excursion length of the electrons. Therefore, the electrons are scattered by surrounding ions and coherence is lost (cf. Fig. 2.17 (b)). Plasma radiation is emitted. With increasing delay, the mean distance between neighboring particles grows larger and the electronic trajectories are less perturbed. At $t > 0.6$ ns, the distance is large enough that a significant number of electrons may return to their parent ions and HHG takes place.

The measurements indicate, that the pump-probe time delay is of major influence onto the harmonic yield and can define the state of the droplet. However, the authors did not further study HHG from this unique target and only a proof-of-principle experiment has been carried out, where the delay has been varied between $t = 0.2$ ns and $t = 1.0$ ns. Reproducing the results by FLETTNER *et al.* therefore is the first task.

3.2.1 Influence of the Pump-Probe Time Delay

A typical spectrum of HHG from water droplets is depicted in Fig. 3.5. The spectrum has been measured with laser system *A* and features the characteristic decrease in intensity according to perturbation theory in the orders 9 to 11, which is followed by the plateau region in the orders 13 to 17. The cutoff region starts with the 19th harmonic order and the highest observed harmonic order (HOHO) is the 27th order.

In order to study the spatio-temporal dynamics of the liquid droplet in detail and to compare the experimental results with the measurement by FLETTNER *et al.*, the pump-probe setup is exploited to perform a scan over the delay t . Figure 3.6 (a) depicts the harmonic intensity versus order and pump-probe time delay, measured with laser system *A*. At a time

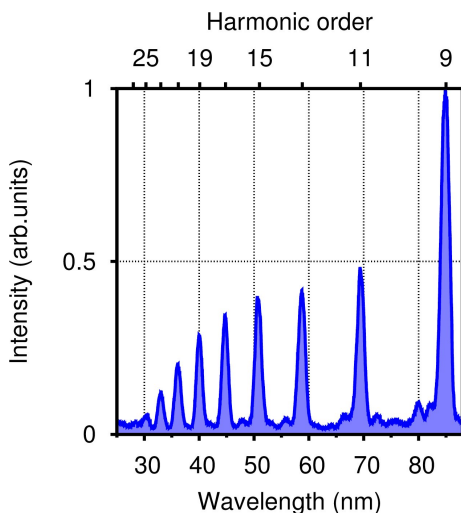


Figure 3.5: Spectrum of HHG from water droplets measured with laser system *A*. The intensity of the pump was set to $I_{\text{pump}} = 7.0 \times 10^{14}$ W/cm² and of the probe pulse $I_{\text{probe}} = 3.7 \times 10^{14}$ W/cm² at $t = 1.0$ ns.

delay of $t = 0.4$ ns, the harmonic yield is weak. Higher harmonic orders than the 17th order are not observed. As t increases, a monotonous raise in the signal of the harmonic radiation is observed, while saturation of the harmonic yield is not detected. The HOHO increases as the delay is extended, which becomes more obviously regarding single spectra for fixed time delays, that are shown in Fig. 3.6 (b). At $t = 0.4$ ns, the HOHO is the 17th harmonic order. Increasing the delay, higher orders are detected and the HOHO continuously increases to the 25th order at $t = 3.0$ ns.

At a first glance, the observations from the measured spectra in Fig. 3.6 seem to agree with the measurements by FLETTNER *et al.* [Fle03] and the explanation of a suppressed harmonic yield at short time delays due to perturbation of the electronic trajectories by high densities seems adaptable. It is also in agreement with the time-dependent density evolution calculated with the model in sec. 2.4.2. With the given laser parameters, the droplet performs a

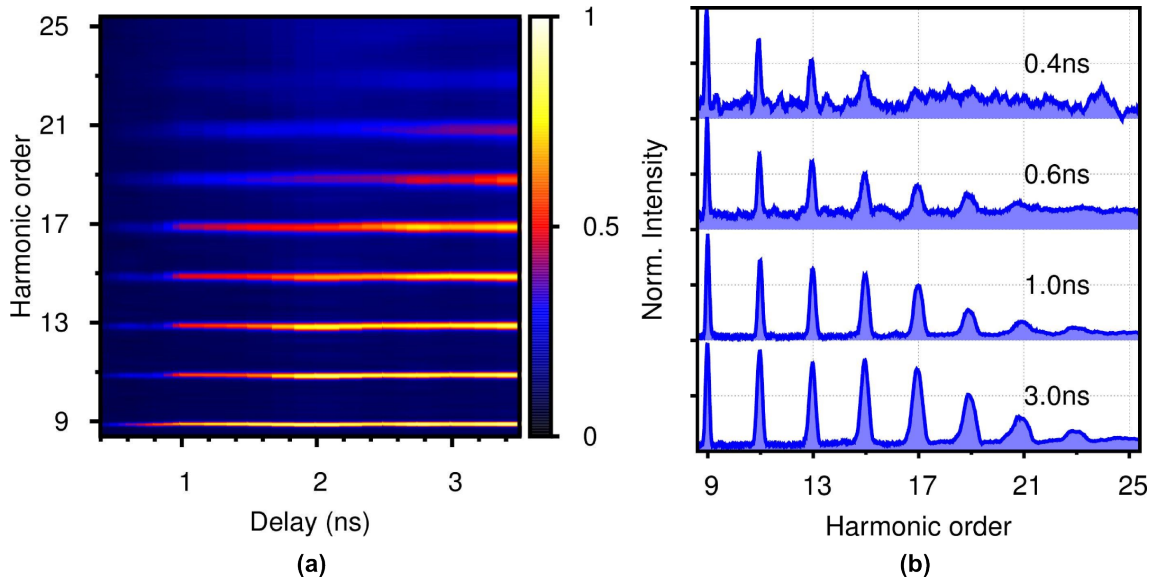


Figure 3.6: (a) Harmonic yield as function of order and pump-probe time delay. The spectra were measured with laser system *A* at an intensity of $4.5 \times 10^{14} \text{ W/cm}^2$ of pump and probe pulse and at a focal position of $z = -2 \text{ mm}$. (b) Outlines from (a). Intensity of the harmonic radiation as function of order for different time delays [Kur13].

transition from a liquid density of $\rho = 3.35 \times 10^{21} \text{ cm}^{-3}$ at $t = 0 \text{ ns}$ to gaseous density of $\rho = 7.32 \times 10^{18} \text{ cm}^{-3}$ at $t = 3.5 \text{ ns}$. As the droplet expands with increasing delay, the inter-particle distance within the target grows larger. Thus, perturbation of electronic trajectories becomes less probable. Additionally, the influence of absorption decreases, resulting in an increasing harmonic order and yield [Alt96].

However, a significant difference is the non-existence of the emission of plasma radiation at delays $t < 0.6 \text{ ns}$. Especially, the sharp transition between the emission schemes is not observed, though all parameters are comparable. Even at shorter delays than in ref. [Fle03] ($t = 0.4 \text{ ns}$), coherent radiation is emitted and only a weak signal of incoherent radiation is observed for orders higher than the 17th. A second difference is the monotonous increase in the harmonic yield and of the HOHO with increasing delay. These discrepancies could probably be attributed to differences in the experimental setups [Spi13]. In the setup presented in this thesis, the distance between source and detector is large. Moreover, narrow entrance and exit slits are used in the spectrometer. Since incoherent plasma radiation is emitted with high divergence into the whole volume, less radiation reaches the detector. The large distance in combination with narrow entrance slits further reduces the amount of plasma radiation reaching the MCP. Harmonic radiation on the other hand is emitted even less divergent than the fundamental radiation and reaches the detector more easily. Additionally, the setup used by FLETTNER *et al.* was in a non-collinear geometry of the pump and the probe pulse, while the setup used in this thesis is a collinear one, which is easier to align. Therefore, the detection of the transition might strongly depend on the applied setup.

The pump-probe time delay is of crucial influence to the harmonic yield and due to the observed monotonous increase of the signal as function of the delay in Fig. 3.6, the development of the harmonic yield for large delays is of interest. Figure 3.7 shows the intensity of the HOH radiation for even larger delays at comparable parameters to Fig. 3.6. Starting at $t = 1.5 \text{ ns}$ with a weak harmonic signal, an increase in the intensity and in the HOHO is observed. At $t = 12.5 \text{ ns}$, the harmonic yield reaches a maximum and decreases for higher

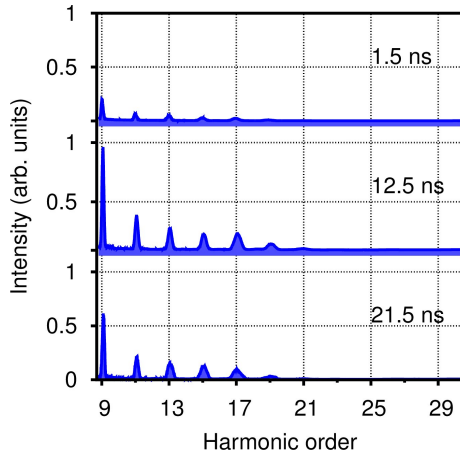


Figure 3.7: Harmonic yield as function of the harmonic order at large pump-probe time delays and comparable parameters to Fig. 3.6. The numbers indicate the delay. The harmonic yields are normalized to the maximum intensity of the 9th HOH at $t = 12.5$ ns [Kur13].

delays (cf. $t = 12.5$ ns and $t = 21.5$ ns).

The monotonic raise in the harmonic signal until a delay of $t = 12.5$ ns can also be explained with the expansion of the target. For delays larger than 12.5 ns, the expansion of the droplet is in such an advanced state, that a part of it has already propagated beyond the focal region and is no longer participating in the HHG process. Therefore, a smaller number of particles contributes to the harmonic signal and the harmonic yield decreases again.

Scanning over the pump-probe time delay and probing the spatio-temporal evolution of the droplet via HHG is a comfortable method for accessing optimized conditions for the harmonic yield. The time delay however is not the only parameter determining the expansion dynamics of the droplet. As explained in 2.4, the pump pulse intensity I_{pump} also determines the expansion velocity (cf. equation (2.12)) and thus the spatio-temporal dynamics of the target. Higher intensities lead to higher expansion velocities and an accelerated movement of the particles. Hence, the influence of I_{pump} onto the harmonic signal is studied in the next section.

3.2.2 Influence of the Intensity of the Pump Pulse

As observed in the last section, diluted droplets support an increase in the harmonic yield and are accessed by the pump-probe time delay. Regarding a fixed time delay in the model describing the density evolution in section 2.4.3, the expansion of the droplet after being hit by the pump pulse is also accelerated by increasing the intensity of the pulse (cf. Fig. 2.3 (a)). Therefore, equal conditions should be producible when the intensity of the pump pulse is varied for a fixed time delay, and an increase of the harmonic yield should be observed with raising intensity of the pump pulse.

Figure 3.8 (a) depicts the harmonic yield versus order and the intensity of the pump pulse I_{pump} for a fixed pump-probe time delay of $t = 1.0$ ns. The spectra were acquired using laser system A. During measurements, the intensity of the probe pulse was set to 3.7×10^{14} W/cm². Harmonic orders below the 15th order are generated for intensities of $I_{\text{pump}} < 1.0 \times 10^{14}$ W/cm², but with a weak signal to noise ratio. As the intensity is increased, a raise in the harmonic yield is observed with a maximum at an intensity of $I_{\text{pump}} = 3.3 \times 10^{14}$ W/cm². The HOHO is the 25th harmonic order, that decreases for higher intensities. Incoherent radiation is emitted for $I_{\text{pump}} > 3.0 \times 10^{14}$ W/cm² at higher orders than the 25th.

To clarify the dependence of the yield of a single harmonic order on I_{pump} , an outline is given for the 25th harmonic order in Fig. 3.8 (b). For the lowest intensity of $I_{\text{pump}} = 1.0 \times 10^{14}$ W/cm², no harmonic radiation is emitted. The yield raises as function of the intensity until a maximum is reached around 3.0×10^{14} W/cm². Further increase of I_{pump} to more than 3.3×10^{14} W/cm² leads to a decrease of the harmonic signal. The emission

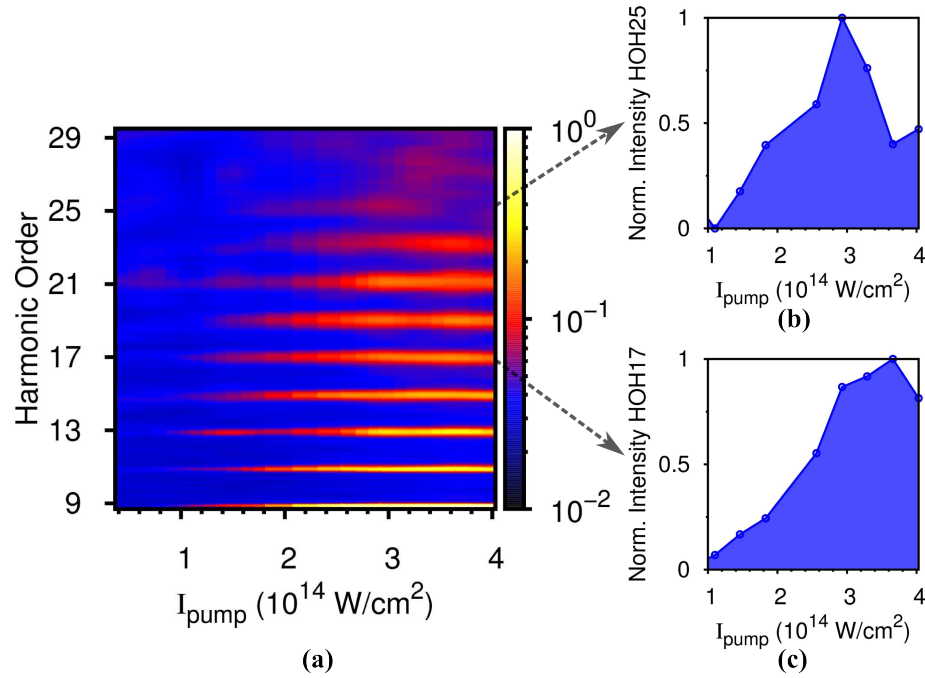


Figure 3.8: (a) Harmonic yield as function of order and intensity of the pump pulse at $t = 1.0 \text{ ns}$ [Kur13]. The intensity of the probe pulse was set to $3.7 \times 10^{14} \text{ W/cm}^2$. Outlines from (a) are depicted for the harmonic orders 25 (b) and 17 (c). Note that the harmonic intensity is scaled logarithmic in (a) while linear in (b) and (c). The spectra were measured with laser system A.

pattern changes to incoherent emission for $I_{\text{pump}} > 3.6 \times 10^{14} \text{ W/cm}^2$, though with low intensity.

A similar behaviour is observed for the 17th order in Fig. 3.8 (c). A weak signal is detected for the lowest intensity which raises as a function of the intensity until a maximum is reached. Compared with the 25th harmonic order, the maximum of the harmonic yield is shifted towards a higher intensity of $I_{\text{pump}} = 3.6 \times 10^{14} \text{ W/cm}^2$ but a decrease in the yield is still observed for the highest intensity.

The measurements indicate that the intensity of the pump pulse critically influences the harmonic yield, and optimized conditions for the harmonic yield can be found by a variation of the intensity of the pump pulse. The above mentioned intensity-dependent expansion of the droplet seems to explain the characteristics of the harmonic signal. However, several effects observed cannot be explained with the model. The decrease of the signal and of the HOHO, as well as the change in the emission pattern to incoherent radiation for high intensities can neither be interpreted using the model nor by the explanation given by FLETTNER *et al.* [Fle03]. Obviously, more parameters contribute to optimized conditions for HHG and define the characteristics of the droplet.

3.2.3 Influence of the Pulse Duration

A third parameter that can influence the dynamics of the droplet is the duration of the laser pulses τ . Figure 3.9 depicts a comparable measurement to Fig. 3.8 (a) but measured with laser system B and a pulse duration of 35 fs. The development of the harmonic yield as a function of the intensity of the pump pulse is in agreement with the measurement with $\tau = 100 \text{ fs}$. No harmonic radiation is emitted for low intensity. The signal increases as the intensity is raised and maximizes around $I_{\text{pump}} = 7.0 \times 10^{14} \text{ W/cm}^2$, where the 27th

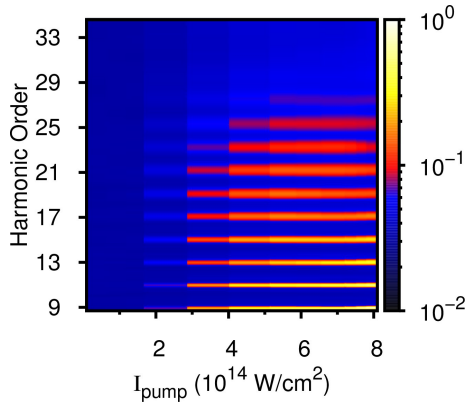


Figure 3.9: Harmonic intensity versus harmonic order and intensity of the pump pulse. The delay was set to $t = 1.0$ ns, while the I_{probe} was determined to be 9.5×10^{14} W/cm². Laser system B has been applied.

harmonic order is the HOHO. The harmonic yield decreases for the highest values of the intensity.

Though a qualitative agreement between the measurements with different pulse durations is observed, the absolute values of the respective intensities differ. The emission of harmonic radiation, as well as optimized conditions for the harmonic yield are shifted towards higher intensities for a pulse duration of 35 fs. The pulse duration therefore influences the dynamics of the droplet and causes a less rapid expansion while higher intensities are applied.

So far three parameters have been found which influence the state of the droplet, the delay, the intensity and the duration of the pump pulse. As described in the model for the density evolution, the delay and the intensity simultaneously affect the state of the target. Regarding their combined influence onto the harmonic yield therefore gives access to more information on optimized conditions for HHG.

3.2.4 Interaction between the Delay and the Intensity of the Pump Pulse

Comparing the dependence of the harmonic yield on the pump-probe time delay in Fig. 3.6 (a) with the dependence on the intensity of the pump pulse in Fig. 3.8, the two measurements agree qualitatively. Both feature a low yield at small values for t and I_{pump} , respectively. In both measurements, the yield and the HOHO increases as the defining parameter is raised (t and I_{pump} , respectively), reach a maximum and decrease afterwards. And in both measurements, no incoherent emission of radiation has been observed neither for a fixed intensity of the probe pulse and short time delays nor for a fixed time delay and a low intensity.

However, there are also discrepancies between the measurements. While the time-dependent expansion agrees with the model for the density evolution (cf. sec. 2.4.3), the intensity-dependent expansion in Fig. refFig:Intensity-Pump is only in agreement with the calculations for the increasing part of the harmonic yield, since the target expands with increasing I_{pump} . The decrease of the yield and the occurrence of incoherent radiation for high intensities cannot be explained by an expanding target since the calculated density with $\rho = 2.2 \times 10^{20}$ cm⁻³ at $I_{\text{pump}} = 4 \times 10^{14}$ W/cm² is too high. Moreover, the model does not provide the reason for the shift in the maximum yield for different harmonic orders. Additional differences can be found regarding the expansion of the droplet in detail (cf. chapter 5).

The expansion of the droplet is described by the ion velocity in equation (2.12), which is used to calculate a density of the droplet as a function of t and I_{pump} . As the ion velocities have been experimentally verified [Düs02], different combinations of t and I_{pump} should lead to the same expansion characteristics and result in the same harmonic yield. In order to test this hypothesis, figure 3.10 depicts measurements of such combinations of t and I_{pump} with almost equal densities of $\rho \approx 1 \times 10^{18}$ cm⁻³. While nearly no harmonic radiation is detected in Fig. 3.10 (a), strong signals are observed in (b) and (c), that feature all characteristics of HHG.

The disagreement between the spectra Fig. 3.10 in (a) and (b) is significant and grows even larger between (a) and (c). Contrarily, it is small between Fig. 3.10 (b) and (c). The main difference between the measurements is the intensity of the pump pulse, that increases from Fig. 3.10 (a) $3.0 \times 10^{13} \text{ W/cm}^2$ to $5.3 \times 10^{14} \text{ W/cm}^2$ in (b) and $8.2 \times 10^{14} \text{ W/cm}^2$ in (c). The intensity is in the same order of magnitude in Fig. 3.10 (b) and (c), while it is more than ten times lower in (a). As the intensity is controlled by a change of the pulse energy, the dynamics of the droplet are dependent on the energy deposited within the target. This is a hint that not only macroscopic changes, like the transition of the droplet from a liquid into a gas takes place, but also transitions on the microscopic level from water molecules in the liquid state to an atomic target via dissociative processes. Hence, not only studying the influence of the intensity onto HHG but also taking energy considerations into account could be useful to identify the spatio-temporal dynamics of the droplet. This aspect will be discussed in more detail in chapter 5.

The above described parameters to influence the expansion of the droplet in different ways. The dynamics are of complex nature and cannot be easily identified. A lot of open question on the state of the droplet arise.

3.3 Conclusions

Three different parameters have been identified with influence on the dynamics of the droplet and thus the harmonic yield. The pump-probe time delay and the intensity of the pump pulse affect the expansion of the droplet. Harmonic radiation has been observed for delays reaching from 0.4 ns to several tens of ns, for a fixed intensity of the pump pulse. Optimized conditions for the harmonic yield have been observed at $t = 12.5 \text{ ns}$, while the highest orders are observed at $t = 3.0 \text{ ns}$.

Considering the intensity-dependent expansion, lower orders of harmonic radiation are detected for intensities below $1.0 \times 10^{14} \text{ W/cm}^2$ and higher orders are observed as the intensity is increased. Optimized conditions are found for $I_{\text{pump}} = 3.0 \times 10^{14} \text{ W/cm}^2$. The use of shorter pulse durations shifts optimized conditions for HHG towards higher intensities.

Although the parameters determining the spatio-temporal dynamics have been identified, the dynamics themselves remain undisclosed. For sure the droplet expands as soon as being hit by the pump pulse but questions arise from the measurements of the harmonic yield as function of the above described parameters. The theoretical model of the droplet expansion assumes a uniform expansion, but the droplet is a highly inhomogeneous target after the interaction with the pump pulse. The side facing the incident laser pulse expands faster and absorbs a higher amount of radiation [Lin04]. Therefore a density gradient must be formed.

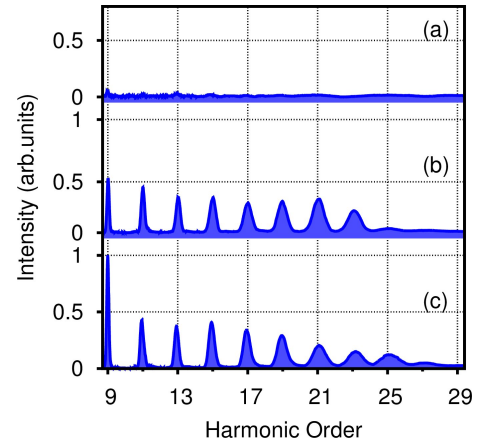


Figure 3.10: Harmonic yield versus order for calculated densities of $\rho \approx 1 \times 10^{18} \text{ cm}^{-3}$ with different values for t and I_{pump} . The spectra were measured with laser system *B* at an intensity of the probe pulse of $9.5 \times 10^{14} \text{ W/cm}^2$. (a) $t = 12.0 \text{ ns}$ and $I_{\text{pump}} = 3.0 \times 10^{13} \text{ W/cm}^2$. (b) $t = 7.0 \text{ ns}$ and $I_{\text{pump}} = 5.2 \times 10^{14} \text{ W/cm}^2$. (c) $t = 5.0 \text{ ns}$ and $I_{\text{pump}} = 8.1 \times 10^{14} \text{ W/cm}^2$. The spectra are normalized to the maximum yield in (c).

The gradient and the energy of the pump pulse affect the composition of the droplet and lead to time and energy-dependent transitions of the droplet on a microscopic level from bonded liquid water molecules into atoms and ions. This influences the harmonic yield. The perturbation of electronic trajectories by surrounding particles for high densities therefore cannot always be applied. Moreover, the target consists of a large number of particles and many emitters contribute to the harmonic signal. Thus, phase-matching aspects have to be taken into account. In fact, a lot of relevant questions arise:

- In which part of the droplet does the HHG take place?
- How do the parameters define the expansion of the droplet and its change of the thermodynamic state? On which time and intensity scales does the change happen?
- What are the phase-matching conditions in the droplet and is there a change during the expansion?
- How does the density of the target influence the harmonic yield?
- What is the reason for the decreasing harmonic yield for high intensities of the pump pulse?
- What happens on the microscopic level of the target?
- Is it possible to access the different states of the target during the expansion process (e.g. liquid state, molecules, clusters, atoms and ions) and can they be identified via HHG?

As the target itself is experimentally and theoretically not well understood, a first approach relying on simple models and experimental observations will be presented in the following sections. Questions concerning the changes of the thermodynamic state of the droplet, i.e. the expansion of the liquid into a gaseous state, as well as phase matching and ionization will be discussed in chapter 4. A more detailed study of microscopic dynamics is given in chapter 5.

Chapter 4

Phase-Matching Experiments

Since high-order harmonic radiation will serve to probe the state of the droplet, the generation process of the radiation from liquid water droplets has to be understood before addressing the imminent questions on how the microscopical dynamics of the droplet are evolving. Since the harmonic yield is critically influenced by phase matching (PM) the determination of optimized PM conditions is described in this chapter.

As described in sec. 2.6, for HHG with more than one particle the phase relationship between the emitted radiation from these particles is crucial for efficient generation of harmonic radiation. Harmonic radiation is always generated in experiments in an ensemble of emitters, which means PM has to be taken into account. However, HHG in other than gaseous targets is rarely studied [DiC09, Gan10, Ghi11, Whe12, Gan13] and PM during HHG using the droplet setup is rather unknown. In this chapter, phase-matching effects during HHG from gas jets and micrometer-sized liquid water droplets are studied [Kur12, Kur13]. To preserve equal conditions of the droplet, the intensity of the pump pulse is mainly kept at equal levels while the intensity of the probe pulse is varied. Thus, basically probe-pulse induced phenomena are studied within this chapter. The results of HHG from droplets are compared with measurements in a Xe gas jet and with theoretical predictions from sec. 2.6.

4.1 Propagation Effects

Phase matching during HHG has been studied extensively in the gas phase using different setups, such as gas cells [Tak07, Bou11], semi-infinite gas cells [Pap01, Ste09] and gas jets [Sal95] (cf. Fig. 2.22). Most of the PM experiments have been performed using a pulsed or a continuous gas jet setup [Sal95, Sal97]. Phase matching in a gas jet is well understood, and several spatial and spectral effects during HHG can be explained with different contributions of the short and the long trajectories of the electrons, which can also be manipulated. Hence, the gas jet is a well defined atomic target with densities in the range of 10^{18} cm^{-3} and with a huge number of experimental and theoretical studies discussing phase-matching aspects, making it the ideal tool for comparisons with the liquid droplet.

4.1.1 Phase Matching in a Xenon Gas Jet

As stated in sec. 3.1.2, the capillary nozzle for the generation of the droplet series can be replaced by a larger nozzle supplying a continuous gas jet. Figure 4.1 depicts a measurement of the intensity of the 15th harmonic order in Xe as a function of the medium position z , similar to the simulations in Fig. 2.15. The focus is placed after the gas jet for $z < 0$ mm, while $z > 0$ mm indicates a focus before the gas jet with respect to the propagation direction. A maximum in the harmonic intensity is observed around

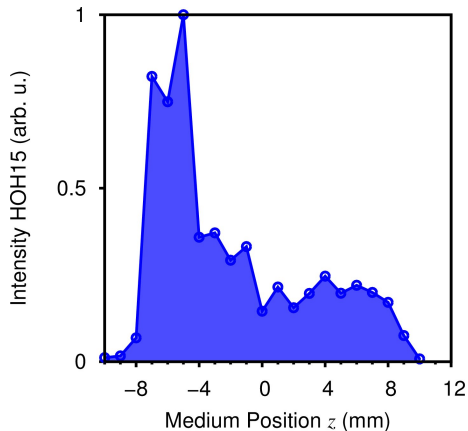


Figure 4.1: Intensity of the 15th harmonic order versus the medium position in a Xe gas jet. Laser system *B* was used with an intensity of $1.3 \times 10^{15} \text{ W/cm}^2$.

$z = -5 \text{ mm}$. The harmonic yield decreases to a minimum which is used to define $z = 0 \text{ mm}$. The minimum is followed by a less intense, plateau-like second maximum at about $z = 5 \text{ mm}$.

The measurement agrees with the calculations by SALIÈRES *et al.* [Sal95]. The position of the maxima, as well as their intensity ratio qualitatively matches with the simulation. As explained in sec. 2.6.1, the maximum for $z < 0 \text{ mm}$ is caused by PM at an off-axis position (cf. Fig. 2.14 (d)). The wave vector mismatch induced by the geometric phase is in this case compensated by the wave vector mismatch induced by the atomic phase at an off-axis position and $z < 0 \text{ mm}$ (cf. Fig. 2.11 (b)), while it is not compensated at an on-axis position. The variation of the total phase is therefore low at an off-axis position, resulting in proper PM conditions for the long trajectory and causing a maximum in the harmonic yield at $z = -5 \text{ mm}$ [Sal98, Gaa02].

The second maximum for $z > 0 \text{ mm}$ corresponds to PM at an on-axis position (cf. Fig. 2.14 (c)). Here, the geometric phase is only given by the Gouy phase. Phase matching is in this situation satisfied as the phase mismatch induced by the Gouy phase is compensated by the phase mismatch induced by the atomic phase for $z > 0 \text{ mm}$ (cf. Fig. 2.11 (a)). This is not satisfied at an off-axis position. The resulting variation of the total phase is low at an on-axis position and good PM conditions lead to a maximum in the harmonic signal around $z = 5 \text{ mm}$. High-order harmonic radiation is mostly generated via the short trajectory [Sal98, Gaa02]. The variation of the total phase around the focus is high for both cases, on and off-axis, which results in a minimum around $z = 0 \text{ mm}$ in the harmonic signal.

While PM of high-order harmonic radiation in Xe gas jets is well studied, it is not using liquid water droplets. The influence of the atomic and geometric phase contributions, as well as phase mismatches induced by free electrons and neutral particles onto HHG from water droplets have not been studied, yet. It is therefore unknown which parameters contribute to PM and how the PM conditions change during the expansion of the droplet. But the measurements in Xe are suitable for a comparison of PM properties with HHG from liquid water droplets.

While PM of high-order harmonic radiation in Xe gas jets is well studied, it is not using liquid water droplets. The influence of the atomic and geometric phase contributions, as well as phase mismatches induced by free electrons and neutral particles onto HHG from water droplets have not been studied, yet. It is therefore unknown which parameters contribute to PM and how the PM conditions change during the expansion of the droplet. But the measurements in Xe are suitable for a comparison of PM properties with HHG from liquid water droplets.

4.1.2 Phase Matching in Water Droplets

Examining the influence of the position of the medium onto HHG is a suitable tool to test the model for the calculated densities of the target (cf. sec. 2.4.2). Since experimental data of a defined gaseous target is provided in the case of Xe, a comparison between the PM properties in Xe and water droplets allows the estimate of the thermodynamical state of the target.

Figure 4.2 (a) depicts the harmonic intensity as a function of the harmonic order and the medium position. The pump-probe time delay has been set to $t = 1.0 \text{ ns}$ and the intensity of both laser pulses has been $4.5 \times 10^{14} \text{ W/cm}^2$ to generate a comparable yield to Fig. 3.6.

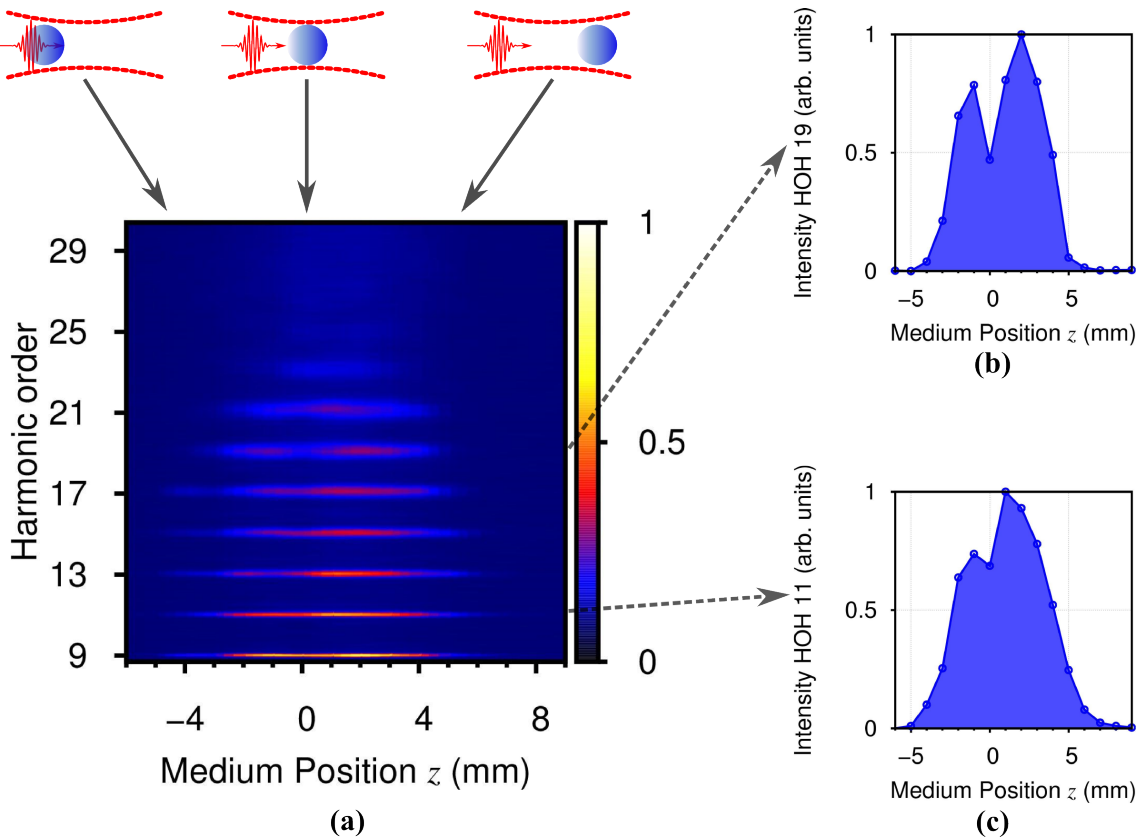


Figure 4.2: (a) Harmonic intensity as a function of the harmonic order and medium position z . The delay was set to $t = 1.0$ ns with an intensity of the pump pulse and of the probe pulse of 4.5×10^{14} W/cm². The schematics at the top indicate the relative position of the focus to the droplet, with respect to the medium position. (b) Outline of the 19th harmonic order and (c) the 11th harmonic order versus medium position. The data has been acquired with laser system A.

As in Fig. 4.1, $z < 0$ mm denotes a focal position after the droplet, whereas $z > 0$ mm indicates a focal position before the droplet with respect to the medium position. The harmonic yield maximizes at two instances, for $z = -1$ mm and $z = 2$ mm, where also the 25th order as HOHO is observed. The minimum in the harmonic signal is situated at $z = 0$ mm. The dependence of the harmonic yield on the medium position becomes more obvious regarding outlines of the 19th harmonic order in Fig. 4.2 (b) and the 11th harmonic order in (c). The typical double-peak structure is observed but more clearly pronounced than in the case of Xe.

With the given laser parameters t and I_{pump} , the density of the droplet is calculated with equation (2.15) to $\rho(t, I_{\text{pump}}) = 2.1 \times 10^{20}$ cm⁻³, which is the density of a dense gas. However, the intensity in the interaction region is changed by moving the focal position. Hence, the intensity of the pump pulse is reduced, when moving the focus to other positions than $z = 0$ mm. According to 3.2.2, this results in a change of the expansion dynamics of the droplet. But by changing the focal position within the *Rayleigh* range ($z_R = 5.42$ mm), the intensity is changed by a factor of 2 and similar conditions for HHG are preserved, as indicated in Fig. 3.8 where the influence of I_{pump} has been studied. A reduction of the intensity of the pump pulse by a factor of 2.7 leads to a density of 3.5×10^{20} cm⁻³. The difference of the densities is below one order of magnitude and the target still is a dense gas. Moreover, the effects described in Fig. 4.2 are observed within a range of 3 mm around the focus, which is below the value of z_R , so that equal states of the droplet are sustained

for HHG.

The double-peak structure therefore can be explained with PM in a gas jet [Sal95, Bou11, Kur13]. Like in the Xe gas jet, the maximum at $z < -1$ mm is attributed to PM at an off-axis position. The second maximum at $z = 2$ mm can be assigned to PM at an on-axis position. The shape of the double-peak structure is pronounced more explicitly, when compared with Fig. 4.1 and therefore is in better agreement with the calculations by SALIÈRES *et al.* [Sal95] (cf. Fig. 2.15). The measurements prove that the thermodynamical phase of the target is the gas phase for the laser parameters applied. However, the amplitudes of the maxima are inverted (cf. Fig. 2.15) [Sal95, Bou11, Kur13]. The contributions from the short trajectory ($z > 0$ mm) now have a higher yield than the contributions assigned to the long trajectories. This is a discrepancy with the measurements in the gas jet that cannot be explained, yet.

4.1.3 Focus and Delay

In order to investigate whether different thermodynamical states can be prepared with a variation of the delay and identified by their PM properties, a measurement of the harmonic yield as a function of the medium position and the delay has been performed. The measurement is a first attempt to investigate changes of the thermodynamical phase of the droplet but it reveals more information than can be explained at this stadium of the thesis. Therefore, references to later sections will be given within the text.

Figure 4.3 depicts the 15th harmonic order as a function of the medium position for different delays. Laser system *B* has been exploited for the measurement, with the intensities $I_{\text{pump}} = 6 \times 10^{14}$ W/cm² and $I_{\text{probe}} = 1.5 \times 10^{15}$ W/cm². The higher value of I_{pump} has been chosen since the harmonic yield maximizes for this intensity, as observed in Fig. 3.9. The reason for the large value of I_{probe} is related to less ionization using shorter pulses, which will be discussed in detail in sec. 4.3. Four different delays are regarded, $t = 0.5$ ns, 1.0 ns, 4.0 ns and 7.0 ns, as they give access to a calculated wide density range from $\rho = 2.3 \times 10^{21}$ cm⁻³ to $\rho = 3.5 \times 10^{18}$ cm⁻³.

Due to the collinear setup, the focus of both pulses is moved simultaneously and therefore the intensity of the pump pulse significantly varies along the z -axis. This is no issue within the Rayleigh range ($z_R = 2.6$ mm) where a density variation of a factor of 2 is calculated. Though, harmonic radiation is detected for values of $|z| > z_R$ where a significant change in the intensity of the pump pulse should lead to varying expansion characteristics of the droplet along the z -axis, which will be discussed in detail in secs. 5.1.2 and 5.2. However, comparable states of the droplet are found within a range of $|z| < 4.1$ mm (black line). The intensity of the probe pulse is varied through the z -axis by nearly a factor of ten from $I_{\text{probe}} = 1.5 \times 10^{15}$ W/cm² at $z = 0$ mm to $I_{\text{probe}} = 1.2 \times 10^{14}$ W/cm² at $z = 7$ mm. Hence, the intensity is high enough for HHG throughout the z -range.

The harmonic yield at $t = 0.5$ ns features the above described characteristic double peak structure. Two maxima at $z = -1$ mm and $z = 2$ mm appear and can be attributed to off and on-axis phase matching, respectively. A minimum at $z = 0$ mm is observed. Harmonic radiation is emitted within a confined area from $z = -2$ mm to $z = 6$ mm. When the delay is increased to $t = 1.0$ ns, harmonic radiation is emitted over a wider z -range. Two maxima are observed, too. The first is at $z = 6$ mm and the second at $z = -3$ mm, while the harmonic

yield is rather constant around $z = 0$ mm. The signal is higher for $z < 0$ mm than at values of $z > 0$ mm, developing an asymmetric shape. Further increase of the delay to $t = 4.0$ ns results in an even less distinct variation of the harmonic yield within the Rayleigh range and a rather constant signal is observed. But two pronounced maxima are detected at $z = 7$ mm and $z = -4$ mm. The yield features a symmetric trend with center around $z = 2$ mm. The situation changes again when $t = 7.0$ ns is regarded. A clear double peak structure is observed with two maxima at $z = -1$ mm and a broad maximum around $z = 4$ mm. A minimum at $z = 0$ mm is detected. The modulation of the intensity is more distinctive than for the previous time delay and more comparable to $t = 0.5$ ns and $t = 1.0$ ns.

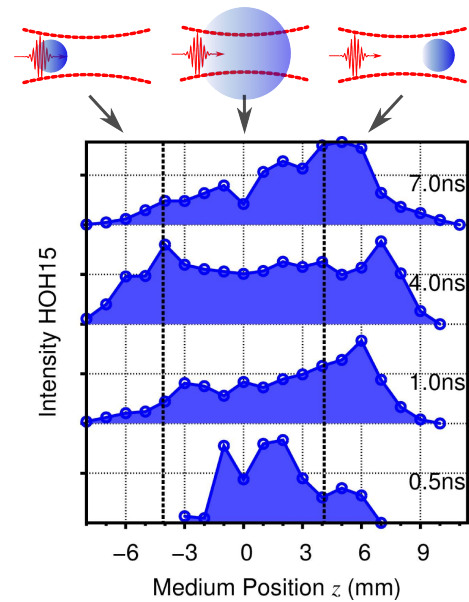


Figure 4.3: Intensity of the 15th harmonic order versus the medium position from water droplets for different delays. Laser system *B* has been used with the intensities $I_{\text{pump}} = 6 \times 10^{14}$ W/cm² and $I_{\text{probe}} = 1.5 \times 10^{15}$ W/cm². Comparable conditions of the droplet are preserved for $|z| < 4.1$ mm (black lines). The scheme at the top indicates the varying expansion of the droplet for different values of z . Each signal has been normalized to its maximum yield.

As in secs. 4.1.1 and 4.1.2, the double peak structure can be explained with PM at an on and an off-axis position for $z < 0$ mm and $z > 0$ mm, respectively [Sal95, Kur12, Kur13]. Harmonic radiation is detected for a larger z -range at positive values of z . This means PM conditions for the short trajectory are satisfied for a wider range than for the long trajectory, which is in agreement with the previous measurements. At a delay of 0.5 ns, the variation of the size of the droplet is with a radius of 0.24 mm small and the harmonic yield develops as in a gaseous target but with a very confined z -range which can be attributed to the small size of the droplet and its high density.

The signal at a delay of $t = 1.0$ ns is comparable to the measurement in a Xe gas jet in Fig. 4.1, though with inverted amplitudes and an extreme suppression of the contribution of the long trajectory. The reason for this is related to the degree of ionization within the target and is discussed in detail in sec. 5.2. The variation of the radius of the droplet is still small with values between $r = 0.47$ mm at $z = 0$ mm and $r = 0.32$ mm at $z = 4.1$ mm and results in a calculated density of the target around $\rho = 4 \times 10^{20}$ cm⁻³, which is a dense gas and in agreement with the observed PM properties. However, a significant amount of radiation with increasing signal is detected at positions $z > 4.1$ mm. As stated above, the expansion behaviour of the droplet changes and is slower for values of $z > 4.1$ mm due to the lower intensity of the pump pulse. But the differing density is still within the same order of magnitude and therefore of minor influence. The observed higher yield is thus attributed to the change in the intensity of the probe pulse, which generates less free electrons that induce a phase mismatch to the PM conditions [Alt96] which will be discussed in detail in sec. 4.3. In conclusion, the maximum at $z = 6$ mm still can be attributed to the contribution from the short trajectory, while the less pronounced maximum at $z = -3$ mm is attributed to the contribution of the long trajectory.

A comparable situation is found for a delay of $t = 7.0$ ns, where a similar development of the harmonic signal is observed. The radius of the droplet is between $r = 3.3$ mm

at $z = 0$ mm and $r = 2.3$ mm at $z = 4.1$ mm, which means the variation of the size becomes larger than at shorter delays. The calculated density of the target however is little affected due to the flat slope of the density curve for large delays and is around $\rho = 3.5 \times 10^{18} \text{ cm}^{-3}$ (cf. Fig. 2.3). The density of the target therefore should be within an equal order of magnitude compared with the measurement in a Xe gas jet. A proof for the calculations can be found by comparing the developments of the signals from xenon and water. In both measurements, the harmonic radiation is detected from $z \approx -8$ mm to $z \approx 9$ mm. A minimum is observed at $z = 0$ mm and a maximum for the contribution of the short trajectory around $z = 5$ mm. Moreover, the ratios of the two maxima I_{short}/I_{long} in H_2O and I_{long}/I_{short} in Xe are comparable in both measurements with a factor of 5:1, though with inverted contributions from short and long trajectories (where $I_{short/long}$ denotes the contributions from short and long trajectories). From the agreement between the measurements in Xe and water can be deduced that the model for the calculation of the density-evolution is confirmed and the target is in the gas phase with a density within the order of $\rho \sim 10^{18} \text{ cm}^{-3}$.

A different behaviour of the harmonic signal is found at $t = 4.0$ ns. The radius of the droplet is between $r = 1.9$ mm at $z = 0$ mm and $r = 1.3$ mm at $z = 4.1$ mm with a calculated density around $\rho = 8 \times 10^{18} \text{ cm}^{-3}$. Although the variation of the size of the droplet is larger, PM conditions are preserved for a wide z -range reaching from $z = -3$ mm to $z = 6$ mm, indicated by the constant harmonic yield. Moreover, the amplitudes of the maxima attributed to short and long trajectory are equal. The experimental results reveal equal conversion efficiencies for both trajectories. The observed development of the harmonic yield features indicate the existence of dynamics within the droplet on the microscopic level but cannot be interpreted at the present stadium of the thesis. An explanation will follow in sec. 5.2.

In summary, the contribution of the long trajectory is suppressed in most cases, while the contribution of the short trajectory is not. By comparing the results with measurements in a gas jet, a qualitative agreement in the development of the harmonic yield as a function of z is found for all delays but $t = 4.0$ ns, which indicates more complex dynamics of the droplet.

Furthermore, indications of the influence of ionization onto the harmonic yield have been observed. The following section therefore studies effects that are caused by free electrons and changes in the PM conditions on time scales shorter than the duration of the driving pulse.

4.2 Ionization-Induced Effects

Free electrons can critically influence HHG. Besides the decrease of the harmonic yield, free electrons can induce a phase mismatch that leads to a change of the spectral features of the emitted radiation [Zho00] (cf. 2.6.1). But the density of free electrons can be controlled by changing the intensity and the duration of the laser pulses applied, and its influence can be probed via HHG. In this section, the effect of ionization onto HHG is studied by the preparation of the droplet with differing densities of free electrons.

4.2.1 Transient Phase Matching

Since plasma effects become more pronounced using intense pulses with long durations, laser system *A* has been used. In order to provide optimum conditions for HHG the

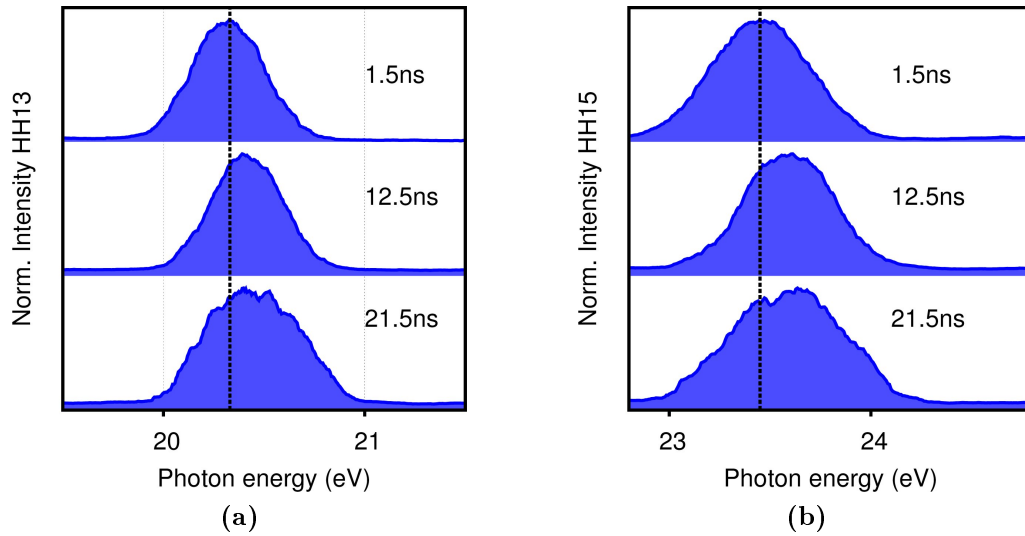


Figure 4.4: Spectral broadening and blue shift for the 13th (a) and 15th (b) harmonic order for different delays. Laser system *A* has been applied with an intensity of $3.6 \times 10^{14} \text{ W/cm}^2$ for both pulses [Kur13]. The black line indicates the calculated central photon energy of the harmonic orders.

intensity of both pulses has been set to a level of $3.6 \times 10^{14} \text{ W/cm}^2$ (cf. sec. 3.2.2 and 4.3), which is high enough to sufficiently ionize the droplet. In Fig. 4.4 (a), normalized spectral profiles of the 13th harmonic order for increasing time delays are depicted. For a delay of $t = 1.5 \text{ ns}$, the harmonic line is centered around a photon energy of 20.33 eV, which is in good agreement with the calculated value of 20.30 eV. The full-width half maximum of the spectral line is $\Delta E = 0.41 \text{ eV}$. Increasing the time delay to 12.5 ns, the harmonic line is shifted towards a higher photon energy of 20.39 eV, and a slight broadening is observed with $\Delta E = 0.43 \text{ eV}$. Further increase of the time delay to 21.5 ns leads to a significant broadening of $\Delta E = 0.61 \text{ eV}$ and an additional blue shift to 20.40 eV. A similar behaviour is observed for the 15th harmonic order, which is depicted in Fig. 4.4 (b). The full-width half maximum increases from $\Delta E = 0.54 \text{ eV}$ at $t = 1.5 \text{ ns}$ via $\Delta E = 0.59 \text{ eV}$ at $t = 12.5 \text{ ns}$ to $\Delta E = 0.71 \text{ eV}$ at $t = 21.5 \text{ ns}$ with a blue shift from 23.45 eV via 23.61 eV to 23.64 eV, respectively. The calculated value for the 15th harmonic order is 23.42 eV.

Obviously, spectral broadening and blue shifting increase as a function of the delay. The intensity of the pulses is high enough to cause a significant amount of free electrons. However, no splitting effect is observed and the intensity is therefore raised to reveal more effects onto the harmonic yield as the density of free electrons rises.

Figure 4.5 depicts the temporal evolution of spectral splitting in (a) for the 13th harmonic order and in Fig. 4.5 (b) for the 15th harmonic order. The intensity of both pulses has been set to $7.0 \times 10^{14} \text{ W/cm}^2$ and the position of the medium has been set to a value $z > 0 \text{ mm}$. In Fig. 4.5 (a), a single harmonic line is detected and still no splitting effect is observed for $t = 1.0 \text{ ns}$. As the time delay is increased to 2.0 ns, a small maximum appears at higher energies. The splitting becomes more pronounced with an increase of the time delay to 6.0 ns. A similar behaviour is observed for the 15th harmonic order in Fig. 4.5 (b).

As explained in sec. 2.6.1, spectral broadening, splitting, and blue-shift depend on the density of free electrons. During the interaction of the probe pulse with the target, the electron density increases rapidly and a temporally varying density of free electrons is created (cf. Fig. 2.16 (a)). The number of free electrons thereby increases monotonically

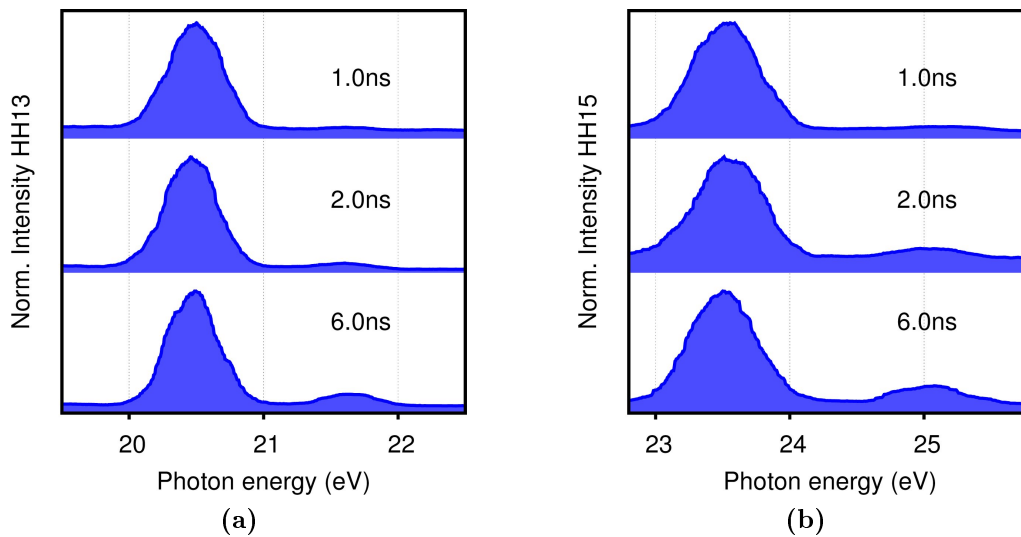


Figure 4.5: Temporal evolution of spectral splitting of the 13th (a) and the 15th harmonic order (b) with an intensity of $7 \times 10^{14} \text{ W/cm}^2$ for both pulses and a focal position of $z < 0 \text{ mm}$ [Kur13].

on the rising edge of the probe pulse. The free electrons induce a phase shift to the harmonic field (cf. equation (2.36)) by a change of the refractive index, which results in the generation of new, higher frequencies. The harmonic line is therefore broadened, while its blue shift results from the monotonic raise of the density of free electrons. Transient phase matching (TPM) conditions therefore exist (cf. sec. 2.6.1) and the spectrum splits [Alt96, Alt99, Wan00, Zho00, Ste09, Kur13]. A more detailed description can be found in Ref. [Zho00]. No effect is observed for short time delays but spectral splitting, blue shift, and broadening become more prominent with increasing time delay. Thus, the density of free electrons rises with the time delay. Moreover, all effects are maximized for the largest delays.

For conclusions from the observed TPM effects, it is helpful to regard the calculated density of the target again. The density of the droplet is decreased from $7.9 \times 10^{19} \text{ cm}^{-3}$ at $t = 1.5 \text{ ns}$ to $4.0 \times 10^{16} \text{ cm}^{-3}$ at $t = 21.5 \text{ ns}$ (cf. figs. 4.4 (a) and (b)) and from $2.2 \times 10^{20} \text{ cm}^{-3}$ at $t = 1.0 \text{ ns}$ to $1.7 \times 10^{18} \text{ cm}^{-3}$ at $t = 6.0 \text{ ns}$ (cf. figs. 4.5 (a) and (b)). The target therefore is in the gas phase and its density becomes diluted as the delay is raised. At high densities, the leading part of the probe pulse ignites a plasma at the surface of the droplet, that screens it from the trailing part [Fen97]. The total ionization therefore is less [Kur13]. For low-density states of the droplet, it is easier for the probe pulse to access the interior and cause massive ionization throughout the target. The result is an increase of the overall ionization with decreasing density of the target, and TPM conditions are induced by the probe pulse [Kur13]. Additionally, the TPM effects confirm that the target is in a gaseous state.

Higher densities of free electrons can be generated with long laser pulses since the ionization probability increases [Chr96]. Free electrons however are an undesired phenomenon during HHG since they destroy PM conditions and decrease the harmonic yield. Therefore short pulses are a more suitable tool for HHG. Their influence onto HHG is studied in the next section.

4.2.2 Influence of the Pulse Duration

In order to study the influence of the pulse duration in a more simple but also well-defined target, the Xe gas jet setup (cf. 3.1.2) is used first to explain the observed effects. Thereafter, HHG from water droplets is described using two different pulse durations.

Short Pulses and Xe Atoms Figure 4.6 (a) and (b) depict spectra of HHG in a Xe gas jet at a background pressure of 4 atm. The measurements were recorded with laser system *A* in (a) with an intensity of $4.6 \times 10^{14} \text{ W/cm}^2$ and a pulse duration of 100 fs and with laser system *B* in (b) with an intensity of $4.2 \times 10^{14} \text{ W/cm}^2$ and a pulse duration of 35 fs.

Both spectra feature all the characteristics described in the previous sections 2.5 and 3.2.1. In Fig. 4.6 (a), the highest observed harmonic order is the 21st order, while it is enhanced to the 25th order in Fig. 4.6 (b). Since the intensity of the laser pulses and the densities of the targets are comparable, the only difference between the measurements in 4.6 (a) and (b) is the pulse duration which causes the four orders larger HOHO.

The reason for the increase of the HOHO lies within the sub-cycle dynamics of the electrons within the laser field. By using shorter pulses, less optical cycles are available to cause ionization. This means with shorter pulse durations, the number of events generating free electrons is lower and the overall ionization is decreased compared with longer pulses [Chr96, Chr97, Pri00, Gan13]. Considering a pulse with a few optical cycles that interacts with a Xe atom, the induced dipole moment of the atom is retarded with respect to the envelope of the electric field. The atomic response therefore becomes non-adiabatic [Chr97]. As a result, the ionization probability is decreased, when compared to longer pulses with equal intensity [Chr96]. Therefore, higher intensities can be applied before the atom is ionized. In a gas jet where an ensemble of atoms is regarded, this leads to a depletion of the ground state at higher intensities and an increased maximum photon energy according to the cutoff law (cf. equation (2.18)). Though the used pulses in Fig. 4.6 are not within the few-cycle regime, the effect of suppressed ionization already becomes observable and the HOHO is increased. Additionally, less ionization leads to a smaller density of free electrons, which means the induced phase mismatch by free electrons is decreased, too.

In the simple, atomic case of Xe, the effects can easily be observed. Considering HHG from water droplets, the situation becomes more complex, as the time and intensity-dependent

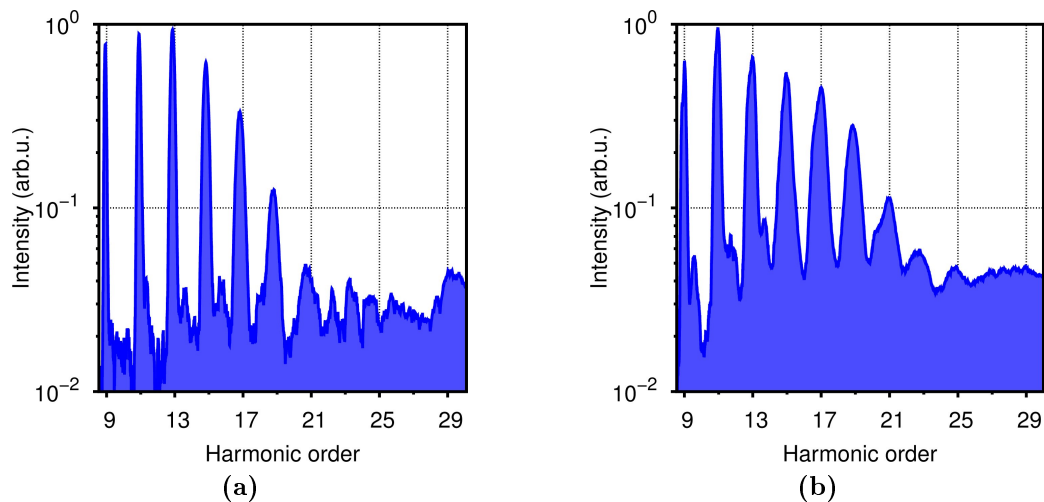


Figure 4.6: HHG in a Xe gas jet. (a) Pulse duration of 100 fs. (b) Pulse duration of 35 fs (b). Note that the spectra are not efficiency corrected by the calibration curve of the spectrometer.

evolution of the droplet has to be taken into account.

Short Pulses and Water Droplets In order to study the influence of the pulse duration onto HHG from water droplets, equal conditions of the droplet have to be prepared. Since the expansion of the droplet varies for pulse durations of $\tau_1 = 100$ fs and $\tau_2 = 35$ fs as observed in sec. 3.2.3, a two times higher intensity of the pump pulse has to be chosen when using 35 fs-pulses to prepare equal states of the target (the reason for the intensity increase will be given in 5.1.3). The parameters of laser system *A* therefore have been set to $\tau_1 = 100$ fs with $I_{\text{pump}} = 4.5 \times 10^{14}$ W/cm² and $I_{\text{probe}} = 4.5 \times 10^{14}$ W/cm² and the parameters of system *B* to $\tau_2 = 35$ fs with $I_{\text{pump}} = 8.4 \times 10^{14}$ W/cm² and $I_{\text{probe}} = 1.9 \times 10^{15}$ W/cm². The time delay has been set to $t = 3.0$ ns for both cases in order to generate a gaseous target with a density of $\rho \approx 3 \times 10^{19}$ cm⁻³ which is comparable to the measurements in the gas jet.

Figure 4.7 depicts spectra acquired with pulses with a duration of 100 fs in (a) and a duration of 35 fs in (b). Though, the intensity of the probe pulse is nearly four times higher in the 35 fs case, both spectra are comparable. The signal of the 9th order is weaker in Fig. 4.7 (a) and a difference in the HOHO is detected. Using pulses with a duration of 100 fs the HOHO is the 27th harmonic order, while it is the 29th harmonic order for 35 fs.

As in the case of the xenon target, a higher maximum photon energy is observed using shorter pulses and can also be attributed to the lower ionization probability. The observations made in HHG from water droplets can also be compared directly with the measurements in the Xe gas jet in Fig. 4.6, since the densities of both targets only differ by a factor of approximately 5 and the difference in the ionization potentials is small ($I_p = 12.13$ eV in Xe and $I_p = 12.61$ eV for the H₂O molecule). The maximum photon energy therefore should be identical for HHG from the gas jet and from water droplets. However, the HOHO is higher in the latter case for both pulse durations. The enhancement could be an indication that HHG takes place in water molecules, as a similar observation has been made in oxygen molecules by SHAN *et al.* [Sha02] and in water by WONG *et al.* [Won10]. The enhanced HOHO using water molecules has been attributed to suppressed ionization due to the orbital symmetry of the water molecule. But the microscopic state of the drop-

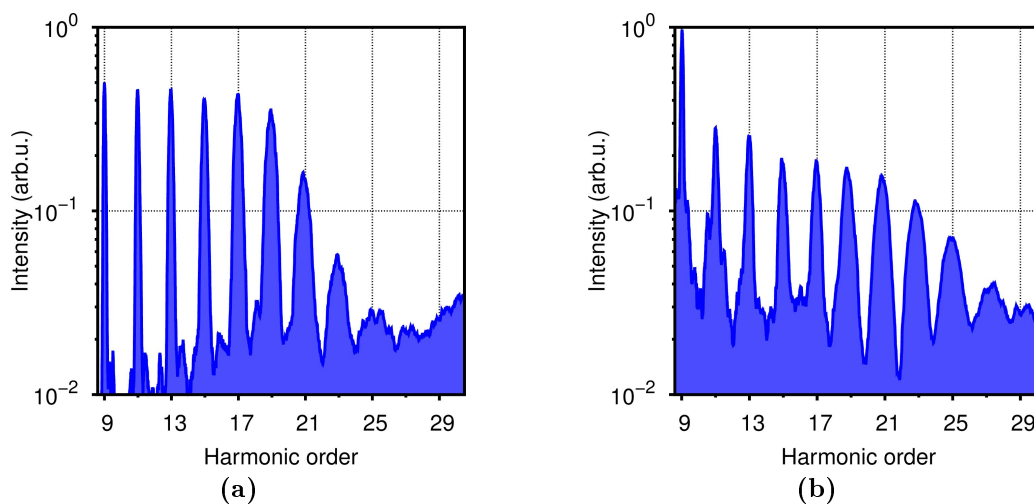


Figure 4.7: Spectra of harmonic radiation for pulse durations of (a) 100 fs (laser system *A*). (b) 35 fs (laser system *B*) for comparable parameters of the laser systems.

let is unknown at this stadium of the thesis and more sophisticated techniques have to be developed in order to reveal its microscopic evolution, which will be presented in sec. 5.3. Nevertheless, ionization is suppressed for shorter pulse durations and higher intensities of the probe pulse can be applied while using pulses with 100 fs duration would perturb PM conditions by generating a heavily ionized target and thus suppress the harmonic radiation. As harmonic radiation can be generated with higher intensities, the interest arises of what will happen at shorter time delays where the density of the target is higher.

Pump-Probe Time Delay As observed in measurements with pulses with a duration of 100 fs in sec. 3.2.1, the delay between pump and probe pulse can critically influence the intensity of the emitted harmonic radiation. In Fig. 3.6, an increase in the XUV signal was detected as a function of the delay, while no abrupt change in the emission pattern from incoherent towards coherent emission of radiation was measured and the HOHO increased steadily up to the 25th order. The time-dependent development of the harmonic signal has been explained with the dilution of the target and less perturbation of electronic trajectories as the droplet expands.

With the explanation given above, no difference in the time-dependent development of the signal of the harmonic radiation should be observed when using laser pulses with a duration of 35 fs. Figure 4.8 depicts a comparable measurement to Fig. 3.6 but the data has been acquired with laser system *B* applying pulses with a duration of 40 fs. The intensity of the pump pulse has been set to $I_{\text{pump}} = 4.5 \times 10^{14} \text{ W/cm}^2$. In order to study the influence of ionization onto the harmonic signal, the intensity of the probe pulse has been set to $I_{\text{probe}} = 1.4 \times 10^{15} \text{ W/cm}^2$, more than three times the value of the long pulse measurement. Figure 4.8 (a) shows the harmonic yield versus order and delay. The intensity of the emitted radiation and the HOHO increases with rising delay. For a short delay of $t < 0.2 \text{ ns}$, the harmonic yield is weak and orders up to the 11th order are generated. As t increases, a monotonous raise in the signal of the harmonic radiation is observed, while a saturation of the harmonic yield is not detected within the delay range. The HOHO increases as the delay is extended, which becomes more obvious regarding single spectra from Fig. 4.8 (a) for fixed time delays that are depicted in (b).

At $t = 0.1 \text{ ns}$, the 9th and the 11th harmonic order are detected, while the latter also is the HOHO. Incoherent radiation is generated at the position of higher orders. Increasing the delay to $t = 0.2 \text{ ns}$, a raise in the harmonic yield is observed and the HOHO is extended to the 25th harmonic order. Additionally, there is radiation from plasma recombination between the 13th and the 15th order, as well as between the 17th and the 19th order, but with a weaker signal. The amount of incoherent emission is further reduced, when t is increased to 0.4 ns. The HOHO is in this case the 27th harmonic order. No significant change is observed when the delay is set to $t = 0.6 \text{ ns}$.

The droplet is prepared in a comparable state in both measurements¹ and similar conditions for HHG should be found. The general development of the harmonic signal is the same in both measurements and the explanation for the time-dependent raise of the harmonic yield can be adapted from sec. 3.2.1. The droplet starts expanding as soon as being hit by the pump pulse and electronic trajectories are less perturbed as the inter-particle distance grows larger. That is why the harmonic yield increases monotonically and higher orders

¹Due to the shorter pulse duration in using 35 fs-pulses, the expansion of the droplet requires a higher intensity to achieve the same expansion velocity compared with a pulse duration of 100 fs. Hence, the density of the droplet is higher in the first case but the difference between the two measurements is below a factor of five in the considered delay range. A detailed discussion will be given in chapter 5

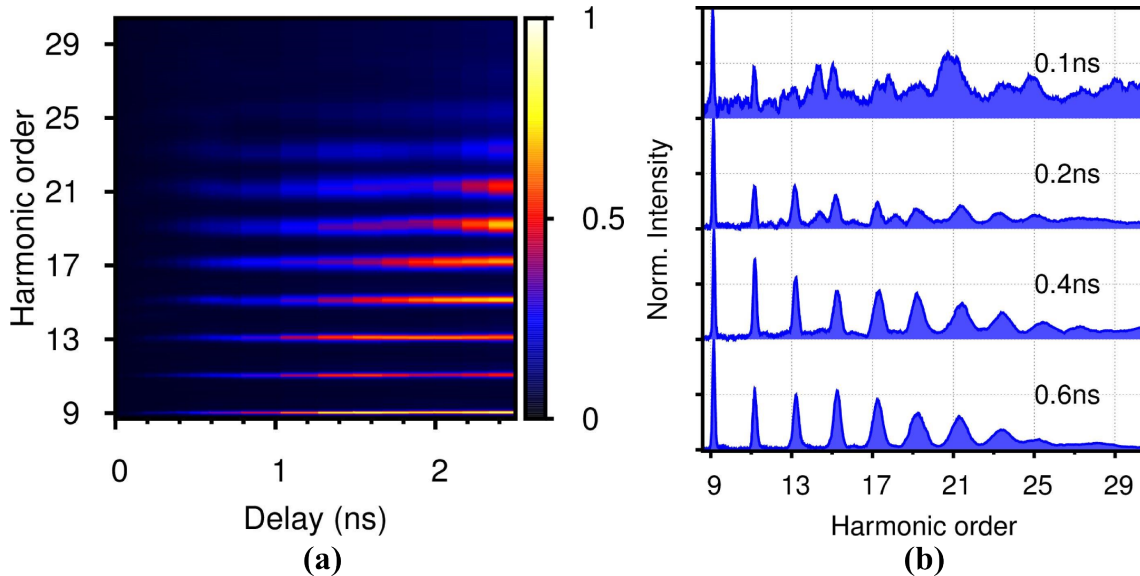


Figure 4.8: (a) Harmonic yield as a function of order and pump-probe time delay. The spectra were measured with laser system *B* at an intensity of $I_{\text{pump}} = 4.5 \times 10^{14} \text{ W/cm}^2$ of pump pulse. The intensity of the probe pulse was $I_{\text{probe}} = 1.4 \times 10^{15} \text{ W/cm}^2$ at a focal position of $z = -2 \text{ mm}$. (b) Outlines from (a). Intensity of the harmonic radiation as function of order for different time delays. The spectra are normalized to the intensity of the 9th harmonic order. Note that the spectra are linearly scaled.

are observed for larger values of t . A qualitative agreement of the spectra is found for time delays larger or equal to $t = 0.6 \text{ ns}$, where also the HOHO is rather comparable with the 21st order using 100 fs pulses and the 25th order using 35 fs pulses. However, a disagreement is found regarding the HOHO at $t = 0.4 \text{ ns}$, which is the 17th order using 100 fs pulses and 27th order using 35 fs pulses. Additionally, no significant amount of incoherent radiation is generated using the pulses with shorter duration, while incoherent radiation has been observed at the position of higher orders using 100 fs-pulses. The two time developments of the harmonic spectra also differ at shorter delays. While no harmonic radiation is observed for $t < 0.4 \text{ ns}$ using 100 fs-pulses, it is when the shorter pulse duration is applied and a significant amount of incoherent radiation is only observed for the shortest time delay. However, no abrupt change in the emission pattern from incoherent to coherent radiation has been observed in both experiments but a continuous transition towards the emission of higher orders as the delay is increased.

Since the droplet is prepared in a comparable state in both measurements, the electronic trajectories are supposed to be perturbed in a similar way by surrounding particles. The expansion of the target can explain the emergence of higher orders with increasing delay, though harmonic radiation is detected at shorter delays using the shorter pulses. Ionization induced by the probe pulse therefore seems to crucially influence the harmonic signal as its amount is higher using 100 fs-pulses while simultaneously the HOHO is decreased at $t = 0.4 \text{ ns}$. Reduced ionization especially becomes prominent regarding short time delays ($t < 0.6 \text{ ns}$), where the density of the target is quite high with $\rho > 1.8 \times 10^{21} \text{ cm}^{-3}$ and plasma screening effects disturb HHG (cf. sec. 4.2.1). Moreover, a higher ionic density within the target may affect the electrons during the excursion in the continuum and lead to the emission of incoherent radiation but this will be studied in detail in sec. 5.2.

The two measurements qualitatively agree when delays of $t > 0.6 \text{ ns}$ are regarded. Comparing the experimental results for even larger delays allows to study the influence of the expansion process as a function of the pulse duration onto the harmonic signal. Figure 4.9 therefore depicts a similar measurement to Fig. 3.7 where delays $t > 3.0 \text{ ns}$ have been

presented. Here, delays of $t = 1.0$ ns, $t = 5.0$ ns and $t = 12.0$ ns are shown at comparable laser parameters to Fig. 4.8. A raise in the signal from $t = 1.0$ ns to $t = 5.0$ ns is observed. Increasing the delay from $t = 5.0$ ns to $t = 12.0$ ns, the yield of the orders up to the 23rd is comparable but decreases for higher orders.

In Fig. 3.7, a maximum in the harmonic signal around $t = 12.5$ ns has been observed followed by a decrease in the signal for larger delays which has been attributed to the expanding target and a limited number of emitters within the focal region. A similar situation is found in Fig. 4.9, though no pronounced maximum has been observed due to the limited available delay. However, the conditions are non-optimized for higher orders at large delays which is attributed to an increasing total ionization as the target expands and the probe pulse easily enters the interior of the droplet as in the case of TPM-conditions (cf. sec. 4.2.1). The presented data indicates that the time-dependent expansion of the droplet is comparable using shorter pulses.

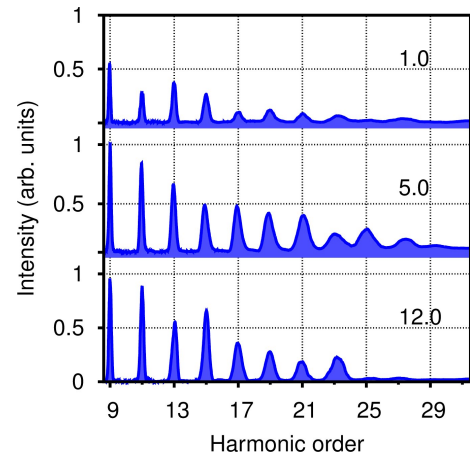


Figure 4.9: Harmonic yield as function of the harmonic order at large pump-probe time delays and comparable parameters to Fig. 4.8. The harmonic yields are normalized to the maximum intensity of the 9th HOH at $t = 5.0$ ns.

In conclusion, using shorter pulses propagates higher orders due to reduced total ionization. From the comparison between the Xe measurements and HHG from droplets, first indications of the presence of water molecules have been observed. Using shorter pulses is the ideal tool to probe the dynamics of the droplet, as harmonic radiation can be generated at higher densities of the target, which gives access to dynamics on shorter time scales. Moreover, higher intensities can be applied before ionization leads to non-optimized conditions for HHG, while the cutoff is enhanced at the same time. But the increase of the intensity of the probe pulse will not automatically result in a higher yield of the harmonic radiation and propagate higher orders since ionization grows larger again. Hence, the influence of the intensity of the probe pulse onto the harmonic signal is the topic of the next section.

4.3 Influence of the Intensity of the Probe Pulse

Ionization induced by the probe pulse can significantly change the PM conditions for HHG and therefore influence the maximum photon energy of the harmonic radiation, as well as the conversion efficiency. Limitations to the cutoff arise as described in the previous section, which are not included in the cutoff law in equation (2.18), where the maximum photon energy increases linearly with the intensity of the driving pulse. Moreover, spectral properties of the emitted radiation like the bandwidth of the harmonic spectral lines or the photon energy can be modified by the generated free electrons (cf. sec. 4.2.1). Since ionization depends on the intensity of the driving pulse, its influence onto HHG from water droplets can be studied by a variation of the intensity of the probe pulse. The following sections therefore describe probe-pulse-induced ionization effects for different pulse durations, as well as different densities of the target.

4.3.1 Transition of Harmonic Orders from the Cutoff into the Plateau

As described by the single-atom response in sec. 2.5.2, the harmonic signal strongly depends on the intensity of the driving pulse. Considering a single harmonic order, it is situated within the cutoff region for low intensity and performs a transition into the plateau region as the intensity is increased. This transition becomes observable by a change in the slope of the harmonic yield as a function of the driving intensity and is less steep in the plateau region (green line in Fig. 2.9) [Sal97]. A second change in the slope is recognized when the intensity is further increased which leads to a depletion of the ground state of the medium and the harmonic yield saturates at a specific intensity I_{sat} (red line in Fig. 2.9) [Wah93]. This feature of the harmonic radiation has been extensively studied using gas jet setups [Wah93, Alt96, deL97] or gas cells [Won10] but it is rather unexplored using condensed phase targets [Kur13]. This section therefore presents measurements of the intensity dependence of the harmonic yield using water droplets as a target.

Two different pulse durations of $\tau_1 = 100$ fs (system *A*) and $\tau_2 = 35$ fs (system *B*) have been applied. The conditions for HHG are equal since the delay and the intensities of the pump pulses² are set to $t = 3.5$ ns with $I_{pump} = 2.0 \times 10^{14}$ W/cm² and $t = 3.0$ ns with $I_{pump} = 9.5 \times 10^{14}$ W/cm², respectively, which creates a gaseous target with densities around $\rho \sim 10^{19}$ cm⁻³ (cf. secs. 3.2.2 and 4.1) and allows to generate the highest cutoff.

Saturation for Long Pulses In Fig. 4.10 (a) the data has been acquired using laser system *A* and shows the harmonic yield as a function of the harmonic order and the intensity of the probe pulse within an intensity range from 1×10^{14} W/cm² to 5.2×10^{14} W/cm². For the lowest applied value of I_{probe} , harmonic radiation up to the 15th order is generated. As the intensity is raised, a monotonic increase in the harmonic signal is observed and higher orders are detected. The HOHO reaches the 17th order at $I_{probe} = 2 \times 10^{14}$ W/cm² and further raises steadily as a function of the intensity towards the 27th order at $I_{probe} = 4.6 \times 10^{14}$ W/cm². Larger intensities result in a decrease of the HOHO and incoherent radiation is detected at the upper border of the spectral range, though with a weak intensity.

For a more precise analysis of the intensity dependence of the harmonic yield, Figs. 4.10 (b) to (e) depict outlines of the 13th, 19th, 21st and 23rd harmonic order, respectively. Due to the limited resolution of the measurement, it is not possible to give exact values of the saturation intensity of the harmonic signal but instead an intensity range can be determined whose center is indicated by the red line. Regarding the 13th harmonic order reveals that the monotonous increase of the signal is followed by a saturation around an intensity of $I_{sat,HOH13} = 4.0 \times 10^{14}$ W/cm² and a decrease for higher intensities. A similar behaviour is observed for the 19th order but the saturation intensity is shifted to an value close to $I_{sat,HOH19} = 4.6 \times 10^{14}$ W/cm². The situation changes for the two higher orders in (d) and (e). While the signal saturates for the 21st order around $I_{sat,HOH21} = 4.6 \times 10^{14}$ W/cm², no saturation is observed for the 23rd order. Additionally, no decrease in the signal is detected for both orders. Obviously, the saturation intensity is a function of the harmonic order and is shifted towards higher values as the driving intensity increases.

For the interpretation of the intensity-dependent development of the harmonic yield, the 19th harmonic order is considered since the transition from the cutoff into the plateau region is well observable and it does not feature the decline around $I_{probe} \approx 3 \times 10^{14}$ W/cm² of the 13th order which stems from poor synchronization between laser and droplet. For a

²Note that a higher value of I_{pump} is needed for τ_2 . See chap. 5 for details.

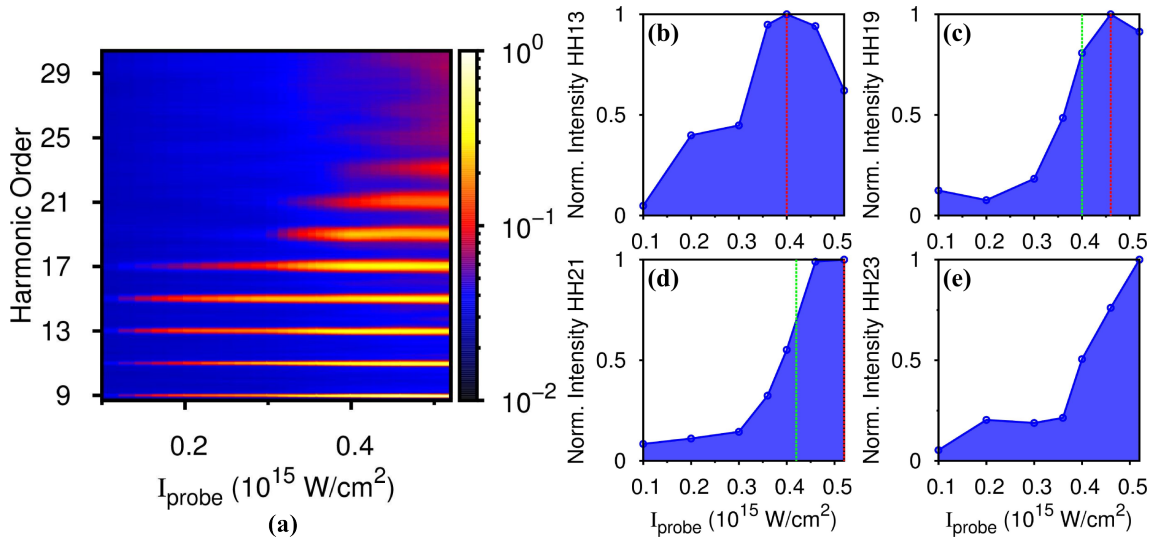


Figure 4.10: (a) Harmonic yield versus order and intensity of the pump pulse. Laser system *A* was used with $I_{\text{pump}} = 2.0 \times 10^{14}$ W/cm² and $t = 3, 5$ ns. Outlines from (a) for the (b) 13th, (c) 19th, (d) 21st and (e) 23rd harmonic order [Kur13]. The green line indicates the center of the intensity range for the transition of the order from the cutoff into the plateau. The red line represents the maximum of the harmonic yield as an indicator for I_{sat} .

low intensity of the probe pulse, the harmonic order is situated within the cutoff region and is only generated at the highest peak intensity within the driving pulse. The highest intensity within the pulse is reached at a region close to the focus, where the variation of the atomic phase is large (cf. Fig. 2.11 (a)). Adequate PM conditions and the number of emitting particles that contribute to this order are therefore confined to a small volume and the harmonic yield is weak [L'H93b, Mac93]. As the intensity is increased, the harmonic yield raises steeply, which stems from the single atom response as depicted in fig. 2.9 [Lew94, Sal97]. The volume where the intensity is high enough to generate the 19th order is successively enlarged and PM conditions are satisfied for a larger region [deL97]. When I_{probe} reaches a value around 4.0×10^{14} W/cm², the intensity is sufficiently high enough to generate higher orders. The 19th order is then shifted to the plateau region (cf. green line in Figs. 2.9 and 4.10 (c)), where phase matching is preserved over an additionally enlarged volume. The slope of the signal flattens [L'H93b, Wah93]. A change of the intensity to a value around $I_{\text{probe}} = 4.6 \times 10^{14}$ W/cm² results in a saturation as the ground state of the medium becomes depleted (red line) [Bel01]. For intensities $I_{\text{probe}} > I_{\text{sat}}$ the medium is significantly ionized by the probe pulse as also electrons of lower orbitals are released. The generated free electrons lead to a defocusing of the fundamental pulse that efficiently decreases the intensity. Additionally, a phase mismatch to the harmonic field is induced by the free electrons, which is large compared with the mismatch induced by the atomic or the geometric phase since it scales with the harmonic order [Alt96, Her02, Kur13]. Thus, a decrease in the signal is observed.

For a given harmonic order, saturation of the signal is observed when the intensity of the driving field exceeds the value needed for the harmonic order to be situated within the plateau. Higher orders require higher intensities for their generation. Therefore, the intensity needed to perform the transition from the cutoff into the plateau region increases as a function of the order, as indicated by the shift in the green lines in Figs. 4.10 (c) and (d). The consequence of this shift is a raise of the saturation intensity as observed in the shift in the red lines [Wah93]. Thus, saturation is only observed in figs. (b) to (d) since the harmonic orders are situated within the plateau, while it is not detected for the 23rd order, as the order remains in the cutoff region for all intensities applied.

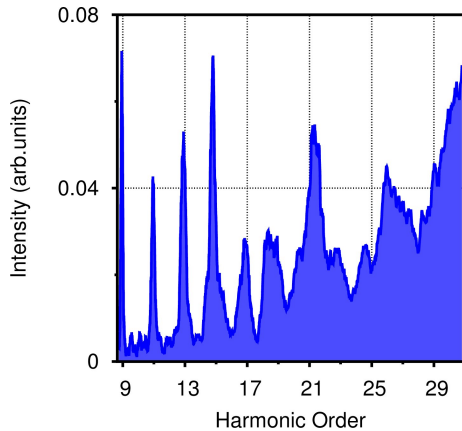


Figure 4.11: Harmonic yield as function of the harmonic order for comparable parameters to Fig. 4.10 but with $I_{\text{probe}} = 1.1 \times 10^{15} \text{ W/cm}^2$. The signal has been normalized to the maximum yield in Fig. 4.10 (c).

At the highest intensities in Fig. 4.10, a decrease in the harmonic yield has been observed which can be attributed to the influence of free electrons and becomes more pronounced for higher intensities. Its dramatic influence can be observed in Fig. 4.11 where a spectrum of the harmonic radiation is depicted for $I_{\text{probe}} = 1.1 \times 10^{15} \text{ W/cm}^2$. The signal has been normalized to the maximum of the 19th order in Fig. 4.10 (c). Harmonic radiation is generated up to the 15th order though a strong signal of incoherent radiation is observed for higher orders. The overall yield is weak compared with lower intensities and the amplitude of the 19th order is decreased to a value of 3% of the value from Fig. 4.10 (c) which is caused by massive ionization within the target.

The influence of free electrons becomes dominating for these high intensities in combination with pulses with a duration of 100 fs. Therefore increasing the intensity to values $I_{\text{probe}} > 8.0 \times 10^{14} \text{ W/cm}^2$

is not advisable since the HHG yield is perturbed and the emission process becomes incoherent. Applying driver pulses with shorter duration can result in decreased ionization of the medium, which has been described in sec. 4.2.2. Higher intensities should be applicable and the saturation intensity should be increased with shorter pulses. Therefore, the same measurement of the intensity-dependence of the emission of harmonic radiation is repeated with laser system *B*.

Saturation for Short Pulses Figure 4.12 (a) depicts similar measurement to Fig. 4.10 (a), where the harmonic yield is shown as a function of order and the intensity of the probe pulse using laser system *B* with a pulse duration of 35 fs and an intensity range from $2.0 \times 10^{14} \text{ W/cm}^2$ to $1.45 \times 10^{15} \text{ W/cm}^2$. At the lowest intensity, the harmonic signal is weak and the HOHO is given by the 19th order. The yield increases monotonically as a function of the intensity, as does the HOHO. For $I_{\text{probe}} = 5.0 \times 10^{14} \text{ W/cm}^2$, the HOHO is the 27th harmonic order and is further raised to the 29th order for higher values of I_{probe} . A saturation in the harmonic yield is observed that also depends on the harmonic order.

The measurement of the overall harmonic spectrum is in good agreement with Fig. 4.10 (a). The increase in the harmonic orders as a function of the intensity matches and even absolute values are in reasonable agreement as observed in the case of the 27th harmonic order, which is generated at a value of $I_{\text{probe}} = 4 \times 10^{14} \text{ W/cm}^2$ for both pulse durations. However, higher orders are generated at lower intensity, which agrees with sec. 4.2.2 and the HOHO is increased compared with the measurement with longer pulse duration. The saturation intensity is shifted towards larger values of I_{probe} .

For a more detailed analysis of the intensity dependence of the harmonic yield, Figs. 4.12 (b) to (e) depict outlines of the 19th, 21st, 23rd and the 29th harmonic order, respectively. As in the previous case with longer pulse durations, the green line indicates the center of the intensity range for the transition of the harmonic order from the cutoff into the plateau region, while the red line symbolizes the intensity range of saturation. For the 19th order, the intensity area where saturation of the harmonic signal sets in is shifted towards higher values of I_{probe} around $\sim 10^{15} \text{ W/cm}^2$, as is the decrease of the harmonic signal. An increase of I_{sat} as a function of the harmonic order is recognized for higher orders but

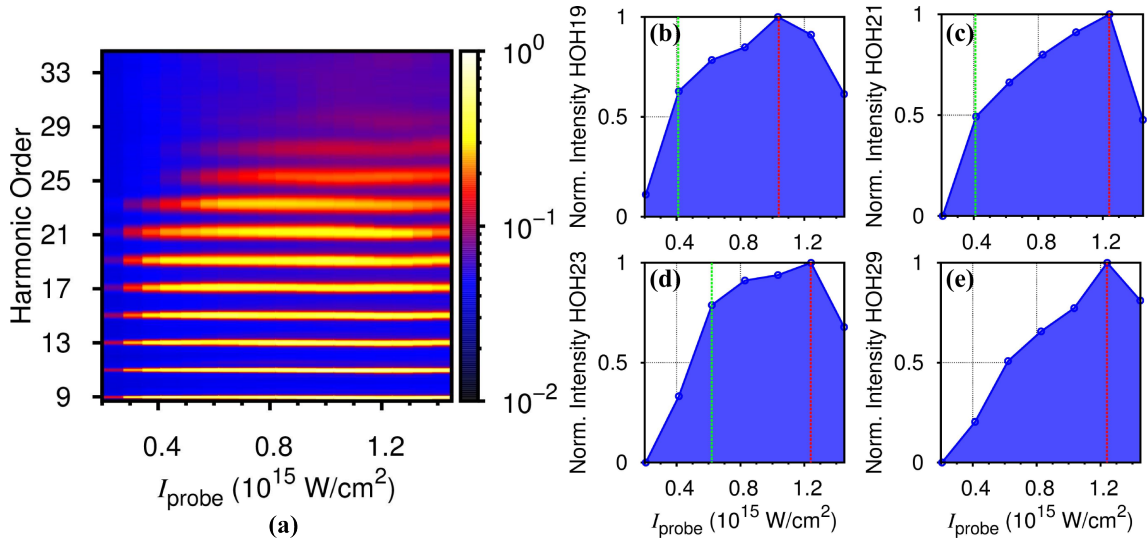


Figure 4.12: (a) Harmonic yield versus order and intensity of the probe pulse with $I_{\text{pump}} = 5 \times 10^{14}$ W/cm 2 at $t = 3.0$ ns. Outlines from (a) for the (b) 19th, (c) 21st, (d) 23rd and (e) 29th harmonic order. The green line indicates the center of the intensity range for the transition of the order from the cutoff into the plateau, the red line represents the maximum of the harmonic yield as indicator for I_{sat} .

saturation of the harmonic yield is detected for all measurements due to the larger intensity range.

The reason for the saturation and the decrease of the harmonic signal is the same as in the case with 100 fs-pulses. Comparing the two measurements of the 19th harmonic order in Figs. 4.10 (c) and 4.12 (b), I_{sat} is increased around a factor of two when 35 fs-pulses are used (red lines). However, the intensity ranges for the transition of the harmonic order into the plateau region are in agreement (green lines), which is reasonable since it is a fixed intensity for each harmonic order. A similar observation is made when the 21st order is regarded. As a larger intensity range is available, transition into the plateau region and saturation of the 23rd order is also detected in Fig. 4.12 (d), which has not been recognized in Fig. 4.10 (e). No transition into the plateau region is observed for the 29th order, since it is always situated within the cutoff.

The comparison of the two characteristic intensities for the transition and saturation in the two measurements in Figs. 4.10 and 4.12 indicates that ionization is suppressed using the pulses with a duration of 35 fs, which is also in agreement with the observations from section 4.2.2. Therefore, higher intensities of the probe pulse can be applied using shorter pulses before the influence of free electrons becomes dominant. This behaviour becomes even more obvious regarding the measurement in Fig. 4.11, where comparable intensities with longer pulses have been applied but the emission of harmonic radiation has been suppressed and incoherent radiation has been generated.

Comparing the results with a measurement of HHG in water molecules in a SIGC setup with pulse durations of 40 fs and a central wavelength of 800 nm by WONG *et al.* [Won10], a value of the saturation intensity of $I_{\text{sat}} = 1.4 \times 10^{14}$ W/cm 2 is given, which is almost a factor of ten lower than the saturation intensity found in the measurements above. However, it is not specified in the publication by WONG *et al.* how the saturation intensity is defined and which harmonic order is considered. The reason for the discrepancy between the measurements by WONG *et al.* and the findings in this thesis therefore cannot be identified, but could also be attributed to the different setups for HHG.

In conclusion, transitions of harmonic orders from the cutoff into the plateau region have

been observed and two different areas for the saturation intensities have been identified, depending on the pulse duration of the driving field. However, the droplet is not a static target since a wide range of densities can be generated through changing the delay. The maximum photon energy is also influenced by both parameters, the delay as shown in secs. 3.2.1 and 4.2.2, as well as by the intensity of the driving field according to the cutoff law as described within this section. The influence of the two parameters onto the evolution of the HOHO during the expansion of the droplet is unknown and is therefore studied in the following section.

4.3.2 The Highest Observed Harmonic Order

Figure 4.13 (a) depicts the HOHO as a function of the intensity of the probe pulse. Laser system *A* has been applied with an intensity of the pump pulse of $I_{\text{pump}} = 2.0 \times 10^{14} \text{ W/cm}^2$, generating a gaseous target. The HOHO scales linearly from the 15th to the 27th harmonic order as the intensity is raised. For the highest value of I_{probe} a reduction to the 25th order is observed. The slope of the linear fit (dashed blue line) is $29.8 \text{ cm}^2/\text{W}$ while the theoretical prediction from the cutoff law from equation (2.18) is depicted as a red line. The value of the theoretical cutoff is higher for the lowest intensity than the fit to the experimental data. Moreover, its slope is steeper and the two lines diverge with increasing intensity, which is in agreement with results from gas jet experiments [L'H93b, Mac93, Wah93].

The lower maximum photon energy than in the theoretical prediction is again caused by ionization. Higher orders are affected at a lower intensity because the induced phase mismatch by the free electrons is a function of the harmonic order [Alt96]. The result is a decrease of the cutoff at $I_{\text{probe}} = 5 \times 10^{14} \text{ W/cm}^2$. Since the HOHO is critically influenced by ionization, it is a first measure to probe the amount of ionization within the target.

The total ionization induced by the probe pulse increases as the droplet expands (cf. sec. 4.2.1). Hence, the influence of ionization onto the HOHO can be studied in more detail when different delays are regarded. Figure 4.13 (b) therefore shows the HOHO as a function of I_{probe} for different time delays and a wider intensity range. Laser system *B* has

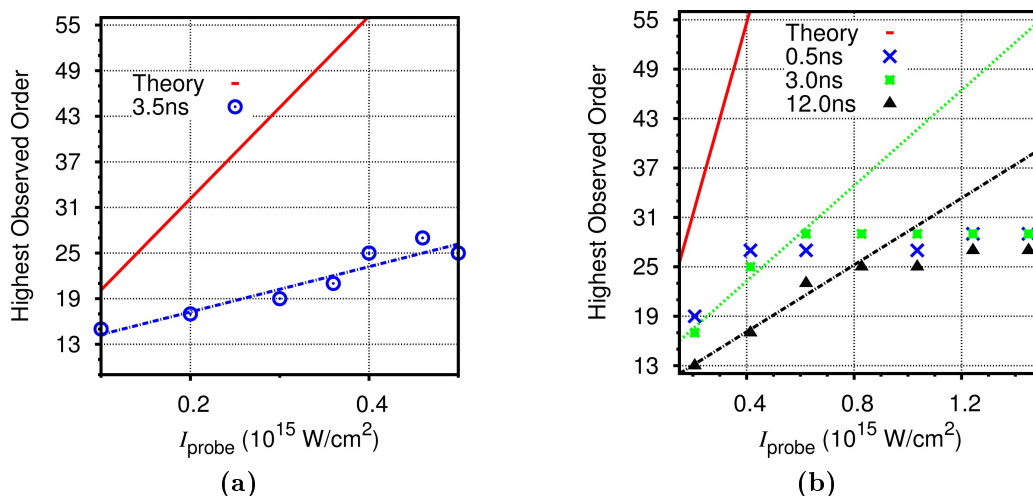


Figure 4.13: Highest observed harmonic orders versus the intensity of the probe pulse. Linear approximations are indicated as dashed lines. (a) Measured with laser system *A* for $t = 3.5 \text{ ns}$, $I_{\text{pump}} = 2.0 \times 10^{14} \text{ W/cm}^2$ and 100fs pulse duration. (b) With laser system *B* for different delays, $I_{\text{pump}} = 5.3 \times 10^{14} \text{ W/cm}^2$ and 40fs pulse duration.

been applied, using an intensity of the pump pulse of $I_{\text{pump}} = 5 \times 10^{14} \text{ W/cm}^2$ as described in the measurements in the last section.

For a delay of $t = 0.5 \text{ ns}$, the HOHO starts with the 19th harmonic order and increases to the 27th order at $I_{\text{probe}} \approx 0.4 \times 10^{15} \text{ W/cm}^2$. A saturation is observed as the intensity is further raised. At a delay of $t = 3.0 \text{ ns}$, the HOHO starts at the 17th order, increases with a lower steepness and saturates at a higher intensity at the 29th order. For a further raise of the delay to 12.0 ns, the first value of the HOHO is the 13th harmonic order, followed by a linear increase to the 25th order. It is raised by one order for the highest intensities. The increasing parts of the two larger delays at low intensities can again be approximated by linear functions as indicated by the dashed lines. Their slopes differ with changing delay and are given by $29.0 \text{ cm}^2/\text{W}$ for $t = 3.0 \text{ ns}$ and $20.3 \text{ cm}^2/\text{W}$ for $t = 12.0 \text{ ns}$.

Though differences in the slopes and the absolute values of the HOHO are observed for different delays, the general trend is comparable: A linear increase is followed by a saturation. There is a small difference in the absolute value of the HOHO between the two measurements at $t = 0.5 \text{ ns}$ and $t = 3.0 \text{ ns}$. Moreover, the maxima of the HOHO are equal, which has also been observed during the study of the time-dependent evolution of the droplet as described in sec. 4.2.2. But it is still below the theoretical value. Comparing the measurements at $t = 5.0 \text{ ns}$ and $t = 12.0 \text{ ns}$, the absolute values differ and higher orders are observed for the shorter delay.

Comparing the slopes of the linear fits in the measurements in Fig. 4.13 (a) at $t = 3.5 \text{ ns}$ and (b) at $t = 3.0 \text{ ns}$ delivers a value of 1.03 which indicates that equal conditions of the droplet are found. This is reasonable since the target is in both cases a gas with comparable density (cf. Fig. 2.3). The situation seems to be different when a delay of $t = 12.0 \text{ ns}$ is considered. The ratio of the slopes at $t = 3.0 \text{ ns}$ and $t = 12.0 \text{ ns}$ is with 1.43 larger and the lower HOHO at the latter delay for a wide intensity range indicates different conditions for HHG. This difference can be attributed to the advanced dilution of the droplet at $t = 12.0 \text{ ns}$, which supports a more easy entry of the pulse into the interior of the target and causes massive ionization. The fundamental radiation is then defocused due to the induced refractive index by the generated free electrons and the PM conditions become poor [Wah93, Alt96]. Another result of the defocusing is the observed saturation of the HOHO. As soon as the intensity is high enough to generate a sufficiently high density of free electrons further increase of the density results in the generation of additional free electrons which lead to larger defocusing effects onto the fundamental radiation. Hence, the available intensity for HHG is limited and the HOHO saturates.

Ionization is a limiting factor in HHG since it leads to poor PM conditions, depletion of the ground state of the medium and defocusing effects that effectively reduce the intensity within the target. However, optimum conditions for the harmonic yield and the HOHO can be achieved by matching the intensity to the density of the target. Shorter pulses are of advantage as they induce less ionization and therefore extend the maximum photon energy. The observation of higher orders at a delay of $t = 0.5 \text{ ns}$ is an interesting feature since the inter-particle distance within the target is low which should lead to a perturbation of the electronic trajectories and result in a suppression of high orders. Hence, an estimate is needed when the distortion of electronic trajectories sets in which will be discussed in the following.

4.4 Mapping Time to Density

So far the time-dependent expansion of the droplet has been studied by varying the time delay between the pump and the probe pulse to generate a wide range of densities of the target. These states influence the harmonic signal, as well as the cutoff of the harmonic radiation (cf. secs. 3.2.1 and 4.2.2). The calculation of the appropriated density has been done by using the model described in sec. 2.4.2 which has been validated in sec. 4.1 using experimental results and allows to estimate the density development of the target as a function of time for the laser parameters applied.

A more intuitive way than considering the time delay for the interpretation of the dependence of the harmonic signal as a function of the expanding droplet is to directly plot the harmonic yield versus the density of the target. This is provided by a mapping of the delay onto the calculated density. A scheme of the mapping of t to ρ is depicted in Fig. 4.14. The measured harmonic yield as a function of the harmonic order and delay is shown in Fig. 4.14 (a). The delay is converted via the calculation in (b) into a density $t \rightarrow \rho(t)$. The harmonic yield is then mapped onto the new density-axis (c).

This mapping technique gives access to the density-dependent development of the harmonic yield. It is used in the following to identify the optimum conditions for HHG and the information imprinted within. Since the density of the target can critically change the conditions which may lead to a suppression of the harmonic yield, a density-dependent

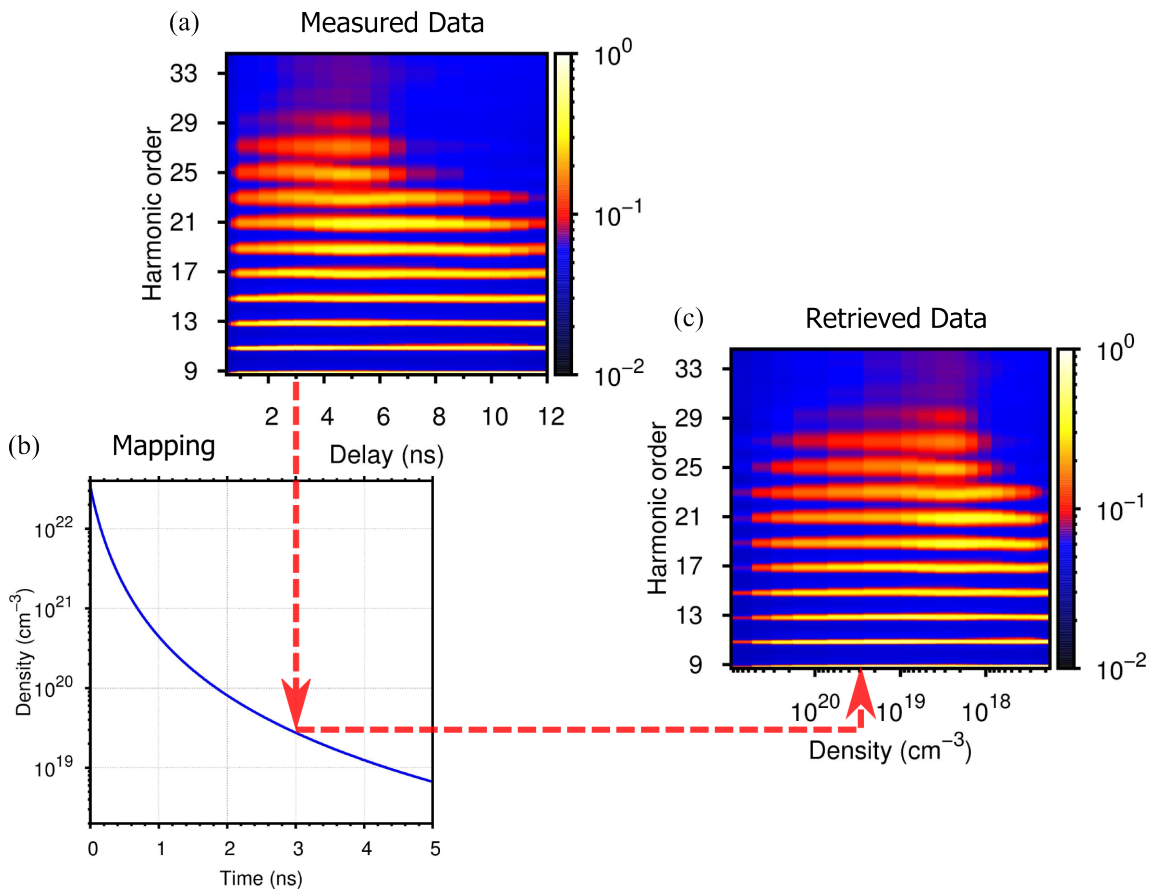


Figure 4.14: Mapping of the pump-probe time delay to the density evolution of the droplet. The measured harmonic yield versus harmonic order and delay (a) is mapped (red dashed arrows) via the calculated droplet density as function of time (b) onto a function of the density evolution of the droplet (c) for a fixed intensity of the laser pulses.

study is performed in the following.

4.5 Selecting Electronic Trajectories via the Density of the Droplet

While common setups for HHG like gas jets or SIGCs are limited to a number density range of the target between $\sim 1 \times 10^{16} \text{ cm}^{-3}$ and $\sim 1 \times 10^{19} \text{ cm}^{-3}$, the liquid droplet setup discloses a density range reaching from $\rho < 1 \times 10^{16} \text{ cm}^{-3}$ to $3.35 \times 10^{22} \text{ cm}^{-3}$, which is liquid density for water. With the use of a high density of the target, several issues arise during HHG, like the suppression of the harmonic yield as observed in secs. 3.2.1 and 4.2.2. The decreasing distance between the particles for high densities of the target has been claimed to be the cause for the suppression of the harmonic signal by inducing a distortion of the electronic trajectories [Fle03]. But how can the strength of the perturbation of electronic trajectories be estimated and what parameter can serve as a measure?

A comparison of the distance between the particles within the target and the excursion distance of the electron should provide a measure for the perturbation of electronic trajectories. Assuming a homogeneous distribution³ of the particles within the droplet, the *mean inter-particle distance* can be calculated by the density of the target and is given by [Her09]:

$$\bar{r} = \sqrt[3]{\frac{1}{\rho}} \quad (4.1)$$

which is within the nm-range for the densities given above. It can be derived experimentally using the density obtained through the mapping technique described in sec. 4.4. In order to compare \bar{r} with the excursion distance of the electron from the parent ion, it is necessary to calculate the electronic trajectories during the interaction with the laser field.

4.5.1 Calculation of Electronic Trajectories

As described by the theory in sec. 2.5.1, the electron can be treated as a classical particle after ionization, which is driven by the electric field (cf. Fig. 2.7). Using the three-step model [Cor93] with a fixed intensity of the electric field allows to calculate the photon energy of the emitted radiation by solving numerically the Newton equations for the movement of the electron. As depicted in Fig. 2.8 (a), the emitted photon energy is determined by the time of ionization t_i . A single value of t_i leads to the emission of the maximum photon energy, which is attributed to the cutoff trajectory. At lower energies, two solutions lead to the emission of an equal photon energy, which are referred as short and long trajectory. Considering a fixed photon energy, the knowledge of its ionization times allows to calculate the trajectory leading to the emission of radiation since it depends on t_i and is given by:

$$x(t) = \frac{e \cdot E_L}{m_e \cdot \omega_L^2} \cdot (\sin(\omega_L t) - \sin(\omega_L t_i) - \omega_L (t - t_i) \cdot \cos(\omega_L t)), \quad (4.2)$$

where the amplitude of the motion is given by $\alpha(E_L, \omega_L) = \frac{e \cdot E_L}{m_e \cdot \omega_L^2}$ [Lei07].

Figure 4.15 (a) depicts a calculation of the electronic displacement x of an electron as a function of time for an intensity of the driving field of $1 \times 10^{14} \text{ W/cm}^2$ at a central wavelength of 780 nm. Three trajectories are shown: the trajectory assigned to the cutoff

³Note that the distribution of particles during the expansion is inhomogeneous for time delays below $t < 200 \text{ ps}$ [Sch02]. During the measurements however, only delays $t > 200 \text{ ps}$ are considered where the assumption of a homogeneous distribution is justified.

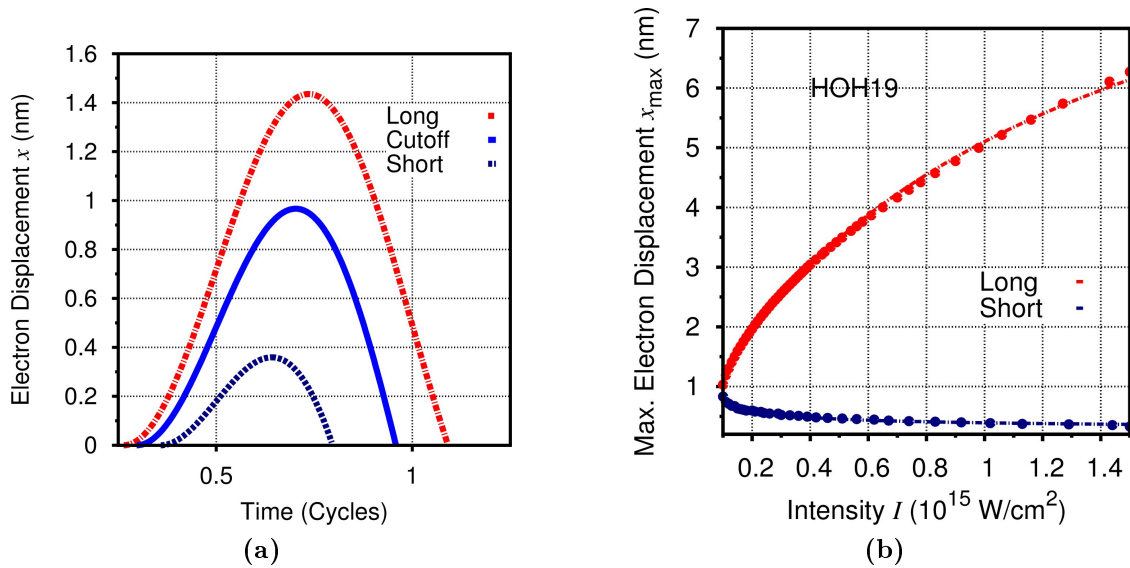


Figure 4.15: (a) Classically calculated long (dashed-dotted), cutoff (solid) and a short (dashed) electron trajectory as a function of time for an intensity of the driving field of 1×10^{14} W/cm 2 at a central wavelength of 780 nm. (b) Classical excursion distance of the electron contributing to the 19 $^{\text{th}}$ harmonic order versus intensity of the driving field.

(solid) and a long (dashed-dotted) and a short (dashed) trajectory, which lead to the same photon energy (see also Fig. 2.8). The maximum displacement x_{\max} is highest for the long trajectory and decreases for the trajectory assigned to the cutoff region. The smallest value of x_{\max} is reached for the short trajectory. Since the amplitude $\alpha(E_L, \omega_L)$ of the excursion of the electron depends on the electric field E_L , increasing the intensity of the driving field results in a larger maximum excursion. However, this also leads to an increase of the cutoff region and the emission of higher orders. A fixed harmonic order therefore performs a transition from the cutoff region into the plateau (cf. sec. 4.3) and is emitted via the short and the long quantum path when situated within the plateau region. It is therefore of interest how the maximum excursion distance develops as a function of the intensity of the driving field.

In order to study the intensity-dependence of x_{\max} , the 19 $^{\text{th}}$ harmonic order is regarded in the following. As observed in Fig. 2.8 (a), there are two ionization times that lead to the same photon energy if the harmonic order is situated within the plateau region. When the intensity of the driving field is increased, these two ionization times are shifted and the trajectories take a different path. Since the trajectories only depend on the ionization times t_i and the intensity of the driving field, a calculation of the ionization times allows to express the trajectories of the 19 $^{\text{th}}$ order as a function of the intensity, too. Figure 4.15 (b) shows a calculation of x_{\max} for the short (blue) and the long (red) trajectory of the 19 $^{\text{th}}$ harmonic order. For the lowest intensity, the radiation is emitted via the single cutoff trajectory, which has a maximum displacement of $x_{\max} = 0.96$ nm. As the intensity is increased, the two trajectories contribute to the emission process which diverge with increasing intensity. The values of x_{\max} are above $x_{\max} = 0.96$ nm for the long trajectory and increase as a function of the intensity. Hence, a distortion of the long trajectory by surrounding particles is more probable in the experiments but the yield of the long trajectory is low and it will therefore not be considered. The maximum displacement for the short trajectory however decreases as a function of the intensity. Moreover, the cutoff trajectory is an upper limit in x_{\max} for the short trajectory. Hence, x_{\max} attributed to

the cutoff is used to compare it with the mean inter-particle distance in order to obtain a density limit for the perturbation of the electronic trajectory.

Comparison with the Mean Inter-Particle Distance As described above, the cutoff trajectory is used for a comparison of the excursion of the electron with the mean inter-particle distance. To attribute an intensity of the driving field to each harmonic order, the cutoff law from equation (2.18) is applied, where the ionization potential of the water molecule is used. This allows a mapping from x_{\max} as a function of the intensity to a function of the harmonic order. Figure 4.16 depicts the displacement of the electron assigned to the cutoff region versus the harmonic order (blue) and the mean inter-particle distance of the target (red) as a function of the density. The maximum displacement x_{\max} increases with rising harmonic order, while \bar{r} (red) increases with decreasing density of the target.

The 19th harmonic order is considered again for the description of the graph. The maximum displacement of this order has a value of 0.96 nm according to Fig. 4.16 and can be assigned to the cutoff trajectory. All lower displacements can be attributed to short trajectories that contribute to the signal of the 19th order, which is the reason for the illustration of the excursion distance as an area.

At a target density of $\rho_1 = 5 \times 10^{21} \text{ cm}^{-3}$, the mean inter-particle distance is $\bar{r} = 0.59 \text{ nm}$. This means for a density of ρ_1 , the distance between two adjacent particles in the target is lower than the excursion distance of the cutoff trajectory and the electron will be perturbed. The generation of the 19th harmonic order is in this case not possible via the cutoff trajectory. In order to prevent the distortion of the electron and to generate radiation at the 19th harmonic order, there are two ways. The first one is to lower the density of the target to a level $\rho < 1.1 \times 10^{21} \text{ cm}^{-3}$, which leads to a mean inter-particle distance of $\bar{r} > 0.96 \text{ nm}$ so that the conditions for recombination of the electron with its parent ion are satisfied (cf. Fig. 4.16). The second way is to keep the density at $\rho_1 = 5 \times 10^{21} \text{ cm}^{-3}$ and to increase the intensity of the driving pulse. The 19th harmonic order then performs a transition from the cutoff into the plateau region (cf. sec. 4.3.1) and is emitted via the interference of short and long trajectory. Selecting the short trajectory and raising the intensity above $I > 2 \times 10^{14} \text{ W/cm}^2$ results in a maximum excursion distance $x_{\max} < 0.59 \text{ nm}$ (cf. Fig. 4.15 (b)) and the condition for recombination is satisfied again. The findings of conditions for the perturbation of the electronic trajectories allow to calculate an upper limit for the density upon which a distortion should be observed by comparing x_{\max} with \bar{r} . As a result, an intensity-dependent maximum tolerable density attributed to the short trajectory ρ_{short} is found and no harmonic radiation should be detected for values of the density exceeding this limit. Moreover, a second maximum density attributed to the cutoff trajectory can be defined ρ_{cutoff} ,

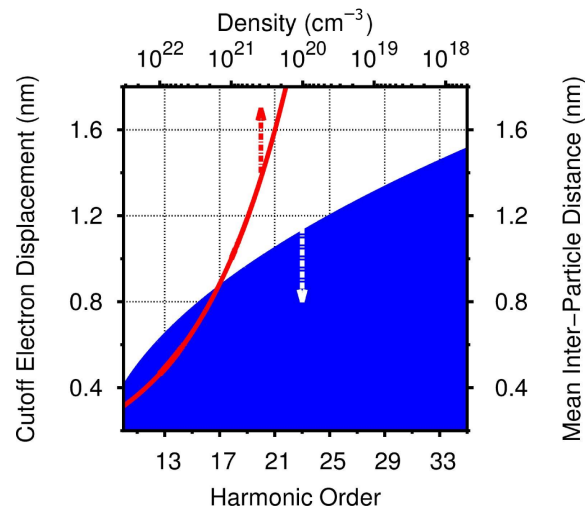


Figure 4.16: Excursion distance of the electron from the parent ion versus harmonic order (blue) and mean inter-particle distance versus the target density (red). The harmonic order has been calculated using the cutoff law in equation (2.18) for a wavelength of 780 nm.

which is a lower limit for all short trajectories. Both limits are necessary, since the harmonic radiation is generated within an intensity distribution in the focal region. This means, not only a single but many short trajectories contribute to the signal with differing maximum excursion distances up to the cutoff trajectory. Hence, both limits will be used for the interpretation of the experimental data.

In conclusion, the above described model indicates that a perturbation of the electronic trajectories is expected when the mean inter-particle distance becomes smaller than the electronic displacement. Two characteristic values for a maximum tolerable target density for each harmonic order are obtained above which the electronic trajectories become perturbed and the harmonic signal is suppressed: One for the cutoff trajectory ρ_{cutoff} , which also acts as a lower density limit for all short trajectories and a second, intensity-dependent limitation for a specific, intensity-dependent short trajectory ρ_{short} . As long as the intensity of the driving field is higher than needed to generate the considered harmonic order within the cutoff, the harmonic signal is not only composed of the contribution of a single trajectory but by all trajectories up to the cutoff trajectory. It therefore should be possible to switch off trajectories by increasing the density of the target, which will be put to a test in the following section.

4.5.2 Selecting Single Trajectories

The harmonic signal is measured as a function of the pump probe time delay and mapped to the density (cf. sec. 4.4). Figure 4.17 depicts the mapped harmonic yield for the (a) 17th, (b) 21st, (c) 25th and (d) 27th order. Laser system *B* has been applied with an intensity of $I_{\text{pump}} = 4.5 \times 10^{14} \text{ W/cm}^2$. For the selection of the short quantum path, a medium position of $z > 0 \text{ mm}$ has been chosen. The intensity of the probe pulse has been set to $I_{\text{probe}} = 1.4 \times 10^{15} \text{ W/cm}^2$ so that all presented harmonic orders can be generated in the plateau region. In fact the calculated maximum order at this intensity is higher than the experimentally observed 29th order, which is caused by the PM conditions as described in sec. 4.3.2. The data is averaged around 5% of the central wavelength of each harmonic order and the error bars indicate the standard deviation. The large errors for the 17th harmonic order at low densities result from poor synchronization between droplet and laser. The blue line indicates the fit curve to the measured data considering densities above $1.5 \times 10^{21} \text{ cm}^{-3}$. In the last section, two theoretical limits for the maximum tolerable density have been derived. The first is the maximum tolerable density assigned to the cutoff trajectory ρ_{cutoff} (black line), which is calculated assuming that the intensity of the driving field fits the level needed to situate the harmonic line in the cutoff. The second is the maximum tolerable density assigned to the short trajectory ρ_{short} (red line), which is computed for the applied intensity of the probe pulse. The red area depicts the density region where the specific harmonic order should not be generated at all due to the distortion of the electronic trajectory according to the model.

The harmonic yield decreases with increasing density and scales $\sim \bar{r} = \sqrt[3]{\frac{1}{\rho}}$ (blue line) with an asymptotic standard error within a range of 2.7% to 4.5% for densities higher than $\rho = 1 \times 10^{21} \text{ cm}^{-3}$. The signal is below the noise level (zero) for the highest density of $\rho = 3.35 \times 10^{22} \text{ cm}^{-3}$.

Regarding the 17th order, the maximum tolerable density for the short trajectory (red line) is with $\rho_{\text{short}} = 3.8 \times 10^{22} \text{ cm}^3$ beyond the density range in the measurement and even larger than the density of liquid water. However, no harmonic radiation is emitted for the highest density. For the given intensity, the model used for obtaining ρ_{short} therefore seems

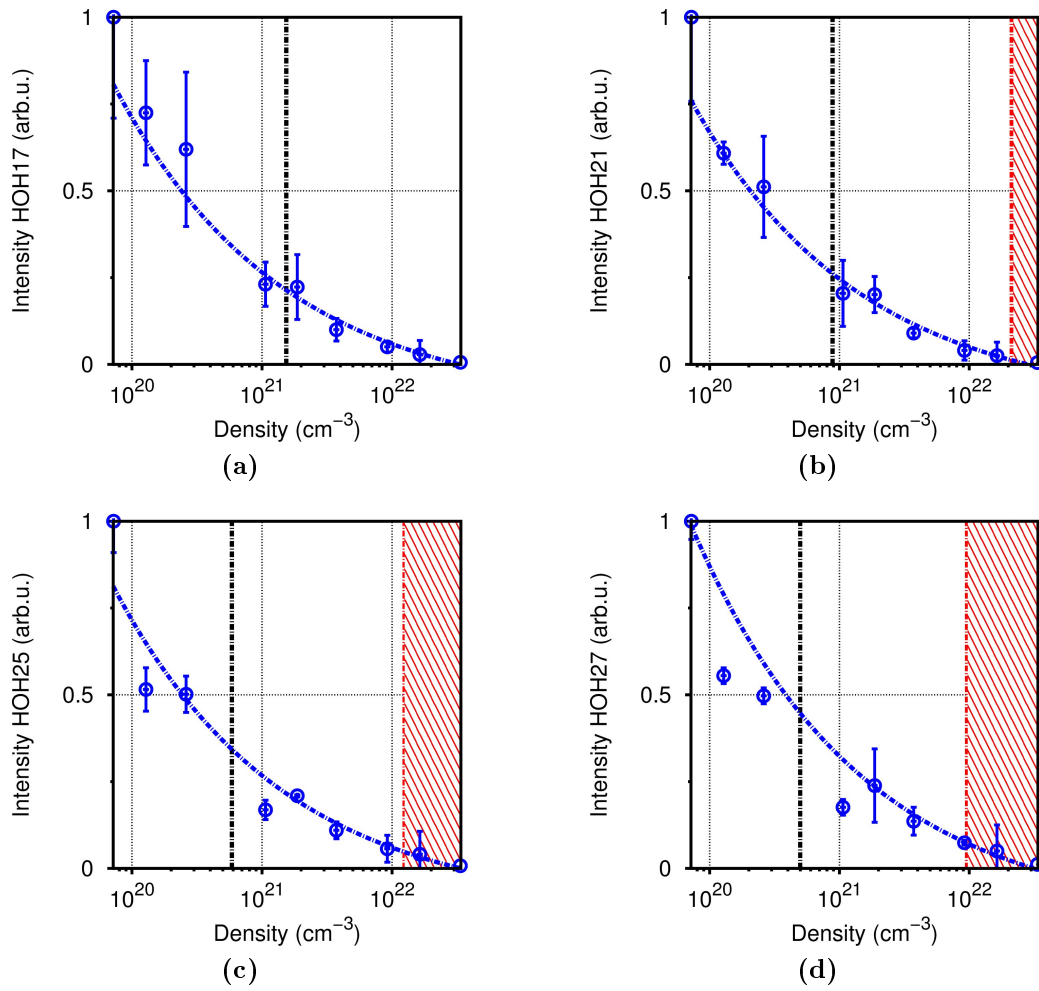


Figure 4.17: Harmonic signal as a function of the density of the droplet for the (a) 17th, (b) 21st, (c) 25th and (d) 27th order according to Fig. 4.8. Laser system *B* has been applied with intensities of $I_{\text{pump}} = 4.5 \times 10^{14} \text{ W/cm}^2$ and $I_{\text{probe}} = 1.4 \times 10^{15} \text{ W/cm}^2$. The blue line indicates the fit curve $\sim \bar{r} = \frac{1}{\sqrt[3]{\rho}}$ to the measured data. The black line is the maximum tolerable density for the cutoff trajectory, the red line indicates the maximum density for the short trajectory. Within the red area, the density is too high for the generation of the harmonic order.

to deliver a too high value for harmonic radiation below the 19th order and the emission process is determined by other factors than the mean inter-particle distance, such as electric potentials between the molecules or re-absorption effects. Though, the maximum tolerable density is shifted towards lower values with increasing harmonic order since the excursion distance of the electrons increases. Therefore, the 21st harmonic order is not emitted for densities higher than $\rho_{\text{short}} = 2.13 \times 10^{22} \text{ cm}^{-3}$, though the fit function indicates a weak signal at higher densities. In order to explain the possibility of a weak signal, the full spectra of the measurements in Fig. 4.18 have to be considered. When the density is decreased to a level below ρ_{short} , the harmonic order is emitted. This is observed in the measurements at a density of $\rho = 1.64 \times 10^{22} \text{ cm}^{-3}$, though the signal of the 21st harmonic order is weak and accompanied by plasma radiation, as indicated by the signal close to the position of the 21st seeming like a redshift in Fig. 4.18. Hence, the indicated weak signal for densities higher than ρ_{short} stems from an incoherent process and can be attributed to the emission of plasma radiation. A comparison with the theoretical predictions of the maximum tolerable density for lower orders also allows to identify the harmonic orders 9 to 19 and plasma lines in between in the full spectrum. A further reduction of the

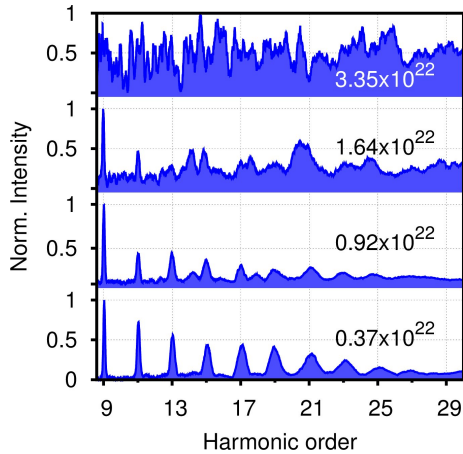


Figure 4.18: Full spectra of the harmonic radiation for different densities of the droplet corresponding to Fig. 4.17. The numbers indicate the number density in cm^{-3} .

density results in an increase of the harmonic signal and the 21st order is clearly visible.

A similar behaviour is observed regarding the 25th and the 27th order. In these cases ρ_{short} (red line) is shifted to $\rho_{\text{short}} = 1.25 \times 10^{22} \text{ cm}^{-3}$ for the 25th order and to $\rho_{\text{short}} = 9.63 \times 10^{21} \text{ cm}^{-3}$ for the 27th order. Though Figs. 4.17 (c) and (d) also show weak signals for densities higher than ρ_{short} , no signal of harmonic radiation is observed for these densities in the spectra in Fig. 4.18. The offset at densities higher than ρ_{short} therefore also stems from incoherent radiation, which is in agreement with the observations in the spectra. Moreover, the 25th harmonic order is clearly visible when the density is lowered to $\rho = 9.2 \times 10^{21} \text{ cm}^{-3}$ and the 27th harmonic order is observed for $\rho = 3.7 \times 10^{21} \text{ cm}^{-3}$. Both densities are below the maximum tolerable density for the short trajectory for each harmonic order, respectively.

The comparison between the calculations and the measurements verify the validity of the computed maximum densities. No harmonic radiation is observed for densities above ρ_{short} (red line) for each harmonic order. As the droplet is expanded, the harmonic orders appear successively when the density reaches a level below ρ_{short} for each order, respectively. The signal then increases proportionally to the mean inter-particle distance \bar{r} , which can be interpreted by regarding the emission process within the focal volume. Since the intensity of the probe pulse is high enough to generate the harmonic orders within the plateau region, HHG takes place within a volume around the focus. A single harmonic order therefore is not only generated at the center of the focus where the intensity is highest, but also at a position with an offset from the focus where the intensity is lower. As depicted in Fig. 4.15 (b), the generation of a harmonic order with a different driving intensity results in a change of the trajectory, where lower intensities cause a higher maximum displacement of the electron. Hence, trajectories which are generated at a position outside of the center of the focus have a larger maximum displacement and are therefore perturbed at lower density compared to trajectories which are generated at the center of the focus. This also means, that the perturbation of electronic trajectories sets in as soon as the density is higher than the maximum density for the cutoff trajectory. By lowering the density of the droplet, the mean inter-particle distance is increased and less trajectories are distorted, which results in an increase of the harmonic yield as a function of \bar{r} for densities higher than ρ_{cutoff} . Since ρ_{short} is a function of the harmonic order, this also describes why no abrupt change in the emission pattern from incoherent radiation to HHG is observed but a continuous transition, where higher orders appear when the density of the target is lowered.

While the harmonic yield increases proportional to \bar{r} for densities higher than ρ_{cutoff} (black line), a larger discrepancy between the fit function and the data is observed for lower densities. In order to further study the density-dependence of the harmonic yield as a function of the harmonic signal, Fig. 4.19 shows the signal of the 21st harmonic order from Fig. 4.17 (b) versus the density of the droplet on a double logarithmic scale. The blue and the green lines indicate linear fits to the data for densities above and below ρ_{cutoff} , respectively. A change in the slope is observed within the vicinity of ρ_{cutoff} .

Two effects cause the change in the increase of the harmonic signal for densities lower

than ρ_{cutoff} . The first is the non-existence of distortions to the electronic trajectories since \bar{r} is larger than the electronic displacement. Therefore all trajectories contribute to the harmonic signal and the yield does no longer scale $\sim \bar{r}$. The second effect is attributed to the expansion of the droplet and the change from a high-density target to a gaseous target at lower densities, which has been shown by PM experiments in sec. 4.1.3. As the droplet expands, the interaction volume between focal region and target becomes larger and the focal volume is successively filled by the droplet. Though the total number of emitters within this volume decreases, PM conditions are optimized which supports a steep increase of the harmonic yield (cf. sec. 4.1.3). Thus, the change in the slope of the harmonic yield as a function of the density of the droplet can be attributed to a change in the characteristics of the medium from a

distortion-dominated droplet due to the low mean inter-particle distance towards a gas-like target where phase matching determines the harmonic yield. For a more detailed analysis of the emission, reabsorption effects have to be considered, which are not respected in the model for calculating the density limits. The reabsorption within the target however is also balanced at densities above ρ_{cutoff} since the target expands. The lower density is therefore compensated by a larger interaction length resulting in a similar absorption in the high-density regime. Reabsorption effects decrease for $\rho < \rho_{\text{cutoff}}$ and therefore contribute to the steeply increasing signal. In conclusion, the maximum density attributed to the cutoff trajectory roughly marks the transition between the high and the low density regime. Whether this also is valid for other intensities will be discussed in the next section.

4.5.3 Correlation between Intensity and Density-Dependence of the Harmonic Signal

In the last section, HHG has been studied in a density range from $3.35 \times 10^{23} \text{ cm}^{-3}$ to $7 \times 10^{19} \text{ cm}^{-3}$ for a fixed intensity of the probe pulse. Applying the model described in section 4.5.1, allowed to define two limits for the density: A maximum density attributed to the cutoff trajectory ρ_{short} and a highest tolerable density for the cutoff trajectory ρ_{cutoff} , for each harmonic order respectively. No harmonic radiation has been detected for $\rho > \rho_{\text{short}}$ due to the larger excursion distance of the electrons than the mean inter-particle distance. The maximum density attributed to the cutoff trajectory ρ_{cutoff} however allowed to distinguish between a density regime where the electronic trajectories are being distorted ($\rho > \rho_{\text{cutoff}}$) and a gas-like target where phase matching is the dominating factor to determine the harmonic yield ($\rho < \rho_{\text{cutoff}}$), as also observed in the experiments concerning propagation effects (cf. 4.1). Though, it is undisclosed if ρ_{cutoff} can also act as a limit to distinguish between the two density regimes for lower intensities of the probe pulse since the maximum excursion distance of the electrons changes. Furthermore, it is unknown how the harmonic yield evolves for lower densities as a function of the intensity. This motivates a detailed study of the signal of the harmonic radiation as a function of a large intensity and density range which is described in the following.

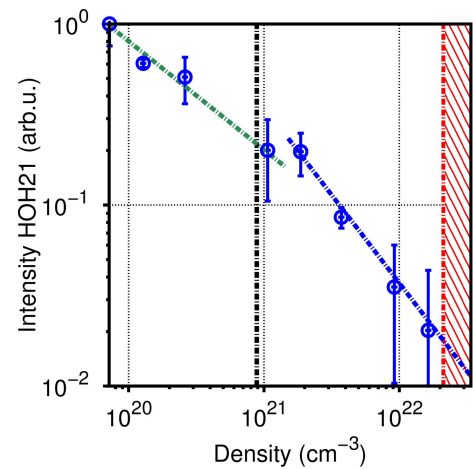


Figure 4.19: Double logarithmically scaled plot of the harmonic signal as a function of the density of the droplet for the 21st harmonic order from Fig. 4.17.

Figure 4.20 depicts the signal of the harmonic radiation versus the mapped density of the

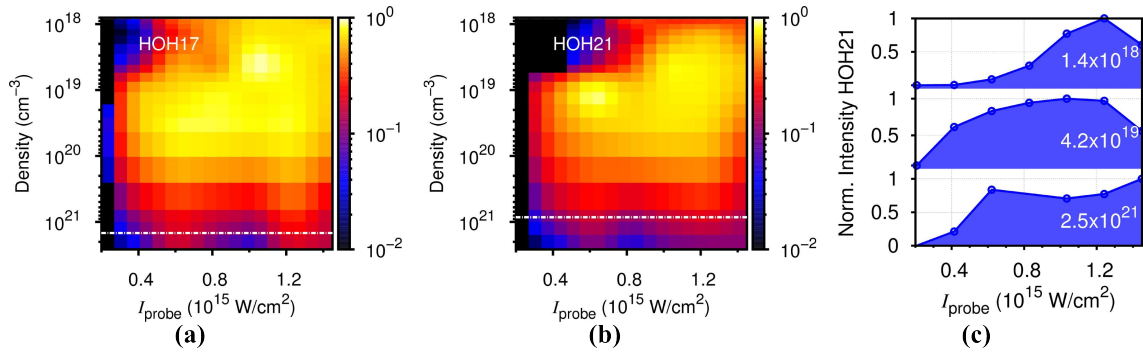


Figure 4.20: Signal of the harmonic radiation versus target density and intensity of the probe pulse for the (a) 17th, (b) 21st and (c) outlines from (b). The numbers in (c) indicate the number density in cm^{-3} . Laser system *B* has been applied with $\tau = 40$ fs and with $I_{\text{pump}} = 5 \times 10^{14} \text{ W/cm}^2$. The data has been averaged around 5% of the maximum of each harmonic order and the harmonic signal has been normalized to the maximum. The dashed white lines indicate the maximum tolerable density attributed to the cutoff trajectory ρ_{cutoff} . Note that the data has been interpolated in (a) and (b) with three points between each intensity and density value for better visibility.

droplet and the intensity of the probe pulse for the 17th in (a) and the 21st order (b). The dashed white line indicates ρ_{cutoff} . Laser system *B* has been applied with an intensity of the pump pulse of $I_{\text{pump}} = 5 \times 10^{14} \text{ W/cm}^2$, in order to generate comparable conditions to the measurements of the previous section.

In general, the signal of all harmonic orders is weak for $\rho < \rho_{\text{cutoff}}$, increases to a broad maximum around a density of $\sim 10^{19} \text{ cm}^{-3}$ and decreases again for lower densities. The 17th order is emitted over almost the whole density and intensity range with a broad maximum in the range of $2 \times 10^{19} \text{ cm}^{-3}$ and a decreasing signal for $\rho > \rho_{\text{cutoff}}$. The situation is similar when the 21st order is regarded, but the radiation is emitted in a more confined area. There are two density regions within an intensity range from the lowest intensity up to $0.4 \times 10^{15} \text{ W/cm}^2$ where the harmonic yield is low: the first for densities higher than $1 \times 10^{21} \text{ cm}^{-3}$ and the second for densities lower than $\rho = 5 \times 10^{18} \text{ cm}^{-3}$.

In order to analyse the two regions of low emission of radiation in more detail, outlines of the 21st harmonic order for fixed densities are considered as depicted in Fig. 4.20 (c). At the lowest density in this comparison, a raise in the harmonic yield is observed which increases $\sim \exp(I_{\text{probe}})$. A change in the slope of the signal is observed around an intensity of $I_{\text{probe}} = 1 \times 10^{15} \text{ W/cm}^2$ which is followed by a narrow maximum around $I_{\text{probe}} = 1.2 \times 10^{15} \text{ W/cm}^2$. The signal decreases for higher intensities. When the density is raised to $\rho = 4.2 \times 10^{19} \text{ cm}^{-3}$, the signal of the harmonic radiation increases steeply but the raise is shifted towards smaller values of I_{probe} . The slope flattens at an intensity of $\sim 5 \times 10^{14} \text{ W/cm}^2$ and a saturation is observed around $I_{\text{probe}} = 1 \times 10^{15} \text{ W/cm}^2$. A decreasing signal is detected for higher intensities again. At the highest density, the harmonic signal is weak and the increase is once more shifted towards a higher intensity. A maximum is reached around a value of $I_{\text{probe}} = 6 \times 10^{14} \text{ W/cm}^2$. Thereafter, only slight variations of the signal are observed at higher intensities and the signal remains at a rather constant level.

The intensity and density dependence of the harmonic yield can be interpreted regarding the results from secs. 4.3 and 4.5.2. For the lowest density of $\rho = 1.8 \times 10^{18} \text{ cm}^{-3}$, the less steep increase can be attributed to the dilution of the target. The decreased density causes a low number of particles residing within the focal volume. Hence, the number of emitters is smaller and a higher intensity is needed to increase the focal volume for generating the

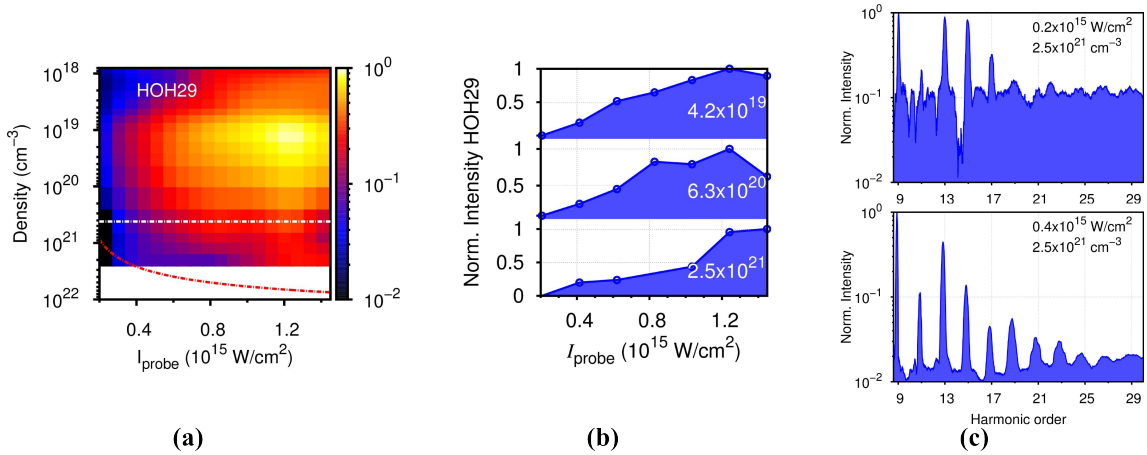


Figure 4.21: (a) Signal of the harmonic radiation versus target density and intensity of the probe pulse of the 29th harmonic order. The dashed white lines in (a) indicate the maximum tolerable density attributed to the cutoff trajectory ρ_{cutoff} , the dashed red line depicts the maximum tolerable density attributed to the short trajectory ρ_{short} for the given intensity. The same laser parameters have been applied as in Fig. 4.20. (b) Outlines of (a) for fixed densities. The numbers in (b) indicate the number density in cm⁻³. (c) Spectrum for an intensity of $I_{\text{probe}} = 0.8 \times 10^{15}$ W/cm² and a density of 2.5×10^{21} cm⁻³.

same amount of radiation as in the case of a higher density. The lower number of emitters also causes a less steep increase of the signal at lower intensities, which has also been observed in experiments using a gas jet setup [Alt96, Her02]. The maximum however is at a comparable position to the measurement with a density of $\rho = 4.2 \times 10^{19}$ cm⁻³. Moreover, the decreasing yield is observed within the same intensity range and can be attributed to the influence of a rising density of free electrons.

A similar behaviour is observed when the density is decreased to $\rho = 4.2 \times 10^{19}$ cm⁻³. The target is a dense gas and the harmonic yield develops as a function of the intensity in agreement with the findings from sec. 4.3.1. Therein, a transition of the harmonic order from the cutoff region into the plateau region has been observed, indicated by a change of the slope of the signal from steep (cutoff) to flat (plateau). The raise of the harmonic yield has been explained with the increasing region of optimized PM conditions. The adjacent saturation and the decrease of the signal can be attributed to the depletion of the medium and an increasing density of free electrons.

At a density above ρ_{cutoff} , the mean inter-particle distance is lower than the maximum excursion distance of most short trajectories within the focal volume. This is especially true for low intensities of the probe pulse since this causes an even larger displacement of the electrons so that the possibility of a perturbation during their excursion within the continuum rises. Thus, the increase of the signal is shifted towards larger values of I_{probe} . At higher intensities, the maximum excursion distance of the short trajectory decreases, but with a flat slope as observed in Fig. 4.15 (b). As a result, the differences in the excursion distances are small for high intensities. Hence, increasing the intensity to values higher than 0.4×10^{15} W/cm² leads to no significant decrease of the excursion distances and the harmonic yield remains at a constant level.

The above described measurements confirm that the target behaves like a gas for densities below ρ_{cutoff} . This is in agreement with the findings of the measurement of propagation effects (cf. sec. 4.1), the studies of the influence of the intensity of the probe pulse (sec. 4.3) and the analysis of the emission process in the last section (cf. sec. 4.5.2). At the maximum density however, the increase of the signal is shifted towards larger values of I_{probe} . The constant signal for high intensities indicate that the trajectories are suppressed for densities

$\rho > \rho_{\text{cutoff}}$. This agrees with the model of the perturbed trajectories in sec. 4.5.1 and the analysis of the emission process in dense targets in sec. 4.5.2. The maximum tolerable density for the trajectory attributed to the cutoff therefore also acts as an upper limit for the beginning of the distortion of electronic trajectories for lower intensities. As a result, the harmonic yield decreases for $\rho > \rho_{\text{cutoff}}$. The electrons attributed to the short trajectory however have a smaller maximum excursion distance x_{max} than the cutoff trajectory and therefore generate harmonic radiation at higher densities than $\rho > \rho_{\text{cutoff}}$ (cf. Fig. 4.15). However, the emission of harmonic radiation via the short quantum path also has a density limit ρ_{short} , upon which no harmonic radiation is emitted (cf. Fig. 4.17). Hence, the model from sec. 4.5.1 is used to calculate the excursion distance of the short trajectory as a function of the intensity in order to obtain the density limit ρ_{short} . Since ρ_{short} also decreases as a function of the harmonic order, it is of advantage to regard the highest observed harmonic order for the observation of the perturbation of the short trajectories.

Figure 4.21 (a) depicts the HOHO, which is the 29th harmonic as a function of the intensity and the mapped density. The general development of the signal of the harmonic radiation of the 29th order as a function of ρ and I_{probe} is comparable to the lower orders shown in Fig. 4.20. The dashed white line indicates ρ_{cutoff} at a density of $4.2 \times 10^{20} \text{ cm}^{-3}$. In order to reveal the trajectory distortions, outlines of Fig. 4.21 (a) are given in (b). For densities $\rho < \rho_{\text{cutoff}}$, the harmonic yield increases as a function of the intensity, forms a maximum and decreases afterwards. When the density is raised to $6.3 \times 10^{20} \text{ cm}^{-3}$, the trajectories become disturbed and the total signal decreases. The higher target density also results in a steeper increase of the signal as a function of the intensity, in agreement with the findings from the previous paragraph. A decrease of the signal is still observed for the highest intensity which can again be attributed to a rising number of free electrons. However, the yield of the emitted radiation is lower, which is caused by the suppression of the trajectories.

When the density is further increased to $2.5 \times 10^{21} \text{ cm}^{-3}$ (cf. Fig. 4.21 (b)), no harmonic radiation of the 29th order is detected for the lowest intensity, as also observed in the upper spectrum in Fig. 4.21 (c). As the intensity is increased to $0.4 \times 10^{15} \text{ W/cm}^2$, a weak signal is detected which remains at a rather constant level until an intensity of $1 \times 10^{15} \text{ W/cm}^2$ is reached. This is also indicated in the lower spectrum in Fig. 4.21 (c). The signal increases for higher intensities until a limit is reached.

In order to interpret the density and intensity-dependence of the 29th order, the findings from sec. 4.5.2 can be used. The dashed red line in Fig. 4.21 (a) indicates the maximum tolerable density for the short trajectory ρ_{short} as a function of the intensity and has been calculated with the model from sec. 4.5.1. Due to a smaller mean inter-particle distance than the maximum electronic displacement, no harmonic radiation is detected for the lowest intensity applied. The harmonic yield increases then as a function of the intensity since the excursion distance decreases and the curved shape of ρ_{short} is also found in the increasing signal for intensities below $0.8 \times 10^{15} \text{ W/cm}^2$. Since ρ_{short} has a higher value for higher intensities, a raise in the signal is observed and the density range within which harmonic radiation is emitted is increased. However, the slope of ρ_{short} is less steep at higher intensities so that a perturbation of electronic trajectories is still present and the harmonic yield is limited.

In conclusion, ρ_{cutoff} and ρ_{short} which have been calculated with the model from sec. 4.5.1 can be used as limits for HHG. This has been verified in the study of the intensity and density dependence of the harmonic radiation in this section. While the target is in the gas phase for densities lower than ρ_{cutoff} where the harmonic yield is determined by PM,

a decrease in the harmonic signal is observed for densities larger than ρ_{cutoff} . This has been attributed to the distortion of the electronic trajectories during the excursion in the continuum. The increase of the density of the target allows to successively "switch-off" the trajectories which contribute to the signal of a harmonic order until only the shortest quantum path remains. Thus, the density of ρ_{short} is a limit for HHG via the short quantum path and no harmonic radiation is observed for densities above.

The presented model is a promising tool to study the electronic excursion distance. Though the three step model is used to calculate the maximum tolerable densities ρ_{cutoff} and ρ_{short} , these limits show a high degree of agreement with the experimental results. Applying a quantum mechanical model and performing a more detailed scan of the densities around ρ_{short} therefore would allow to measure the excursion distance of the electrons with a high precision. In addition, the time of ionization could be recalculated which represents an alternative to the method of adding the second harmonic of the fundamental radiation during the generation process [Dud06, Sha12b]. Since the excursion distance of a trajectory is defined by the time of ionization, the selection of a confined amount of trajectories additionally allows to decrease the intrinsic attosecond chirp of the harmonic radiation [Mai03] and therefore gives rise to a shaping of attosecond pulses.

The measurements in Fig. 4.21 indicate that optimized conditions for HHG are found for densities below ρ_{cutoff} , where the harmonic yield increases with a steep slope. Within this density range, the droplet however still gives access to HHG in a target with higher density than in common gas phase experiments. The larger number of potential emitters therefore anticipates that a higher number of XUV photons is emitted. Hence, the conversion efficiency is measured in the next section.

4.6 The Conversion Efficiency

Optimizing the conditions for efficient HHG critically depends on the density of the droplet, as described in sec. 4.5. This means, the ratio of the conversion of radiation of the fundamental laser pulse into the XUV-spectral domain is also a function of the density. Hence, measuring the average power of the driving pulse and of the attosecond pulse train of the integrated harmonic signal allows to calculate the conversion efficiency (CE) from the near-infrared to the XUV spectral domain.

In order to measure the CE from the fundamental to harmonic radiation, the spectrometer in Fig. 3.2 is replaced by an XUV diode (AXUV100, International Radiation Detectors, Inc.), which has a flat response of 0.25 A/W for wavelengths from 30 nm to 50 nm, including the harmonic orders 13 to 43 in the measurement. The fundamental radiation is blocked using three aluminum filters (Lebow Co.) with a thickness of 200 nm and a measured transmission of 54 % each. Additionally, there is another aluminum filter with a thickness of 300 nm directly in front of the diode with a measured transmission of 14 % in order to block any scattered fundamental radiation. Each filter is specified for transmission within a wavelength range from 17 nm to 64 nm. The divergence of the full harmonic beam is low enough, that all XUV-radiation reaches the detector, which was placed at a distance of 105 cm. Laser system *B* has been applied with an intensity of the pump pulse of $I_{\text{pump}} = 6.3 \times 10^{14} \text{ W/cm}^2$ in order to support a high yield for HHG as indicated in Fig. 3.9. A high intensity of the probe pulse of $I_{\text{probe}} = 1.2 \times 10^{15} \text{ W/cm}^2$ was used since the highest yield has been observed at this intensity in the studies concerning the influence of the probe pulse in sec. 4.3.1. Additionally, the short trajectory is selected by choosing a medium position of $z > 0 \text{ mm}$ as it exhibits a higher conversion efficiency (cf. secs. 4.1 and

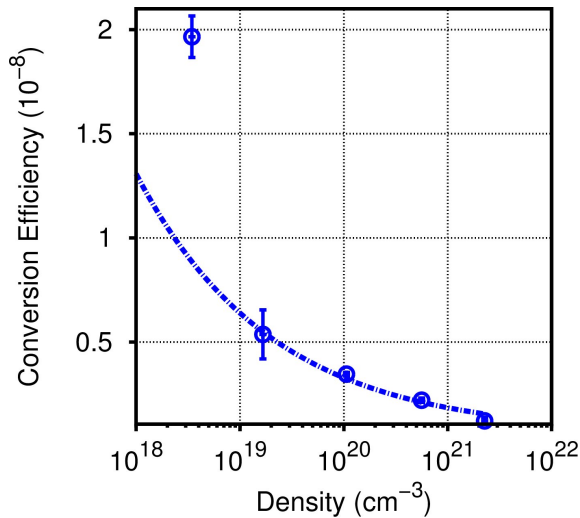


Figure 4.22: Conversion efficiency versus mapped density. Laser system *B* has been used with $I_{pump} = 6.3 \times 10^{14} \text{ W/cm}^2$ and $I_{probe} = 1.2 \times 10^{15} \text{ W/cm}^2$. The blue dashed curve indicates a fit $\sim \bar{r} = \frac{1}{\sqrt[3]{\rho}}$. Each of the measured data values is averaged over 20000 laser pulses. The error bars resemble the standard deviation.

$\rho < 1 \times 10^{19} \text{ cm}^{-3}$ is well below the limit of ρ_{cutoff} from section 4.5.2 and the perturbation of the trajectories therefore is low. Hence, the generation of harmonic radiation in this density regime is determined by the PM conditions and less re-absorption effects due to the expansion of the droplet which leads to an increased CE.

The shift of the optimized conditions for HHG towards a density of $\rho = 2 \times 10^{18} \text{ cm}^{-3}$ is also observed in Figs. 4.20 (a) and (b) while it is not for the 29th harmonic order in Fig. 4.21 (a). This indicates that most of the radiation is emitted within the lower orders up to the 21st, which is reasonable since these orders are situated within the plateau region and therefore have a higher contribution to the integrated signal. The maximum value of the CE however is well below the findings from experiments in a xenon gas jet, where a conversion efficiency of $\sim 10^{-5}$ for a single harmonic within the plateau region was measured [Her02, Tak02]. Therein, a loose focusing geometry was used with a focal length of several meters in order to optimize the PM conditions. Further experiments in gas targets indicate that the emission of the 25th order scales with the focal length $\sim f^2$ for low and $\sim f^4$ for high target densities [Bou11]. In the measurement of the CE from water droplets however, a tight focusing geometry of $f = 500 \text{ mm}$ has been applied. This means the conditions for the CE can be enhanced by changing the focal geometry. Moreover, the optimum density has not been identified yet which could be realized by increasing the pump-probe time delay that was limited during the measurements. Neglecting the influence of the free electrons for lower densities than the presented and approximating the data with an exponential function for the lower densities, gives a CE of 3.7×10^{-7} at a density of $\rho = 1 \times 10^{17} \text{ cm}^{-3}$. Considering a longer focal length and the scaling law $\sim f^2$ [Bou11], a CE within the range of $\sim \times 10^{-5}$ can be reached. Though this extrapolation is naive it demonstrates that the liquid droplet setup as a target for HHG is a promising

4.5). In order to prepare the droplet at different densities, the pump-probe delay is varied and the data is processed using the mapping technique from sec. 4.4.

Figure 4.22 depicts the transmission-corrected measured CE as a function of the mapped density. It is within the range of 10^{-8} and increases proportional to the mean inter-particle distance $\sim \bar{r} = \frac{1}{\sqrt[3]{\rho}}$ for densities above $\rho = 1 \times 10^{19} \text{ cm}^{-3}$ with an asymptotic standard error of 4.5%. A steep increase is detected for the lowest density of $\rho = 3.4 \times 10^{18} \text{ cm}^{-3}$, which is not within the scaling of \bar{r} . It is also the maximum of the CE in the considered density range with a value of 1.96×10^{-8} .

At high densities, the mean inter-particle distance is smaller and the distortion of the trajectories sets in, leading to a suppression of the harmonic yield. As the density is decreased, less trajectories are perturbed and the CE increases as a function of \bar{r} . For the maximum CE, the density of

tool for future applications. However, a spectrally resolved analysis of the CE would allow a more detailed insight into the density-dependent generation of harmonic order.

4.7 Conclusions

In PM experiments from liquid water droplets, similar characteristics of the harmonic radiation to experiments in gas jets have been found at low densities. The conclusion of the measurements is that the droplet performs a transition from the liquid phase into the gas phase and that the model for the time-dependent density evolution provides the correct estimates for the parameters applied in the experiments. However, some discrepancies have been observed. The amplitudes of the harmonic yield attributed to the short and the long trajectory are inverted when compared with the gas jet and first indications for dynamics on the atomic level have been disclosed (cf. sec. 4.1). Enhanced ionization has been recognized in diluted targets by the detection of transient phase-matching effects (cf. sec. 4.2.1).

The use of shorter pulses suppresses ionization and higher orders become observable at higher densities of the target compared to long pulses. Moreover, first indications of HHG in water molecules have been noticed during the temporal evolution of the droplet (cf. sec. 4.2.2) and will be further studied in chapter 5.

A saturation in the harmonic yield has been demonstrated that depends on the harmonic order and shifts towards higher intensities when shorter pulses are applied due to the lower ionization. Optimized conditions for the saturation intensity, the harmonic yield and the HOHO have been found by matching the intensity of the probe pulse to the density of the target by adjusting the time delay (cf. sec. 4.3).

Using a mapping of the pump-probe time delay to the density of the target (cf. sec. 4.4) allows to compare the calculated excursion distance with the mean inter-particle distance of the droplet (cf. sec. 4.5). This delivers two theoretical limits for the maximum tolerable density upon which the target becomes too dense and a perturbation of the electronic trajectories sets in. The first is an upper density limit for the trajectory assigned to the cutoff while the second is valid for the short trajectory. The theoretical limits have been experimentally verified using the mapping technique and a scaling of the harmonic yield proportional to the mean inter-particle distance is observed for densities above the maximum density for the cutoff trajectory (cf. sec. 4.5.2). These findings indicate that it is possible to select a single trajectory which contributes to the signal of a fixed harmonic order by increasing the density of the target. This could be relevant considering the direct shaping of attosecond-pulses as it seems to be a promising approach to exclude the intrinsic chirp during HHG.

The conversion efficiency of HHG from liquid water droplets is below the values observed in experiments using rare gas targets but the experimental conditions still allow an optimization which is promising to overcome the results from the gas targets (cf. sec. 4.6).

Although a transition of the droplet from the liquid into the gas phase has been identified, changes on the atomic level remain undisclosed. It is uncertain how the transition takes place and whether the target consists of clusters, molecules, atoms or ions. Moreover, the parameter range for defining the microscopic state of the droplet has not been identified. However, the inversion of the amplitudes of the harmonic yield attributed to short and long trajectory when compared to the yield from Xe atoms indicate that the identification is possible, which follows in the next chapter.

Chapter 5

Revealing the Dynamics of the Droplet

The transition of the droplet from the liquid phase into a gaseous target has been described in the last chapter in secs. 4.1 and 4.5. The parameters characterizing the change of the thermodynamical phase were identified to be the pump-probe time delay in sec. 3.2.1 and the intensity of the pump pulse in sec. 3.2.2. While the influence of the delay has been studied extensively in the last chapter (cf. secs. 3.2.1, 4.2.2 and 4.5), the influence of the intensity of the pump pulse is still to be discussed. Moreover, it is undisclosed what the microscopic composition of the target is and whether it consists of clusters, molecules, atoms or ions and which parameter range determines the different microscopic states. Hence, the expansion process itself has to be studied precisely.

The interaction of intense laser pulses with water droplets has been studied under atmospheric conditions but on time scales from microseconds to milliseconds where complex macroscopical expansion dynamics were observed [Lin04]. The time scales of the dynamics covered by this thesis are within the nanosecond range and below, where changes of the target are even more complex. There are no measurements concerning the expansion of the droplet on these short time scales and in fact, not even a theoretical approach has described the dynamics so far, since the changes on the microscopic level within the droplet are too dramatic to accurately model them [Lin04]. However, there are measurements of plasma expansion in water under atmospheric conditions which study the evolution of the electron density [Sch02, ST06, Bro11]. The combination of these findings allows to develop a simplified model describing the thermodynamical expansion of the droplet, which can help to provide some insight into the target within the scope of this thesis.

5.1 The Expansion of the Droplet

In order to expand the droplet with laser pulses, the energy of the laser pulse has to be transferred into kinetic energy of the particles within the droplet. This process occurs by the absorption of photons. Liquid water however is transparent for wavelengths around 800 nm since the imaginary part of the absorption coefficient is with $\kappa = 1.43 \times 10^{-7}$ low [Kou93] (cf. Fig. 5.1 and also equation (2.34)). This means linear absorption is negligible. However, the imaginary part of the refractive index is almost three orders of magnitude higher for 1600 nm and increases towards the mid-IR-region [Kou93]. Photons therefore can be absorbed by non-linear processes (cf. sec. 2.2). The intensity of the laser pulses applied for HHG in this thesis are sufficiently high enough to deposit energy within the droplet via non-linear absorption processes which induces a change of the thermodynamical phase of the droplet.

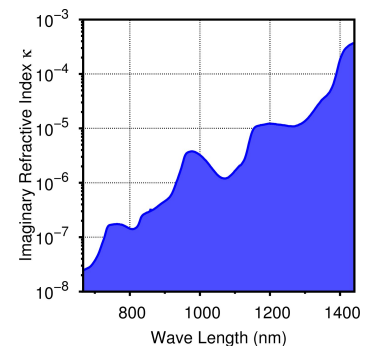


Figure 5.1: Imaginary part of the refractive index versus wavelength for liquid water at a temperature of 22 °C by KOU *et al.* [Kou93].

The model describing this change is introduced in the following.

5.1.1 Laser-Induced Breakdown

Figure 5.2 (a) depicts a schematic of the interaction of a laser pulse (solid red) that is focused (dashed red) to an intensity of $\sim 10^{14}$ W/cm² and interacts with the droplet (blue). The intensity is high enough to ionize the particles within the target (ions as red plus and electrons as black minus pictographs). The molecules at the side of the droplet facing the incident radiation are therefore ionized by the leading part of the pulse via tunnel ionization as described in sec. 2.2. An electronic plasma is ignited and the density of free electrons increases rapidly (cf. sec. 2.3). The trailing part is subsequently scattered and absorbed by the free electrons and the plasma is heated [Fen97] (cf. Fig. 5.2 (b)).

Additional secondary electrons are generated by collisional processes outside the focal region. The electrons with the highest energy can initiate up to 250 secondary electrons though their number is limited to 0.01 % of the total energy distribution of the electrons [Sch02]. The plasma becomes overdense (cf. sec. 2.3) and the resulting electron cloud at the surface of the droplet acts as a shield that screens the interior of the droplet from the trailing part of the pulse (cf. Fig. 5.2 (c)). This process is called *laser-induced breakdown* (LIB). Applying high intensities of the laser pulses, the screening effect can shield 10 % to 25 % of the energy of the pulse from entering the droplet [Fen97], while the total absorption is limited to maximum 50 % of the energy of the laser pulse [Sch01].

After 200 fs, the thickness of the plasma is about the order of the wavelength of the driving pulse [Fei04, ST06]. At this time, a part of the kinetic energy of the electrons is transferred into kinetic energy of the ions. The energy transfer requires time and the plasma therefore starts expanding after a delay between 20 ps [ST06] and 30 ps [Sch02]. The expanding plasma itself transfers energy via collisional processes to neutral H₂O molecules at the side of the droplet opposite to the incident pulse and the plasma moves in a cylindrical shape through the droplet [Cou03, Lin04] (cf. Fig. 5.2 (d)). However, measurements of LIB in bulk water indicate that the total ionization is only ~ 6 % of the particles, which still is sufficient for a plasma triggered expansion [Bro11].

Since the expansion process starts at the side of the droplet facing the incident laser pulse and moves through the target, the whole mechanism is highly inhomogeneous for time delays shorter than 200 ps [Sch02]. A gradient in the density and in the microscopic structure of the target (clusters, molecules, atoms, ions) evolves in all three dimensions, as well as in time (cf. sec. 2.4). At the time scales considered within this thesis, the evolution of the droplet is of such complexity as the parameters change in a drastic manner that no simulation can accurately calculate its dynamics [Lin04]. First attempts applying Monte-Carlo methods are limited to electron-H₂O collisions in water samples on larger time scales with only 20 electrons but completely neglect ions [Dat07].

Experimental results however reveal the threshold of the laser-induced breakdown to $I_{\text{LIB}} = 6.4 \times 10^{13}$ W/cm² for pulse durations of 100 fs and a wavelength of 800 nm, which therefore is a lower limit for the plasma driven expansion [Sch01, Bro11]. Measurements of LIB in liquid water indicate an expansion velocity of 30 $\mu\text{m}/\text{ns}$ at an intensity of $I = I_{\text{LIB}}$ [Sch02]. This is in reasonable agreement with the model used in this thesis (cf. sec. 2.4.1), though the calculated value using equation (2.12) is lower with 21 $\mu\text{m}/\text{ns}$.

To summarize, the expansion of the droplet is caused by LIB if the intensity threshold for the plasma-triggered expansion of $I_{\text{LIB}} = 6.4 \times 10^{13}$ W/cm² is exceeded. Hence, the change of the thermodynamical of the droplet is a function of the intensity of the pump pulse, as described by the model describing the density evolution in sec. 2.4.2. In order to

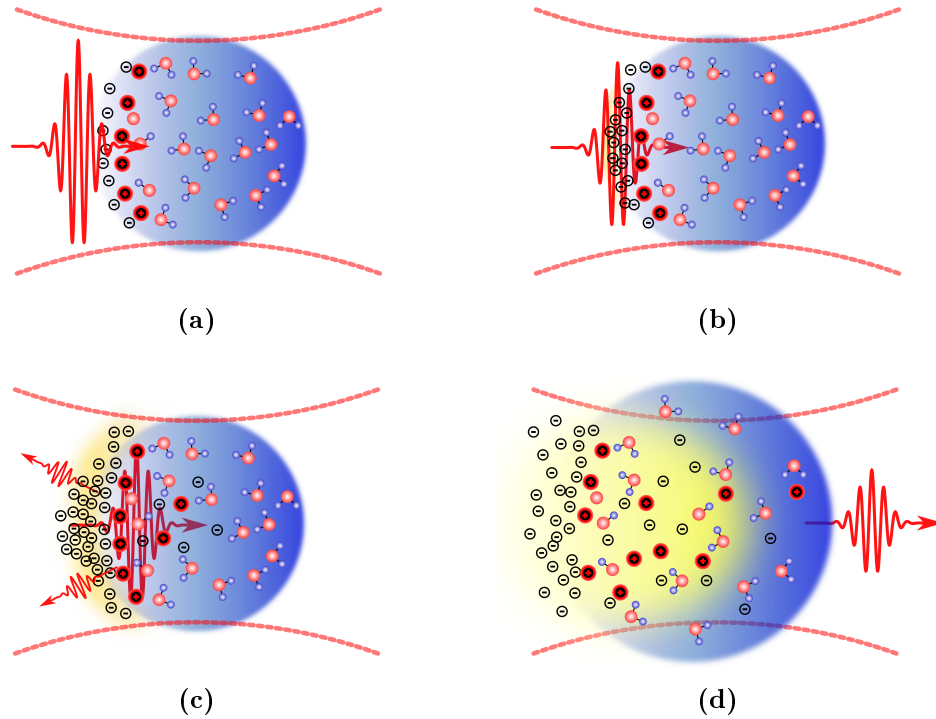


Figure 5.2: Schematic of the laser-induced breakdown. As the pulse propagates through the droplet in (a) to (d), the droplet performs a plasma triggered expansion. The figures depict: the droplet (blue), the focusing geometry (dashed-red), the pump pulse (solid red), electrons (black minuses), ions (red pluses), water molecules and its fragments.

experimentally validate the influence of I_{pump} onto the expansion process, the signal of the harmonic radiation as a function of the pump pulse is studied in the following.

5.1.2 The Influence of the Intensity of Pump Pulse

The results of the PM experiments in the last chapter allow to conclude that the droplet can be prepared in a gaseous state and that its density is correctly estimated by the model for the time-dependent density evolution of the droplet in sec. 2.4.2. This model has been validated by measurements of propagation effects in sec. 4.1, by the observation of the intensity-dependence of the harmonic yield and by studying the excursion distances of electronic trajectories in sec. 4.5. Hence, different combinations of the intensity of the pump pulse and the delay which lead to equal calculated densities should generate similar conditions of the droplet for HHG. However, significant differences in the harmonic spectra and in the harmonic yield have been observed in sec. 3.2.4 for such combinations of I_{pump} and t . A threshold intensity for LIB indicates that the influence of the intensity of the pump pulse has to be considered more carefully for the preparation of the target. In this section, the intensity-dependent evolution of the droplet is studied for intensities higher than the threshold intensity for LIB, $I_{\text{LIB}} = 6.4 \times 10^{13} \text{ W/cm}^2$. This is done by a detailed analysis of the influence of I_{pump} onto the signal of the harmonic radiation, in order to gain information on the intensity-dependent expansion of the droplet.

Long Pulses Figure 5.3 (a) depicts the harmonic yield as a function of the harmonic order and the intensity of the pump pulse for a fixed pump probe time delay of $t =$

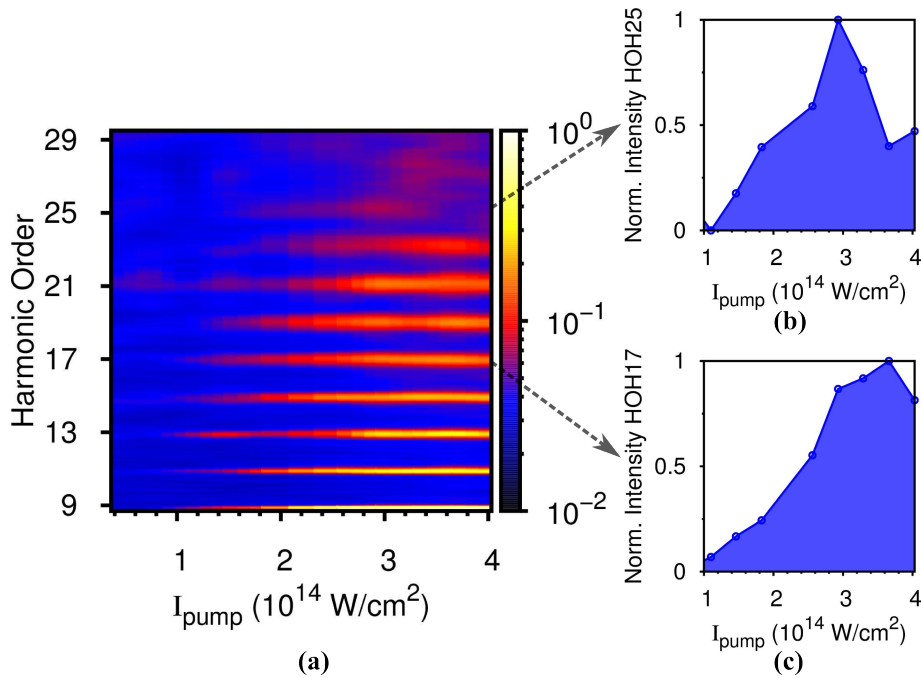


Figure 5.3: (a) Harmonic yield as function of order and intensity of the pump pulse at $t = 1.0 \text{ ns}$ [Kur13]. The intensity of the probe pulse was set to $3.7 \times 10^{14} \text{ W/cm}^2$. Outlines from (a) are depicted for the harmonic orders 25 (b) and 17 (c). Note that the intensity axis is scaled logarithmic in (a) while linear in (b) and (c). The spectra were measured with laser system A.

1.0 ns. This is the same measurement as in Fig. 3.8 and shown here again for reasons of comparison. Laser system A has been applied, delivering pulses with a duration of 100 fs. An intensity of the probe pulse of $3.7 \times 10^{14} \text{ W/cm}^2$ has been chosen since optimized PM conditions are obtained for this intensity for a wide range of harmonic orders (cf. sec. 4.3). Intensities of the pump pulse larger than $I_{\text{pump}} = 6.4 \times 10^{13} \text{ W/cm}^2$ are above the threshold intensity of I_{LIB} , which is valid for all intensities applied except the lowest. Hence, assuming an expansion of the droplet according to the LIB model is justified. While harmonic radiation below the 15th order is generated with a weak signal-to-noise ratio at intensities $I_{\text{pump}} < 1.0 \times 10^{14} \text{ W/cm}^2$, higher orders successively become observable as the intensity is raised. Coinciding with the raise of the HOHO, an increasing harmonic signal is detected with a maximum around an intensity of $I_{\text{pump}} = 3.3 \times 10^{14} \text{ W/cm}^2$. The emission pattern changes for the highest intensities towards incoherent radiation which is detected for $I_{\text{pump}} > 3.0 \times 10^{14} \text{ W/cm}^2$ and at higher orders than the 25th.

A more detailed analysis is possible by regarding the outlines for fixed harmonic orders in Fig. 5.3 (b) and (c). Considering the 25th harmonic order, no radiation is emitted for an intensity below $I_{\text{pump}} < 1.0 \times 10^{14} \text{ W/cm}^2$. The signal increases with raising intensity, until a maximum is reached around $3.0 \times 10^{14} \text{ W/cm}^2$. If the intensity is increased onwards to $I_{\text{pump}} = 3.3 \times 10^{14} \text{ W/cm}^2$, the signal of the harmonic radiation is decreased and superimposed by incoherent radiation. An analogue behaviour is observed for the 17th order in Fig. 3.8 (c). A weak signal at low intensity is followed by an increase towards a maximum around $I_{\text{pump}} = 3.6 \times 10^{14} \text{ W/cm}^2$. The maximum is shifted towards a higher intensity compared with the 25th harmonic order but a decreasing yield is still detected for the highest intensity.

Two effects can be deduced from the measurements: The first is the intensity-dependent expansion of the droplet, the second is a rising density of free electrons due to ionization induced by the pump pulse [Kur13]. Considering the intensity-dependent expansion, the

model for the calculation of the density from sec. 2.4.2 allows to convert the intensity range in Fig. 5.3 to a density range reaching from $\rho = 1.6 \times 10^{21} \text{ cm}^{-3}$ to $\rho = 5 \times 10^{20} \text{ cm}^{-3}$. Thus, the target is within the density regime of a dense gas throughout the measurement (cf. sec. 2.3).

A weak harmonic yield is detected for intensities below $I_{\text{pump}} = 1 \times 10^{14} \text{ W/cm}^2$. At this intensity, the calculated density of the droplet is $\sim 1 \times 10^{21} \text{ cm}^{-3}$. This density however is in the vicinity of the maximum tolerable density attributed to the cutoff trajectory ρ_{cutoff} obtained in section 4.5. The density ρ_{cutoff} is associated with a limit where the characteristics of the target change. For densities higher than ρ_{cutoff} (i.e. lower intensities than $1 \times 10^{14} \text{ W/cm}^2$), the mean-inter particle distance is lower than the excursion distance of the electrons and the trajectories are perturbed. Hence, the harmonic yield is suppressed as observed in the measurement. For densities lower than ρ_{cutoff} (i.e. higher intensities than $1 \times 10^{14} \text{ W/cm}^2$), the mean inter-particle distance is larger than the electronic excursion distance and the harmonic yield is determined by PM, causing the steep increase of the harmonic yield.

The decreasing signal for the highest intensities is caused by the second effect, a rising density of free electrons. The next task therefore is to determine whether the free electrons are generated by the pump pulse or by the probe pulse. In order to identify the pulse causing the massive ionization, the results on the saturation intensity (cf. sec. 4.3.1) and density-dependence of the harmonic yield are used (cf. sec. 4.5.3).

Considering an intensity of $I_{\text{pump}} = 4 \times 10^{14} \text{ W/cm}^2$ in Fig. 5.3, the decrease of the signal is clearly visible in the outlines. The calculated density for this intensity is $\rho = 5 \times 10^{20} \text{ cm}^{-3}$. In sec. 4.3.1, the saturation intensity I_{sat} has been defined for the probe pulse as an intensity where a depletion of the ground state sets in, and became observable by a saturation of the harmonic yield. In the measurements described in this section however, the intensity of the probe pulse is below the saturation intensity and no extensive generation of free electrons is induced by the probe pulse. However, the density in the measurement from this section is ten times higher than in the measurement of the saturation intensity. In order to exclude an effect caused by the difference in the densities between the two measurements, the findings from sec. 4.5.3 have to be taken into account, where the harmonic yield has been studied as a function of the intensity of the probe pulse and of the target density. Comparing the two densities of $\rho = 5 \times 10^{19} \text{ cm}^{-3}$ and $\rho = 5 \times 10^{20} \text{ cm}^{-3}$ in Fig. 4.20, the target is in both cases a dense gas with $\rho < \rho_{\text{cutoff}}$ and the harmonic yield is determined by PM and re-absorption. Hence, a decreasing signal due a high density can also be excluded, and the reduced yield is assigned to ionization induced by the pump pulse.

The decreasing signal for intensities higher than $3.3 \times 10^{14} \text{ W/cm}^2$ in Fig. 5.3 therefore allows the conclusion that the droplet gets highly ionized by the pump pulse and a plasma is ignited throughout the droplet. This leads to changing PM conditions induced by free electrons (cf. equation (2.36)) [Alt96, Kur13]. As a result, the harmonic yield and the HOHO are suppressed. The absolute value for the decrease differs for each harmonic order, as indicated in Fig. 5.3 (c), which is related to varying phase-matching conditions for differing harmonic orders. The expansion of the droplet therefore is in agreement with the LIB model for pulses with a duration of 100 fs.

Short Pulses A different intensity dependence of the harmonic yield has already been observed when studying the influence of the probe-pulse duration (cf. sec. 4.2.2). It has been found that a shorter pulse duration results in less ionization within the target. Since

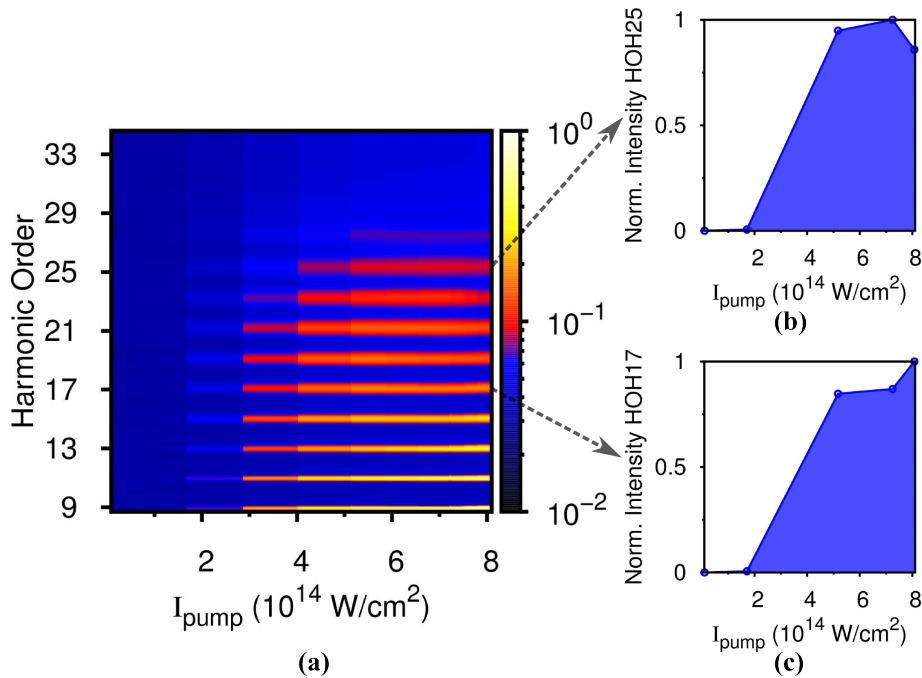


Figure 5.4: (a) Harmonic intensity versus harmonic order and intensity of the pump pulse. The delay was set to $t = 1.0 \text{ ns}$, while the I_{probe} was determined to be $9.5 \times 10^{14} \text{ W/cm}^2$. Outlines from (a) are depicted for the harmonic orders 25 (b) and 17 (c). Note that the intensity axis is scaled logarithmic in (a) while linear in (b) and (c). The spectra were measured with laser system *B*.

the expansion of the droplet via LIB is based on ionization, a difference in the harmonic yield to the measurements described above should become observable when applying pulses with a duration below 100 fs. Figure 5.4 (a) therefore shows the intensity of the harmonic radiation as a function of the order and of I_{pump} for a fixed pump-probe time delay of 1.0 ns, which is the same measurement as in Fig. 3.9. Laser system *B* has been exploited with pulse durations of 35 fs. The intensity of the probe pulse has been set to $I_{\text{probe}} = 9.5 \times 10^{14} \text{ W/cm}^2$ which is slightly lower than the saturation intensity and therefore provides optimized conditions for HHG (cf. Fig. 4.12). The measurement is comparable to the above described intensity study (cf. Fig. 5.3) but note that the range of the intensity is larger.

The harmonic signal is weak at low intensities in Fig. 5.4 but a significant increase in the harmonic yield sets in at intensities $I_{\text{pump}} > 2.0 \times 10^{14} \text{ W/cm}^2$. Moreover, higher orders become observable as the intensity is raised. Optimized conditions for the harmonic signal are detected at intensities around $7.0 \times 10^{14} \text{ W/cm}^2$, where the HOHO is given by the 29th order. Outlines are depicted in Figs. 5.4 (b) for the 25th harmonic order and for the 17th order in (c).

Considering the 25th harmonic order, no radiation is emitted for the lowest intensity and only a weak signal is observed for $I_{\text{pump}} < 2 \times 10^{14} \text{ W/cm}^2$. The signal increases steeply for higher values of I_{pump} , until a maximum is reached around $7.0 \times 10^{14} \text{ W/cm}^2$. Further increase of the intensity results in a decreasing yield. A comparable intensity-dependence is observed for the 17th order Fig. 5.4 (c), but no decrease is observed for the highest intensity.

Comparing the measurements with differing pulse durations in Figs. 5.3 and 5.4, the harmonic yield as a function of the pump-pulse intensity develops similarly. A low yield is followed by a steep increase as a function of the intensity, and a maximum is observed. This indicates that the above described explanation for the intensity-dependence of the signal is similar for the short pulses. However, optimized conditions for HHG are shifted

towards higher intensities when pulses with a duration of 35 fs are applied and the decrease in the signal at high values of I_{pump} is less pronounced in the case of the 25th order and not observed at all for the 17th order. This is not in consistency with the model for the calculation of the density, since the target gets more diluted for higher intensities of the pump pulse which promotes a higher yield as observed in sec. 4.5.2. Moreover, no incoherent radiation is detected. But considering the influence of the pulse duration onto HHG (cf. sec. 4.2.2), one observation was a lower ionization probability using shorter pulses. In combination with the fact that the expansion process is based on ionization through LIB, this might be a hint for the need of a higher intensity of the pump pulse in order to generate equal conditions for HHG. Hence, the threshold intensity for LIB seems to be higher for pulses with short duration. A determination of I_{LIB} for 35 fs-pulses therefore follows.

5.1.3 The Threshold Intensity for Laser-Induced Breakdown

The measured value for the threshold intensity of LIB in water using 100 fs pulses at a central wavelength of 800 nm is $I_{\text{LIB}} = 6.4 \times 10^{13} \text{ W/cm}^2$ [Sch01, Bro11]. The threshold intensity for LIB however is also depends on the wavelength. It increases for wavelengths between 400 nm and 1000 nm, which stems from the increasing linear absorption coefficient within this wavelength range [Noa99] (cf. Fig. 5.1). It also depends on the pulse duration since less ionization is induced using shorter pulses (cf. sec. 4.2.2) and therefore increases as the pulse duration is decreased [Fen97, Noa99, ST06].

In order to estimate the threshold of I_{LIB} for pulses with a duration of 35 fs, the data provided by NOACK *et al.* is used [Noa99], which is depicted in Fig. 5.5. The graph shows I_{LIB} as a function of the pulse duration where the data has been measured using laser pulses with wavelengths of $\lambda = 532 \text{ nm}$ for $\tau > 3 \text{ ps}$ and $\lambda = 580 \text{ nm}$ for $\tau < 3 \text{ ps}$. The dashed line displays an approximation using a function $\sim \tau^{-a}$ where a is a fitting parameter. The shortest pulse duration in the data is $\tau = 100 \text{ fs}$ where $I_{\text{LIB}}(\tau = 100 \text{ fs}) = 1.11 \times 10^{13} \text{ W/cm}^2$. An extrapolation of the fit curve delivers a value of $I_{\text{LIB}}(\tau = 35 \text{ fs}) = 2.5 \times 10^{13} \text{ W/cm}^2$, which is a factor of $\Delta I_{\text{LIB}} = 2.25$ times higher.

However, the above calculated value is gained from data acquired with a wavelength of 580 nm and therefore cannot be considered as a reference value. Multiplying the scaling factor of 2.25 with the above described measured value at a wavelength of 800 nm and pulses with a duration of 100 fs by SCHAFFER *et al.* [Sch01] delivers a threshold intensity of $I_{\text{LIB}}(\tau = 35 \text{ fs}) = 1.4 \times 10^{14} \text{ W/cm}^2$ for a wavelength of 800 nm and pulses with a duration of 35 fs. Although this is only a rough estimate for the increase of I_{LIB} , it provides a value close to the experimentally retrieved intensity, as will be shown in the following.

Figure 5.6 depicts single spectra of HHG from water droplet for pulse durations of (a) 100 fs and (b) 35 fs for different intensities of the pump pulse. Equal laser parameter to the Figs. 5.3 and 5.4 are chosen, respectively. The spectra are normalized to the maximum signal of each series of measurements, which is detected at the highest intensity of the pump pulse shown. The lowest intensity in Fig. 5.6 (a) is slightly higher than I_{LIB} . However, only a weak signal of harmonic radiation is observed. As the intensity is

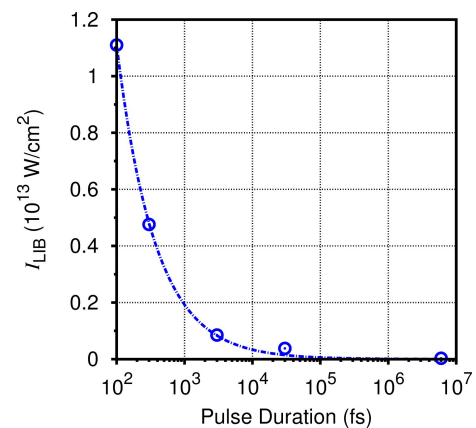


Figure 5.5: Measured threshold intensity for LIB I_{LIB} at a wavelength around $\lambda = 580 \text{ nm}$ by NOACK *et al.* [Noa99].

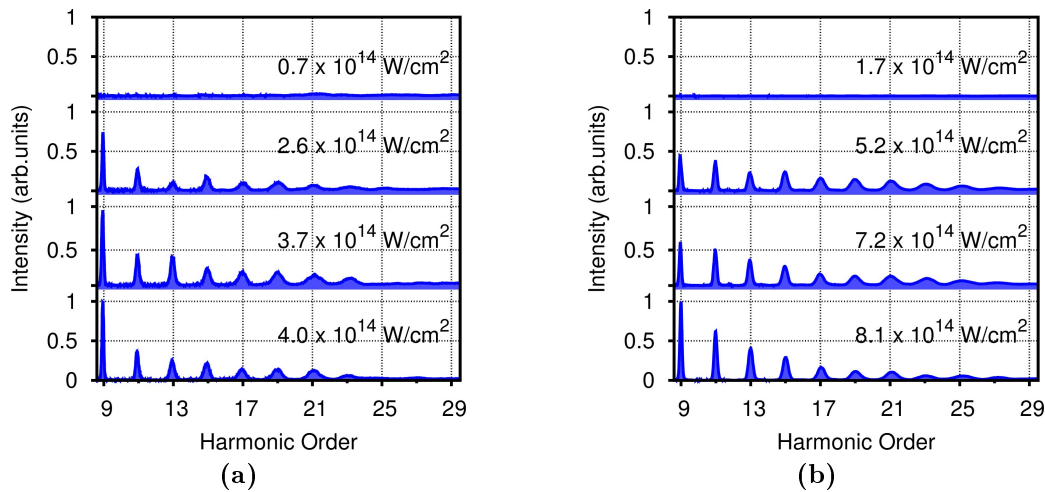


Figure 5.6: Single spectra of the harmonic radiation from water droplets for a pulse duration of (a) 100 fs and (b) 35 fs. The numbers within the single spectra indicate the intensity of the pump pulse.

raised to $I_{\text{pump}} = 2.6 \times 10^{14} \text{ W/cm}^2$, the signal increases and harmonic radiation up to the 25th order is observed. For a value of $I_{\text{pump}} = 3.7 \times 10^{14} \text{ W/cm}^2$, the harmonic yield is further enhanced, while no significant difference is observed for the highest intensity.

A similar intensity dependence of the signal of the harmonic radiation is observed for pulse durations of 35 fs in Fig. 5.6 (b). The lowest intensity is above the calculated threshold of $I_{\text{LIB}} (\tau = 35 \text{ fs}) = 1.4 \times 10^{14} \text{ W/cm}^2$, but no harmonic radiation is detected. When the intensity is increased, harmonic radiation up to the 27th order is observed. Further raise of the intensity results in a stronger harmonic yield, as in the case of Fig. 5.6 (a).

Comparing the two measurements, an equal intensity dependence of the signal of the harmonic radiation is detected, though the intensity ratio between the measurements is approximately $\Delta I_{\text{pump}} \sim 2$. In both cases, the harmonic yield is weak for intensities slightly above I_{LIB} , but a raise in the signal is observed as the intensity is increased. Moreover, comparable HOHOs are generated and also a similar spectral intensity distribution is found. However, a more precise analysis of ΔI_{pump} is needed in order to obtain a quantified value for the ratio of the intensities.

In order to receive a numerical value for ΔI_{pump} , the findings from sec. 5.1.2 are considered. As observed in the outlines in Figs. 5.3 (b) and (c) as well as in Figs. 5.4 (b) and (c), the development of the harmonic yield as a function of the intensity is comparable for both pulse durations and the harmonic yield maximizes at a specific intensity for each order. This optimum intensity of the pump pulse is a measure for the preparation conditions of the droplet for HHG. Hence, choosing the intensities where the harmonic yield maximizes is a suitable measure to compare the two experimental results.

Figure 5.7 shows the intensity of the pump pulse where the maximum harmonic yield has been detected as a function of the harmonic order for a pulse duration of 100 fs (red) and 35 fs (blue). The same laser parameters have been applied as in the previous measurements. The optimum intensity is for both pulse durations rather constant as a function of the harmonic order and a decrease is only observed for higher orders¹. Hence, the two measurements of the optimum intensity can be approximated by linear functions (dashed lines).

¹Note that the 19th and the 21st order are not considered for a pulse duration of 35 fs since the lower value of the optimum intensity stems from poor synchronization between laser and droplet.

Comparing the two linear fits allows a more precise statement of the intensity ratio for the two pulse durations. By dividing the two linear functions, a value of the ratio for the optimum intensity of $\Delta I_{\text{pump}} = 2.097$ is received. This is close to the calculated value of 2.25 with a difference of $\sim 9\%$. This difference in the intensity threshold might be related to the use of pulses with a central wavelength of 780 nm instead of 800 nm where the imaginary part of the refractive index slightly differs (cf. Fig. 5.1). However, the agreement between the calculated and the experimentally retrieved value of ΔI_{pump} justifies the assumption of a two times higher threshold for LIB when using 35 fs-pulses. Hence, by applying the experimentally retrieved scaling factor of $\Delta I_{\text{pump}} \approx 2.1$ on the value for 100 fs pulses by SCHAFFER *et al.* [Sch01], a threshold intensity for the LIB with pulses of 35 fs of $I_{\text{LIB}} (\tau = 35 \text{ fs}) = 1.34 \times 10^{14} \text{ W/cm}^2$ is obtained.

This means, the plasma triggered expansion of the droplet sets in at a higher intensity when short pulses are applied. Consequently, the model for the calculation of the density evolution of the droplet in sec. 2.4.2 has to be rescaled when using shorter pulses. This has been considered in the measurements in the previous chapters by multiplying the intensity in the model with the inverse of the intensity ratio $1/\Delta I_{\text{LIB}} \approx 0.48$, which corrects the calculation of the density.

Furthermore, the finding of an approximately two times higher intensity threshold for LIB allows to interpret the intensity-dependence of the harmonic yield in Fig. 5.4, as it is the reason for the shift of the intensity dependence of the harmonic yield towards higher intensities than in Fig. 5.3. As in the case of 100 fs-pulses, only a weak signal of harmonic radiation is detected for intensities lower than I_{LIB} . The harmonic yield then develops according to the findings for the longer pulses, which can be interpreted by considering the calculated density with the re-scaled model. In Fig. 5.4, the density varies from $\rho \sim 1 \times 10^{21} \text{ cm}^{-3}$ at $I_{\text{pump}} = I_{\text{LIB}}$ to $\rho \sim 5 \times 10^{20} \text{ cm}^{-3}$ at $I_{\text{pump}} = 8 \times 10^{14} \text{ W/cm}^2$. Hence, equal values for ρ are calculated to the measurement with 100 fs-pulses in Fig. 5.3 and the droplet is prepared in a comparable state. That is why a similar behaviour of the harmonic signal as a function of the intensity is observed although the intensity range is different.

In summary, the intensity threshold for the plasma-triggered expansion of the droplet I_{LIB} depends on the wavelength, as well as on the pulse duration. Using data by NOACK *et al.* [Noa99] for wavelengths of $\sim 580 \text{ nm}$ allows to estimate the threshold intensity for a pulse duration of 35 fs and a central wavelength of 800 nm to be $I_{\text{LIB}} (\tau = 35 \text{ fs}) = 1.4 \times 10^{14} \text{ W/cm}^2$. A comparison of the measurements of HHG for pulse durations of 35 fs and 100 fs allows to retrieve a threshold intensity for 35 fs pulses of $I_{\text{LIB}} (\tau = 35 \text{ fs}) = 1.34 \times 10^{14} \text{ W/cm}^2$ from the experimental data. Using the higher threshold intensity for short pulses enables to extend the model for the calculation of the density to pulse durations of 35 fs. Applying this extended model allows to interpret the dependence of the harmonic yield as a function of the intensity of the pump pulse for short pulses and to observe the intensity-dependent transition of the droplet from the liquid into the gas phase.

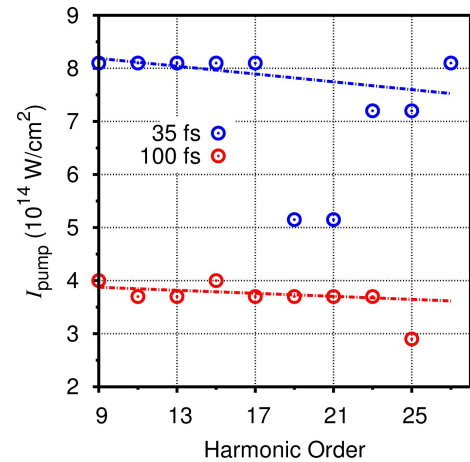


Figure 5.7: Optimum intensity of the pump pulse for HHG versus harmonic order for a pulse duration of 100 fs (red) and 35 fs (blue). The dashed lines indicate linear fits to the measured data.

Using the liquid droplet source is an excellent tool for the extension of threshold intensities of LIB in liquids for short pulses, since the source is not limited to water but also other liquids can be applied. Moreover, the process is under vacuum conditions and no atmosphere influences the expansion process which allows measurements with high precision.

So far the influence of I_{pump} has been studied for a fixed time delay of $t = 1.0$ ns. But the transition of the droplet from a liquid state into a gaseous target is also time dependent, as observed in secs. 3.2.1, 4.1 and 4.2.2. Moreover, a too high intensity of the pump pulse seems to lead to a highly ionized target and the harmonic yield is decreased. Hence, studying the signal of the harmonic radiation as a function of time and the intensity of the pump pulse allows investigate the expansion process in more detail.

5.1.4 The Time and Intensity-Dependent Expansion Process

Free electrons can severely influence the harmonic yield, as observed when studying the intensity-dependence of the pump pulse in the sections above. Since a plasma is ignited by pump pulse during the expansion of the droplet via the LIB mechanism, the lifetime of free electrons may exceed the nanosecond range. Hence, an ionized target can be prepared which can be probed by HHG. However, also the probe pulse can lead to ionization, which becomes more prominent in diluted targets (cf. sec. 4.2.1). In order to distinguish between ionization induced by the pump and the probe pulse for different densities of the target, the harmonic yield is studied as a function of the intensity of the pump pulse and of the delay between the two pulses.

Figure 5.8 depicts the signal of the harmonic radiation of the 17th order in (a) as a function of the delay and of the intensity of the pump-pulse. Laser system *B* has been applied, delivering pulses with a duration of 40 fs and an intensity of the probe pulse of $I_{\text{probe}} = 9.5 \times 10^{14}$ W/cm². The dashed white line indicates the threshold intensity for LIB. In this case, the mapping technique from sec. 4.4 is not applied since the density is a function of t and I_{pump} and therefore varies throughout the graph. In general however, the target is diluted for high values of t and I_{pump} with $\rho \sim 5 \times 10^{17}$ cm⁻³ (top right corner) while it is dense with $\rho \sim 5 \times 10^{21}$ cm⁻³ for low values of t and I_{pump} (bottom left corner). The difference in the density of the target along the intensity-axis is thereby of a factor below ten (cf. Fig. 2.3).

The 17th harmonic order is generated for almost all delays and intensities. An increasing signal as a function of the delay is observed for $t < 7$ ns, whereas a decrease is recognized for larger values of t . A similar situation is detected regarding the intensity dependence, where the harmonic yield raises as a function of the intensity and a broad maximum is observed around $t = 6.0$ ns and $I_{\text{pump}} > 6 \times 10^{14}$ W/cm². The signal decreases for larger values of t . However, the signal is weak at two instances: First, independent of the intensity of the pump pulse at short time delays and second for $I_{\text{pump}} < I_{\text{LIB}}$ at all time delays.

The first region where the signal is weak can be interpreted by considering the results from sec. 4.5.3. The density of the target is high at short time delays and the mean inter-particle distance is lower than the excursion distance of the electrons. The electronic trajectories are therefore perturbed and the harmonic yield is suppressed. A similar situation is given for the second region featuring a weak signal. The reason here is a low intensity $I_{\text{pump}} < I_{\text{LIB}}$ which results in an expansion that is not based on LIB as described in sec. 5.1.3. Hence, energy is deposited within the droplet without igniting a plasma which is less efficient and results in a less rapid expansion process. The density of the target therefore is high and the electronic trajectories are distorted and reabsorption occurs.

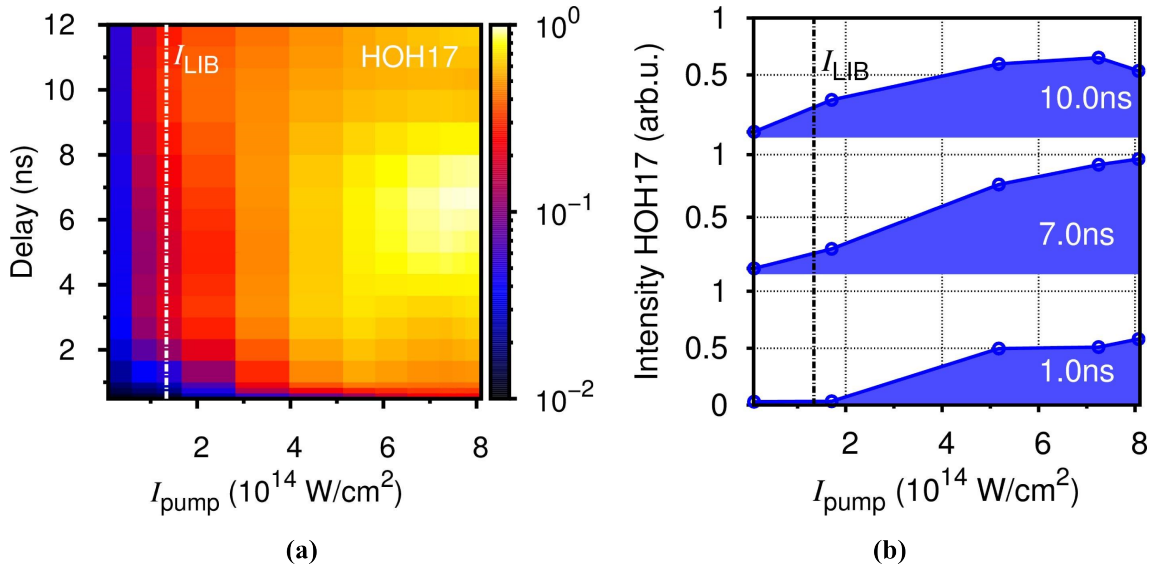


Figure 5.8: Harmonic yield of the (a) 17th versus the time delay and the intensity of the pump pulse. The dashed white line indicates the threshold intensity for LIB. The intensity of the probe pulse was set to $9.5 \times 10^{14} \text{ W/cm}^2$. Note that the data has been interpolated with three points between each intensity and delay value for better visibility. (b) Outlines from (a) for different time delays. The dashed black line indicated the threshold intensity for LIB. The signals are normalized to the maximum of the harmonic yield.

For intensities above I_{LIB} , the expansion of the droplet agrees with the LIB model and the harmonic yield increases. For the interpretation at intensities of $I_{\text{pump}} > I_{\text{LIB}}$, fixed delays are considered in the following.

Figure 5.8 (b) depicts outlines of the signal of the 17th harmonic order for different time delays. For the largest delay, the signal increases until a maximum is reached around $I_{\text{pump}} = 7 \times 10^{14} \text{ W/cm}^2$. A decrease is observed for the highest intensity. On the contrary, a strictly monotonic raise of the yield is observed when the delay is decreased to 7.0 ns, where also the maximum of the harmonic signal is observed. Further decrease of the delay to 1.0 ns results in a reduction of the conversion efficiency and the maximum harmonic yield drops. However, a still monotonous increase of the signal as a function of the intensity is observed.

The raise in the signal of the harmonic radiation as a function of I_{pump} can be interpreted by considering the intensity-dependent expansion of the droplet. For a fixed time delay, the droplet expands as a function of I_{pump} and its density is reduced. Hence, PM conditions improve, reabsorption effects are reduced, and the harmonic yield increases which is in agreement with the results described in sec. 5.1.2. The differing maximum yield between the three delays however stems from the time-dependent expansion of the droplet. The target is in a diluted state for a delay of $t = 10.0 \text{ ns}$. The number of emitters therefore is low and the harmonic yield is weak. Contrarily, the density of the target is too high at $t = 1.0 \text{ ns}$ and the PM conditions are not optimized. Hence, the harmonic yield is weak again. Optimized conditions are found for $t = 7.0 \text{ ns}$ with a density of the target of $\rho = 3 \times 10^{18} \text{ cm}^{-3}$. The position of the maximum yield at this density is in agreement with the findings from Fig. 4.20 (a), where the influence of the intensity of the probe pulse and of the density of the target onto the harmonic yield were studied. Hence, similar conditions for HHG are generated within the droplet in the two measurements. This validates the model for the density evolution of the target from sec. 2.4.2 with the included intensity correction from sec. 5.1.3, since different combinations of t and I_{pump} are applied which lead to a comparable calculated density of the target and also a comparable harmonic yield

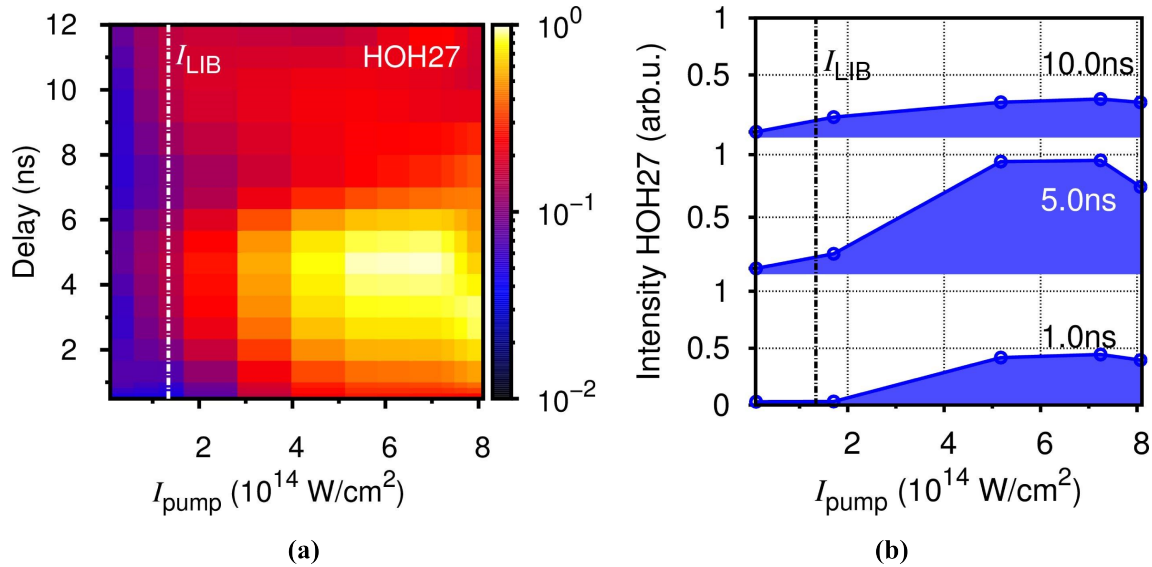


Figure 5.9: Harmonic yield of the (a) 27th order versus the time delay and the intensity of the pump pulse. The dashed white line indicates the threshold intensity for LIB. The intensity of the probe pulse was set to $9.5 \times 10^{14} \text{ W/cm}^2$. Note that the data has been interpolated with three points between each intensity and delay value for better visibility. (b) Outlines from (a) for different time delays. The dashed black line indicated the threshold intensity for LIB.

as a function of the density.

While the monotonic increase of the signal for the two shorter delays considered above has been attributed to the expansion of the droplet, the decrease for the highest intensity and $t = 10.0 \text{ ns}$ has not been observed before. The dilution of the target between $I_{\text{pump}} = 7 \times 10^{14} \text{ W/cm}^2$ and $8 \times 10^{14} \text{ W/cm}^2$ as reason can be excluded since the ratio of the densities is with 1.1 too small. But the density of the target is below $1 \times 10^{18} \text{ cm}^{-3}$ which might as well be an indication for ionization induced by the probe pulse, as observed in the TPM-experiments in sec. 4.2.1. However, the intensity of the probe pulse is below the saturation intensity and the decrease of the signal therefore might be as well attributed to ionization induced by the pump pulse as in the case of the 25th order in Fig. 5.4. In order to identify the reason for the decreasing signal, higher harmonic order are considered. Since the short trajectory is selected during the experiments, higher orders exhibit a larger excursion time within the continuum τ_{exc} (cf. Fig. 2.8). Hence, the induced phase mismatch by ionization is larger and it is more likely to detect an ionization induced effect within the signal of a higher order, as observed in sec. 5.1.2.

Figure 5.9 (a) depicts the harmonic yield of the 27th order versus the time delay and the intensity of the pump pulse. The same laser parameters as in Fig. 5.8 have been applied. As in the case of the 17th order, the signal is weak at two instances: At short time delays, independent of the intensity of the pump pulse and for all time delays with values of $I_{\text{pump}} < I_{\text{LIB}}$. The reason for the weak signal is again the high density of the target and the resulting distortion of electronic trajectories.

Considering the intensity range, the radiation is emitted in a comparable way to the 17th order. However, the range of the time delay is more confined and the maximum is shifted towards lower delays. This effect has also been observed in the measurements concerning the probe-pulse intensity and the density of the target in Fig. 4.21 and therefore can be assigned to the dilution of the target. Ionization-induced effects however are only observable in the upper intensity regime of the pump pulse and therefore require a more detailed analysis of the harmonic yield.

Figure 5.9 (b) therefore depicts outlines of Fig. 5.9 (a) for different delays. As in the case of the 17th harmonic order, the signal increases for all three delays as a function of the intensity which can also be attributed to the expansion of the droplet. However, a decreasing yield of the harmonic radiation is observed for the highest intensity at all three time delays. For the reduced signal at the largest delay, the density of the target is in a diluted state (cf. Fig. 4.21 (a)). Hence, the reduced signal at 10 ns and the highest intensity might stem from an effect induced by the probe pulse. However, the intensity of the pump pulse is high and might as well induce a sufficient amount of ionization, as observed in Fig. 5.3 (b). An explicit assignment to ionization induced by the pump or the probe pulse is therefore not possible.

This is different regarding $I_{\text{pump}} = 8 \times 10^{14} \text{ W/cm}^2$ at the delays of $t_1 = 1.0 \text{ ns}$ and $t_2 = 5.0 \text{ ns}$, where the density of the target is high with $\rho_1 = 5 \times 10^{20} \text{ cm}^{-3}$ and $\rho_2 = 8.3 \times 10^{18} \text{ cm}^{-3}$, respectively. A comparison with the measurement of the harmonic yield as a function of I_{probe} and ρ in Fig. 4.21 (a) reveals that the two densities ρ_1 and ρ_2 are situated before the maximum yield of the harmonic radiation for the given intensity of the probe pulse of $I_{\text{probe}} = 9.5 \times 10^{14} \text{ W/cm}^2$. Hence, the signal is expected to increase when the density of the target is decreased. However, a reduced signal is detected when the density of the droplet is reduced by the raise of the intensity of the pump pulse from $I_{\text{pump}} = 7 \times 10^{14} \text{ W/cm}^2$ to $I_{\text{pump}} = 8 \times 10^{14} \text{ W/cm}^2$. This means, the lower signal at the highest intensity is not caused by the probe pulse but the effect can be attributed to an increasing amount of ionization within the target which is induced by the pump pulse.

In conclusion, the droplet is expanded when higher intensities of the pump pulse are applied. Moreover, a severe ionization can be induced by the pump pulse when applying intensities $I_{\text{pump}} > 6 \times 10^{14} \text{ W/cm}^2$ as observed by a decreasing yield of the harmonic radiation. In order to estimate the degree of ionization within the target and to gain information on the composition of the target, more sophisticated methods have to be applied which will be presented in the next section.

5.2 An Ionized Target

First indications for the generation of an ionized target have been recognized in the last section by a decreasing signal of the harmonic radiation for high intensities of the pump pulse. However, this measurement did not allow any conclusion onto the amount of ions residing within the droplet. A precise determination of the number of ions within the target cannot be easily done because of the complexity of the dynamics of the droplet on the considered time scales. But a comparison of the measurements applying high intensities of the pump pulse from the last section with the simulations of the influence of an ionic medium onto HHG by STRELKOV *et al.* described in sec. 2.6.2 [Str05], can assist in delivering a measure of whether the composition of the target is dominated by ions or neutral particles.

As described by the theory in sec. 2.6.2, an ionic target can critically influence the electronic trajectories during the excursion in the continuum. The ionic field therein deflects the electron in a way that recombination may become impossible which leads to a suppression of the harmonic yield. The simulations by STRELKOV *et al.* study the influence of ions neighboring an atom which interacts with an intense laser pulse for varying densities of the target [Str05]. Different trajectories of the electron contributing to the harmonic signal were simulated for the case of argon and an intensity of the driving field of $2 \times 10^{14} \text{ W/cm}^2$. The results are depicted in Fig. 2.18 (b) and exhibit a lesser affection of the short trajec-

tory than the long trajectory, as indicated by the steeper decrease of the signal of the long trajectory as a function of the density of the target. The reason for the trajectory splitting has been attributed to the different excursion times of the quantum paths. For a fixed harmonic order, the excursion time τ_{exc} of the electron within the continuum is larger for the long trajectory (cf. Figs. 2.8 and 4.15). Hence, the accumulated phase by the surrounding ions is higher for the long trajectory than for the short trajectory. The signal from the long trajectory is therefore efficiently suppressed. Additionally, the influence of a neutral atomic target has been simulated, which is depicted in Fig. 2.18 (a). In comparison to the ionic target, harmonic radiation is detected at higher densities and no splitting effect between the two trajectories is observed. This means, if the droplet is prepared in a state where its composition is dominated by ions, a similar decrease of the harmonic yield should be observed when the density of the target is increased. Hence, the measurement of HHG with differing intensities of the pump pulse can be used to retrieve a measure for the amount of ions within the target which is derived from more precise analysis of the data from sec. 5.1.4.

5.2.1 Distinguishing between Neutral and Ionic Targets

In order to compare the measurements from sec. 5.1.4 with the simulation, the delay is mapped onto the calculated density (cf. sec. 4.4). Figure 5.10 depicts the measured signal of the harmonic radiation of the (a) 17th and (b) 27th order versus the density of the target for different intensities of the pump pulse. Moreover, the simulation by STRELKOV *et al.* [Str05] is shown for total emitted radiation of a short and a long trajectory for a harmonic order from the plateau region emitted by an argon atom which is surrounded by an ionized medium. In the measurements, laser system *B* has been applied with $I_{\text{probe}} = 9.5 \times 10^{14} \text{ W/cm}^2$ and a medium position $z > 0 \text{ mm}$, so that the short trajectory was selected.

In both figures, the simulated signal of the long trajectory decreases rapidly until a

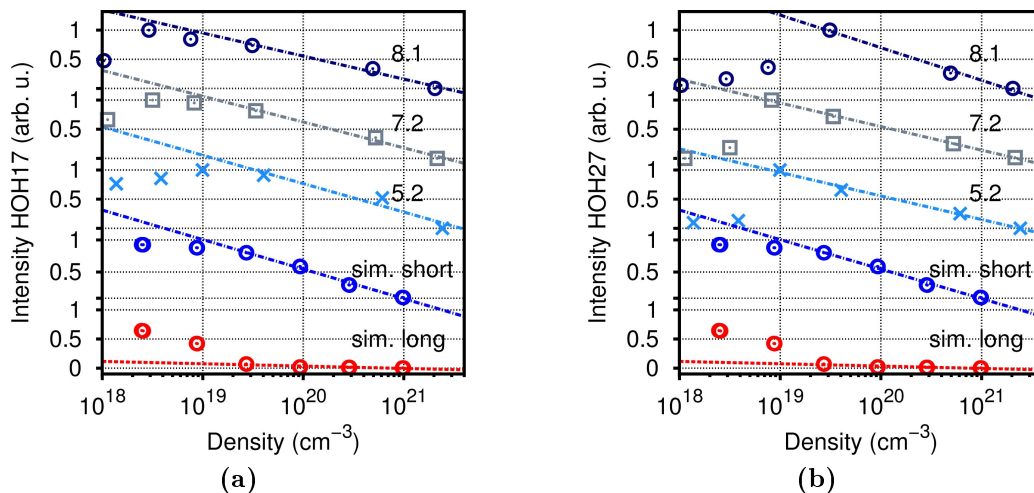


Figure 5.10: Density-dependent development of the harmonic yield simulated for the short and long trajectory by STRELKOV *et al.* [Str05] and measured harmonic yield of the short trajectory for the (a) 17th and (b) 27th harmonic order. Laser system *B* has been applied with $I_{\text{probe}} = 9.5 \times 10^{14} \text{ W/cm}^2$. The numbers indicate different intensities of the pump pulse in units of 10^{14} W/cm^2 . Linear approximations are indicated by the dashed lines. The signals have been normalized to the maximum yield at each intensity of the pump pulse.

density $\rho < 1 \times 10^{19} \text{ cm}^{-3}$ is reached and the slope flattens. The opposite behaviour is observed for the short trajectory, where the signal remains at a nearly constant level for densities $\rho < 1 \times 10^{19} \text{ cm}^{-3}$ and decreases thereafter. Regarding the 17th harmonic order, the signals of all depicted intensities of the pump pulse show a similar density dependence. The harmonic yield is weak for the lowest density but an increase towards a maximum as a function of ρ is detected. Increasing the density of the target to values $\rho > 1 \times 10^{19} \text{ cm}^{-3}$ results in a linear decrease of the signal. Approximating the decreasing signals with linear functions (dashed lines) indicates that the slope of the decrease is with $m_j \sim -0.2 \text{ cm}^3$ similar to the simulation of the short trajectory with $m_{\text{short}} \approx -0.22 \text{ cm}^3$ (where j denotes the intensity of the pump pulse in 10^{14} W/cm^2), while the difference is large between the measurements and the simulation of the long trajectory with $m_{\text{long}} = -0.002 \text{ cm}^3$. A similar behaviour is observed for the 27th harmonic order in Fig. 5.10 (b). A weak signal is observed for low densities which increases towards a maximum. For the largest intensity of the pump pulse however, the maximum is shifted towards higher densities. Thereafter, the yield is reduced linearly as the density is increased.

The weak signal for low densities can be attributed to the dilution of the target and has already been described in the last section. A higher interest lies in the linear decreasing part of the signal. The good agreement of the slopes with the theoretical model is a proof for the selection of the short trajectory via the position of the moderately. Moreover, the slope of the linear approximation of the 27th order at the highest intensity of the pump pulse seems with $m_{8,1} = -0.24 \text{ cm}^3$ to be slightly steeper than the simulated slope. This is reasonable since larger values of I_{pump} are supposed to result in a larger amount of ions within the target, as observed in sec. 5.1.4. Hence, a deflection of the electronic trajectories by the ionic fields is more probable and a steeper decrease of the signal is recognized. On the contrary, a less ionized target promotes a less steep slope of the decreasing signal, as observed in the simulation concerning a neutral target in Fig. 2.18 (b). Therefore, the slope m_j can be used as a measure of the amount of ions within the droplet. A lower value of m_j indicates a larger number of ions while a higher value indicates a neutral target. Since higher orders are more affected by ionization due to the larger excursion time of the electrons, the average value of the slopes \bar{m}_j for the 21st to the 29th harmonic order is therefore calculated.

Figure 5.11 depicts \bar{m}_j (crosses) as a function of the intensity of the pump pulse. The value of mean slope for $I_{\text{pump}} = 1.7 \times 10^{14} \text{ W/cm}^2$ is close to the simulation for a neutral medium (green line)² and decreases with increasing intensity of the pump pulse. The simulation for an ionic medium is reached at $I_{\text{pump}} = 8 \times 10^{14} \text{ W/cm}^2$.

The comparison between the measurements and the simulation validates that the amount of ions

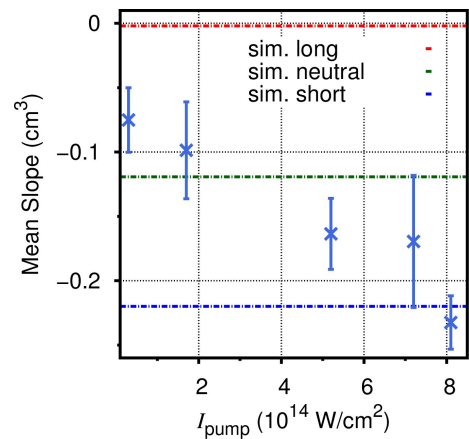


Figure 5.11: Averaged slope of the linear fit to the harmonic orders 21 to 29 versus intensity of the pump pulse (crosses). The error bars result from the averaging over the different orders. The figure also depicts the fits to the linear approximations of the simulated contribution of the short (blue line) and long trajectory (red line) for an ionized medium as well as the contribution of the short trajectory for a neutral medium (green line) by STRELKOV *et al.* [Str05].

²Note that the value of \bar{m}_j for the lowest intensity has to be regarded as a guidance level since $I_{\text{pump}} < I_{\text{LIB}}$ and the expansion process differs from LIB.

within the target depends on the intensity of the pump pulse. The slope of the linear decrease allows to state that the target is mainly composed of neutral particles for low intensities of the pump pulse, while ions are pre-dominant for high intensities. Hence, the slope \bar{m}_j allows to estimate the microscopic composition of the target by distinguishing whether a neutral or an ionic target is generated. According to this measure, the influence of ions within the target becomes significant for intensities of the pump pulse $I_{\text{pump}} > 5 \times 10^{14} \text{ W/cm}^2$ as the trajectories become distorted and the signal is decreased. Consequently, the target is mainly composed of neutral particles for lower intensities and the distortion of the emission process by ionic fields is negligible. For higher values of I_{pump} in this measurement, a perturbation by neutral particle can be excluded since the considered densities result in a larger mean inter-particle distance than the excursion length of the electronic trajectories. This is in agreement with the findings from sec. 4.5, where a neutral target was generated with $I_{\text{pump}} = 4.5 \times 10^{14} \text{ W/cm}^2$ and experiments validated a perturbation of the electronic trajectories by neutral particles at densities above $1 \times 10^{21} \text{ cm}^{-3}$.

Since the laser parameters are now determined for the generation of a target with an ion-dominated composition, the effects of an ionized target onto HHG can be studied in more detail. By applying a high intensity of the pump pulse, even the observation of the simulated splitting between the short and the long trajectory due to the deflection of the electrons by the ionic field is experimentally accessible, as described in the following.

5.2.2 Ionization-Induced Trajectory Splitting

In order to measure the ion-induced splitting of the harmonic signal between the short and the long trajectory from the simulation in Fig. 2.18 (b) [Str05], the contributions of the two quantum paths to the harmonic yield have to be recorded separately. This can be arranged by choosing the relative position between focus and target, as explained in sec. 4.1. A focal position before the droplet with respect to the propagation direction therein selects the short trajectory, while it is vice versa for the long trajectory. But for the comparison of the measurement with the simulation, it is necessary to determine the density-dependence of the harmonic yield. Hence, the signal is recorded for different delays and afterwards mapped onto the density (cf. sec. 4.4). Applying laser system B with $I_{\text{probe}} = 1.0 \times 10^{15} \text{ W/cm}^2$ and an intensity of the pump pulse of $I_{\text{pump}} = 6 \times 10^{14} \text{ W/cm}^2$ generates a medium ionized target, so that a splitting effect should be observable but less strong pronounced than in a highly ionized target, according to Fig. 5.11.

Figure 5.12 depicts the spectrally integrated signal of the (a) 17th and (b) 19th orders which are situated within the plateau region, as well as the 21st harmonic order from the cutoff region in Fig. 5.12 (c) as a function of the density for the short (blue) and long (red) trajectory. Figures 5.12 (a) and (b) feature a similar behaviour of the harmonic signal versus the density of the droplet. The contribution of the short trajectory remains at a constant level and decreases after a density of $5 \times 10^{20} \text{ cm}^{-3}$ is reached. The contribution assigned to the long trajectory however has a low signal for low densities. An increase is observed towards a density of $1.5 \times 10^{19} \text{ cm}^{-3}$ while the signal decreases for higher densities more steeply than the contribution of the short trajectory. The yields of both trajectories converge for the highest density.

Considering the density range between the position of the maximum signal and the highest value of ρ , a splitting of the trajectories is observed. It is in qualitative agreement with

the simulation from Fig. 2.18 (b) but less pronounced. This has been expected since a medium-ionized target is generated for the given intensity of the pump pulse which results in a less strong deflection of the electrons during the excursion in the continuum so that the difference between the two trajectories is less distinct. A further indication that the target is not completely ionized is that a signal of harmonic radiation is still detected for densities $\rho > 1 \times 10^{21} \text{ cm}^{-3}$, whereas the simulation predicts a decrease to zero for a fully ionized target. The simulation for a neutral target however in Fig. 2.18 (b) indicates a reduction of the harmonic yield by a factor of two, which is close to the measured values in Fig. 5.12. Hence, there are ions within the target but their number is limited. A splitting however is observed and can be attributed to the difference in the excursion time between the short and the long trajectory. But how can be verified that this effect is caused by ions and not by neutral particles due to a high density of the target as described in sec. 4.5.2?

Two observations allow to assign the difference between the two trajectories to an effect caused by ionization: First, the splitting is observed for densities $\rho < 1 \times 10^{21} \text{ cm}^{-3}$, which means the density of the target is within a regime where the mean inter-particle distance is large compared to the excursion distance of the electrons. Hence, a perturbation of the trajectories due to a high density can be excluded (cf. sec. 4.5.2). Second, the two signals converge for the highest density while an increasing difference should be observed if the splitting was induced by neutral particles since the long trajectory is affected more severely (cf. sec. 4.5.1). Furthermore, the splitting is exclusively detected in the simulation for an ionized target and not for a medium consisting of neutral particles. Thus, the difference in the density dependence of the trajectories can be attributed to an ion-induced deflection of electronic trajectories due to an ionized target.

Regarding the 21st harmonic order in Fig. 5.12 (c), the density-dependent development of the short and the long trajectory is almost equal and features in both cases a weak yield at the lowest density. The low contrast between the trajectories of the 21st order can be assigned to a position of the harmonic spectral line within the cutoff region. Hence, the radiation is emitted via a single trajectory with only

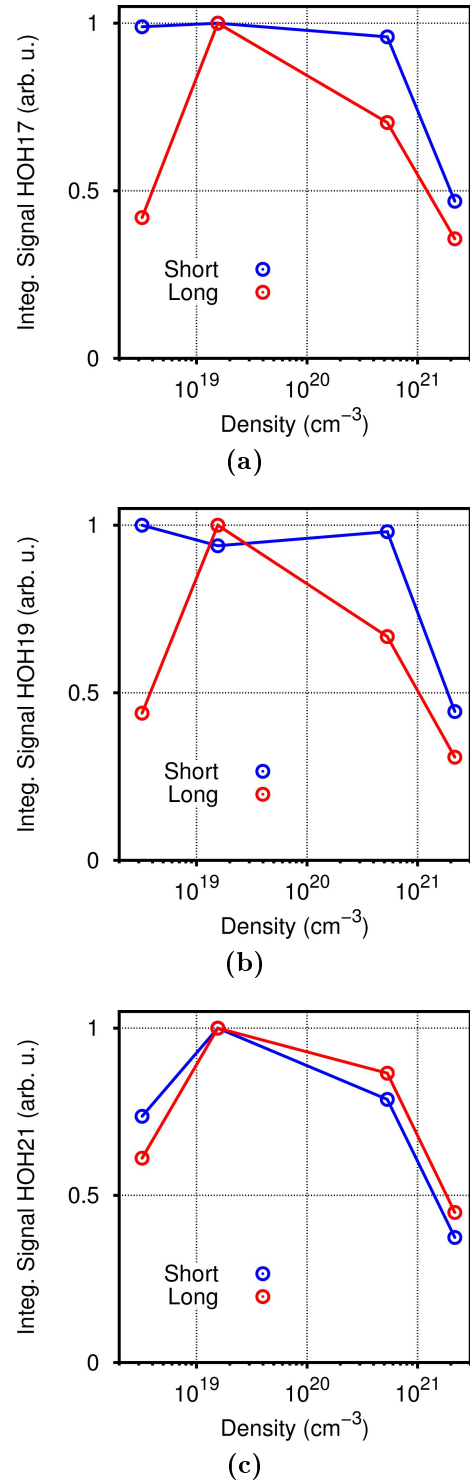


Figure 5.12: Integrated harmonic signal of the (a) 17th, (b) 19th and (c) 21st harmonic order versus density. The short (blue) and long (red) trajectories are selected via the focal position with $z > 0 \text{ mm}$ for the short trajectory and $z < 0 \text{ mm}$ for the long trajectory.

one excursion time and no splitting is possible. The signals are therefore supposed to be equal and an eventual difference in the yield is caused by noise. Moreover, the evolution of the harmonic yield is comparable with the measurements of the long trajectory in Figs. 5.12 (a) and (b), though the amplitude of the signals is slightly higher. In fact the amplitude is between the values of the short and the long trajectory from Fig. 5.12 (a) and (b). This is in agreement with the simulation for an ionized target from Fig. 2.18 (b), where the signal of the contribution of the trajectory assigned to the cutoff lies between the values of the short and long trajectories. This shift results from an excursion time of the cutoff-trajectory between the value of long and short trajectory (cf. Fig. 2.8). Since the excursion of the long trajectory within the continuum is larger, the induced phase mismatch by free electrons is higher and the signal decreases. The excursion time successively decreases for the cutoff and the short trajectory, resulting in less perturbed signals. Hence, the yield of the cutoff trajectory between the contribution from the short and the long trajectory.

So far the influence of an ionic target onto different quantum paths has been studied for high densities of the droplet. However, a discrepancy between the simulation and the measurement has been observed at lower densities. While the short trajectory develops in agreement with the simulation and remains at a constant level for low densities, a decrease of the signal of the long trajectory is observed. The decreasing signal is detected for densities $\rho < 1 \times 10^{19} \text{ cm}^{-3}$ and therefore is beyond optimum density conditions for HHG (cf. Fig. 4.20). Hence, the decrease of the signal is not caused by a lower number of emitters but it can be attributed to ionization induced by the probe pulse, which has also been observed in more diluted targets for the short trajectory in sec. 4.2.1.

The splitting of the trajectories additionally allows to interpret the inversion of the maxima in the harmonic yield assigned to the short and the long trajectory compared with measurements in a gas jet, which has been observed during the study of the focal position onto the PM conditions in sec. 4.1. Therein, a high intensity of the pump pulse has been applied. Large values of I_{pump} lead to an ion-dominated target so that the long trajectory was suppressed while the short was less affected. At lower densities, the free electrons were generated by the probe pulse and a suppression of the contribution of the long trajectory due to its longer excursion time in the continuum was observed again. As a result, the signals of the two quantum paths were inverted in comparison with the measurement in the gas jet.

In conclusion, ionization induced by the pump pulse can generate an ionic target. The amount of ions within the droplet depends on the intensity of the pump pulse and can be qualitatively identified via HHG. A splitting of the trajectory contributions induced by ionization has been experimentally observed, which is in agreement with the simulated results by STRELKOV *et al.* [Str05]. This splitting allowed to attribute the detected inversion of the conversion efficiency of the long and of the short trajectory during PM experiments in sec. 4.1 to an ionization-induced effect. Moreover, by tuning the intensity of the pump pulse, the composition of the target can be manipulated from a neutral towards an ion-dominated target. Changes on the atomic level between clusters, molecules and atoms remain undisclosed. However, only intensities of the pump pulse higher than I_{LIB} have been considered yet, although harmonic radiation has been detected for intensities of the pump pulse lower than the threshold intensity for LIB (cf. Fig. 5.8). Hence, energy of the fundamental radiation has to be deposited within the droplet and has to contribute to its expansion. The generation of high-order harmonic radiation for $I_{\text{pump}} < I_{\text{LIB}}$ is therefore studied in more detail in the following.

5.3 High-Order Harmonic Generation below the Threshold for Laser-Induced Breakdown

The interaction of the droplet with the pump pulse for intensities of $I_{\text{pump}} < I_{\text{LIB}}$ results in a different expansion mechanism than the LIB-model (cf. sec. 5.1.1). Since the intensity is insufficient to ignite a plasma, the amount of ionization within the target is low. The droplet is therefore mainly composed of neutral particles, such as water molecules and water clusters, and its expansion is less rapid (cf. sec. 5.2). Hence, the density is larger than calculated with the model from sec. 2.4.2, and the harmonic yield is strongly suppressed as depicted in Fig. 5.13. Therein, the signal of the harmonic radiation is shown as a function of the harmonic order and of the pump-probe time delay. Laser system B has been applied with $I_{\text{probe}} = 9.5 \times 10^{14} \text{ W/cm}^2$. Harmonic radiation is detected up to the 17th order, although the intensity of the pump pulse is with $I_{\text{pump}} = 3 \times 10^{13} \text{ W/cm}^2$ below the threshold intensity for LIB. The signal is weak and incoherent radiation is detected for higher orders than the 17th.

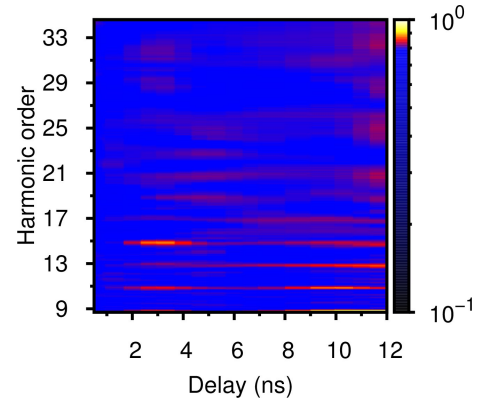


Figure 5.13: Harmonic yield versus order and delay for $I_{\text{pump}} = 3 \times 10^{13} \text{ W/cm}^2$ and $I_{\text{probe}} = 9.5 \times 10^{14} \text{ W/cm}^2$.

Since harmonic radiation is observed for $I_{\text{pump}} < I_{\text{LIB}}$, the thermodynamical phase of the droplet has to be changed as HHG is not possible in the liquid phase for the wavelength applied (cf. sec. 4.5.2). As observed in the determination of the estimate of ions within the target in sec. 5.2, information on the structure of the target on the atomic level is imprinted onto the harmonic yield. Various experiments have shown that this information can be retrieved [Kan05, Ita04, Smi09, Voz11, Ruf13]. However, a determination of the microscopic state of the droplet is non-trivial due to its complex dynamics on the considered time scales [Lin04]. However, a simplified consideration on the energy deposited within the target may assist in a first attempt to track information on the changes on the atomic level from the signal of the harmonic radiation.

Regarding two H_2O molecules forming a hydrogen bond, the binding energy between the two molecules is $E_{2\text{H}_2\text{O}} = 0.24 \text{ eV}$ [Nel04]. The droplet however consists of $N \approx 1.40 \times 10^{14}$ water molecules, which dynamically bond with an average number of 3.4 surrounding water

molecules at a time. This means, the water molecules form clusters inside the droplet. Assuming a homogeneous deposition of the energy within the target, the total amount of energy needed for breaking all hydrogen bonds in the liquid droplet is given by [Nel04]:

$$E_{\text{H-bonds}} = 0.06 \times 10^{15} \text{ eV} \approx 0.01 \text{ mJ}. \quad (5.1)$$

The energy of the pump pulse in Fig. 5.13 has been set to 0.05 mJ, which is sufficiently high for breaking all bonds (cf. Fig. 5.14).

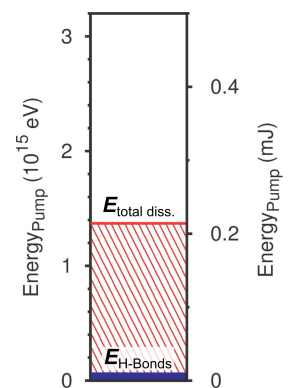


Figure 5.14: Threshold energies for breaking all bonds within the droplet (blue), as well as for total dissociation (red).

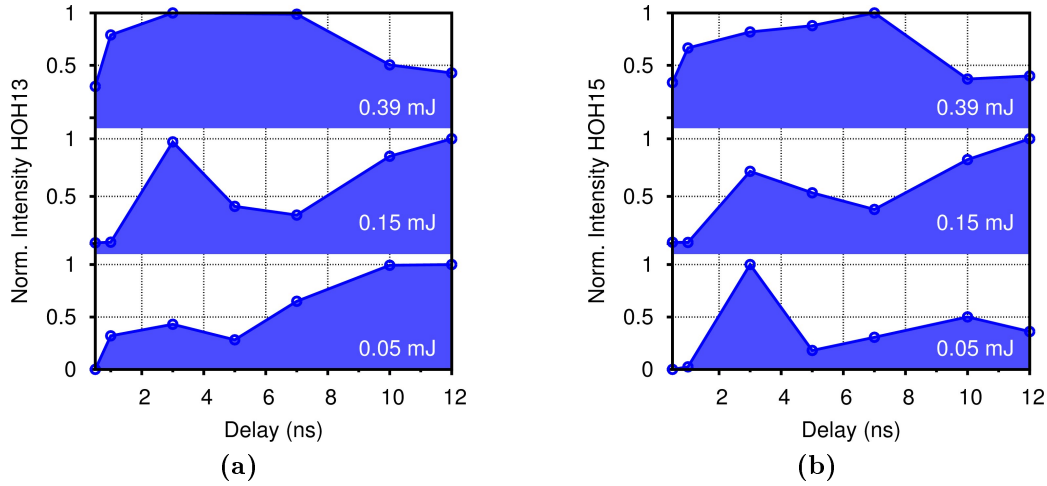


Figure 5.15: Outlines of Fig. 5.13. (a) 15th and (b) 17th harmonic order versus pump probe time delay for different energies of the pump pulse. The harmonic yield has been spectrally averaged around 5% of each harmonic order and normalized to the each maximum.

However, the absorption is less than in the case of the LIB-Model, where at maximum 50% of the energy are absorbed [Sch01]. Moreover, the radiation is not absorbed homogeneously throughout the target, resulting in a gradient in the composition of the droplet along the propagation axis of the pulse. The spherical shape of the droplet also acts as a lens and focuses the IR-Pulse into the interior of the target, where a larger fraction of the energy is absorbed, instead of ionizing at the surface [Cou03]. The intensity therefore may increase again above the threshold for LIB and ignite a plasma within the interior of the droplet. This leads to an expansion according to the LIB-Model, but less accelerated than in the measurements from the last section since it is surrounded by liquid water [Gei10]. For the applied pulse energy however, a total dissociation of all molecules within the target is not possible since this would require an energy of

$$E_{\text{diss.}} \approx 0.22 \text{ mJ} \quad (5.2)$$

for breaking all covalent bonds between the hydrogen atoms and the oxygen atoms (with $E_{\text{HO-H}} = 5.12 \text{ eV}$ and $E_{\text{O-H}} = 4.41 \text{ eV}$ [Nel04], cf. Fig. 5.14). Hence, the composition of the target is mainly a fragmentation into water molecules and clusters. Although this is a naive estimate, it may assist in the interpretation of the data in Fig. 5.13.

Figure 5.15 depicts the signal of the (a) 15th and (b) 17th harmonic order as a function of the pump probe time delay for the laser parameter given above, but different energies of the pump pulse. While the signal develops in agreement with the findings from sec. 5.1.4 for the highest energy (where $I_{\text{pump}} < I_{\text{LIB}}$), an oscillation of the harmonic yield as function of the delay is detected for the lower two energies. At an energy of the pump pulse of 0.15 mJ, the intensity of $1.7 \times 10^{14} \text{ W/cm}^2$ is slightly above I_{LIB} , while it is below the threshold for LIB for the lowest energy. The harmonic yield develops for both lower energies comparable as a function of time. The signal increases towards a maximum around 3 ns, which is followed by local minimum and an adjacent raise.

In order to interpret the oscillating signal, the considerations on the deposited energy are taken into account. For the lower two energies, the threshold for breaking all hydrogen bonds is reached in both cases. However, the energy needed for total dissociation is not

Element	Symbol	Ionization Energy (eV)
Xenon	Xe	12.1298
Hydrogen	H	13.60
Oxygen	O	13.62
Hydrogen Molecule	H ₂	15.43
Water Molecule	H ₂ O	12.61
Water Hexamer	(H ₂ O) ₆	8.75
Bulk Water	(H ₂ O) _n	6.5

Table 1: Ionization energies for different states of water and reference atoms for the HOMO and ground state, respectively [Bro11, SM12, NIS13].

exceeded (cf. Fig. 5.14). Reminding that the total absorption is below 50 %, at maximum 11 % and 33 % of E_{diss} , are reached for $E_{\text{pump}} = 0.05 \text{ mJ}$ and $E_{\text{pump}} = 0.15 \text{ mJ}$, respectively. Hence, the target is in both cases dominated by neutral particles, where larger fragments are expected for the lower energy of the pump pulse. As the delay is increased, the fragments of the droplet depart and conditions for HHG improve with the reduced density, as observed by the maximum of the yield in Fig. 5.15 (see also sec. 4.5.2). But a homogeneous expansion of the droplet does not explain the oscillating signal. Hence, dynamics between the fragments have to be considered. As the deposited energy of the fundamental pulse is transferred into kinetic energy of the particles within the droplet, energy is also transferred between adjacent particles via collisional processes. This leads to additional dissociation of the fragments of the droplet. The time scale for the dissociation of one water molecule from a water cluster is within the ps-range [Lee13]. Since the droplet is a macroscopic target, the transfer of the energy throughout the medium by collisional processes needs time. This allows to interpret the minimum in the harmonic signal around 6 ns as a time where a notable amount of dissociation is reached. Hence, the mean inter-particle distance is reduced and electronic trajectories are perturbed during HHG. As the delay is increased, the dilution advances and the mean inter-particle distance increases beyond the limit of the electronic excursion distance again. As a result, an increase in the harmonic yield is observed.

The first maximum of the signal of the harmonic radiation at 3 ns therefore can be interpreted as a HHG in a target consisting mainly of water molecules and clusters. This is also in agreement with the low yield throughout the delay range since less emitters lead to a reduced signal (cf. Fig. 5.13). Moreover, the HOHO remains at a constant level over a large delay range at the 17th order. The low HOHO might be related to the lower ionization potential in water clusters or bulk water, as depicted in table 1. However, the target features far more complex dynamics than observable in the above described measurement. Moreover, the expansion process at low energies of the pump pulse is highly inhomogeneous and the study of the harmonic yield as a function of the pump-probe time delay for different energies of the pump pulse has to be considered as a first attempt for revealing the dynamics of the droplet on the atomic level. Also the considerations on the absorbed energy within the target only permits a basic interpretation of the data, but a detailed analysis exceeds the limits of this thesis. However, HHG is the ideal tool to reveal the dynamics of the droplet on and below the ns time scale as it allows to probe the state of the target in-situ. Hence, further research is needed to identify the different microscopic states of the target.

5.4 Conclusions

The expansion processes is based on nonlinear absorption. For high intensities of the pump pulse, the laser induced breakdown model (LIB) describes the intensity-dependent expansion of the droplet (cf. sec. 5.1.1). Through measurements of the intensity-dependence of the harmonic yield as a function of the pump-pulse intensity, the model for the density calculation from sec. 2.4.2 was verified. However, significant differences in the optimum intensity parameters for HHG were observed, when comparing measurements with different pulse durations. These differences were assigned to a lower amount of ionization induced by the pump pulse, when using short pulses (cf. sec. 5.1.2).

Since the intensity threshold for LIB depends on the pulse duration, a scaling factor had to be implemented in the model for the calculation of the density which corrects the intensity for shorter pulses. In order to obtain this scaling factor, the yields of the emitted harmonic radiation were studied for two different pulse durations as a function of I_{pump} . As a result, a 2.1 times higher threshold intensity for LIB has been obtained for short pulses in comparison to long pulses. The resulting threshold intensity is in reasonable agreement with the theoretical value with a difference below 5%.

For high intensities of the pump pulse, a target mainly composed of ions can be generated. By mapping the harmonic yield to the density and comparing the experimental data with a simulation of the influence of an ionic medium onto HHG, a measure for the ionization within the droplet has been obtained. This measure indicates that the target is mainly composed of neutral particles for low intensities, while it is dominated by ions for high intensities of the pump pulse (cf. sec. 5.2.1).

Generating a highly-ionized target, a trajectory-dependent decrease of the harmonic signal was observed. While the long trajectory was strongly suppressed in an ionized medium, the short trajectory remained nearly unaffected. This difference in the decrease of the harmonic yield has been assigned to the varying excursion time of the trajectories within the continuum (cf. sec. 5.2.2).

Finally, first indications for changes of the medium composition on the atomic level from clusters and molecules towards a molecular or atomic target were detected by an oscillating signal of the high-order harmonic radiation as a function of the pump probe time delay (cf. sec. 5.3).

Chapter 6

Conclusion and Outlook

Conclusion

In this thesis, high-order harmonic generation (HHG) from liquid water molecules has been systematically studied. In order to identify the rich dynamics of the droplet on the macroscopic, as well as on the microscopic level, high-order harmonic spectroscopic methods have been applied through in-situ measurements. Three parameters have been identified which determine the state of the target by pump-probe experiments. The intensity of the pump pulse and the pump-probe time delay affect the expansion of the droplet and therefore determine its density evolution. Moreover, the duration of the applied laser pulses critically influences the conversion of the fundamental radiation into the XUV-spectral domain.

A first attempt to determine the thermodynamical phase of the droplet after being hit by the pump pulse is the study of the phase matching (PM) properties of the target by measuring the harmonic yield. Similar characteristics of the harmonic radiation to experiments in gas jets have been found at low target densities. These measurements allowed to deduce that the droplet performs a transition from the liquid phase into the gas phase after being hit by the pump pulse. Applying a model for the calculation of ion velocities allowed to estimate the time and intensity-dependent density evolution of the droplet. This model provided a calculated density which has been in reasonable agreement with the observed PM effects and has therefore been used to estimate the density evolution for the laser parameters applied in the experiments. However, some discrepancies were observed since a higher conversion efficiency has been detected for the short trajectory compared with the long trajectory. This is a reversed conversion efficiency for the trajectories in comparison with HHG in a gas jet. The inversion of the amplitudes of the harmonic yield has been attributed to a suppression of the long trajectory in an ionized medium due to its larger excursion time within the continuum, compared with the short trajectory.

In diluted targets with densities in the lower gaseous density regime, spectral broadening and spectral splitting of the harmonic orders have been observed and were assigned to transient phase matching effects. Since free electrons critically influence the harmonic yield, the dependence of the pulse duration onto HHG has been studied, where shorter pulses allow to observe harmonic radiation at higher densities of the target.

The saturation intensity of the harmonic yield has been determined, and optimized conditions for HHG have been identified by matching the intensity of the probe pulse to the density of the target.

For a detailed analysis of the influence of the target density onto the HHG process, the electronic excursion distances in the continuum were simulated. By comparing the maximum electronic excursion distance with the thermodynamical mean inter-particle distance, two theoretical limits were obtained for the maximum tolerable density upon which the target becomes too dense and a perturbation of the electronic trajectories by adjacent particles

sets in. The first limit acts as an orientation between a perturbation-dominated, high-density and the phase matching density regime, while no emission of harmonic radiation is possible for densities above the second boundary.

By mapping the pump-probe time delay to the density of the target, a scaling of the harmonic yield proportional to the mean inter-particle distance has been observed for densities above the first theoretical limit. In agreement with the simulations, no harmonic radiation was detected for densities higher than the second theoretical limit. This approach provides a methodology selecting a single trajectory which contributes to the signal of a fixed harmonic order by increasing the density of the target.

Finally, the conversion efficiency of HHG from liquid water droplets has been measured. It is below the values observed in experiments using rare gas targets, the experimental conditions however still allow an optimization which is promising to overcome the results obtained in gas targets.

After identifying the different effects that limit the harmonic yield, optimized conditions for HHG were chosen and the harmonic radiation has been used to study the transition of the droplet from the liquid into the gas phase through an in-situ measurement. For high intensities of the pump pulse, the laser-induced breakdown model (LIB) describes the intensity-dependent expansion of the droplet. Applying pulses with intensities in the LIB-regime, the model for the calculation of the density was verified. However, significant differences in the optimum intensity parameters for HHG were observed, when comparing measurements with different pulse durations. These differences were assigned to a lower amount of ionization induced by the pump pulse, when using short pulses.

Since the intensity threshold for LIB depends on the pulse duration, a scaling factor had to be implemented in the model for the calculation of the density evolution of the target which corrects the intensity for shorter pulses. It was obtained by comparing the harmonic yield for different durations of the driving pulse. As a result, a 2.1 times higher threshold intensity for LIB has been obtained for short pulses in comparison to long pulses. The resulting threshold intensity is with a difference below 5% in reasonable agreement with the theoretical value.

Measurements of the harmonic yield for high intensities of the pump pulse indicated that the target was mainly composed of ions. By mapping the harmonic yield to the density and comparing the experimental data with a simulation of HHG in an ionic medium, an estimate of the amount of ionization within the droplet was obtained. This measure indicated that the target has been mainly composed of neutral particles for low intensities of the pump pulse, while it was dominated by ions for high intensities.

Generating a highly-ionized target, a trajectory-dependent decrease of the harmonic signal as a function of the density of the target was observed. While the long trajectory was strongly suppressed in an ionized medium, the short trajectory remained nearly unaffected. This difference in the decrease of the harmonic yield has been assigned to the varying excursion time of the trajectories within the continuum.

Finally, first indications for changes in the composition of the generating medium on the atomic level from clusters and molecules towards a molecular or atomic target were detected in a neutral target by an oscillating signal of the high-order harmonic radiation as a function of the pump probe time delay.

Outlook

The liquid droplet allows to generate harmonic radiation in an unrivaled density range, reaching from liquid density to the density range of diluted gases. Moreover, the composition of the target can be manipulated on the atomic level, providing a molecular, atomic or ionic target in a single setup. However, the droplet source is not limited to water as a target, but many liquids could be applied, and a whole new area of materials would become available for the investigation of light-matter interaction with sub-fs time and sub-nm spatial resolution.

Since the work presented in this thesis is a first encounter to identify the dynamics of the droplet on the nanosecond time scale and beneath, a vast number of interesting studies arises which have the ability to extend measurements on the attosecond time scale to the liquid phase. A special interest lies upon the possibility of a precise determination of the microscopical state of the droplet for intensities of the pump pulse below the threshold intensity for LIB, since first indications for a target consisting of clusters have been observed. A possible method for revealing the dynamics on the atomic level would be a study of the harmonic yield as a function of the ellipticity of the driving field, as it is a common method to reveal dynamics on the atomic level [Dre12, Sha12a, Möl12]. Comparable measurements in rare gas clusters revealed a *cluster-to-itself* recombination, where the released electron recombines with a different atom within the cluster, resulting in a higher recombination probability compared with an atomic target [Ruf13]. This might be a way to exactly identify the changes on the atomic level. But also the two-color HHG technique is suitable, since it is highly sensitive on symmetries within the target [Dud06, Sha12b].

Moreover, a combination of the setup with intense few-cycle pulses, using techniques such as polarization gating [Tch03], filamentation [Ste12] or hollow-core fibers [Nis96, Nag11] seems promising, since ionization within the droplet is further reduced and the dynamics can be probed with minimum influence of the probe pulse. Few-cycle pulses would also be of advantage for an exact determination of the maximum tolerable density for HHG, since the number of trajectories contributing to the signal is low. This would allow to precisely retrieve the excursion distance of the electron, and directly leads to its time of ionization and provide a novel method for the measurement of attosecond dynamics in a macroscopic target.

The true benefits of the liquid droplet however lie within the possibility of adding non-liquid materials to the droplet [Cha06, Vas13]. This enables a study of HHG with large particles, while similarly extending the target material towards the edge of solid state physics. Figure 6.1 depicts preliminary results of HHG from water droplets doped with gold nano-spheres. The figure shows the intensity ratio between doped water droplets and pure water as a function of the harmonic order for different sizes of the nanoparticles. In comparison with pure water, an enhancement is observed which is most distinct for harmonic orders within the cutoff region and seems to depend on the size of the nanoparticles. The largest amplification of the harmonic yield of a factor of ~ 4 is detected for a size of 30 nm.

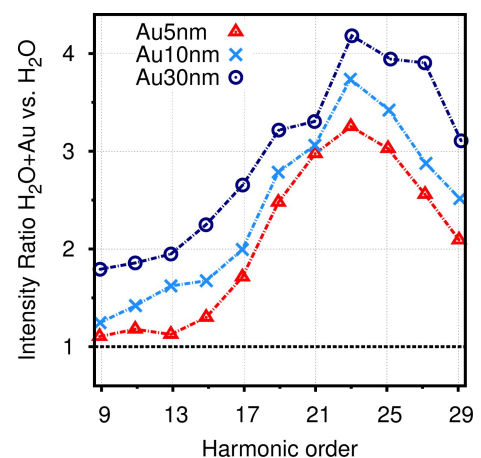


Figure 6.1: Intensity ratio between water droplets doped with gold nano-spheres and pure water as a function of the harmonic order for different sizes of the nanoparticles.

While enhancement of harmonic orders within the plateau region has been observed in experiments with nanoparticle containing plasma plumes [Gan08, Gan09, Gan10, Gan13], the amplification of the cutoff region is a novel feature. The reason might be related to the cluster-to-itself recombination [Ruf13], but also plasmonic enhancement effects might contribute the larger amount of radiation [Kim08, Pfu13], though it is discussed whether plasmonic resonances are able to contribute to HHG or not [Siv12]. In this case also a measurement of the ellipticity dependence of the harmonic yield might assist in revealing the reason for the enhanced harmonic yield.

In conclusion, there is a large number of possible experiments, which makes the liquid droplet as a target for HHG the most versatile source at present time and a promising tool to study light-matter interaction. High-density targets with of molecular dynamics become accessible as a source for attosecond physics experiments.

Bibliography

- [Ahn12a] D. Ahn, D. Jang, T. Choi, D. Kim, *Surface processing technique based on opto-hydrodynamic phenomena occurring in laser-induced breakdown of a microdroplet*, Applied Physics Letters **100**(10), 104104 (2012).
- [Ahn12b] D. Ahn, C. Seo, D. Kim, *Removal of metals and ceramics by combined effects of micro liquid jet and laser pulse*, Journal of Applied Physics **112**(12), 124916 (2012).
- [Aki92] Y. Akiyama, K. Midorikawa, Y. Matsunawa, Y. Nagata, M. Obara, H. Tashiro, K. Toyoda, *Generation of high-order harmonics using laser-produced rare-gas-like ions*, Phys. Rev. Lett. **69**, 2176–2179 (1992).
- [Alt96] C. Altucci, T. Starczewski, E. Mevel, C.-G. Wahlström, B. Carré, A. L’Huillier, *Influence of atomic density in high-order harmonic generation*, J. Opt. Soc. Am. B **13**(1), 148–156 (1996).
- [Alt99] C. Altucci, R. Bruzzese, C. de Lisio, M. Nisoli, S. Stagira, S. De Silvestri, O. Svelto, A. Boscolo, P. Ceccherini, L. Poletto, G. Tondello, P. Villoresi, *Tunable soft-x-ray radiation by high-order harmonic generation*, Phys. Rev. A **61**, 021801 (1999).
- [Amm86] M. Ammosov, N. B. Delone, K. P., *Tunnel ionization of complex atoms and of atomic ions in an alternating electromagnetic field*, Sov. Phys. JETP **64**, 1191–1194 (1986).
- [Bal97] P. Balcou, P. Salieres, A. L’Huillier, M. Lewenstein, *Generalized phase-matching conditions for high harmonics: The role of field-gradient forces*, Phys. Rev. A **55**(4), 3204–3210 (1997).
- [Bar11] A. Barty, C. Caleman, H. Chapman, *Self-terminating diffraction gates femtosecond X-ray nanocrystallography measurements*, Nature Photonics **6**, 35–40 (2011).
- [Bel98] M. Bellini, C. Lyngå, A. Tozzi, M. B. Gaarde, T. W. Hänsch, A. L’Huillier, C.-G. Wahlström, *Temporal Coherence of Ultrashort High-Order Harmonic Pulses*, Phys. Rev. Lett. **81**, 297–300 (1998).
- [Bel01] M. Bellini, C. Corsi, M. Gambino, *Neutral depletion and beam defocusing in harmonic generation from strongly ionized media*, Physical Review A **64**, 023411 (2001).
- [Ber98] M. Berglund, L. Rymell, *Cryogenic liquid-jet target for debris-free laser-plasma soft x-ray generation*, Review of Scientific Instruments **69**, 1998 (1998).
- [Ber12] J. Bertrand, H. Wörner, P. Salières, D. Villeneuve, P. Corkum, *Linked attosecond phase interferometry for molecular frame measurements*, Nature Physics **9**, 174–178 (2012).

- [Bou11] W. Boutu, T. Auguste, J. P. Caumes, H. Merdji, B. Carré, *Scaling of the generation of high-order harmonics in large gas media with focal length*, Phys. Rev. A **84**, 053819 (2011).
- [Bro11] M. Brown, T. Erickson, K. Frische, W. Roquemore, *Hot electron dominated rapid transverse ionization growth in liquid water*, Opt. Express **19**(13), 12241–12247 (2011).
- [Bru08] E. Brunetti, R. Issac, D. A. Jaroszynski, *Quantum path contribution to high-order harmonic spectra*, Phys. Lett. A **77**, 023422 (2008).
- [Cha06] H. Chapman, A. Barty, M. Bogan, S. Boutet, M. Frank, S. Hau-Riege, S. Marchesini, B. Woods, S. Bajt, W. Benner, R. London, E. Plonjes, R. Kuhlmann, M. Treusch, S. Dusterer, T. Tschentscher, J. Schneider, E. Spiller, T. Moller, C. Bostedt, M. Hoener, D. Shapiro, K. Hodgson, D. van der Spoel, F. Burmeister, M. Bergh, C. Caleman, G. Huldt, M. Seibert, F. Maia, R. Lee, A. Szoke, N. Timneanu, J. Hajdu, *Femtosecond diffractive imaging with a soft-X-ray free-electron laser*, Nature Physics **2**, 839–843 (2006).
- [Cha11] H. Chapman, et al., *Femtosecond X-ray protein nanocrystallography*, Nature **470**, 73 – 78 (2011).
- [Chi06] C. Chirila, M. Lein, *Influence of nuclear vibration on harmonic generation in molecules*, Journal of Physics B **39**, 437–444 (2006).
- [Chr96] I. P. Christov, J. Zhou, J. Peatross, A. Rundquist, M. M. Murnane, H. C. Kapteyn, *Nonadiabatic Effects in High-Harmonic Generation with Ultrashort Pulses*, Phys. Rev. Lett. **77**, 1743–1746 (1996).
- [Chr97] I. P. Christov, M. M. Murnane, H. C. Kapteyn, *High-Harmonic Generation of Attosecond Pulses in the “Single-Cycle” Regime*, Phys. Rev. Lett. **78**, 1251–1254 (1997).
- [Cia07] M. Ciappina, C. Chirila, M. Lein, *Influence of Coulomb continuum wave functions in the description of high-order harmonic generation with H_2^+* , Physical Review A **75**(043405), 1–4 (2007).
- [Con99] E. Constant, D. Garzella, E. Mével, C. Dorrer, C. Le Blanc, F. Salin, P. Agostini, *Optimizing High Harmonic Generation in Absorbing Gases: Model and Experiment*, Physical Review Letters **82**, 1668–1671 (1999).
- [Cor93] P. Corkum, *Plasma perspective on strong field multiphoton ionization*, Physical Review Letters **71**, 1994–1997 (1993).
- [Cor06] C. Corsi, A. Pirri, A. Sali, E. Tortora, M. Bellini, *Direct Interferometric Measurement of the Atomic Dipole Phase in High-Order Harmonic Generation*, Phys. Rev. Lett. **97**, 023901 (2006).
- [Cou03] F. Courvoisier, V. Boutou, C. Favre, S. Hill, J. Wolf, *Plasma formation dynamics within a water microdroplet on femtosecond time scales*, Optics Letters **28**(3), 206–208 (2003).

- [Dac09] H. Dachraoui, T. Auguste, A. Helmstedt, P. Bartz, M. Michelswirth, N. Mueller, W. Pfeiffer, P. Salieres, U. Heinzmann, *Interplay between absorption, dispersion and refraction in high-order harmonic generation*, Journal of Physics B **42**(17), 175402 (2009).
- [Dat07] H. Date, K. Sutherland, H. Hasegawa, M. Shimozuma, *Ionization and excitation collision prprocess of electrons in liquid water*, Nuclear Instruments & Methods in Physics Research B **265**, 515–520 (2007).
- [deL97] C. deLisio, C. Altucci, R. Bruzzese, F. DeFilippo, S. Solimeno, M. Bellini, P. Foggi, *Harmonic generation in an ionized gas medium with a 100-femtosecond, high repetition rate laser source at intermediate intensities*, Applied Phycs B: Lasers and Optics **64**(3), 323–330 (1997).
- [DiC09] A. DiChiara, E. Sistrunk, T. Miller, P. Agostini, L. DiMauro, *An investigation of harmonic generation in liquid media with mid-infrared laser*, Optics Express **17**, 20959 – 20965 (2009).
- [Dit96] T. Ditmire, E. T. Gumbrell, R. A. Smith, J. W. G. Tisch, D. D. Meyerhofer, M. H. R. Hutchinson, *Spatial Coherence Measurement of Soft X-Ray Radiation Produced by High Order Harmonic Generation*, Phys. Rev. Lett. **77**, 4756–4759 (1996).
- [Don96] T. D. Donnelly, T. Ditmire, K. Neuman, M. D. Perry, R. W. Falcone, *High-Order Harmonic Generation in Atom Clusters*, Phys. Rev. Lett. **76**, 2472–2475 (1996).
- [Dre12] I. Dreissigacker, M. Lein, *Quantitative theory for the lateral momentum distribution after strong-field ionization*, Chemical Physics **414**, 69–72 (2012).
- [Dud06] N. Dudovich, O. Smirnova, J. Levesque, Y. Mairesse, M. Ivanov, D. Villeneuve, P. Corkum, *Measuring and controlling the birth of attosecond XUV pulses*, nature physics **2**, 781–786 (2006).
- [Düs01] S. Düsterer, H. Schwoerer, W. Ziegler, C. Ziener, R. Sauerbrey, *Optimization of EUV radiation yield from laser-produced plasma*, Applied Physics B **73**, 693–698 (2001).
- [Düs02] S. Düsterer, *Laser-plasma interaction in droplet-targets*, Doktorarbeit, Friedrich Schiller Universität Jena (2002).
- [Egg97] Eggers, *Nonlinear dynamics and breakup of free-surface flows*, Review of Modern Physics **69**, 865 (1997).
- [Fal10] M. Falge, V. Engel, M. Lein, *Vibrational-state and isotope dependence of high-order hamonic generation in water molecules*, Phys. Rev. A **81**, 023412 (2010).
- [Far11] J. P. Farrell, S. Petretti, J. Förster, B. K. McFarland, L. S. Spector, Y. V. Vanne, P. Decleva, P. H. Bucksbaum, A. Saenz, M. Gühr, *Strong Field Ionization to Multiple Electronic States in Water*, Phys. Rev. Lett. **107**, 083001 (2011).
- [Fei04] M. Feit, A. Komashko, A. Rubenchik, *Ultra-short pulse laser interaction with transparent dielectrics*, Applied Physics A-Materials Scinece & Processing **79**(7), 1657–1661 (2004).

- [Fen97] Q. Feng, J. Moloney, A. Newell, E. Wright, K. Cook, P. Kennedy, D. Hammer, B. Rockwell, C. Thompson, *Theory and simulation on the threshold of water breakdown induced by focused ultrashort laser pulses*, IEEE Journal of Quantum Electronics **33**(2), 127–137 (1997).
- [Fer88] M. Ferray, A. L’Huillier, X. Li, L. Lompre, G. Mainfray, C. Manus, *Multiple-Harmonic Conversion of 1064-nm Radiation in Rare-Gases*, Journal of Physics B - Atomic Molecular and Optical Physics **21**(3), L31–L35 (1988).
- [Fle03] A. Flettner, T. Pfeiffer, D. Walter, C. Winterfeld, C. Spielmann, G. Gerber, *High-harmonic generation and plasma radiation from water microdroplets*, Applied Physics B **77**, 747–751 (2003).
- [Gaa02] M. Gaarde, K. Schafer, *Quantum path distributions for high-order harmonics in rare gas atoms*, Physical Review A: Atomic, Molecular, and Optical Physics **65**(3), 031406 (2002).
- [Gal12] L. Gallmann, C. Cirelli, U. Keller, *Attosecond Science: Recent Highlights and Future Trends*, Ann. Rev. Phys. Chem. **63**, 447–469 (2012).
- [Gan05] R. Ganeev, M. Suzuki, M. Baba, H. Kuroda, *Harmonic generation from chromium plasma*, Applied Physics Letters **86**(13) (2005).
- [Gan08] R. Ganeev, M. Suzuki, M. Baba, M. Ichihara, H. Kuroda, *High-order harmonic generation in Ag nanoparticle-containing plasma*, J. Phys. B: At. Mol. Opt. Phys. **41**, 045603 (2008).
- [Gan09] R. Ganeev, H. Singhal, P. Naik, I. Kulagin, P. Redkin, J. Chakera, M. Tayyab, R. Kahn, P. Gupta, *Enhancement of high-order harmonic generation using a two-color pump in plasma plumes*, Phys. Rev. A **80**, 033845 (2009).
- [Gan10] R. Ganeev, L. Elouga Bom, T. Ozaki, *Generation of higher harmonics of femtosecond radiation in clusters*, Optics and Spectroscopy **108**, 1022 – 1031 (2010).
- [Gan13] R. Ganeev, C. Hutchison, T. Witting, F. Frank, S. Weber, W. Okell, E. Fiordilino, D. Cricchio, F. Persico, A. Zaïr, J. Tisch, J. Marangos, *High-order harmonic generation in fullerenes using few- and multi-cycle pulses of different wavelengths*, Journal of the Optical Society of America B **30**, 7–12 (2013).
- [Gei10] Y. Geints, A. Kabanov, G. Matvienko, V. Oshlakov, A. Zemlyanov, S. Golik, O. Burkin, *Broadband emission spectrum dynamics of large water droplets exposed to intense ultrashort laser radiation*, Optics Letters **35**, 2717 – 2719 (2010).
- [Ghi11] S. Ghimire, A. D. DiChiara, E. Sistrunk, P. Agostini, L. F. DiMauro, D. A. Reis, *Observation of high-order harmonic generation in a bulk crystal*, Nature Physics **7**(2), 138–141 (2011).
- [Hae10] S. Haessler, J. Caillat, W. Boutu, C. Giovanetti-Teixeira, T. Ruchon, T. Auguste, Z. Diveki, P. Breger, A. Maquet, B. Carre, R. Taieb, P. Salieres, *Attosecond imaging of molecular electronic wavepackets*, Nature Physics **6**(3), 200–206 (2010).

- [Hae13] P. Haessler, V. Strelkov, L. Elouga Bom, M. Khokhlova, O. Gobert, J.-F. Hergott, F. Lepetit, M. Perdrix, T. Ozaki, P. Salières, *Phase distortions of attosecond pulses produced by resonance-enhanced high harmonic generation*, New Journal of Physics **15**, 013051 (2013).
- [Har12] A. Harth, M. Schultze, T. Lang, T. Binhammer, S. Rausch, U. Morgner, *Two-color pumped OPCPA system emitting spectra spanning 1.5 octaves from VIS to NIR*, Opt. Express **20**(3), 159062 (2012).
- [Hay01] N. Hay, R. de Nalda, T. Halfmann, K. Mendham, M. Mason, M. Castillejo, J. Marangos, *High-order harmonic generation from organic molecules in ultrashort pulses*, European Physical Journal D: Atomic, Molecular and Optical Physics **14**(2), 231–240 (2001).
- [Hen93] B. Henke, E. Gullikson, Davis J., *X-ray interactions: photoabsorption, scattering, transmission, and reflection at $E=50-30000$ eV, $Z=1-92$* , Atomic Data and Nuclear Data Tables **54**(2), 182–342 (1993).
- [Hen01] M. Hentschel, R. Kienberger, C. Spielmann, G. A. Reider, N. Milosevic, T. Brabec, P. Corkum, U. Heinzmann, M. Drescher, F. Krausz, *Attosecond metrology*, Nature **414**(6863), 509–513 (2001).
- [Her09] P. Hertz, *Über den gegenseitigen durchschnittlichen Abstand von Punkten, die mit bekannter mittlerer Dichte im Raume angeordnet sind*, Mathematische Annalen **67**, 387–398 (1909).
- [Her02] J.-F. Hergott, M. Kovacev, H. Merdji, C. Hubert, Y. Mairesse, E. Jean, P. Breger, P. Agostini, B. Carré, P. Salières, *Extreme-ultraviolet high-order harmonic pulses in the microjoule range*, Phys. Rev. A **66**, 021801 (2002).
- [Ita04] J. Itatani, J. Levesque, D. Zeidler, H. Niikura, H. Pepin, J. Kieffer, P. Corkum, D. Villeneuve, *Tomographic imaging of molecular orbitals*, Nature **432**, 867–871 (2004).
- [Kan95] C. Kan, C. E. Capjack, R. Rankin, N. H. Burnett, *Spectral and temporal structure in high harmonic emission from ionizing atomic gases*, Phys. Rev. A **52**(6), R4336 (1995).
- [Kan05] T. Kanai, S. Minemoto, H. Sakai, *Quantum interference during high-order harmonic generation from aligned molecules*, Nature **435**, 470–474 (2005).
- [Kel65] L. Keldysh, *Quantum transport equations for high electric fields*, Soviet Physics - JETP **20**, 1307–1314 (1965).
- [Kie04] R. Kienberger, E. Goulielmakis, M. Uiberacker, A. Baltuska, V. Yakovlev, F. Bammer, A. Scrinzi, T. Westerwalbesloh, U. Kleineberg, U. Heinzmann, M. Drescher, F. Krausz, *Atomic transient recorder*, Nature **427**(6977), 817–821 (2004).
- [Kim08] S. Kim, J. Jin, Y.-J. Kim, I.-Y. Park, Y. Kim, S.-W. Kim, *High-harmonic generation by resonant plasmon field enhancement*, Nature **453**, 757–760 (2008).
- [Klü12] K. Klünder, *Electron Wave Packet Dynamics on the Attosecond Time Scale*, Doktorarbeit, Lund University (2012).

- [Kou93] L. Kou, D. Labrie, P. Chylek, *Refractive indices of water and ice in the 0.65- to 2.5 μm spectral range*, Applied Optics **32**, 3531–3540 (1993).
- [Kra09] F. Krausz, M. Ivanov, *Attosecond Physics*, Reviews of Modern Physics **81**, 163–234 (2009).
- [Kre13] M. Kretschmar, C. Hernandez-Garcia, D. S. Steingrube, L. Plaja, U. Morgner, M. Kovačev, *Spatial contributions of electron trajectories to high-order-harmonic radiation originating from a semi-infinite gas cell*, Phys. Rev. A **88**, 013805 (2013).
- [Kru88] W. Kruer, *The Physics of Laser Plasma Interactions* (Addison-Wesley, New York, 1988).
- [Kur09] H. Kurz, *XUV-Spektroskopie mit einer Wasserquelle*, Diploma thesis, Diploma Thesis, Leibniz Universität Hannover (2009).
- [Kur12] H. G. Kurz, D. S. Steingrube, D. Ristau, M. Lein, U. Morgner, M. Kovačev, *Phase-matching aspects in high-order harmonic generation from liquid water droplets*, Research in Optical Sciences, OSA Technical Digest **HM3C.7** (2012).
- [Kur13] H. G. Kurz, D. S. Steingrube, D. Ristau, M. Lein, U. Morgner, M. Kovačev, *High-order-harmonic generation from dense water microdroplets*, Phys. Rev. A **87**, 063811 (2013).
- [LD00] L. Le Déroff, P. Salières, B. Carré, D. Joyeux, D. Phalippou, *Measurement of the degree of spatial coherence of high-order harmonics using a Fresnel-mirror interferometer*, Phys. Rev. A **61**, 043802 (2000).
- [Le08] A. Le, R. Della Picca, P. Fainstein, D. Telnov, M. Lein, C. Lin, *Theory of high-order harmonic generation from molecules by intense laser pulses*, Journal of Physics B **41**(081002), 1–4 (2008).
- [Lee13] H. Lee, K. Kim, *Dynamics and Structural Changes of Small Water Clusters on Ionization*, Journal of Computational Chemistry **34**, 1589–1597 (2013).
- [Lei03] M. Lein, P. Corso, J. Marangos, P. Knight, *Orientation dependence of high-order harmonic generation in molecules*, Phys. Rev. A **67**, 023819 (2003).
- [Lei07] M. Lein, *Molecular imaging using recolliding electrons*, Journal of Physics B: Atomic, Molecular and Optical Physics **40**, R137–R173 (2007).
- [Lew94] M. Lewenstein, P. Balcou, M. Ivanov, Yu. A. L’Huillier, P. Corkum, *Theory of high.harmonic generation by low-frequency laser fields*, Physical Review A **49**, 2117–2132 (1994).
- [L’H91] A. L’Huillier, K. Schafer, K. Kulander, *Theoretical Aspects of Intense Field Harmonic-Generation*, Journal of Physics B - Atomic Molecular and Optical Physics **24**, 3315–3341 (1991).
- [L’H93a] A. L’Huillier, Balcou, *High-order harmonic generation in rare gases with a 1-ps 1053-nm laser*, Physical Review Letters **70**, 774–777 (1993).

- [L'H93b] A. L'Huillier, M. Lewenstein, P. Salières, P. Balcou, M. Y. Ivanov, J. Larsson, C. G. Wahlström, *High-order Harmonic-generation cutoff*, Phys. Rev. A **48**, R3433–R3436 (1993).
- [Li08] W. Li, X. Zhou, R. Lock, S. Patchkivskij, A. Stolow, K. H.C., M. Murnane, *Time-Resolved Dynamics in N₂O₄ Probed using High Harmonic Generation*, Science **322**, 1207 (2008).
- [Lin04] A. Lindinger, J. Hagen, L. Socaciu, T. Bernhardt, L. Woste, D. Duft, T. Leisner, *Time-resolved explosion dynamics of H₂O droplets induced by femtosecond laser pulses*, Applied Optics **43**(27), 5263–5269 (2004).
- [Lyn99] C. Lyngå, M. B. Gaarde, C. Delfin, M. Bellini, T. W. Hänsch, A. L' Huillier, C.-G. Wahlström, *Temporal coherence of high-order harmonics*, Phys. Rev. A **60**, 4823–4830 (1999).
- [Mac93] J. J. Macklin, J. D. Kmetec, C. L. Gordon, *High-order harmonic generation using intense femtosecond pulses*, Phys. Rev. Lett. **70**, 766–769 (1993).
- [Mai60] T. Maiman, *Stimulated Optical Radiation in Ruby*, Nature **187**, 493–494 (1960).
- [Mai03] Y. Mairesse, A. de Bohan, L. Frasinski, H. Merdji, L. Dinu, P. Monchicourt, P. Breger, M. Kovacev, R. Taieb, H. Carre, B. Muller, P. Agostini, P. Salieres, *Attosecond synchronization of high-harmonic soft x-rays*, Science **302**(5650), 1540–1543 (2003).
- [Mai08] Y. Mairesse, J. Levesque, N. Dudovich, P. B. Corkum, D. M. Villeneuve, *High harmonic generation from aligned molecules - amplitude and polarization*, Journal of Modern Optics **55**(16), 2591 – 2602 (2008).
- [McF08] B. K. McFarland, J. Farrell, P. H. Bucksbaum, M. Gühr, *High Harmonic Generation from Multiple Orbitals in N₂*, Science **322**, 1232–1235 (2008).
- [McP87] A. McPherson, G. Gibson, H. Jara, U. Johann, T. Luk, I. McIntyre, K. Boyer, C. Rhodes, *Studies of Multiphoton Production of Vacuum Ultraviolet-Radiation in the Rare-Gases*, Journal of the Optical Society of America B **4**(4), 595–601 (1987).
- [Möl12] M. Möller, Y. Cheng, S. D. Khan, B. Zhao, K. Zhao, M. Chini, G. G. Paulus, Z. Chang, *Dependence of high-order-harmonic-generation yield on driving-laser ellipticity*, Phys. Rev. A **86**, 011401 (2012).
- [Mor07] U. Morgner, *Nichtlineare Optik* (Vorlesungsskript, 2007).
- [Muy78] E. Muybridge, *The Horse in Motion*, Library of the Congress (1878).
- [Nag11] T. Nagy, V. Pervak, P. Simon, *Optimal pulse compression in long hollow core fibers*, Optics Letters **36**, 224422–03 (2011).
- [Nel04] D. Nelson, M. Cox, *Lehninger - Principles of Biochemistry* (W. H. Freeman, 2004), 4. Auflage.
- [Nis96] M. Nisoli, S. De Silvestri, O. Svelto, *Generation of high energy 10fs pulses by a new pulse compression technique*, Applied Physical Letters **68**, 2793–2795 (1996).

- [NIS13] NIST, *Ground levels and ionization energies for the neutral atoms* (Technical Report, National Institute of Standards and Metrology, online, 1933 - 2013).
- [Noa99] J. Noack, A. Vogel, *Laser-Induced Plasma Formation in Water at Nanosecond to Femtosecond Time Scales: Calculation of Thresholds, Absorption Coefficients, and Energy Density*, IEEE Journal of Quantum Electronics **35**, 0018–9197/99 (1999).
- [Pap01] N. Papadogiannis, C. Kalpouzos, E. Goulielmakis, G. Nersisyan, D. Charalambidis, F. Auge, F. Weihe, P. Balcou, *Kilohertz extreme-ultraviolet light source based on femtosecond high-order harmonic generation from noble gases*, Applied Physics B - Lasers and Optics **73**(7), 687–692 (2001).
- [Pau01] P. M. Paul, E. S. Toma, P. Breger, G. Mullot, F. Augé, P. Balcou, H. G. Muller, P. Agostini, *Observation of a Train of Attosecond Pulses from High Harmonic Generation*, Science **292**(5522), 1689–1692 (2001).
- [Per66] A. M. Perelomov, V. S. Popov, M. V. Terent'ev, *Ionization of Atoms in an Alternating Electric Field*, Sov. Phys. JETP **23**, 924 (1966).
- [Pfu13] N. Pfullmann, C. Waltermann, M. Noack, S. Rausch, T. Nagy, C. Reinhardt, M. Kovacev, V. Knittel, R. Bratschitsch, D. Akemeier, A. Hütten, A. Leitenstorfer, U. Morgner, *Bow-tie nano-antenna assisted generation of extreme ultraviolet radiation*, New Journal of Physics **15**, 093027 (2013).
- [Pri00] E. Priori, G. Cerullo, M. Nisoli, S. Stagira, S. De Silvestri, P. Villoresi, L. Polletto, P. Ceccherini, C. Altucci, R. Bruzzese, C. de Lisio, *Nonadiabatic three-dimensional model of high-order harmonic generation in the few-optical-cycle regime*, Phys. Rev. A **61**, 063801 (2000).
- [Pue70] H. Puell, *Heating of Laser Produced Plasmas Generated at Plane Solid Targets I. Theory*, Zeitschrift für Naturforschung Part A-Astrophysik, Physik und Physikalische Chemie **A 25**(12), 1807–& (1970).
- [Qué06] F. Quéré, C. Thaury, P. Monot, S. Dobosz, P. Martin, J.-P. Geindre, P. Audebert, *Coherent Wake Emission of High-Order Harmonics from Overdense Plasmas*, Phys. Rev. Lett. **96**, 125004 (2006).
- [Ray79] L. Rayleigh, *The capillary phenomena of liquid jet*, Proc. Roy Soc., London **29**, 71–79 (1879).
- [Ruf13] H. Ruf, C. Handschin, E. Cireasa, N. Thire, A. Ferre, S. Petit, D. Descamps, E. Mevel, E. Constant, V. Blanchet, B. Fabre, Y. Mairesse, *Inhomogeneous High Harmonic Generation in Krypton Clusters*, Phys. Rev. Lett. **110**, 084902 (2013).
- [Sak95] H. Sakai, K. Miyazaki, *High-Order Harmonic Generation in Nitrogen Molecules with Subpicosecond Visible Dye-Laser Pulses*, Applied Physics B - Lasers and Optics **61**(5), 493–498 (1995).
- [Sal95] P. Salières, A. L'Huillier, M. Lewenstein, *Coherence Control of High-Order Harmonics*, Phys. Rev. Lett. **74**, 3776–3779 (1995).
- [Sal97] P. Salières, A. L'Huillier, P. Antoine, M. Lewenstein, *Study of spatial and temporal coherence of high order harmonics*, arXive (1997).

- [Sal98] P. Salières, P. Antoine, A. de Bohan, M. Lewenstein, *Temporal and Spectral Tailoring of High-Order Harmonics*, Physical Review Letters **81**(25), 5544–5547 (1998).
- [Sch01] C. Schaffer, *Interaction of Femtosecond Laser Pulses with Transparent Materials*, Doktorarbeit, Harvard University (2001).
- [Sch02] C. Schaffer, N. Nishimura, E. Glezer, A. Kim, E. Mazur, *Dynamics of femtosecond laser-induced breakdown in water from femtoseconds to microseconds*, Optics Express **10**(3), 196–203 (2002).
- [Sch10] M. Schultze, M. Fiess, N. Karpowicz, J. Gagnon, M. Korbman, M. Hofstetter, S. Neppl, A. L. Cavalieri, Y. Komninos, T. Mercouris, C. A. Nicolaides, R. Pazourek, S. Nagele, J. Feist, J. Burgdoerfer, A. M. Azzeer, R. Ernstorfer, R. Kienberger, U. Kleineberg, E. Goulielmakis, F. Krausz, V. S. Yakovlev, *Delay in Photoemission*, Science **328**(5986), 1658–1662 (2010).
- [Sha02] B. Shan, X.-M. Tong, Z. Zhao, Z. Chang, C. D. Lin, *High-order harmonic cutoff extension of the O₂ molecule due to ionization suppression*, Phys. Rev. A **66**, 061401 (2002).
- [Sha12a] D. Shafir, B. Fabre, J. Higuete, H. Soifer, M. Dagan, D. Descamps, E. Mével, S. Petit, H. J. Wörner, B. Pons, N. Dudovich, Y. Mairesse, *Role of the Ionic Potential in High Harmonic Generation*, Phys. Rev. Lett. **108**, 203001 (2012).
- [Sha12b] D. Shafir, H. Soifer, B. Bruner, M. Dagan, Y. Mairesse, S. Patchkovskii, M. Ivanov, O. Smirnova, N. Dudovich, *Resolving the time when an electron exits a tunnelling barrier*, Nature **485**, 343–346 (2012).
- [Siv12] M. Sivi, M. Duwe, B. Abel, C. Ropers, *Nanostructure-enhanced atomic line emission*, Nature **485**, E1–E3 (2012).
- [SM12] J. Segarra-Martí, M. Merchán, D. Roca-Sanjuán, *Ab initio calculation of the ionization potential of water clusters (H₂O)_n (n=2-6)*, The Journal of Chemical Physics **136**, 244306 (2012).
- [Smi09] O. Smirnova, Y. Mairesse, S. Patchkovskii, N. Dudovich, D. Villeneuve, P. Corkum, M. Ivanov, *High harmonic interferometry of multi-electron dynamics in molecules*, Nature **460**, 972 – 977 (2009).
- [Spi13] C. Spielmann, Private Communications (2013).
- [ST06] C. Sarpe-Tudoran, A. Assion, M. Wollenhaupt, M. Winter, T. Baumert, *Plasma dynamics of water breakdown at a water surface induced by femtosecond laser pulses*, Applied Physical Letters **88**(26) (2006).
- [Sta03] H. Stapelfeldt, T. Seidemann, *Colloquium: Aligning molecules with strong laser pulses*, Reviews of Modern Physics **75**, 543–557 (2003).
- [Ste09] D. Steingrube, T. Vockerodt, E. Schulz, U. Morgner, M. Kovacev, *Phase-matching of high-order harmonics in a semi-infinite gas cell*, Phys. Rev. A **80**, 043819 (2009).
- [Ste11] D. Steingrube, *High-order harmonic generation with ultra-short pulses from filamentation*, Doktorarbeit, Leibniz Universität Hannover (2011).

- [Ste12] D. Steingrube, M. Kretschmar, D. Hoff, E. Schulz, T. Binhammer, G. Hansinger, P. Paulus, U. Morgner, M. Kovacev, *Sub-1.5-cycle pulses from a single filament*, *Optics Express* **20**, 24049–24058 (2012).
- [Str85] D. Strickland, G. Mourou, *Compression of amplified chirped optical pulses*, *Opt. Commun.* **55**, 447–449 (1985).
- [Str05] V. Strelkov, V. Platonenko, A. Becker, *High-harmonic generation in a dense medium*, *Phys. Rev. A* **71**(3), 053808–1–053808–8 (2005).
- [Tak02] E. Takahashi, Y. Nabekawa, K. Midorikawa, *Generation of 10 μ J coherent extreme-ultraviolet light by use of high-order harmonics*, *Opt. Lett.* **27**(21), 1920–1922 (2002).
- [Tak07] E. J. Takahashi, T. Kanai, K. L. Ishikawa, Y. Nabekawa, K. Midorikawa, *Dramatic Enhancement of High-Order Harmonic Generation*, *Physical Review Letters* **99**, 053904 (2007).
- [Tch03] O. Tcherbakoff, E. Mevel, D. Descamps, J. Plumridge, E. Constant, *Time-gated high-order harmonic generation*, *Phys. Rev. A* **68**, 043804 (2003).
- [Teu09] U. Teubner, P. Gibbon, *High-harmonics from laser-irradiated plasma surfaces*, *Review of Modern Physics* **81**, 445–479 (2009).
- [Tor07] R. Torres, N. Kajumba, J. G. Underwood, J. Robinson, S. Baker, J. Tisch, R. de Nalda, W. Bryan, R. Velotta, C. Altucci, I. Turcu, J. Marangos, *Probing Orbital Structure of Polyatomic Molecules by High-Order Harmonic Generation*, *Physical Review Letters* **98**, 203007 (2007).
- [Tos03] V. Tosa, E. Takahashi, Y. Nabekawa, K. Midorikawa, *Generation of high-order harmonics in a self-guided beam*, *Phys. Rev. A* **67**, 063817 (2003).
- [Tre97] R. Trebino, K. DeLong, D. Fittinghoff, J. Sweetser, M. Krumbügel, B. Richman, *Measuring ultrashort laser pulses in the time-frequency domain using frequency-resolved optical gating*, *Rev. Sci. Instrum.* **68**(9), 3277–3295 (1997).
- [Vas13] P. Vasa, M. Singh, R. Bernard, A. K. Dharmadhikari, J. Dharmadhikari, D. Mathur, *Supercontinuum generation in water doped with gold nanoparticles*, *Applied Physics Letters* **103**, 111109 (2013).
- [Vel01] R. Velotta, N. Hay, M. Mason, M. Castillejo, J. Marangos, *High-order Harmonic Generation in Aligned Molecules*, *Physical Review Letters* **87**, 183901 (2001).
- [Voc12] T. Vockerodt, *Generation of harmonic radiation in self-guided filaments in gaseous media*, *Doktorarbeit, Leibniz Universität Hannover* (2012).
- [Voz11] C. Vozzi, M. Negro, F. Calegari, G. Sansone, M. Nisoli, S. De Silvestri, S. Stagira, *Generalized molecular orbital tomography*, *Nature Physics* **7**(10), 822–826 (2011).
- [Wah93] C.-G. Wahlström, J. Larsson, A. Persson, T. Starczewski, S. Svanberg, P. Salières, P. Balcou, A. L’Huillier, *High-order harmonic generation in rare gases with an intense short-pulse laser*, *Phys. Rev. A* **48**, 4709–4720 (1993).

- [Wan00] Y. Wang, Y. Liu, X. Yang, Z. Xu, *Spectral splitting in high-order harmonic generation*, Phys. Rev. A **62**, 063806 (2000).
- [Wea80] Weast, *CRC Handbook of Chemistry and Physics* (CRC Press, 1980).
- [Web31] C. Weber, *Zum Zerfall eines Flüssigkeitsstrahls*, Journal of Applied Mathematics and Mechanics **11**, 136–154 (1931).
- [Whe12] J. Wheeler, A. Borot, S. Monchocé, H. Vincenti, A. Ricci, A. Malvache, R. Lopez-Martens, F. Quéré, *Attosecond lighthouses from plasma mirrors*, Nature Photonics **6**, 829–833 (2012).
- [Win08] C. Winterfeld, C. Spielmann, G. Gerber, *Colloquium: Optimal control of high-harmonic generation*, Review of Modern Physics **80**, 117–140 (2008).
- [Wir11] A. Wirth, M. Hassan, I. GrguraÅi, J. Gagnon, A. Moulet, T. T. Luu, S. Pabst, R. Santra, Z. A. Alahmed, A. M. Azzeer, V. S. Yakovlev, V. Pervak, F. Krausz, E. Goulielmakis, *Synthesized Light Transients*, Science **334**(195), 195–200 (2011).
- [Won10] M. C. H. Wong, J.-P. Brichta, V. R. Bhardwaj, *High-harmonic generation in H₂O*, Optics Letters **35**, 1947–1949 (2010).
- [Won11] M. C. H. Wong, J.-P. Brichta, M. Spanner, S. Patchkovskii, V. R. Bhardwaj, *High-harmonic spectroscopy of molecular isomers*, Phys. Rev. A **84**, 051403 (2011).
- [Wör10a] H. Wörner, D. Bertrand, J.B. Kartashov, P. Corkum, D. Villeneuve, *Following a chemical reaction using high-harmonic interferometry*, Nature **466**, 09185 (2010).
- [Wör10b] H. Wörner, J. Bertrand, P. Hockett, P. Corkum, D. Villeneuve, *Controlling the Interference of Multiple Orbitals in High-Harmonic Generation*, Physical Review Letters **104**, 233904 (2010).
- [Wör11] H. Wörner, J. Bertrand, B. Fabre, J. Higuët, H. Ruf, A. Dubrouil, S. Patchkovskij, M. Spanner, Y. Mairesse, V. Blanchet, E. Mevel, E. Constant, P. Corkum, D. Villeneuve, *Conical Intersection Dynamics in NO₂ Probed by Homodyne High-Harmonic Spectroscopy*, Science **334**, 103–107 (2011).
- [Zha11] S.-F. Zhao, C. Jin, R. Lucchese, A.-T. Le, C. Lin, *High-order-harmonic generation using gas-phase H₂O molecules*, Phys. Rev. A **83**, 033409 (2011).
- [Zha12] K. Zhao, Q. Zhang, M. Chini, Y. Wu, X. Wang, Z. Chang, *Tailoring a 67 attosecond pulse through advantageous phase-mismatch*, Optics Letters **37**, 3891–3893 (2012).
- [Zho00] F. Zhong, J. Deng, X. Hu, Z. Li, Z. Zhang, Z. Xu, *The effect of ionization of gases on the high harmonic splitting*, Phys. Lett. A **278**, 35–43 (2000).

List of Figures

2.1	Ionization mechanisms for different intensities. All figures show the atomic potential (black), the electron wave function (blue), the external electric field (solid red) and the ionization threshold (dashed black). The different ionization mechanisms are (a) MPI, (b) ATI, (c) TI and (d) OTBI. See text for details.	6
2.2	Schematic of the laser-droplet interaction. (a) depicts the incident pump pulse (solid red line) and its focusing geometry (dashed red line). The droplet is shown (blue), as well as contained water molecules. (b) shows the expanding droplet after being hit by the pump pulse. Since more energy of the laser pulse is absorbed at the side facing the incident pump pulse, the formation of a density gradient along the propagation direction of the laser is likely (black).	9
2.3	Temporal evolution of the density of the droplet after being hit by a laser pulse with (a) a fixed degree of ionization $Z = 1$ but different intensities and (b) for different degrees of ionization Z but fixed intensity of $5.0 \times 10^{14} \text{ W/cm}^2$	11
2.4	Schematics of possible spatio-temporal dynamics of the droplet after being hit by the pump pulse. (a) depicts the expanding volume of the droplet (blue) as a molecular gas. The focusing geometry (dashed red line) and water molecules (oxygen as red circles and hydrogen as small blue circles) are shown. (b) Dissociation into fragments of water molecules. The target decays into an atomic gas. (c) Cluster development and fragmentation of the target into water clusters of different sizes. (d) Plasma ignition with ions (red pluses), electrons (black minuses) and neutral particles.	13
2.5	Measured spectrum of high-order harmonic radiation from water droplets generated with intense laser pulses. The three regimes are indicated by the numbers and divided by the dashed lines. (I) describes the decrease in intensity according to perturbation theory, (II) the plateau region and (III) the cutoff.	14
2.6	Three-step model according to CORKUM. The figures (a) - (c) depict the atomic potential (black), the electronic wave function (blue) and the incident laser field (red). The ionization threshold is indicated by the dashed line. (a) shows the tunnel ionization process. (b) acceleration of the electron in the laser field. (c) Recombination of electron and parent ion with emission of one XUV photon. . . .	15
2.7	Electron trajectories (blue) for different ionization times as a function of time and the electric field (red) with $I = 1 \times 10^{14} \text{ W/cm}^2$ at a central wavelength of 780 nm.	15
2.8	(a) Kinetic energy of electrons (blue) and excursion time (red) as function of the ionization time. (b) Kinetic energy of electrons (blue) and excursion time (red) as function of the recombination time.	16
2.9	Calculated intensity of the 45 th harmonic order in a single neon atom as a function of the driving intensity by LEWENSTEIN <i>et al.</i> [Lew94]. The green line indicates the intensity needed for the harmonic to transit from the cutoff into the plateau region. The red line indicates the saturation intensity.	18

2.10	From microscopic to macroscopic response. The incident laser pulse (red) is focused (dashed red) onto the droplet (light blue). The single particles emit harmonic radiation of the fundamental frequency. The coherent sum of all emitted XUV photons forms the XUV pulse (dark blue).	20
2.11	Calculated phase contributions for the 27 th harmonic order at an intensity of 5×10^{15} W/cm ² . A phase slope factor of $\alpha = 24 \times 10^{15}$ cm ² /W is estimated, so that the harmonic is situated within the plateau [Gaa02]. (a) On-axis phase contributions as function of the propagation direction z for a fixed value of the radial coordinate r . (b) Off-axis phase contributions as function of z	21
2.12	Scheme of the atomic wave vector in the focal region (blue). Lines of equal intensity are shown in red.	21
2.13	Scheme of the geometric wave vector in the focal region (blue). Wave fronts of the fundamental radiation are shown in red.	22
2.14	Sum of figs. 2.12 and 2.13 at different propagation positions. Depicted are the wave vector of the q^{th} HOH \mathbf{k}_q (solid blue), q times the geometric wave vector \mathbf{k}_{geo} (red) and the atomic wave vector \mathbf{k}_{at} (dashed blue). (a) on axis before the focus, (b) at the focus, (c) on axis after the focus and (d) off-axis before the focus.	22
2.15	Conversion efficiency of the 45 th harmonic order in a neon gas jet as function of the position of the medium z from SALIÈRES <i>et al.</i> [Sal95]. The inset shows the radial dependence of the CE as function of z . For positions $z < 0$, the focus is positioned after the medium with respect to the propagation direction, and vice versa.	24
2.16	Simulation of the HHG process by ZHONG <i>et al.</i> [Zho00]. (a) Intensity of the fundamental pulse (red), the intensity of the 19 th harmonic order (blue) and the ionization rate (black) as function of time. (b) Intensity of the harmonic radiation versus photon energy for different gas pressures.	24
2.17	Excursion of the electron in the presence of a surrounding medium. (a) atomic medium and (b) ionic medium.	25
2.18	Emitted energy of harmonic radiation as function of the medium density simulated by STRELKOV <i>et al.</i> [Str05]. Short (blue) and long trajectory (red) as well as the quantum path leading to the cutoff (black) for (a) an atomic medium and (b) an ionic medium	26
2.19	Transition density for short (blue) and long (red) trajectory as function of the intensity of the laser pulse simulated by STRELKOV <i>et al.</i> [Str05].	27
2.20	Schematic of attosecond pulse generation with few-cycle pulses (red). (a) Multi-cycle pulse. (b) and (c) few-cycle pulses. Different values of ϕ_{CEO} lead to varying number of ionization events (ionization potential in dashed black). (a) $\phi_{CEO} = \frac{\pi}{2}$ results in a sine wave form with two ionization events. (b) $\phi_{CEO} = 0$ leads to a cosine wave form with a single ionization event.	27
2.21	Schematic of isolated attosecond pulse generation with few-cycle laser pulses. The HOH spectrum develops a continuum in the cutoff region (blue). The continuous part of the spectrum is then filtered (red) and results in an isolated attosecond pulse.	28
2.22	Schemes of the semi-infinite gas cell (a) and the gas jet setup (b). The incident laser pulse (red) is focused (dashed-red) into the interaction region and XUV-radiation is emitted (blue).	28
2.23	Schematic of the generation of a determined series of liquid droplets.	29
3.1	Optical setup for the generation of the pump and the probe pulse using a Mach-Zehnder interferometer. Two CPA laser systems were used: (a) modified Alpha 10C/CS by Thales and (b) KMLabs Dragon (see text for details).	32

3.2	Experimental overview for HHG from liquid droplets. The capillary nozzle for droplet generation can be replaced by a larger nozzle to perform HHG in gas jets (see text for details).	33
3.3	Setup of the liquid droplet source.	33
3.4	Measurement by FLETTNER <i>et al.</i> [Fle03]. Harmonic yield from water droplets as function of the harmonic order and the pump-probe time delay.	35
3.5	Spectrum of HHG from water droplets measured with laser system <i>A</i> . The intensity of the pump was set to $I_{\text{pump}} = 7.0 \times 10^{14} \text{ W/cm}^2$ and of the probe pulse $I_{\text{probe}} = 3.7 \times 10^{14} \text{ W/cm}^2$ at $t = 1.0 \text{ ns}$	36
3.6	(a) Harmonic yield as function of order and pump-probe time delay. The spectra were measured with laser system <i>A</i> at an intensity of $4.5 \times 10^{14} \text{ W/cm}^2$ of pump and probe pulse and at a focal position of $z = -2 \text{ mm}$. (b) Outlines from (a). Intensity of the harmonic radiation as function of order for different time delays [Kur13].	37
3.7	Harmonic yield as function of the harmonic order at large pump-probe time delays and comparable parameters to Fig. 3.6. The numbers indicate the delay. The harmonic yields are normalized to the maximum intensity of the 9 th HOH at $t = 12.5 \text{ ns}$ [Kur13].	38
3.8	(a) Harmonic yield as function of order and intensity of the pump pulse at $t = 1.0 \text{ ns}$ [Kur13]. The intensity of the probe pulse was set to $3.7 \times 10^{14} \text{ W/cm}^2$. Outlines from (a) are depicted for the harmonic orders 25 (b) and 17 (c). Note that the harmonic intensity is scaled logarithmic in (a) while linear in (b) and (c). The spectra were measured with laser system <i>A</i>	39
3.9	Harmonic intensity versus harmonic order and intensity of the pump pulse. The delay was set to $t = 1.0 \text{ ns}$, while the I_{probe} was determined to be $9.5 \times 10^{14} \text{ W/cm}^2$. Laser system <i>B</i> has been applied.	40
3.10	Harmonic yield versus order for calculated densities of $\rho \approx 1 \times 10^{18} \text{ cm}^{-3}$ with different values for t and I_{pump} . The spectra were measured with laser system <i>B</i> at an intensity of the probe pulse of $9.5 \times 10^{14} \text{ W/cm}^2$. (a) $t = 12.0 \text{ ns}$ and $I_{\text{pump}} = 3.0 \times 10^{13} \text{ W/cm}^2$. (b) $t = 7.0 \text{ ns}$ and $I_{\text{pump}} = 5.2 \times 10^{14} \text{ W/cm}^2$. (c) $t = 5.0 \text{ ns}$ and $I_{\text{pump}} = 8.1 \times 10^{14} \text{ W/cm}^2$. The spectra are normalized to the maximum yield in (c).	41
4.1	Intensity of the 15 th harmonic order versus the medium position in a Xe gas jet. Laser system <i>B</i> was used with an intensity of $1.3 \times 10^{15} \text{ W/cm}^2$	44
4.2	(a) Harmonic intensity as a function of the harmonic order and medium position z . The delay was set to $t = 1.0 \text{ ns}$ with an intensity of the pump pulse and of the probe pulse of $4.5 \times 10^{14} \text{ W/cm}^2$. The schematics at the top indicate the relative position of the focus to the droplet, with respect to the medium position. (b) Outline of the 19 th harmonic order and (c) the 11 th harmonic order versus medium position. The data has been acquired with laser system <i>A</i>	45
4.3	Intensity of the 15 th harmonic order versus the medium position from water droplets for different delays. Laser system <i>B</i> has been used with the intensities $I_{\text{pump}} = 6 \times 10^{14} \text{ W/cm}^2$ and $I_{\text{probe}} = 1.5 \times 10^{15} \text{ W/cm}^2$. Comparable conditions of the droplet are preserved for $ z < 4.1 \text{ mm}$ (black lines). The scheme at the top indicates the varying expansion of the droplet for different values of z . Each signal has been normalized to its maximum yield.	47

4.4	Spectral broadening and blue shift for the 13 th (a) and 15 th (b) harmonic order for different delays. Laser system <i>A</i> has been applied with an intensity of 3.6×10^{14} W/cm ² for both pulses [Kur13]. The black line indicates the calculated central photon energy of the harmonic orders.	49
4.5	Temporal evolution of spectral splitting of the 13 th (a) and the 15 th harmonic order (b) with an intensity of 7×10^{14} W/cm ² for both pulses and a focal position of $z < 0$ mm [Kur13].	50
4.6	HHG in a Xe gas jet. (a) Pulse duration of 100 fs. (b) Pulse duration of 35 fs (b). Note that the spectra are not efficiency corrected by the calibration curve of the spectrometer.	51
4.7	Spectra of harmonic radiation for pulse durations of (a) 100 fs (laser system <i>A</i>). (b) 35 fs (laser system <i>B</i>) for comparable parameters of the laser systems.	52
4.8	(a) Harmonic yield as a function of order and pump-probe time delay. The spectra were measured with laser system <i>B</i> at an intensity of $I_{\text{pump}} = 4.5 \times 10^{14}$ W/cm ² of pump pulse. The intensity of the probe pulse was $I_{\text{probe}} = 1.4 \times 10^{15}$ W/cm ² at a focal position of $z = -2$ mm. (b) Outlines from (a). Intensity of the harmonic radiation as function of order for different time delays. The spectra are normalized to the intensity of the 9 th harmonic order. Note that the spectra are linearly scaled.	54
4.9	Harmonic yield as function of the harmonic order at large pump-probe time delays and comparable parameters to Fig. 4.8. The harmonic yields are normalized to the maximum intensity of the 9 th HOH at $t = 5.0$ ns.	55
4.10	(a) Harmonic yield versus order and intensity of the pump pulse. Laser system <i>A</i> was used with $I_{\text{pump}} = 2.0 \times 10^{14}$ W/cm ² and $t = 3, 5$ ns. Outlines from (a) for the (b) 13 th , (c) 19 th , (d) 21 st and (e) 23 rd harmonic order [Kur13]. The green line indicates the center of the intensity range for the transition of the order from the cutoff into the plateau. The red line represents the maximum of the harmonic yield as an indicator for I_{sat}	57
4.11	Harmonic yield as function of the harmonic order for comparable parameters to Fig. 4.10 but with $I_{\text{probe}} = 1.1 \times 10^{15}$ W/cm ² . The signal has been normalized to the maximum yield in Fig. 4.10 (c).	58
4.12	(a) Harmonic yield versus order and intensity of the probe pulse with $I_{\text{pump}} = 5 \times 10^{14}$ W/cm ² at $t = 3.0$ ns. Outlines from (a) for the (b) 19 th , (c) 21 st , (d) 23 rd and (e) 29 th harmonic order. The green line indicates the center of the intensity range for the transition of the order from the cutoff into the plateau, the red line represents the maximum of the harmonic yield as indicator for I_{sat}	59
4.13	Highest observed harmonic orders versus the intensity of the probe pulse. Linear approximations are indicated as dashed lines. (a) Measured with laser system <i>A</i> for $t = 3.5$ ns, $I_{\text{pump}} = 2.0 \times 10^{14}$ W/cm ² and 100 fs pulse duration. (b) With laser system <i>B</i> for different delays, $I_{\text{pump}} = 5.3 \times 10^{14}$ W/cm ² and 40 fs pulse duration.	60
4.14	Mapping of the pump-probe time delay to the density evolution of the droplet. The measured harmonic yield versus harmonic order and delay (a) is mapped (red dashed arrows) via the calculated droplet density as function of time (b) onto a function of the density evolution of the droplet (c) for a fixed intensity of the laser pulses.	62
4.15	(a) Classically calculated long (dashed-dotted), cutoff (solid) and a short (dashed) electron trajectory as a function of time for an intensity of the driving field of 1×10^{14} W/cm ² at a central wavelength of 780 nm. (b) Classical excursion distance of the electron contributing to the 19 th harmonic order versus intensity of the driving field.	64

- 4.16 Excursion distance of the electron from the parent ion versus harmonic order (blue) and mean inter-particle distance versus the target density (red). The harmonic order has been calculated using the cutoff law in equation (2.18) for a wavelength of 780 nm. 65
- 4.17 Harmonic signal as a function of the density of the droplet for the (a) 17th, (b) 21st, (c) 25th and (d) 27th order according to Fig. 4.8. Laser system *B* has been applied with intensities of $I_{\text{pump}} = 4.5 \times 10^{14} \text{ W/cm}^2$ and $I_{\text{probe}} = 1.4 \times 10^{15} \text{ W/cm}^2$. The blue line indicates the fit curve $\sim \bar{r} = \frac{1}{\sqrt[3]{\rho}}$ to the measured data. The black line is the maximum tolerable density for the cutoff trajectory, the red line indicates the maximum density for the short trajectory. Within the red area, the density is too high for the generation of the harmonic order. 67
- 4.18 Full spectra of the harmonic radiation for different densities of the droplet corresponding to Fig. 4.17. The numbers indicate the number density in cm^{-3} 68
- 4.19 Double logarithmically scaled plot of the harmonic signal as a function of the density of the droplet for the 21st harmonic order from Fig. 4.17. 69
- 4.20 Signal of the harmonic radiation versus target density and intensity of the probe pulse for the (a) 17th, (b) 21st and (c) outlines from (b). The numbers in (c) indicate the number density in cm^{-3} . Laser system *B* has been applied with $\tau = 40 \text{ fs}$ and with $I_{\text{pump}} = 5 \times 10^{14} \text{ W/cm}^2$. The data has been averaged around 5% of the maximum of each harmonic order and the harmonic signal has been normalized to the maximum. The dashed white lines indicate the maximum tolerable density attributed to the cutoff trajectory ρ_{cutoff} . Note that the data has been interpolated in (a) and (b) with three points between each intensity and density value for better visibility. 70
- 4.21 (a) Signal of the harmonic radiation versus target density and intensity of the probe pulse of the 29th harmonic order. The dashed white lines in (a) indicate the maximum tolerable density attributed to the cutoff trajectory ρ_{cutoff} , the dashed red line depicts the maximum tolerable density attributed to the short trajectory ρ_{short} for the given intensity. The same laser parameters have been applied as in Fig. 4.20. (b) Outlines of (a) for fixed densities. The numbers in (b) indicate the number density in cm^{-3} . (c) Spectrum for an intensity of $I_{\text{probe}} = 0.8 \times 10^{15} \text{ W/cm}^2$ and a density of $2.5 \times 10^{21} \text{ cm}^{-3}$ 71
- 4.22 Conversion efficiency versus mapped density. Laser system *B* has been used with $I_{\text{pump}} = 6.3 \times 10^{14} \text{ W/cm}^2$ and $I_{\text{probe}} = 1.2 \times 10^{15} \text{ W/cm}^2$. The blue dashed curve indicates a fit $\sim \bar{r} = \frac{1}{\sqrt[3]{\rho}}$. Each of the measured data values is averaged over 20000 laser pulses. The error bars resemble the standard deviation. 74
- 5.1 Imaginary part of the refractive index versus wavelength for liquid water at a temperature of 22 °C by KOU *et al.* [Kou93]. 77
- 5.2 Schematic of the laser-induced breakdown. As the pulse propagates through the droplet in (a) to (d), the droplet performs a plasma triggered expansion. The figures depict: the droplet (blue), the focusing geometry (dashed-red), the pump pulse (solid red), electrons (black minuses), ions (red pluses), water molecules and its fragments. 79
- 5.3 (a) Harmonic yield as function of order and intensity of the pump pulse at $t = 1.0 \text{ ns}$ [Kur13]. The intensity of the probe pulse was set to $3.7 \times 10^{14} \text{ W/cm}^2$. Outlines from (a) are depicted for the harmonic orders 25 (b) and 17 (c). Note that the intensity axis is scaled logarithmic in (a) while linear in (b) and (c). The spectra were measured with laser system *A*. 80

5.4	(a) Harmonic intensity versus harmonic order and intensity of the pump pulse. The delay was set to $t = 1.0$ ns, while the I_{probe} was determined to be 9.5×10^{14} W/cm ² . Outlines from (a) are depicted for the harmonic orders 25 (b) and 17 (c). Note that the intensity axis is scaled logarithmic in (a) while linear in (b) and (c). The spectra were measured with laser system <i>B</i>	82
5.5	Measured threshold intensity for LIB I_{LIB} at a wavelength around $\lambda = 580$ nm by NOACK et al. [Noa99].	83
5.6	Single spectra of the harmonic radiation from water droplets for a pulse duration of (a) 100 fs and (b) 35 fs. The numbers within the single spectra indicate the intensity of the pump pulse.	84
5.7	Optimum intensity of the pump pulse for HHG versus harmonic order for a pulse duration of 100 fs (red) and 35 fs (blue). The dashed lines indicate linear fits to the measured data.	85
5.8	Harmonic yield of the (a) 17 th versus the time delay and the intensity of the pump pulse. The dashed white line indicates the threshold intensity for LIB. The intensity of the probe pulse was set to 9.5×10^{14} W/cm ² . Note that the data has been interpolated with three points between each intensity and delay value for better visibility. (b) Outlines from (a) for different time delays. The dashed black line indicated the threshold intensity for LIB. The signals are normalized to the maximum of the harmonic yield.	87
5.9	Harmonic yield of the (a) 27 th order versus the time delay and the intensity of the pump pulse. The dashed white line indicates the threshold intensity for LIB. The intensity of the probe pulse was set to 9.5×10^{14} W/cm ² . Note that the data has been interpolated with three points between each intensity and delay value for better visibility. (b) Outlines from (a) for different time delays. The dashed black line indicated the threshold intensity for LIB.	88
5.10	Density-dependent development of the harmonic yield simulated for the short and long trajectory by STRELKOV et al. [Str05] and measured harmonic yield of the short trajectory for the (a) 17 th and (b) 27 th harmonic order. Laser system <i>B</i> has been applied with $I_{\text{probe}} = 9.5 \times 10^{14}$ W/cm ² . The numbers indicate different intensities of the pump pulse in units of 10^{14} W/cm ² . Linear approximations are indicated by the dashed lines. The signals have been normalized to the maximum yield at each intensity of the pump pulse.	90
5.11	Averaged slope of the linear fit to the harmonic orders 21 to 29 versus intensity of the pump pulse (crosses). The error bars result from the averaging over the different orders. The figure also depicts the fits to the linear approximations of the simulated contribution of the short (blue line) and long trajectory (red line) for an ionized medium as well as the contribution of the short trajectory for a neutral medium (green line) by STRELKOV et al. [Str05].	91
5.12	Integrated harmonic signal of the (a) 17 th , (b) 19 th and (c) 21 st harmonic order versus density. The short (blue) and long (red) trajectories are selected via the focal position with $z > 0$ mm for the short trajectory and $z < 0$ mm for the long trajectory.	93
5.13	Harmonic yield versus order and delay for $I_{\text{pump}} = 3 \times 10^{13}$ W/cm ² and $I_{\text{probe}} = 9.5 \times 10^{14}$ W/cm ²	95
5.14	Threshold energies for breaking all bonds within the droplet (blue), as well as for total dissociation (red).	95

-
- 5.15 Outlines of Fig. 5.13. (a) 15th and (b) 17th harmonic order versus pump probe time delay for different energies of the pump pulse. The harmonic yield has been spectrally averaged around 5% of each harmonic order and normalized to the each maximum. 96
- 6.1 Intensity ratio between water droplets doped with gold nano-spheres and pure water as a function of the harmonic order for different sizes of the nanoparticles. . . 101

List of Tables

1	Abbreviations.	III
2	Mathematical symbols.	V
1	Ionization energies for different states of water and reference atoms for the HOMO and ground state, respectively [Bro11, SM12, NIS13].	97

Curriculum Vitae

Personal Details

Heiko Gustav Kurz
Lister Straße 35
30163 Hannover

born 25th of April 1982 in Gifhorn, Germany
married, German

Professional Experience

since 11/2013 Research fellow at the Institute of Quantum Optics,
Leibniz Universität Hannover

09/2009–10/2013 Grant of a Phd-fellowship within the cluster of excellence *Centre for Quantum Engineering and Space-Time Research (QUEST)*, Leibniz Universität Hannover

Education

06/2008–07/2009 Diploma student at the Ultrafast Laser Laboratory
project: *XUV-Spektroskopie mit einer Wasserquelle*
Institut für Quantenoptik, Gottfried Wilhelm Leibniz Universität Hannover

01/2007–07/2007 Visiting student at the MOLPOL-laboratory of the Laser-Centers Riga
University of Latvia
Project: *Dark and bright resonances in KCs-molecules*

10/2003–06/2008 Gottfried Wilhelm Leibniz Universität Hannover
Studies in general physics

08/2002–06/2003 Alternatice Civillian Service at
Gesellschaft für integrative Behindertenarbeit mbH

08/1989–06/2002 Humboldt-Gymnasium Gifhorn
Abitur

Scientific Publications

- 2013 H. G. KURZ, D. S. STEINGRUBE, D. RISTAU, M. LEIN, U. MORGNER AND M. KOVACEV
High-Order Harmonic Generation from Dense Water Microdroplets
Physical Review A Vol. **87** 063811 (2013)
- 2012 H. G. KURZ, D. STEINGRUBE, D. RISTAU, AND M. LEIN, U. MORGNER AND M. KOVACEV,
Phase-matching aspects in high-order harmonic generation from liquid water drop-lets in Research in Optical Sciences, OSA Technical Digest (Optical Society of America, 2012), HM3C.7., HILAS 2012

Contributions to International Conferences

- 2013 H. G. KURZ, M. KRETSCHMAR, T. NAGY, D. RISTAU, M. LEIN, U. MORGNER AND M. KOVACEV
Non-Adiabatic Effects in High-Order Harmonic Generation from Liquid Water Droplets
ATTO2013, 4th International Conference on Attosecond Physics Paris, France
- 2013 H. G. KURZ, D. S. STEINGRUBE, D. RISTAU, M. LEIN, U. MORGNER AND M. KOVACEV
Systematic studies of high-order harmonic generation from water microdroplets
noindent *523rd Wilhelm und Else Heraeus Seminar* Bad Honef, Germany
- 2012 H. G. KURZ, D. STEINGRUBE, D. RISTAU, AND M. LEIN, U. MORGNER AND M. KOVACEV
Transient Phase Matching during High-Order Harmonic Generation in Water Drop-lets
XVIIIth International Conference on Ultrafast Phenomena Lausanne, Switzerland
- 2012 H. G. KURZ, D. STEINGRUBE, D. RISTAU, AND M. LEIN, U. MORGNER AND M. KOVACEV
Phase-matching Studies of High-Order Harmonic Generation from Water Microdroplets
Gordon Research Conference on Multiphoton Processes Mount Holyoke College South Hadley, USA

- 2012 H. G. KURZ, D. STEINGRUBE, D. RISTAU, AND M. LEIN, U. MORGNER AND M. KOVACEV
Phase-matching aspects in high-order harmonic generation from liquid water drop-lets
High-Intensity Lasers and High-Field Phenomena (HILAS) Berlin, Germany
- 2010 H. G. KURZ, D. STEINGRUBE, T. VOCKERODT, D. RISTAU, AND M. LEIN, U. MORGNER AND M. KOVACEV
High-harmonic generation from water microdroplets
Gordon Research Conference on Multiphoton Processes Tilton, USA

Danksagung

Am Ende möchte ich mich bei allen Personen bedanken, die zum Gelingen dieser Arbeit maßgeblich beigetragen haben.

Ein besonderer Dank gebührt Uwe Morgner und Milutin Kovačev, die mir die Möglichkeit geboten haben in diesem äußerst interessanten Forschungsgebiet zu arbeiten und mit viel Optimismus und Rat für Unterstützung gesorgt haben.

Manfred Lein möchte ich danken für die fachliche Unterstützung und die Übernahme des Korreferats.

I would like to thank especially Hamed Merdji for taking over the review of my thesis.

Bei Herrn Prof. Clemens Walther bedanke ich mich für den Vorsitz bei der Disputation.

Danke an alle Korrekturleser, insbesondere aber an Thomas, der sich viel Mühe gemacht hat meine Gedankengänge nachzuvollziehen und zu hinterfragen.

Vielen Dank an Martin, Moritz, Tino, Hauke, Stefan, Guido und Thomas für das schöne Betriebsklima.

Martin, Daniel und Tamas danke ich für die fachliche Unterstützung und die gute Zusammenarbeit.

Ein herzlicher Dank geht auch an Kai-Martin Knaak, der mit Rat und Tat in elektronischen Fragen zur Seite stand. Weiterhin danke ich dem Team der Feinmechanikwerkstatt für die Unterstützung durch die Herstellung diverser Komponenten.

Dem Sekretariat möchte ich für all die Organisation drumherum danken.

Schließlich möchte ich mich bei der gesamten Arbeitsgruppe Morgner für die schöne Arbeitsatmosphäre und die große Hilfsbereitschaft bedanken.

Ganz besonders möchte ich meinen Freunden und meiner Familie für ihre Unterstützung in den letzten Jahren danken. Vor allem aber danke ich Christiane.

Vielen Dank!

